CWP-747
April 2013



Wavefield tomography using extended images

Tongning Yang

- Doctoral Thesis -
Geophysics

Defended on March 27, 2013

Advisor:	Prof. Paul Sava
Committee Members:	Prof. Dave Hale
	Prof. Yaoguo Li
	Prof. Mark Lusk
	Prof. Paul Martin

Center for Wave Phenomena
Colorado School of Mines
Golden, Colorado 80401
303.384.2178
http://cwp.mines.edu

WAVEFIELD TOMOGRAPHY USING EXTENDED IMAGES

by

Tongning Yang

ABSTRACT

Estimating an accurate velocity model is crucial for seismic imaging to obtain a good understanding of the subsurface structure. The objective of this thesis is to investigate methods of velocity analysis by optimizing seismic images.

A conventional seismic image is obtained by zero-lag crosscorrelation of wavefields extrapolated from a source wavelet and recorded data on the surface using a velocity model. The velocity model provides the kinematic information needed by the imaging algorithm to position the reflectors at correct locations and to focus the image. In complex geology, wave-equation migration is a powerful tool for accurately imaging the earth's interior; the quality of the output image, however, depends on the accuracy of the velocity model. Given such a dependency between the image and model, analyzing the velocity information from the image is still not intuitive and often ambiguous. If the nonzero space- and time-lags information are preserved in the crosscorrelation, the output are image hypercube defined as extended images. Compared to the conventional image, the extended images provide a straightforward way to analyze the image quality and to characterize the velocity model accuracy.

Understanding the reflection moveout is the key to developing velocity model building methods using extended images. In the extended image space, reflections form coherent objects which depend on space (lags) and time (lags). These objects resemble cones which ideally have their apex at zero space and time lags. The symmetry axis of the cone lies along the time-lag axis. The apex of the cone is located at zero lags only if the velocity model is accurate. This corresponds to the situation when reflection energy focuses at origin in both the space- and time-lag common-image gathers (the slices at zero time and space lags, respectively). When the velocity model is inaccurate, the cone shifts along the time-lag axis. This results in residual moveout in space-lag gathers (zero time-lag slice) and defocusing in

time-lag gathers (zero space-lag slice). These phenomena are correlated, and they are a rich source of information for velocity model updates.

The extended image distortions caused by velocity model errors can be used to design velocity model building algorithms. When the extended image cones shift, the distance and direction of their apex away from zero time lag constrain model errors. This information can be used to construct an image perturbation, from which a slowness perturbation is inverted under the framework of linearized wave-equation migration velocity analysis. Alternatively, one can formulate a non-linear optimization problem to reconstruct the model by minimizing this image error. This approach requires the adjoint-state method to compute the gradient of the objective function, and iteratively update the model in the steepest-descent direction.

The space-lag subset of extended images has been used to reconstruct the velocity model by differential semblance optimization for a decade. The basis of the method is to penalize the defocusing in the gathers and to focus the reflection energy at zero lags by optimizing the model. The assumption that defocusing is caused by velocity model error is violated where the subsurface illumination is uneven. To improve the robustness and accuracy of the technique, the illumination compensation must be incorporated into the model building. The illumination compensation effectively isolates the defocusing due to uneven illumination or missing data. The key is to construct an illumination-based penalty operator by illumination analysis. Such a penalty automatically downweights the defocusing from illumination effects and allows the inversion to suffer less from the effects of uneven illumination and to take into account only the image error due to inaccurate velocity models.

One major issue for differential semblance optimization with space-lag gathers is the cost of computing and storing the gathers. To address the problem, extended space- and time-lag point gathers can be used as an alternative to the costlier common-image gathers. The point gathers are subsets of extended images constructed sparsely in subsurface on reflectors. The point gathers share similar reflection moveout characteristics with space-lag gathers, and thus differential semblance optimization can be implemented with such gathers. The point

gathers reduce the computational and storage cost required by space-lag gathers especially in 3-D applications. Furthermore, the point gathers avoid the dip limitation in space-lag gathers and more accurately characterize the velocity information for steep reflections.

TABLE OF CONTENTS

ABSTRACT iii

LIST OF FIGURES ix

ACKNOWLEDGMENTS xv

CHAPTER 1 GENERAL INTRODUCTION 1

1.1 Thesis Organization 3

1.2 Publications 5

CHAPTER 2 MOVEOUT ANALYSIS OF EXTENDED IMAGES 8

2.1 Summary 8

2.2 Introduction 9

2.3 Wave-equation Imaging Conditions 11

2.3.1 Moveout analysis for extended images – point source 12

2.3.2 Moveout analysis for extended images – plane-waves 21

2.4 Examples 26

2.5 Discussion 37

2.6 Conclusions 42

CHAPTER 3 WAVE-EQUATION MIGRATION VELOCITY ANALYSIS WITH TIME-SHIFT IMAGING 43

3.1 Summary 43

3.2 Introduction 44

3.3 Theory 47

3.4 Example 52

3.5 Discussion 64

3.6 Conclusions 65

CHAPTER 4 IMAGE-DOMAIN WAVEFIELD TOMOGRAPHY WITH EXTENDED COMMON-IMAGE-POINT GATHERS 67

4.1 Summary 67

4.2 Introduction 68

4.3 Theory 71

4.4 Examples 76

4.5 Discussion 88

4.6 Conclusions 89

CHAPTER 5 ILLUMINATION COMPENSATION FOR IMAGE-DOMAIN WAVEFIELD TOMOGRAPHY 90

5.1 Summary 90

5.2 Introduction 91

5.3 Theory 94

5.3.1 Gradient computation for DSO 94

5.3.2 Construction of illumination-based penalty 97

5.3.3 Gradient computation with illumination-based penalty 101

5.4 Examples 101

5.5 Discussion 122

5.6 Conclusions 123

CHAPTER 6 3D IMAGE-DOMAIN WAVEFIELD TOMOGRAPHY USING TIME-LAG EXTENDED IMAGES 124

6.1 Summary 124
6.2 Introduction 125
6.3 Theory 127
6.4 Examples 130
6.5 Discussion 141
6.6 Conclusions 142
6.7 Acknowledgments 143
6.8 Disclaimer 143
CHAPTER 7 GENERAL CONCLUSIONS 144
7.1 Main Results 144
7.1.1 Moveout characterization of extended images 144
7.1.2 Velocity analysis using time-lag gathers 144
7.1.3 Velocity analysis using space- and time-lag extended images 145
7.1.4 Illumination compensated wavefield tomography 145
7.2 Future Work 146
7.2.1 More waves: from reflection to full wavefields 146
7.2.2 More parameters: from isotropy to anisotropy 146
7.2.3 More domains: from image domain to image and data domains 147
REFERENCES CITED 148
APPENDIX - PERMISSION OF PAPERS 155
A.1 Permission From Publishers 155
A.2 Permission From Co-authors 155

LIST OF FIGURES

Figure 2.1 Geometry of a reflection experiment. S, R and C identify the positions of the source, receiver and reflection, respectively. The reflector is located at distance d from the source position in the direction of the vector n. The position of the CIG relative to the source is indicated by the vectors c and z. 13

Figure 2.2 (a) Source wavefield in a homogeneous medium represented by a cone in space-time. (b) Receiver wavefield in a homogeneous medium represented by the mirror image of the source wavefield relative to the reflector. (c) Intersections of the source and receiver wavefields reconstructed with correct velocity. The projection of the intersection onto Cartesian spatial coordinates indicates the position of the reflector. . 14

Figure 2.3 Geometric illustration of the imaging condition. The black line represents a planar reflection. The red and blue arrow lines represent the source and receiver ray, respectively. The solid lines are the corresponding wavefronts and they intersect at the depth of the reflection, which corresponds to the conventional imaging condition. The dash lines are the wavefront shifted by $\boldsymbol{\lambda}$ and they intersect at the same CIG location but right above the original depth, which corresponds to the extended imaging condition. 16

Figure 2.4 (a) Source wavefield in a homogeneous medium constructed using an incorrect velocity. The wavefield forms a cone in space-time and has a different shape compared with the wavefield constructed with the correct velocity model. (b) Receiver wavefield in a homogeneous medium constructed using an incorrect velocity. The wavefield forms a cone in space-time and has a different shape relative to the wavefield constructed in the correct velocity, and is also shifted along the time axis. (c) Intersections of the source and receiver wavefields reconstructed with incorrect velocity. The curved line, which is the projection of the intersection onto Cartesian spatial coordinates, indicates the position of the reflector. The image is distorted compared to the case when the correct velocity model is used. 19

Figure 2.5 Cartoon describing wave propagation in an inhomogeneous medium. The wavepaths in the local region around the reflection point can be approximated with straight lines. 22

Figure 2.6 Cone formed by the envelope of the moveout surfaces corresponding to individual plane-waves for a horizontal reflector in (a) the correct velocity case, the focus of the cone occurs at zero space- and time-lags and (b) the incorrect velocity case, the focus of the cone shifts to a nonzero time-lag. Cone formed by the envelope of the moveout surfaces corresponding to individual plane-waves for a dipping reflector in (c) the correct velocity case, the focus of the cone occurs at zero space- and time-lags and (d) the incorrect velocity case, the focus of the cone shifts to a nonzero time-lag. The thick line corresponds to the slice of the cone cut at zero time-lag. 27

Figure 2.7 Migrated images corresponding to (a) correct velocity and (b) incorrect velocity. 29

Figure 2.8 Space-lag CIG for $\tau = \{-0.20, 0, +0.20\}$ s. Panels (a)-(c) correspond to correct velocity. Panels (d)-(f) correspond to incorrect velocity. The dash and solid line overlain corresponds to the derived analytic functions of point source and plane-wave source, respectively. 31

Figure 2.9 Time-lag CIG for $\lambda_x = \{-0.3, 0, +0.3\}$ km. Panels (a)-(c) correspond to correct velocity. Panels (d)-(f) correspond to incorrect velocity. The dash and solid line overlain corresponds to the derived analytic functions of point source and plane-wave source, respectively. 32

Figure 2.10 Migrated images corresponding to (a) correct velocity and (b) incorrect velocity. 33

Figure 2.11 Envelope of the moveout surfaces at different time-lag for correct velocity. Panels (a)-(c) correspond to slices at $\tau = \{-0.15, 0, +0.15\}$ s, respectively. Panels (d)-(f) show the same slices overlain by the derived analytic envelope function. 35

Figure 2.12 Envelope of the moveout surfaces at different time-lag for incorrect velocity. Panels (a)-(c) correspond slices to $\tau = \{-0.15, 0, +0.15\}$ s, respectively. Panels (d)-(f) show the same slices overlain by the derived analytic envelope function. 36

Figure 2.13 Velocity profile of the Sigsbee model. 37

Figure 2.14 The migrated images corresponding to (a) correct velocity model and (b) incorrect velocity model. 38

Figure 2.15 Moveout surfaces at different time-lags for correct velocity. Panels (a) and (b) correspond to slices of the cone at $\tau = \{-0.15, 0\}$ s, respectively. 39

Figure 2.16 Moveout surfaces at different time-lags for incorrect velocity. Panels (a) and (b) correspond to slices of the cone at $\tau = \{-0.15, 0\}$ s, respectively. 40

Figure 3.1 Velocity profiles of the layers model. (a) The true velocity model. (b) The background velocity model with a constant velocity of the first layer 1.5 km/s. (c) The updated velocity model. 53

Figure 3.2 Images migrated with (a) the true velocity model, (b) the background velocity model, and (c) the updated velocity model. The dash lines represent the true position of the reflections. 54

Figure 3.3 Time-shift CIGs migrated with the background model (a) at $x = 1.2$ km, (b) at $x = 1.8$ km, and (c) at $x = 2.3$ km. Time-shift CIGs migrated with the updated model at (d) $x = 1.2$ km, (e) at $x = 1.8$ km, and (f) at $x = 2.3$ km. The overlain solid lines represent picked focusing error. The dash lines represent zero time shift. 55

Figure 3.4 (a) Focusing error panel corresponding to the background model. (b) Focusing error panel corresponding to the updated model. 56

Figure 3.5 Velocity profiles of Sigsbee 2A model. (a) The true velocity model, (b) the background velocity model, and (c) the updated model. 58

Figure 3.6 Images migrated with (a) the true velocity model, (b) the background velocity model, and (c) the updated velocity model. 59

Figure 3.7 Time-shift CIGs migrated with the background model, (a) at $x = 13.0$ km, (b) at $x = 14.8$ km, and (c) at $x = 16.6$ km. Time-shift CIGs migrated with the updated model, (d) at $x = 13.0$ km, (e) at $x = 14.8$ km, and (f) at $x = 16.6$ km. The overlain solid lines represent picked focusing error. The dash lines represent zero time shift. 60

Figure 3.8 (a) Focusing error panel corresponding to the background model. (b) Focusing error panel corresponding to the updated model. 61

Figure 3.9 Angle-domain CIGs migrated with the background model, (a) at $x = 13.0$ km, (b) at $x = 14.8$ km, and (c) at $x = 16.6$ km. Angle-domain CIGs migrated with the updated model, (d) at $x = 13.0$ km, (e) at $x = 14.8$ km, and (f) at $x = 16.6$ km. 62

Figure 4.1 The penalty operators for CIPs on (a) horizontal reflector and (b) vertical reflector. 72

Figure 4.2 (a) The true velocity model, (b) the initial velocity model, and (c) the updated velocity model. 77

Figure 4.3 The images migrated with (a) the true velocity model, (b) the initial velocity model, and (c) the updated velocity model. 78

Figure 4.4 The space-lag CIGs constructed for the vertical reflector at x=1 km migrated with (a) the correct velocity, (b) the initial velocity, and CIGs at constructed for the horizontal reflector x=2.5 km migrated with (c) the correct velocity, (d) the initial velocity. 79

Figure 4.5 The CIPs at x=1 km, z=0.8 km migrated with (a) the correct velocity, (b) the initial velocity, compared with Figure 4.4(a) and Figure 4.4(b). CIPs at x=1.7 km, z=2.5 km migrated with (c) the correct velocity, (d) the initial velocity, compared with Figure 4.4(c) and Figure 4.4(d). . . . 80

Figure 4.6 (a) The true velocity variation which is the target of inversion. The gradient constructed from (b) CIPs on the horizontal reflector only, (c) CIPs on the vertical reflector only, (d) CIPs on both the horizontal and vertical reflectors. 81

Figure 4.7 (a) The true model used to generate the data. (b) The initial model used in the velocity inversion. (c) The updated model after 20 iterations of inversion using CIPs. 83

Figure 4.8 (a) The migrated image and (b) the angle-domain gathers obtained using the true model. 84

Figure 4.9 (a) The migrated image overlain with the CIPs location, and (b) the angle-domain gathers obtained using the initial model. 85

Figure 4.10 The weighting function based on the subsurface illumination. 86

Figure 4.11 (a) The migrated image overlain with the CIPs locations, and (b) the angle-domain gathers obtained using the updated model. 87

Figure 5.1 (a) The true model used to generate the data, and (b) the initial constant model for inversion. 102

Figure 5.2 The shot gathers at 2.0 km showing a gap of 0.6 km in the acquisition surface. The gap simulate an obstacle which prevents data acquisition, e.g., a drilling platform. 103

Figure 5.3 (a) The migrated image, (b) space-lag gathers, and (c) angle-domain gathers obtained using the true model and gap data. 104

Figure 5.4 (a) The migrated image, (b) space-lag gathers, and (c) angle-domain gathers obtained using the true model and full data. 105

Figure 5.5 (a) The migrated image, (b) space-lag gathers, and (c) angle-domain gathers obtained using the initial model and gap data. 106

Figure 5.6 (a) The migrated image, (b) space-lag gathers, and (c) angle-domain gathers obtained using the initial model and gap data. 107

Figure 5.7 (a) The conventional DSO penalty operator. (b) The gathers obtained with demigration/migration showing the illumination effects. (c) The illumination-based penalty operator constructed from the gathers in Figure 5.7(b). 108

Figure 5.8 The reconstructed models using (a) the conventional DSO penalty, and (b) the illumination-based penalty. 109

Figure 5.9 (a) The migrated image, (b) space-lag gathers, and (c) angle-domain gathers obtained using the reconstructed model with the DSO penalty. 110

Figure 5.10 (a) The migrated image, (b) space-lag gathers, and (c) angle-domain gathers obtained using the reconstructed model with the illumination-based penalty. 111

Figure 5.11 (a) The true model and (b) the initial model in the target area of the Sigsbee model. 114

Figure 5.12 (a) The migrated image, (b) space-lag gathers, and (c) angle-domain gathers obtained using the reconstructed model with the true model. . 115

Figure 5.13 (a) The migrated image, (b) space-lag gathers, and (c) angle-domain gathers obtained using the reconstructed model with the initial model. 116

Figure 5.14 (a) The gathers obtained with demigration/migration showing the illumination effects. (b) The illumination-based penalty operator constructed from the gathers in Figure 5.14(a). The light areas cover the defocusing due to the illumination. 117

Figure 5.15 The reconstructed models using (a) the DSO penalty and (b) the illumination-based penalty. 118

Figure 5.16 (a) The migrated image, (b) space-lag gathers, and (c) angle-domain gathers obtained using the reconstructed model with the DSO penalty. 119

Figure 5.17 (a) The migrated image, (b) space-lag gathers, and (c) angle-domain gathers obtained using the reconstructed model with the illumination-based penalty. 120

Figure 6.1 (a) The layered velocity model, and (b) migrated image obtained with the initial model, the constant velocity of the first layer of the true model. 131

Figure 6.2 Time-lag gathers obtained with the initial model. The gather is located at at $x = 2.25$ km, $y = 2.25$ km. The yellow dash line corresponds to the picked focusing error $\Delta\tau$. 132

Figure 6.3 (a) The sensitivity kernel obtained with a single shot, and (b) the gradient obtained with all shots. 133

Figure 6.4 (a) The focusing error extracted from the time-lag gathers. (b) The gradient mask obtained using 6.11. 134

Figure 6.5 The gradient obtained after applying the mask. 135

Figure 6.6 North Sea field data example. (a) The inital model used for the inversion, and (b) the migrated image obtained with the initial model. 137

Figure 6.7 North Sea field data example. (a) The updated model obtained after the inversion, and (b) the migrated image obtained with the updated model. 138

Figure 6.8 Angle-domain gathers obtained with the initial model at (a) $y = 3$ km, (b) $y = 6$ km, and (c) $y = 9$ km. 139

Figure 6.9 Angle-domain gathers obtained with the updated model at (a) $y = 3$ km, (b) $y = 6$ km, and (c) $y = 9$ km. 140

Figure A.1 Permission from journal *Geophysics*. 155

Figure A.2 Permission from journal *Geophysical Prospecting*. 155

Figure A.3 Permission from co-author Jeffrey Shragge. 156

Figure A.4 Permission from co-author Paul Sava. 156

ACKNOWLEDGMENTS

Five years ago, when I landed in Denver at night after an almost 26-hour trip, there were moments I was so unsure about what the future holds for me, and it was interacting to think about how my Ph.D. life in a foreign country would be And now, as my Ph.D. study is approaching an end, I would say that it is not much different from the ordinary life, there were good times, bad times, cheers and frustrations. However, it meant so much to me because not only did I learn so much in several years of Ph.D. study, but I also learned "how to learn", and this will benefit me for life time.

Looking back at my journey, there were so much unforgettable memories but the first thing came to my mind is the desire to express my gratitude to my advisor Paul Sava. I was motivated by him to work on velocity model building and his great knowledge helped me identify the appropriate topic for my thesis. I also learned countless skills from Dr. Sava to overcome challenges and accomplish my research and thesis. The list includes seismic imaging, migration velocity analysis, reproducible programming, and time management. I also acknowledge my committee members: Dr. Dave Hale, Dr. Yaoguo Li, Dr. Mark Lusk, and Dr. Paul Martin for their suggestions and comments on my research and course work. Other professors at CWP and in the Geophysics Department are great sources of knowledge as well. Dr. Ilya Tsvankin solidified the fundamentals of seismology for my study. I learned digital signal processing and geophysical computing skills in an enjoyable and exciting way from Dr. Dave Hale. Dr. Yaoguo Li taught me about the inverse problem. The passion for education and the insight into science of Dr. Roel Snieder is a great lesson in my scientific career. Dr Ken Larner's "red pencil" made me aware of the importance of scientific writing and communication.

The advice and help received from senior students such as Myoung Jae Kwon, Yuanzhong Fan, Xiaoxiang Wang, and Jia Yan, have made me feel that I belong to a big warm family.

Academic study is not perfect without fruitful discussions with fellow students. The iTeam seminar time is always enjoyable thanks to all the members (Jia Yan, Ashley Fish, Jeff Godwin, Thomas Cullison, Ran Xuan, Gabriela Melo, Francesco Perrone, Esteban Diaz, Natalya Patrikeeva, Jason Jennings, Yuting Duan, Detchai Ittharat). The numerous discussions with Simon Luo, Luming Liang, Clement Fleury, and Yong Ma have also been inspiring and intriguing.

I would like to take the opportunity to thank my mentor Ioan (Nick) Vlad, who helped me survive in Trondheim, Norway when I interned with Statoil. Special thanks also go to Madhav Vyas and Petr Jilek, who guided and mentored me during the internship at BP. Their scientific insight always inspired new ideas for projects and motivated lots of interesting discussions.

The nice staff at CWP and in the department are a "must have" in my Ph.D. study. Pam, Michelle and Dawn tackled all the administrative burdens. John was always there for all the Linux computer issues and offered "first aid" in his math clinic seminar. Shingo and Barbara smoothed all our publication processes and are great listeners for everyone. Diane taught me all the necessary skills to improve my manuscripts.

At last, I would like to thank my parents. They have always been there for me, loved and supported me unconditionally, and were extremely proud for everything I have achieved. It is impossible to calculate how much I owe my wife, Hui Peng, who always stands by my side and gives all the love and support I need through tough times. My parents and my wife are the rocks of all my determination and courage to take the responsibilities, overcome the challenges, and chase my dreams.

CHAPTER 1

GENERAL INTRODUCTION

Imaging is one of the most important tasks in seismic exploration. The goal of seismic imaging is to provide accurate information for subsurface structures and to guide well drilling for oil and gas production. In practice, seismic imaging is referred to as seismic migration. It converts seismic data recorded on the surface into a reflectivity map of the subsurface. During this procedure, a velocity model is required to provide kinematic information for wave propagation in the medium. Therefore, one needs not only the data, but also a velocity model for migration to generate a subsurface image.

Nowadays, the focus of exploration has moved to regions characterized by complex subsurface structure. In such areas, wavefield-based migration, e.g. one-way wave-equation migration or reverse-time migration, is a powerful tool for accurately imaging the earth's interior (Gray et al., 2001; Etgen et al., 2009). The realization of such a capability, however, relies on the fact that the velocity model used for migration is accurate and has sufficiently high resolution. This is because wavefield-based migration is sensitive to velocity model error, and thus the quality of the final image greatly depends on the accuracy of the velocity model. As a result, a key challenge for imaging in complex geology is an accurate determination of the velocity model and it remains one of the most difficult problems (Virieux and Operto, 2009; Symes, 2009).

Velocity model building methods can be divided into two categories according to the domain in which the velocity estimation is implemented. The first category comprises the data-domain approaches which use the recorded seismic data as the input (Bishop et al., 1985; Mora, 1987; Song et al., 1995; Pratt, 1999; Vigh and Starr, 2008a). The second category contains the image-domain approaches which take migrated images as the input (Al-Yahya, 1989; Stork, 1992; Biondi and Sava, 1999; Sava and Biondi, 2004a; Shen and Symes, 2008).

In this thesis, I focus on the image-domain velocity analysis methods.

Image-domain velocity analysis methods are developed based on the principle that the quality of the seismic image is optimized when the data are migrated with the correct velocity model. Thus, the velocity model is updated by optimizing the properties measuring the coherence of migrated images. Although the image quality relies on the velocity model accuracy, it is not straightforward, however, to extract the velocity information from the image. Instead, the velocity information is obtained from common image gathers, i.e. a group of images sorted by chosen parameters such as offset (Mulder and ten Kroode, 2002), shot index (Al-Yahya, 1989), or angle (Sava and Fomel, 2003; Biondi and Symes, 2004).

Conventional ray-based velocity analysis approaches use common-image gathers generated from Kirchhoff migration to reconstruct the velocity model (Toldi, 1989; Liu, 1997; Chauris et al., 2002). Such methods, however, fail to produce a good velocity model in complex geology, e.g. subsalt environments. One major reason which accounts for this failure is that in these regions, the gathers suffer from the artifacts caused by the inherent multi-pathing problem of ray-based imaging algorithms. Furthermore, the ray-based imaging algorithms also become unstable since the sharp and high velocity contrast (salt body) violates the asymptotic assumption.

Wave-equation migration consists of two main steps: the wavefield reconstruction and the application of an imaging condition. The conventional image is obtained by zero-lag cross-correlation. The extended images, which are common-image gathers from wave-equation migration, are obtained by preserving the information from non-zero cross-correlation lags in the imaging condition. Compared to the gathers from Kirchhoff migration, extended images are free of artifacts caused by multi-pathing problem (Stolk and Symes, 2004). Thus, the extended images are robust and effective to characterize and extract the velocity information, and suitable for velocity analysis in complex subsurface areas. In addition, wave-equation engine is also preferred in velocity model building as it can handle complicated wave propagation phenomena and is consistent with the finite-frequency characteristic of wave-

equation migration. Consequently, wavefield-based velocity analysis methods (also known as image-domain wavefield tomography) using extended images are expected to produce more accurate, higher resolution velocity models (Shen and Calandra, 2005; Shen and Symes, 2008).

1.1 Thesis Organization

The goal of this thesis is to understand the characteristics of extended images and to develop velocity model building methods using extended images and to improve the accuracy of velocity analysis based on extended images.

In **Chapter 2**, I derive the analytic formula describing the moveout of extended images. This formula characterizes the kinematics of extended images obtained from a single source and from multiple sources. The analysis connects the velocity model error and corresponding features of the extended images. I show that space- and time-lag extension are correlated and form coherent objects resembling cones in the extended space. When the velocity model error exists, the cone is shifted along the time-lag direction. This result shows that both the residual moveout in space-lag gathers and defocusing in time-lag gathers are the consequences of shifted cones due to the incorrect velocity model. The velocity model building methods introduced in the rest of the thesis are based on the theoretical analysis developed in this chapter.

In **Chapter 3**, I propose a wave-equation migration velocity analysis method using time-lag extended images. The analysis in Chapter 2 show that focusing error measures the shift of the cone along the time-lag axis, and thus characterizes the velocity model error. This focusing error is extracted to construct an image perturbation using the Born approximation. The image perturbation is then used to invert for the slowness perturbation by formulating a linearized relationship between the image and slowness perturbations. The model is updated by the obtained slowness perturbation. This method is more efficient to obtain the image perturbation than conventional methods because no expensive migration scan is required.

In **Chapter 4**, I develop a wavefield tomography method using space- and time-lag extended images which are constructed locally on reflections as common-image point gathers. These point gathers characterize the velocity model error in a way similar to space-lag gathers. Unlike space-lag gathers, the point gathers use only lags to evaluate velocity information and thus avoid the bias toward depth caused by constructing the gathers with depth axis. Additionally, the computational and storage cost for the point gathers are reduced since they are sparsely sampled on reflectors in the subsurface. The inverse problem is formulated using the principle of differential semblance optimization, the penalty operator is designed to penalize the residual moveout at nonzero lags and focus the energy at zero lags. The gradient is computed using the adjoint-state method. The space- and time-lag point gathers can be used as an efficient alternative to space-lag gathers when differential semblance optimization is implemented and improves the accuracy of model building in areas with steeply dipping structures.

In **Chapter 5**, I introduce an illumination compensation strategy for differential semblance optimization (DSO) using space-lag gathers. In DSO, a penalty operator is used to highlight the defocusing in space-lag gathers caused by incorrect velocity models. The uneven illumination, however, also gives rise to defocusing indistinguishable from those due to velocity model errors. In order to mitigate such negative impact of uneven illumination, our method replaces the conventional penalty operator by an illumination-based penalty operator which is constructed from the illumination analysis. Illumination gathers are constructed through demigration- migration thus capturing the illumination effects. The illumination-based penalty operator is then obtained by taking the inverse of the illumination gathers. The new penalty operator removes the defocusing due to uneven illumination and leaves only the image features due to the velocity error in the model update. By eliminating the illumination effects, this approach improves the accuracy and robustness of conventional velocity analysis techniques using space-lag gathers in complex geology such as subsalt areas.

In **Chapter 6**, I develop a 3D wavefield tomography using time-lag extended images and apply it to a 3D ocean-bottom cable data. This method uses focusing information extracted from time-lag gathers just like the approach proposed in Chapter 2. However, instead of constructing an image perturbation, the focusing error is used directly to construct the objective function and compute the gradient via the adjoint-state method. Although it shares many similarities to wave-equation traveltime inversion, this approach has a more robust focusing error measurement in presence of noise and complex structure because the focusing information is evaluated from time-lag gathers. The technique is efficient in 3D compared to differential semblance optimization where the 5D space-lag gathers are too expensive to compute and store. A real data example demonstrates that the image is more coherent and focused after applying the velocity updates, which helps the interpretation of the reservoirs.

Finally, I draw conclusions for the thesis and suggest future work directions in **Chapter 7**. In summary, this thesis provide a quantitative analysis for moveout of extended images, with a particular focus on the image features caused by the velocity model error. Based on the analysis, several wavefield tomography methods using different variation of extended images are developed to reconstruct the velocity models in complex geology. An illumination compensation scheme is also introduced aimed at improving the robustness of the method in uneven illuminated subsalt areas. Future research involves using diving waves and multiple for additional model information, extension of the methods into anisotropic media, and combining the methods with full-waveform inversion.

1.2 Publications

Chapters 2-6 of the thesis have been published in, submitted to, or will be submitted to journals listed below:

- **Yang, T.**, Sava, P.C., 2010, Moveout analysis of wave-equation extended images, *Geophysics*, v. 75, pp. S151-S161 (Chapter 2)

- **Yang, T.**, Sava, P.C., 2011, Wave-equation migration velocity analysis with time-shift imaging, *Geophysical Prospecting*, v. 59, pp. 635-650 (Chapter 3)

- **Yang, T.**, Sava, P.C., 2012, Image-domain wavefield tomography with extended common-image-point gathers, *Geophysical Prospecting*, submitted for publication (Chapter 4)

- **Yang, T.**, Shragge, J., Sava, P.C., 2012, Illumination compensation for image-domain wavefield tomography, *Geophysics*, submitted for publication (Chapter 5)

- **Yang, T.**, Sava, P.C., 2013, 3D image-domain wavefield tomography using time-lag extended images, *Geophysics*, to be submitted for publication (Chapter 6)

  The idea discussed in Chapter 5 also contributes to the following article:

- Shragge, J., **Yang, T.**, Sava, P.C., 2013, Time-lapse image-domain tomography using adjoint-state methods, *Geophysics (Letters)*, submitted for publication.

In addition to the articles list above, I have also published the following expanded abstracts in conference proceedings at international conferences:

- **Yang, T.**, Shragge, J., and Sava, P.C., 2012, Illumination compensation for subsalt image-domain wavefield tomography, Proceedings of the 82nd Annual International Meeting, Society of Exploration Geophysicists.

- Shragge, J., **Yang, T.**, and Sava, P.C., 2012, Time-lapse image-domain velocity analysis using adjoint-state methods, Proceedings of the 82nd Annual International Meeting, Society of Exploration Geophysicists.

- **Yang, T.**, Shragge, J. and Sava, P.C., 2012, Illumination compensation for image-domain wavefield tomography, Proceedings of the 74th Annual International Meeting, European Association of Geoscientists and Engineers.

- **Yang, T.** and Sava, P.C., 2012, Image-domain wavefield tomography for complex geologic structures, EAGE/ACGGP First Latin American Geophysics Workshop, Geophysical Imaging in Complex Areas and Reservoir Characterization, Cartagena, Columbia.

- **Yang, T.** and Sava, P.C., 2011, Image-domain waveform tomography with two-way wave-equation, Proceedings of the 81st Annual International Meeting, Society of Exploration Geophysicists.

- **Yang, T.** and Sava, P.C., 2011, Waveform inversion in the image domain, Proceedings of the 73rd Annual International Meeting, European Association of Geoscientists and Engineers.

- **Yang, T.** and Sava, P.C., 2010, Wave-equation migration velocity analysis with extended common-image-point gathers, Proceedings of the 80th Annual International Meeting, Society of Exploration Geophysicists.

- **Yang, T.** and Sava, P.C., 2010, Differential semblance wavefield tomography using extended images, Proceedings of the 72nd Annual International Meeting, European Association of Geoscientists and Engineers.

- **Yang, T.** and Sava, P.C., 2009, Wave-equation migration velocity analysis using focusing of extended images, EAGE/SEG Subsalt Imaging Workshop: Focus on Azimuth, Cairo, Egypt.

- **Yang, T.** and Sava, P.C., 2009, Wave-equation migration velocity analysis using extended images, Proceedings of the 79th Annual International Meeting, Society of Exploration Geophysicists.

- **Yang, T.** and Sava, P.C., 2008, Wave-equation extended images applied to semblance and depth focusing velocity analysis, Proceedings of the 78th Annual International Meeting, Society of Exploration Geophysicists.

CHAPTER 2

MOVEOUT ANALYSIS OF EXTENDED IMAGES

A paper published in *Geophysics*, 2010, 75, no. 4, S151-S161

Tongning Yang [1,2] and Paul Sava [1]

2.1 Summary

Conventional velocity analysis applied to images produced by wave-equation migration with a cross-correlation imaging condition makes use either of moveout information from space-lags or of focusing information from time-lags. However, more robust velocity estimation methods can be designed to simultaneously take advantage of the semblance and focusing information provided by the migrated images. Such a velocity estimation requires characterization of the moveout surfaces defined jointly for space- and time-lag common-image gathers (CIG). The analytic solutions to the moveout surfaces can be derived by solving the system of equations representing the shifted source and receiver wavefields. The superposition of the surfaces from many experiments (shots) is equivalent to the envelope for the family of the individual CIG. The envelope forms a shape which can be characterized as a cone in the extended space of depth, space- and time-lags. When imaged with the correct velocity, the apex of the cone is located at the correct reflection depth and at zero space- and time-lags. When imaged with the incorrect velocity, the apex of the cone shifts both in the depth direction and along the time-lag axis. The characteristics of the cones are directly related to the quality of the velocity model. Thus, their analysis provides a rich source of information for velocity model building. Synthetic examples are used to verify the derived formulae characterizing the moveout surfaces. The analytic formulae match the numeric

[1]Center for Wave Phenomena, Colorado School of Mines
[2]Corresponding author

experiments well, thus demonstrate the accuracy of the formulae. Based on all the information provided by the extended imaging condition, future application for velocity update can benefit from the combination of the robustness of the depth focusing analysis and of the high resolution of the semblance analysis.

2.2 Introduction

A key challenge for imaging in complex geology is an accurate determination of the velocity model in the area under investigation. Migration velocity analysis is based on the principle that image accuracy indicators are optimized when data are correctly imaged. A common procedure for migration velocity analysis is to examine the alignment of images created with data from many complementary experiments. An optimal choice for image analysis in complex areas is the angle domain gathers which is free of complicated artifacts present in surface offset gathers (Stolk and Symes, 2004). If images constructed by illuminating a point from various directions are flat, then the velocity model used for imaging is said to be accurate. This idea is usually referred to as the *semblance principle* (Yilmaz, 2001) and it represents the foundation of most velocity analysis methods in use today.

Often, semblance analysis is performed in the angle domain. Several methods have been proposed for angle decomposition (Sava and Fomel, 2003; Yoon and Marfurt, 2006; Higginbotham and Brown, 2009). Most of these procedures require decomposition of extrapolated wavefields or of migrated images in components that are related to the reflection angles. This imaging procedure requires the application of an *extended imaging condition* (Sava and Fomel, 2006) which implements a point-by-point comparison of the source and receiver wavefields extrapolated from the surface. In general, the comparison is done using simple image processing procedures applied at every location in the subsurface. If the source and receiver wavefields match each other kinematically, then their cross-correlation maximizes at zero lag in space and time; otherwise, their cross-correlation does not maximize at zero lag indicating wavefield reconstruction error which may have different causes, e.g., velocity model inaccuracy.

The source and receiver wavefields used for imaging are 4D objects, functions of spatial coordinates and time (or frequency). For simplicity, we discuss in this paper only imaging conditions in the time-domain, although our analysis applies equally well to imaging conditions in the frequency-domain. For such 4D objects, the images obtained by extended imaging conditions are characterized in general by a 3D space-lag vector and a 1D time-lag. The images constructed with space- and time-lags can be decomposed into functions of reflection angles using geometric relations between incident and reflected rays (Sava and Fomel, 2006).

Conventional migration velocity analysis exploits separately either space-lag information, by *semblance analysis* (Sava and Biondi, 2004a,b; Shen and Calandra, 2005; Schleicher, 2008; Xia et al., 2008), or time-lag information, by *depth focusing analysis* (Faye and Jeannot, 1986a; MacKay and Abma, 1992, 1993; Nemeth, 1995a, 1996; Sava and Fomel, 2006). The semblance analysis is based on the space-lag gathers, or more specifically, the horizontal space-lag gathers. It may suffer from the fact that the gathers become less sensitive for steeply dipping reflectors, and thus the quality of the common-image gather is degraded, as discussed in Biondi and Shan (2002) and Biondi and Symes (2004). Similar problem exists for the depth focusing analysis based on the time-lag gathers. However, the depth focusing analysis is in general superior in robustness to semblance analysis in the processing of real data, especially land data, even though its resolution is smaller, as indicated by the analysis of Sava and Fomel (2006).

If we consider the velocity estimation as an inverse problem, we suggest here that a more robust velocity analysis approach optimizes migrated images using all available information provided by the space and time-lags. In this way, we can have more constraints on the inversion and leverage at the same time the robustness of depth focusing analysis and the high resolution of semblance analysis.

In this paper, we analyze the moveout function for common-image gathers constructed by extended imaging conditions applied after conventional wavefield extrapolation. We first

derive the analytic expression of the moveout function for extended images under the homogeneous media assumption. Next, we focus on the common-image gathers in multi-shot experiments and quantitatively analyze their characteristics, especially the features related to velocity model error. Finally, different synthetic examples are used to verify the derived analytic moveout functions and to illustrate the application of the analysis to complex geologic models.

2.3 Wave-equation Imaging Conditions

Under the single scattering assumption, the seismic data can be considered to consist of only primary reflected waves (waves bounce only once in the subsurface). Seismic migration based on Born approximation can be applied to produce a structural description of the subsurface. The seismic migration procedure consists of two main steps: wavefield reconstruction and imaging condition. Wavefield reconstruction involves constructing solutions to a wave-equation with recorded seismic data as initial and boundary conditions. Various numeric solutions for the acoustic wave-equation can be chosen depending on the specific requirements of cost and accuracy. However, regardless of the specific implementation, the reconstruction of both source and receiver wavefields is similar. In a known background velocity model, we forward propagate and backward propagate in time, to obtain the source and receiver wavefields from the source wavelet and recorded seismic data, respectively. The reconstructed source and receiver wavefields can be defined as four-dimensional functions of spatial location $\mathbf{x} = (x, y, z)$ and time t,

$$u_s = u_s(\mathbf{x}, t) \ , \tag{2.1}$$
$$u_r = u_r(\mathbf{x}, t) \ , \tag{2.2}$$

where u_s and u_r stand for the source and receiver acoustic wavefields, respectively.

An imaging condition is designed to extract the locations where reflections occur in the subsurface from these reconstructed wavefields. The image $r(\mathbf{x})$ is obtained by exploiting the space and time coincidence of the reconstructed source and receiver wavefields at every

location in the subsurface. A conventional imaging condition (Claerbout, 1985) forms an image as the cross-correlation of the source and receiver wavefields evaluated at zero lag:

$$r(\mathbf{x}) = \sum_t u_r(\mathbf{x}, t)\, u_s(\mathbf{x}, t) \ . \tag{2.3}$$

An alternative extended imaging condition (Rickett and Sava, 2002; Sava and Fomel, 2006) generalizes the conventional imaging condition by preserving the information from non-zero cross-correlation lags in the output image:

$$r(\mathbf{x}, \boldsymbol{\lambda}, \tau) = \sum_t u_s(\mathbf{x} - \boldsymbol{\lambda}, t - \tau)\, u_r(\mathbf{x} + \boldsymbol{\lambda}, t + \tau)\,. \tag{2.4}$$

The quantities $\boldsymbol{\lambda}$ and τ represent the spatial and temporal cross-correlation lags between the source and receiver wavefields. Like the conventional imaging condition, the extended imaging condition also exploits the space and time coincidence of the wavefields cross-correlation, but it preserves in the output the information corresponding to non-zero space- and time-lags. Due to the existence of the lags, the output images are "hypercubes" characterized by different lags at each subsurface location x. We refer to these hypercubes as wave-equation extended images. Such hypercubes can help us analyze the accuracy of reconstructed wavefields. If the local cross-correlation between the source and receiver wavefields is maximized at zero lag for all four dimensions, those wavefields are extrapolated correctly. If this is not true, we may conclude that the wavefield reconstruction is incorrect, indicating incorrect velocity or incorrect wavefield extrapolation or irregular illumination, or the failure of the single scattering assumption, e.g., due to the presence of multiples. In this paper, we consider that the errors in wavefield reconstruction are caused by the incorrect velocity model only.

2.3.1 Moveout analysis for extended images – point source

The characteristics of extended images can be studied by analyzing common-image gathers (CIG). A reflection event analyzed in CIG is represented by a multi-variable function $z = z(\boldsymbol{\lambda}, \tau)$, and the geometric shape of this function is often referred to as "moveout" by analogy with surface seismic data. Therefore, extended images are characterized by moveout

surface in CIG. Understanding of the moveout surface in the case of correct and incorrect velocity is essential for the purpose of migration velocity analysis (MVA). How the extended images can be used for MVA is discussed in another publication (Yang and Sava, 2009).

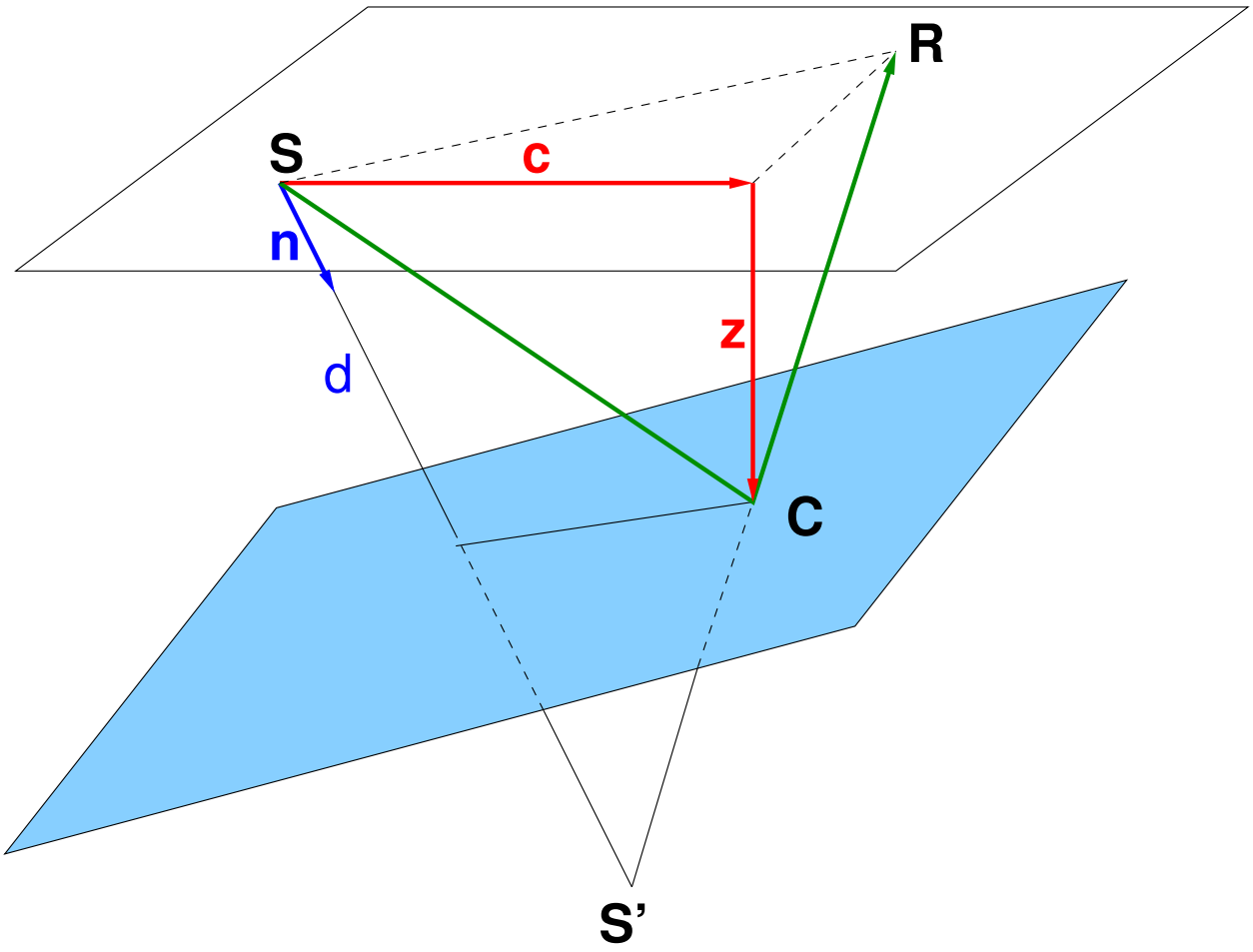


Figure 2.1: Geometry of a reflection experiment. **S**, **R** and **C** identify the positions of the source, receiver and reflection, respectively. The reflector is located at distance d from the source position in the direction of the vector $\mathbf{n}$. The position of the CIG relative to the source is indicated by the vectors $\mathbf{c}$ and $\mathbf{z}$.

Consider the reflection geometry depicted in Figure 2.1: the unit vector $\mathbf{n} = \{n_x, n_y, n_z\}$ and the distance d identify the position of a reflection plane relative to the seismic source **S**; the vector $\mathbf{c} = \{c_x, c_y, 0\}$ identifies the fixed horizontal position of CIG relative to the source position, the vector $\mathbf{z} = \{0, 0, z\}$ represents the depth of the image constructed by the imaging condition. We consider here the case where the extended imaging condition involves

the time-lag τ and only the horizontal space-lag $\boldsymbol{\lambda} = \{\lambda_x, \lambda_y, 0\}$, but the same logic applies to a more general case where the space-lag $\boldsymbol{\lambda}$ is three-dimensional.

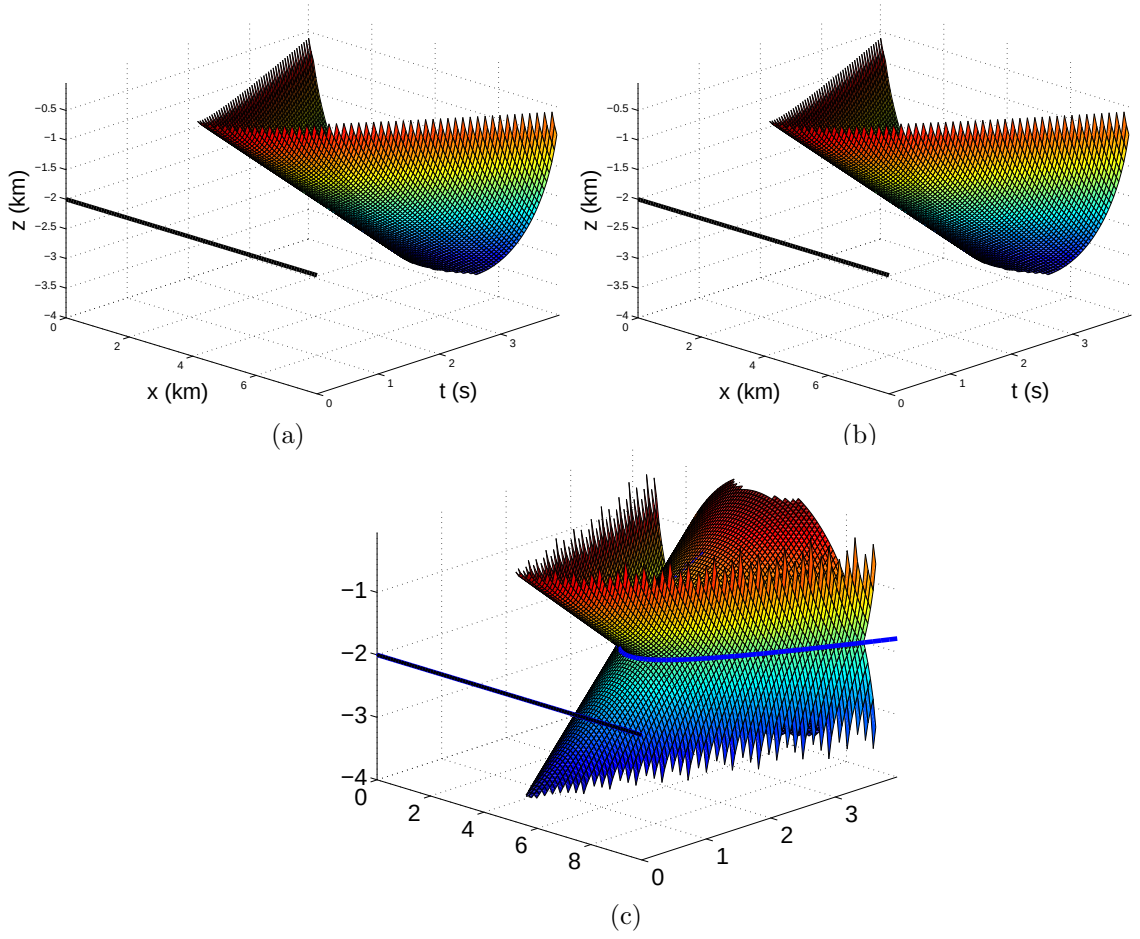


Figure 2.2: (a) Source wavefield in a homogeneous medium represented by a cone in space-time. (b) Receiver wavefield in a homogeneous medium represented by the mirror image of the source wavefield relative to the reflector. (c) Intersections of the source and receiver wavefields reconstructed with correct velocity. The projection of the intersection onto Cartesian spatial coordinates indicates the position of the reflector.

Under the assumption of homogeneous media, a wavefield characterizing wave propagation from a point source can be represented by a cone in space-time. The source wavefield is represented by a cone with the origin at zero time and at the source location on the surface, as shown in Figure 2.2(a). Likewise, we construct the receiver wavefield as the mirror image of the source wavefield relative to the reflector indicated by the black line, as shown in Fig-

ure 2.2(b). Using this description of the seismic wavefields, we can represent the source and receiver wavefields in space-time by the analytic expressions:

$$\|\mathbf{c}+\mathbf{z}\| = Vt\ , \tag{2.5}$$
$$\|\mathbf{c}+\mathbf{z}-2d\mathbf{n}\| = Vt\ , \tag{2.6}$$

where V is the velocity of the medium, t is the propagation time of the wavefield, $d\mathbf{n}$ characterizes the position of the reflector, $\mathbf{z}=\{0,0,z\}$ with z representing the depth of the image.

As discussed before, the imaging conditions identify the position of the reflector by exploiting the time and space coincidence of source and receiver wavefields. In other words, an image forms at the spatial positions where the source and receiver wavefields intersect. Mathematically, this condition is equivalent to identifying the positions which are solutions to the system given by 2.5-2.6, i.e. by solving the system for the reflection depth z at coordinates $\{c_x, c_y\}$. Figure 2.2(a)-Figure 2.2(c) illustrate the procedure. Figure 2.2(a) and Figure 2.2(b) represent the source and receiver wavefields respectively, and the cones are symmetric relative to the reflector. The intersections of the cones occur at different times. However, the locations of the intersections are consistent with the position of the reflector since their projection on the $x-z$ plane matches the reflector perfectly.

Likewise, the extended imaging condition seeks to find the intersections between the source and receiver wavefields. However, the procedure is different because both wavefields are shifted by the space- and time-lags in the cross-correlation. The shifted wavefields are functions of the space quantity $\boldsymbol{\lambda}=\{\lambda_x,\lambda_y,0\}$ and time quantity τ. Thus, the extended imaging condition is represented by the system

$$\|\mathbf{c}+\mathbf{z}+\boldsymbol{\lambda}\| = V\left(t+\tau\right)\ , \tag{2.7}$$
$$\|\mathbf{c}+\mathbf{z}-2d\mathbf{n}-\boldsymbol{\lambda}\| = V\left(t-\tau\right)\ . \tag{2.8}$$

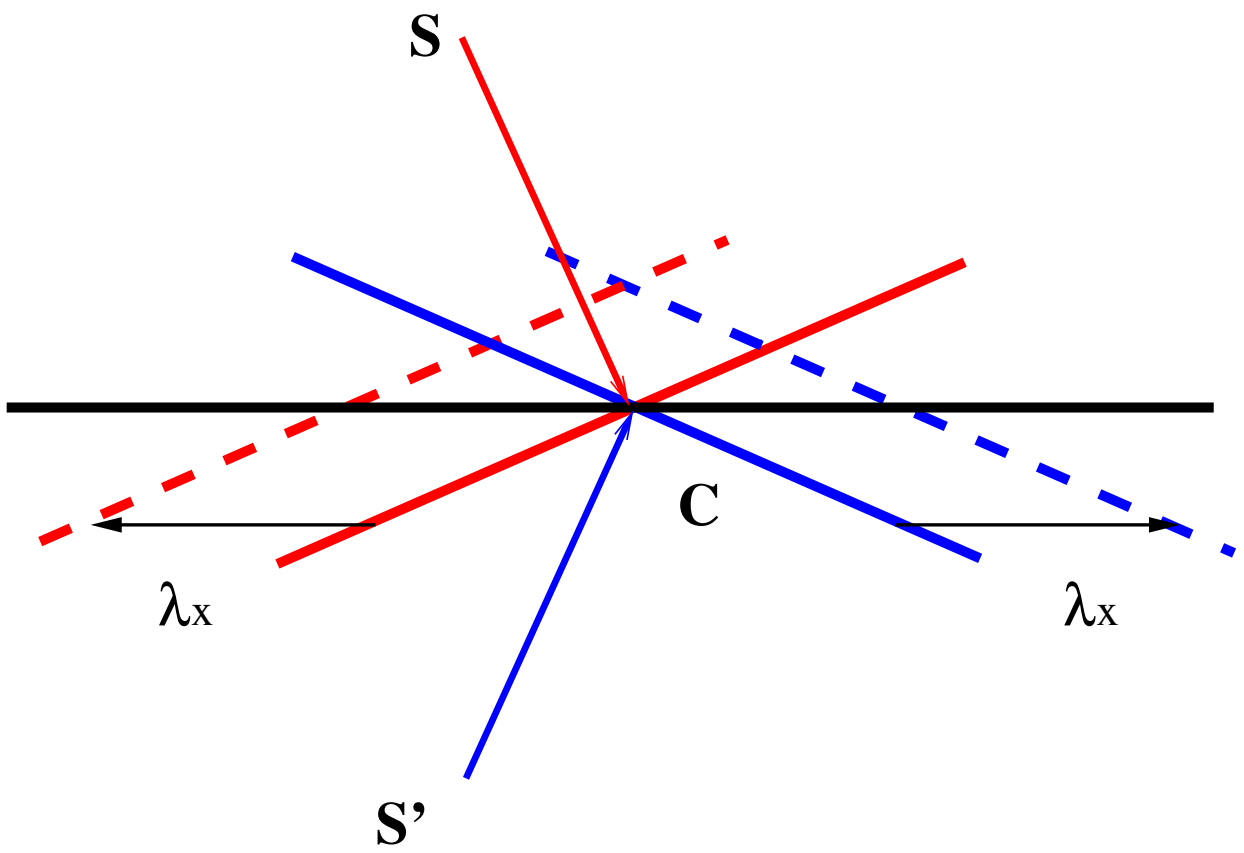


Figure 2.3: Geometric illustration of the imaging condition. The black line represents a planar reflection. The red and blue arrow lines represent the source and receiver ray, respectively. The solid lines are the corresponding wavefronts and they intersect at the depth of the reflection, which corresponds to the conventional imaging condition. The dash lines are the wavefront shifted by $\boldsymbol{\lambda}$ and they intersect at the same CIG location but right above the original depth, which corresponds to the extended imaging condition.

The application of the extended imaging condition in 2.4 is equivalent to solving 2.7-2.8 for $\mathbf{z}$. Figure 2.3 shows an example of the extended imaging condition with horizontal spatial lag λ_x only. The black line represents a planar reflector, C is the reflection point at the considered CIG location where the source wavefield is reflected. Thus, the source and receiver wavefields, denoted by the red and blue solid lines respectively, intersect at C. Finding this intersection corresponds to applying the conventional imaging condition in 2.3, and to solving the system of 2.5-2.6. If we shift the wavefields, the wavefronts, denoted by the red and blue dash lines, move and intersect at a new location. Finding this new intersection corresponds to applying the extended imaging condition in equation 2.4, and to solving the system of equations 2.7-2.8 for $\mathbf{z}$. The solution represents the moveout function $z = z(\boldsymbol{\lambda}, \tau)$ at fixed CIG coordinates $\mathbf{c} = \{c_x, c_y, 0\}$. This moveout function describes how the depth of the image z changes with the space- and time-lags.

A unique solution to the system of 2.7-2.8 leads to the following expression:

$$z(\boldsymbol{\lambda}, \tau) = (dn_z)\, K + V\tau \sqrt{K^2 + \frac{\|\mathbf{c} + \boldsymbol{\lambda}\|^2}{(dn_z)^2 - (V\tau)^2}}\,, \tag{2.9}$$

where

$$K = 1 - \frac{(\mathbf{c} \cdot \mathbf{n})\, d - \left(n_x^2 + n_y^2\right) d^2 + (\mathbf{c} - d\mathbf{n}) \cdot \boldsymbol{\lambda}}{(dn_z)^2 - (V\tau)^2}\,. \tag{2.10}$$

2.9 represents the moveout function characterizing the shape of the extended images.

To better understand the characteristics of the moveout function, we analyze two special cases of the extended images. The first case corresponds to imaging with space-lags only, which is the slice of the moveout surface at $\tau = 0$. Since the square-root term vanishes owing to zero time-lag, we obtain a linear moveout function. The coefficient depends on the reflection angles, which justifies the angle decomposition methods based on slant-stacks applied to space-lag CIG (Sava and Fomel, 2003; Biondi and Symes, 2004; Fomel, 2004). The second case corresponds to imaging with time-lag only, which is the slice of the moveout surface at $\boldsymbol{\lambda} = 0$. For this special case, the moveout function is still nonlinear.

As discussed before, the goal of our research is to understand the features of extended images related to the velocity model error. A quantitative analysis of the influence of the velocity error on the extended images is required to achieve this goal. When incorrect velocity is used for wavefield reconstruction, the wavefields are incorrectly extrapolated. Consequently, applying the imaging condition produces distorted images. As a result, we first must understand the influence of an incorrect velocity model on the reconstructed wavefields because analytic descriptions of source and receiver wavefields are the key step for deriving the moveout function. To simplify the problem, we denote the migration velocity $V_m = \rho_V V$, where ρ_V is a constant factor by which the migration velocity differs from the correct velocity.

The source wavefield is reconstructed as in the preceding situation, except that we use an incorrect migration velocity. The wavefield is represented by the cone with the arc length different from the case of correct velocity. Figure 2.4(a) shows the source wavefield reconstructed with incorrect velocity. The wavefield is described by the equation

$$\|\mathbf{c} + \mathbf{z}\| = V_m t \ . \tag{2.11}$$

The situation of the receiver wavefield is more complicated. Unlike the source wavefield, the receiver wavefield is reconstructed by backward propagation of the recorded data. In other words, we reconstruct the cone representing the source wavefield from its origin while we reconstruct the cone representing the receiver wavefield from its depth slice on the surface. If the correct velocity is used, the cone for the receiver wavefield obtained is exactly the mirror image of the cone for the source wavefield, and both cones are symmetric in space and generated at the same time. In contrast, if an incorrect velocity is used, the cone representing the receiver wavefield has an incorrect arc length, as for the source wavefield. Furthermore, the origin of the cone is shifted from its true position in space and time, and the symmetry axis between the two cones deviates from its true spatial location. In summary, the receiver wavefield reconstructed using an incorrect velocity is represented by a cone with incorrect arc length, origin and symmetry axis.

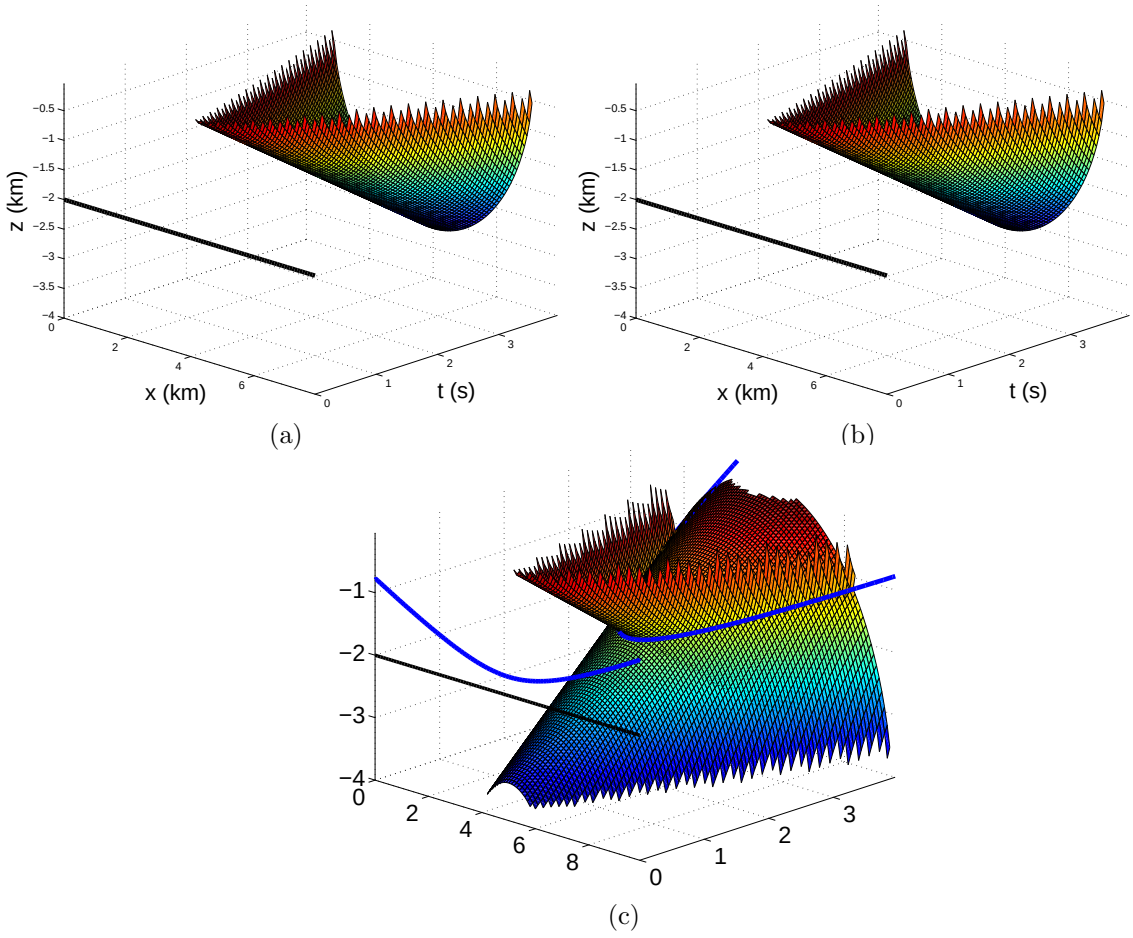


Figure 2.4: (a) Source wavefield in a homogeneous medium constructed using an incorrect velocity. The wavefield forms a cone in space-time and has a different shape compared with the wavefield constructed with the correct velocity model. (b) Receiver wavefield in a homogeneous medium constructed using an incorrect velocity. The wavefield forms a cone in space-time and has a different shape relative to the wavefield constructed in the correct velocity, and is also shifted along the time axis. (c) Intersections of the source and receiver wavefields reconstructed with incorrect velocity. The curved line, which is the projection of the intersection onto Cartesian spatial coordinates, indicates the position of the reflector. The image is distorted compared to the case when the correct velocity model is used.

As the receiver wavefield shifts in time, the reconstructed source and receiver wavefields are not triggered at the same time. It is necessary to introduce a new variable to describe such a deviation in time. Using the concepts of focusing depth d_f and migration depth d_m (MacKay and Abma, 1992), we have $d_f = d/\rho_V$, $d_m = d\rho_V$. We thus define the deviation in time as focusing error t_d, which is quantified by the following formula:

$$t_d = \frac{d_f - d_m}{V_m} = \frac{d(1-\rho_V^2)}{V\rho_V^2} \ . \tag{2.12}$$

Since the formulae for d_f and d_m are derived under the assumptions of constant velocity, small offset angle and horizontal reflector, the formula for focusing error is an approximation when we consider the problem in the real world. If velocity V_m is correct, the focusing depth and migration depth are identical and equal to the true depth of the reflection, and the focusing error t_d vanishes. Depending on the ratio between the migrated velocity and true velocity, the term t_d can be positive or negative.

As the receiver wavefield also shifts in space, symmetry between both wavefields is maintained but the symmetry plane changes. The plane defined by $d\mathbf{n}$ in the case of correct velocity now becomes $d_f\mathbf{n}_m$, where d_f is the focusing depth of the reflection point, and $\mathbf{n}_m$ is a new normal vector which is a function of source-receiver location, correct normal $\mathbf{n}$ and the migrated velocity V_m, and can be measured from the migrated image. Given this notation, the receiver wavefield is described by

$$\|\mathbf{c} + \mathbf{z} - 2d_f\mathbf{n}_m\| = V_m\,(t + 2t_d) \ . \tag{2.13}$$

Figure 2.4(b) shows the receiver wavefield in the case of a horizontal reflector when V_m is smaller than V. Solving the system of 2.11-2.13, we obtain the coordinates of the image when the incorrect velocity is used for imaging, as shown in Figure 2.4(c). This solution is equivalent to applying the conventional imaging condition and finding the intersections between the incorrectly reconstructed source and receiver wavefields.

Likewise, we introduce the space and time-lags and obtain the expression for the shifted source and receiver wavefields for the case of imaging with incorrect velocity:

$$\|\mathbf{c}+\mathbf{z}+\boldsymbol{\lambda}\| = V_m\left(t+\tau\right) , \tag{2.14}$$

$$\|\mathbf{c}+\mathbf{z}-2d_f\mathbf{n}_m-\boldsymbol{\lambda}\| = V_m\left(t+2t_d-\tau\right) . \tag{2.15}$$

Solving this system gives the expression for the moveout function of space-lag $\boldsymbol{\lambda}$ and time-lag τ for incorrect velocity

$$z\left(\boldsymbol{\lambda},\tau\right) = \left(d_f n_{mz}\right) K' + V_m\left(\tau-t_d\right)\sqrt{K^2+\frac{\|\mathbf{c}+\boldsymbol{\lambda}\|^2}{\left(d_f n_{mz}\right)^2-V_m^2\left(\tau-t_d\right)^2}} , \tag{2.16}$$

where quantity K' is defined by

$$K' = 1-\frac{\left(\mathbf{c}\cdot\mathbf{n}_m\right)d_f-\left(n_{mx}^2+n_{my}^2\right)d_f^2+\left(\mathbf{c}-d_f\mathbf{n}_m\right)\cdot\boldsymbol{\lambda}}{\left(d_f n_{mz}\right)^2-V_m^2\left(\tau-t_d\right)^2} . \tag{2.17}$$

Comparing the moveout function in 2.16 to the moveout function in 2.9, we observe that the equations share a similar form, although the formula corresponding to the incorrect velocity is more complicated. The complexity arises from the additional term t_d, as well as from the fact that d, V and $\mathbf{n}$ are replaced by d_f, V_m and $\mathbf{n}_m$. Owing to the existence of t_d, the square-root term is preserved when $\tau = 0$; the space-lag moveout function thus has a nonlinear dependence on the variables.

2.3.2 Moveout analysis for extended images – plane-waves

The analytic results discussed in the preceding section have complicated forms and correspond to single-shot experiment, which is not how MVA procedures are implemented in practice. Moreover, the moveout functions are derived based on the assumption of homogeneous media. Therefore, we must reduce the complexity of moveout functions and generalize the analysis to inhomogeneous media.

Figure 2.5 illustrates a seismic reflection occurring in an inhomogeneous medium. The wave propagation is arbitrary due to the inhomogeneity, as indicated by the curved wave paths. The corresponding wavefield can also have arbitrary geometric shape rather than a regular cone, thus we cannot describe the wavefields using analytic formulas and derive analytic moveout functions. However, if we restrict the observation to the immediate vicinity

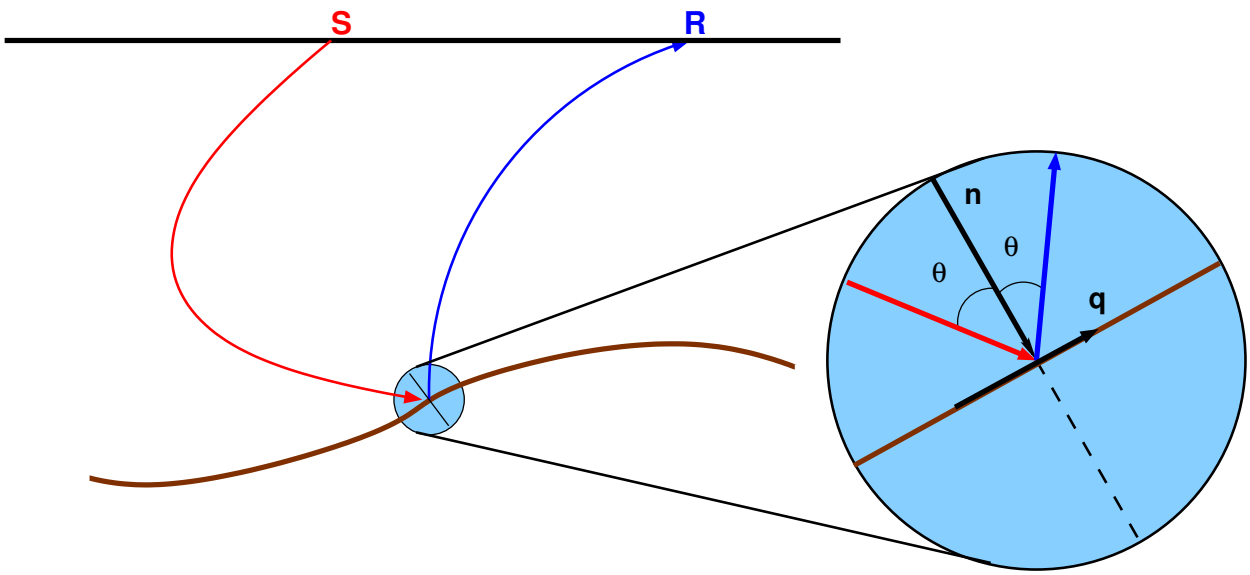


Figure 2.5: Cartoon describing wave propagation in an inhomogeneous medium. The wavepaths in the local region around the reflection point can be approximated with straight lines.

of the reflection point, which means we consider the moveout surface in a small range of lags, we can approximate the irregular wavefront by a plane. Although the shapes of wavefronts are arbitrary in heterogeneous media, they can be approximated as plane-waves in the vicinity of the reflection point. Using the same geometry shown in Figure 2.1, the source and receiver plane-waves are described by:

$$\mathbf{p}_s \cdot \mathbf{x} = V\tau \,, \tag{2.18}$$

$$\mathbf{p}_r \cdot (\mathbf{x} - 2d\mathbf{n}) = V\tau \,, \tag{2.19}$$

where $\mathbf{p}_s$ and $\mathbf{p}_r$ are the unit direction vectors of the source and receiver plane-waves, respectively, and $\mathbf{x}$ is the vector sum of $\mathbf{c}$ and $\mathbf{z}$. V is defined as the velocity in the locally homogeneous medium around the reflection point, and thus be identical for both the wavefields.

We can also obtain the shifted source and receiver plane-waves by introducing the space- and time-lags

$$\mathbf{p}_s \cdot (\mathbf{x} + \boldsymbol{\lambda}) = V(t + \tau) \ , \tag{2.20}$$
$$\mathbf{p}_r \cdot (\mathbf{x} - 2d\mathbf{n} - \boldsymbol{\lambda}) = V(t - \tau) \ . \tag{2.21}$$

Solving the system of equations 2.20-2.21 leads to the expression

$$(\mathbf{p}_s - \mathbf{p}_r) \cdot \mathbf{x} = 2V\tau - (\mathbf{p}_s + \mathbf{p}_r) \cdot \boldsymbol{\lambda} - 2d\mathbf{p}_r \cdot \mathbf{n} \ , \tag{2.22}$$

which characterizes the moveout function of space- and time-lags at an common-image point.

Furthermore, we have the following relations for the reflection geometry:

$$\mathbf{p}_s - \mathbf{p}_r = 2\mathbf{n}\cos\theta \ , \tag{2.23}$$
$$\mathbf{p}_s + \mathbf{p}_r = 2\mathbf{q}\sin\theta \ , \tag{2.24}$$

where $\mathbf{n}$ and $\mathbf{q}$ are unit vectors normal and parallel to the reflection plane, and θ is the reflection angle. Combining 2.22-2.24, we obtain the moveout function for plane-waves:

$$z(\boldsymbol{\lambda}, \tau) = d_0 - \frac{\tan\theta\,(\mathbf{q} \cdot \boldsymbol{\lambda})}{n_z} + \frac{V\tau}{n_z \cos\theta} \ . \tag{2.25}$$

The quantity d_0 is defined as

$$d_0 = \frac{d - (\mathbf{c} \cdot \mathbf{n})}{n_z} \ , \tag{2.26}$$

and represents the depth of the reflection corresponding to the chosen CIG location. This quantity is invariant for different plane-waves, thus assumed constant here.

When incorrect velocity is used for imaging, based on the analysis in the preceding section, we can obtain the moveout function

$$z(\boldsymbol{\lambda}, \tau) = d_{0f} - \frac{\tan\theta_m\,(\mathbf{q}_m \cdot \boldsymbol{\lambda})}{n_{mz}} + \frac{V_m\,(\tau - t_d)}{n_{mz}\cos\theta_m} \ , \tag{2.27}$$

where d_{0f} is the focusing depth of the corresponding reflection point, V_m is the migration velocity, t_d is the focusing error, $\mathbf{n}_m$ and $\mathbf{q}_m$ are vectors normal and parallel to the migrated reflector, respectively. And they can be measured from the migrated image.

In the analysis above, we derive the moveout functions describing extended images for a single seismic experiment. However, typical imaging employs multi-shot seismic experiments for better illumination of subsurface and imaging redundancy which indicates the velocity accuracy. Thus, it is important to understand the characteristics of extended images in such complete seismic reflection experiments.

Since the wave equation is a linear partial differential equation, its solutions comply with the linear superposition principle. This is also true for extended images. Thus, the extended images in multi-shot experiments are a linear superposition of extended images from all single-shot experiments. The extended images from one shot (plane-wave) at each subsurface location can be considered as a surface in the extended space $z - \boldsymbol{\lambda} - \tau$. The extended images constructed from many shots constitute a family of surfaces. This is a one-parameter family with the reflection angle θ as the parameter because one reflection angle θ corresponds to one shot (plane-wave). By definition, the envelope of a family of surfaces is a surface tangent to each member of the family at some points. Therefore, the extended images in multi-shot experiments are equivalent to the envelope for the family consisting of the surfaces represented by the extended images from all single-shot experiments. Based on the formula for the extended images from one plane-wave, we can derive the envelope formula by solving the following system of equations:

$$G\left(\theta, (z, \boldsymbol{\lambda}, \tau)\right) = 0 \,, \tag{2.28}$$

$$\frac{\partial G}{\partial \theta}\left(\theta, (z, \boldsymbol{\lambda}, \tau)\right) = 0 \,, \tag{2.29}$$

where G represents the implicit definition of the moveout function 2.25 for correct velocity and 2.27 for incorrect velocity, θ is the reflection angle and also the parameter for the family of surfaces. Solving the system yields the following solutions:

$$z\left(\boldsymbol{\lambda}, \tau\right) = d_0 + \frac{V\tau}{n_z}\sqrt{1 - \left(\frac{n_z\left(\mathbf{q}\cdot\boldsymbol{\lambda}\right)}{V\tau}\right)^2} \tag{2.30}$$

for correct velocity, and

$$z\left(\boldsymbol{\lambda},\tau\right)=d_{0f}+\frac{V_m\left(\tau-t_d\right)}{n_{mz}}\sqrt{1-\left(\frac{n_{mz}\left(\mathbf{q}_m\cdot\boldsymbol{\lambda}\right)}{V_m\left(\tau-t_d\right)}\right)^2} \tag{2.31}$$

for incorrect velocity.

Analyzing the envelope functions for the cases of correct and incorrect velocities, we note that both envelope functions share a similar form; so they should have similar properties. The envelope functions become singular when $\tau=0$ or $\tau=t_d$, because at these special time-lags, all the individual surfaces corresponding to various experiments intersect at the same location. Mathematically, the envelope function is equivalent to a singular delta function at this τ. Also, the square-root term in both the formulas contains a subtraction, we must ensure that the quantity under the square-root is non-negative; otherwise, the formula fails. This failure implies that the range of space-lag $\boldsymbol{\lambda}$ is limited, which suggests that we must restrict the range of $\boldsymbol{\lambda}$ when we measure the moveout of reflections. Given the envelope functions shown in 2.30-2.31, we conclude that the envelope surfaces form cones regardless of the dipping angle and velocity model used for imaging, as shown in Figure 2.6(a) - Figure 2.6(d). and Figure 2.6(b), corresponding to correct and incorrect velocities respectively, for a horizontal reflector and in Figure 2.6(c) and Figure 2.6(d) for a dipping reflector. However, the shapes of the cones change with both velocity and reflector dip. The cones are incomplete due to the limitations of acquisition aperture. When the velocity used for imaging is correct, the apex of the cone is located at zero lags and at the correct depth of the reflection point. In contrast, when the velocity is incorrect, the cone is shifted in both depth and in the time-lag directions. The shift in time-lag is exactly the focusing error t_d defined before and the location of the shifted apex is the focusing depth d_{0f}.

If we slice the cone at negative time-lags, the slices correspond to upper half of the cone and thus curve downward. In contrast, the slices corresponds to lower half of the cone curve upward. The events present in the zero time-lag slice in the case of incorrect velocity are characterized by the residual moveout used in conventional migration velocity analysis (Sava and Biondi, 2004a,b; Shen and Symes, 2008), as indicated by the thick line in the Figures

Figure 2.6(b) and Figure 2.6(d). Based on the analysis presented here, we can evaluate the accuracy of the velocity model by examining the position of the apex of the cone. If the apex occurs at zero space- and time-lag, the velocity model is correct. If the apex shifts to non-zero time-lags, then the migration velocity is incorrect. Thus, the position of the apex of the cone can be used as an indicator of velocity error.

To summarize, in inhomogeneous media, no analytic moveout function exists to describe moveout surfaces for extended images. However, by restricting our analysis to the vicinity of the reflection point, and by assuming that the velocity change above the image points is relatively uniform, we can use a plane-wave approximation to derive the analytic functions characterizing extended images. The parameters describing the moveout functions are effective parameters which represent the velocity errors accumulated along wave propagation paths just as the traveltime errors used in conventional traveltime tomography. These parameters can be transformed into local medium parameters through a tomographic procedure which we do not discuss here.

2.4 Examples

We illustrate the validity of the moveout functions derived in the preceding sections with several synthetic models. The first model consists of a horizontal reflector embedded in a constant velocity medium, while the second model consists of a dipping reflector embedded in a constant velocity medium. We use the first model to verify the accuracy of the moveout function for point sources and plane-wave sources, and use the second model to verify the accuracy of the envelope functions for plane-wave sources. Extended images are generated for both correct and incorrect velocities. The incorrect velocity is obtained by scaling the correct velocity with a constant factor.

The migrated images corresponding to the horizontal reflector are shown in Figure 2.7(a) and Figure 2.7(b) for correct and incorrect velocities, respectively. The reflector is at $z = 1.5$ km. The correct velocity is 2.5 km/s, and the scaling factor is 0.9. The extended images are constructed at CIG location $c_x = 0.5$ km, as indicated by the vertical line. Thus, for

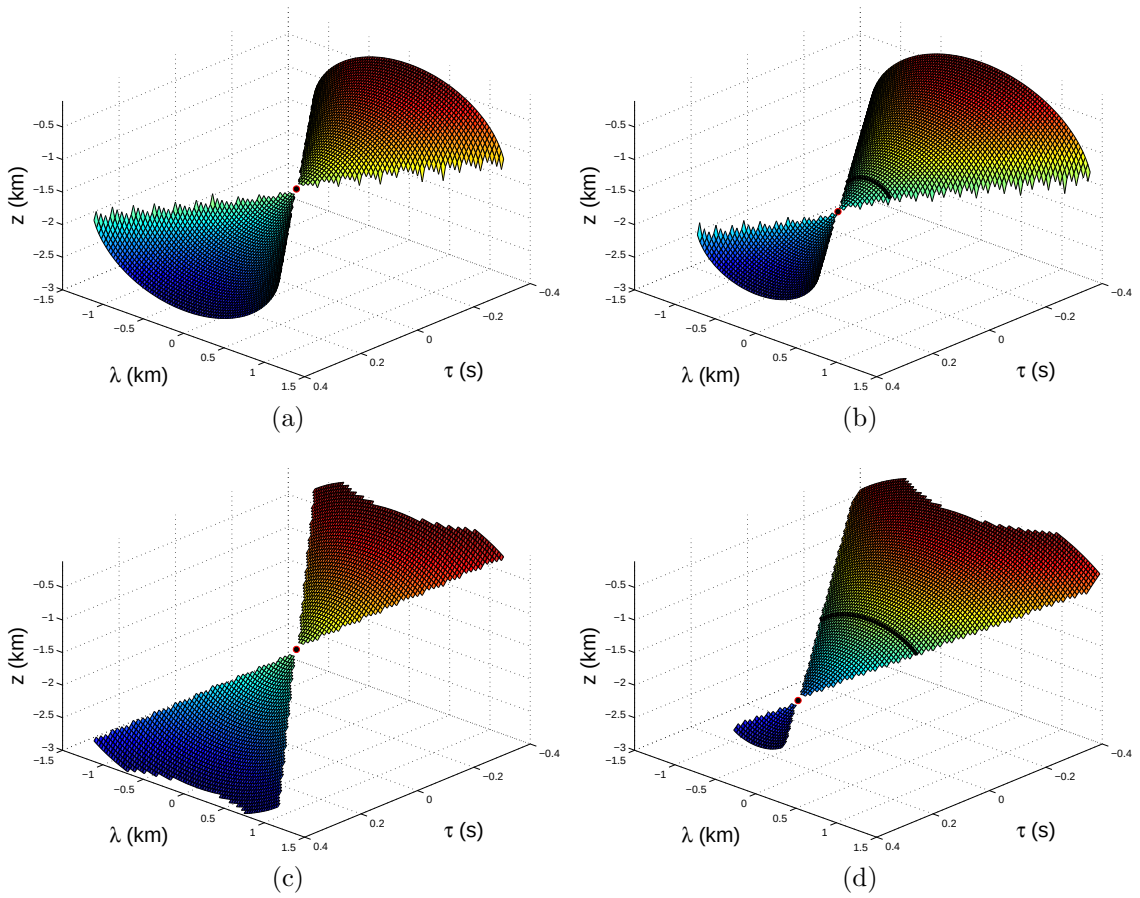
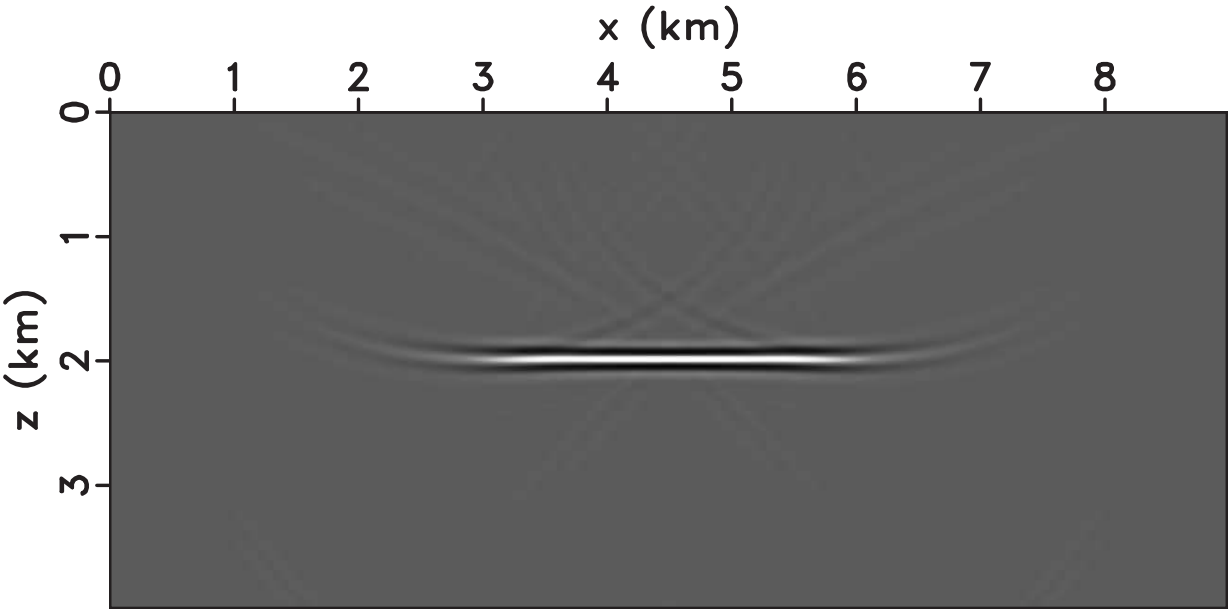


Figure 2.6: Cone formed by the envelope of the moveout surfaces corresponding to individual plane-waves for a horizontal reflector in (a) the correct velocity case, the focus of the cone occurs at zero space- and time-lags and (b) the incorrect velocity case, the focus of the cone shifts to a nonzero time-lag. Cone formed by the envelope of the moveout surfaces corresponding to individual plane-waves for a dipping reflector in (c) the correct velocity case, the focus of the cone occurs at zero space- and time-lags and (d) the incorrect velocity case, the focus of the cone shifts to a nonzero time-lag. The thick line corresponds to the slice of the cone cut at zero time-lag.

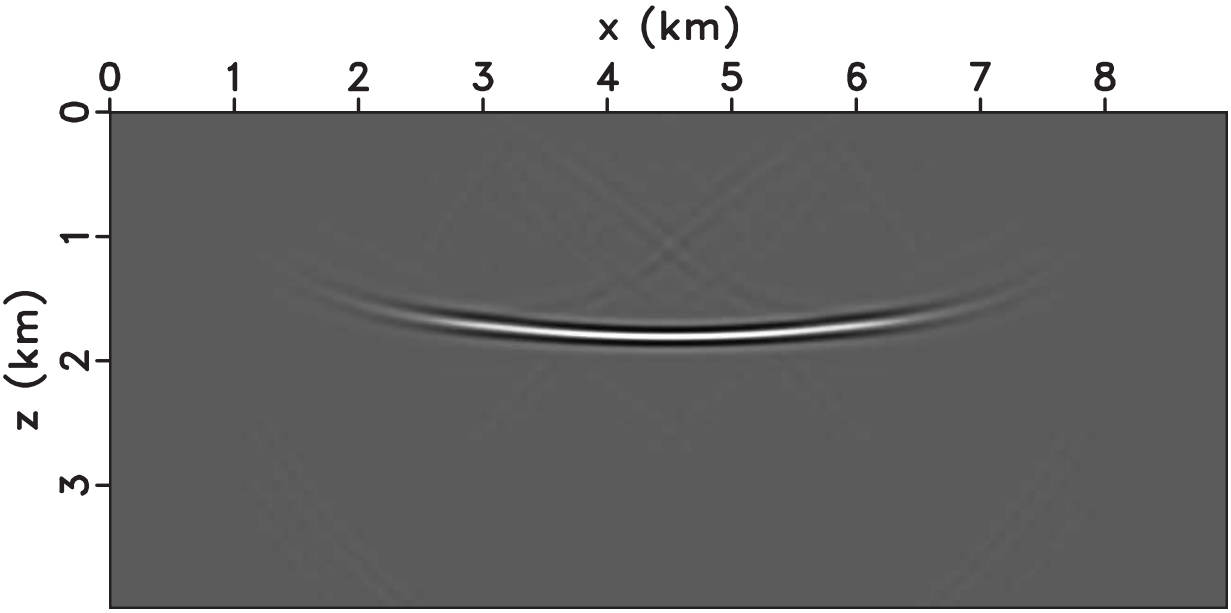
a source located at $x = 3$ km, the CIG analyzed are located at $x = 3.5$ km. To verify the accuracy of the moveout function, we overlay the analytic moveout functions on extended images at either fixed time-lags or at fixed horizontal space-lags.

The migrated images corresponding to the horizontal reflector are shown in Figure 2.7(a) and Figure 2.7(b) for correct and incorrect velocities, respectively. The reflector is at $z = 1.5$ km. The correct velocity is 2.5 km/s, and the scaling factor is 0.9. The extended images are constructed at CIG location $c_x = 0.5$ km, as indicated by the vertical line. Thus, for a source located at $x = 3$ km, the CIG analyzed are located at $x = 3.5$ km. To verify the accuracy of the moveout function, we overlay the analytic moveout functions on extended images at either fixed time-lags or at fixed horizontal space-lags.

Figure 2.8(a)-Figure 2.8(c) and Figure 2.8(d)-Figure 2.8(f) depict space-lag extended images corresponding to the chosen CIG location for correct and incorrect velocities, respectively. From left to right, the panels correspond to slices at $\tau = \{-0.20, 0, +0.20\}$ s. In each column, the upper panels correspond to correct velocity while the lower panels correspond to incorrect velocity. The dashed lines overlain correspond to the analytic functions 2.9 and 2.16 while the solid lines correspond to the analytic functions 2.25 and 2.27. In this case, because of the horizontal reflector, the dip is not changed. Thus, $\mathbf{n}$ and $\mathbf{n}_m$ are the same here. Notice that, at $\tau = 0$ the moveout event is linear for correct velocity and nonlinear for incorrect velocity, as expected. Comparing the analytic functions derived for point and plane sources, we can observe that the point source formulae accurately describe the moveout curves in this example. In contrast, since the plane-wave formulae are approximations to the point source formulae, they are only accurate at small lags and become less accurate for large lags. Finally, we mention that the mismatch at large lag values between the formulae and moveout curves shown in Figure Figure 2.8(c) and Figure 2.8(f) is caused by the diffractions due to truncation of the acquisition array. Such effects are not properly characterized by our formulae which apply strictly to reflection but not to diffraction.



(a)



(b)

Figure 2.7: Migrated images corresponding to (a) correct velocity and (b) incorrect velocity.

Figure 2.9(a)-Figure 2.9(c) and Figure 2.9(d)-Figure 2.9(f) depict time-lag extended images for correct and incorrect velocities, respectively. From left to right, the panels correspond to $\lambda_x = \{-0.3, 0, +0.3\}$ km. In each column, the upper panels correspond to correct velocity while the lower panels correspond to incorrect velocity. The dashed line overlain on each panel corresponds to the analytic functions 2.9 and 2.16 while the solid lines correspond to the analytic functions 2.25 and 2.27. In both cases, the analytic formulae of point source accurately describes the moveout surface characterizing extended images. Likewise, the formulae of plane-waves are also good approximations to the point source ones at small range of lags. This illustrates the accuracy of the analysis of the moveout functions for the extended images.

Figure 2.10(a) and Figure 2.10(b) show the migrated images of the dipping reflector corresponding to correct and incorrect velocities, respectively. The dip of the reflector is about 24°. The correct velocity is 2.5 km/s, and the scaling factor is 0.9. To obtain the images, we use 50 plane-wave sources equally spaced in horizontal slowness and stack the images from all individual experiments. As discussed before, the stacked moveout surfaces correspond to the envelope of the surfaces obtained from individual shots. We choose $x =$ 3.0 km as the CIG location. The reflection corresponding to the CIG location is at $z =$ 1.3 km.

Figure 2.11(a)-Figure 2.11(f) depict the moveout surfaces at different time-lags. From left to right, the upper panels display the slices at $\tau = \{-0.15, 0.0, +0.15\}$ s. The lower panels correspond to the same slices but overlain with the derived analytic envelope function $z(\lambda_x, \tau)$ given by equation 2.30 for various τ. Since the correct velocity is used for imaging, the apex of the cone should be located at zero space- and time-lags. As expected, all events intersect at the same location at zero space-lag and a well focused image can be observed in the panel at $\tau = 0$. For incorrect velocity, the cones shift so that their apex is not located at zero time-lag. The slice at zero time-lag therefore shows a curved event. Figure 2.12(a)-Figure 2.12(f) depict envelopes of moveout surfaces for different time-lags. From left to

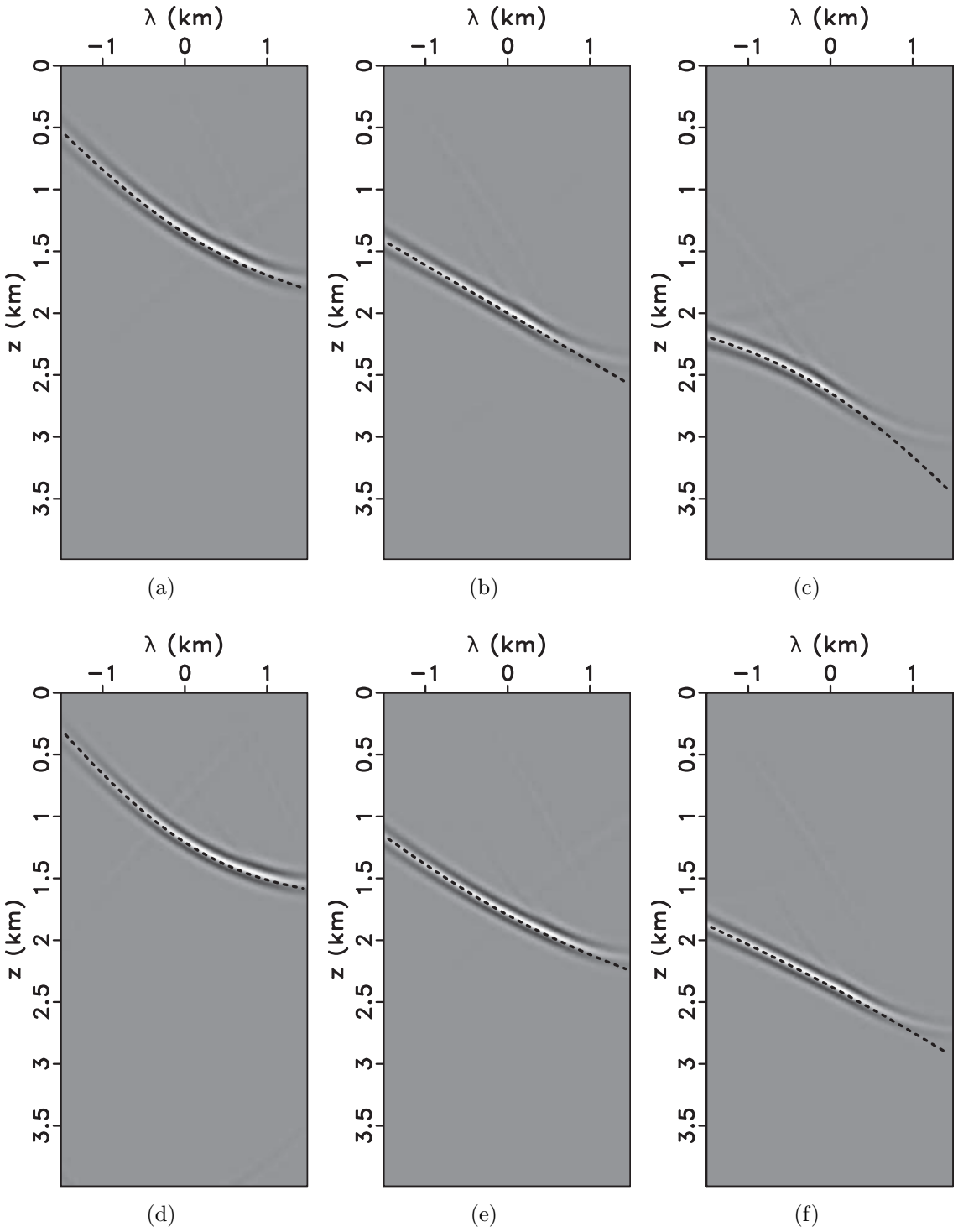


Figure 2.8: Space-lag CIG for $\tau = \{-0.20, 0, +0.20\}$ s. Panels (a)-(c) correspond to correct velocity. Panels (d)-(f) correspond to incorrect velocity. The dash and solid line overlain corresponds to the derived analytic functions of point source and plane-wave source, respectively.

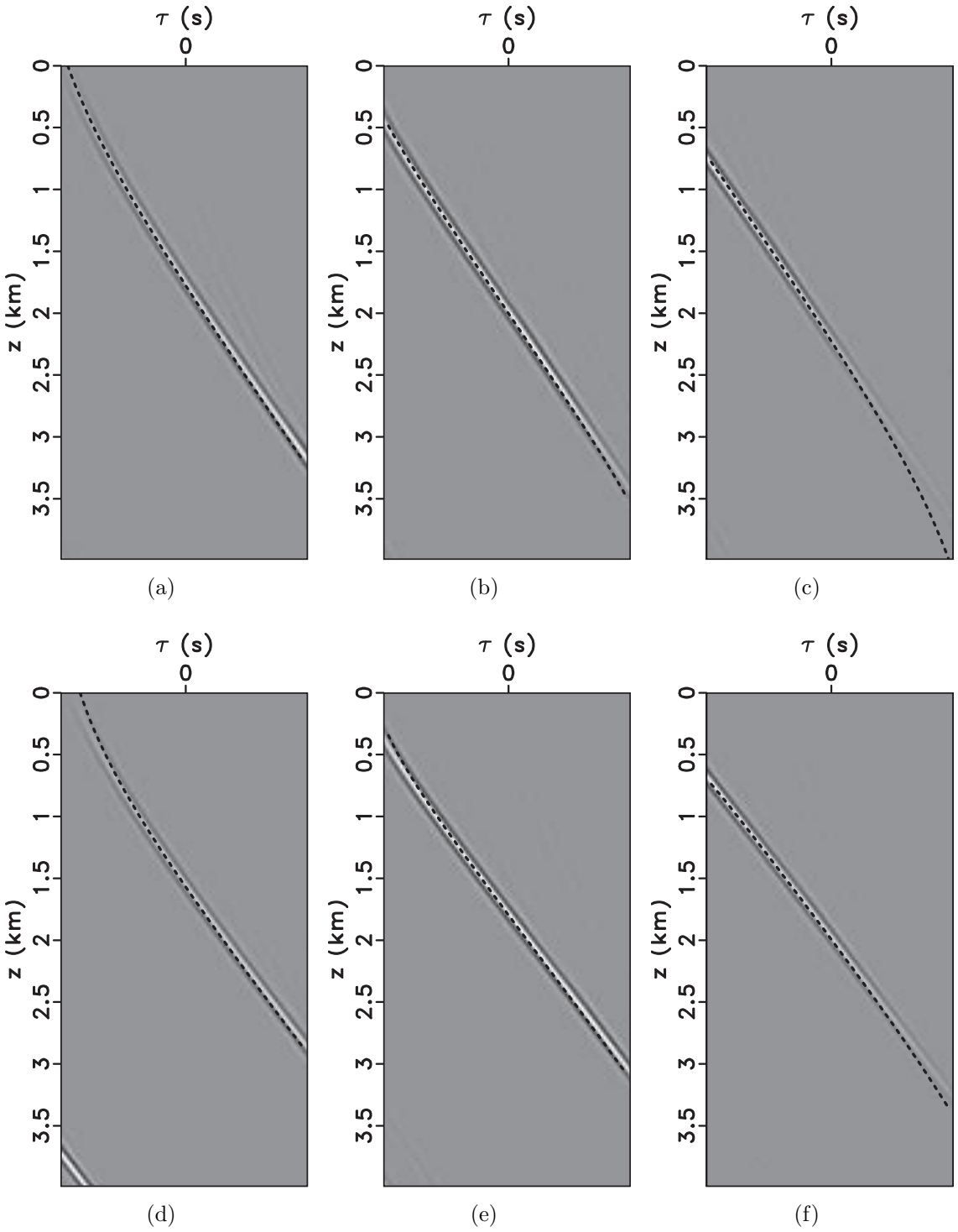
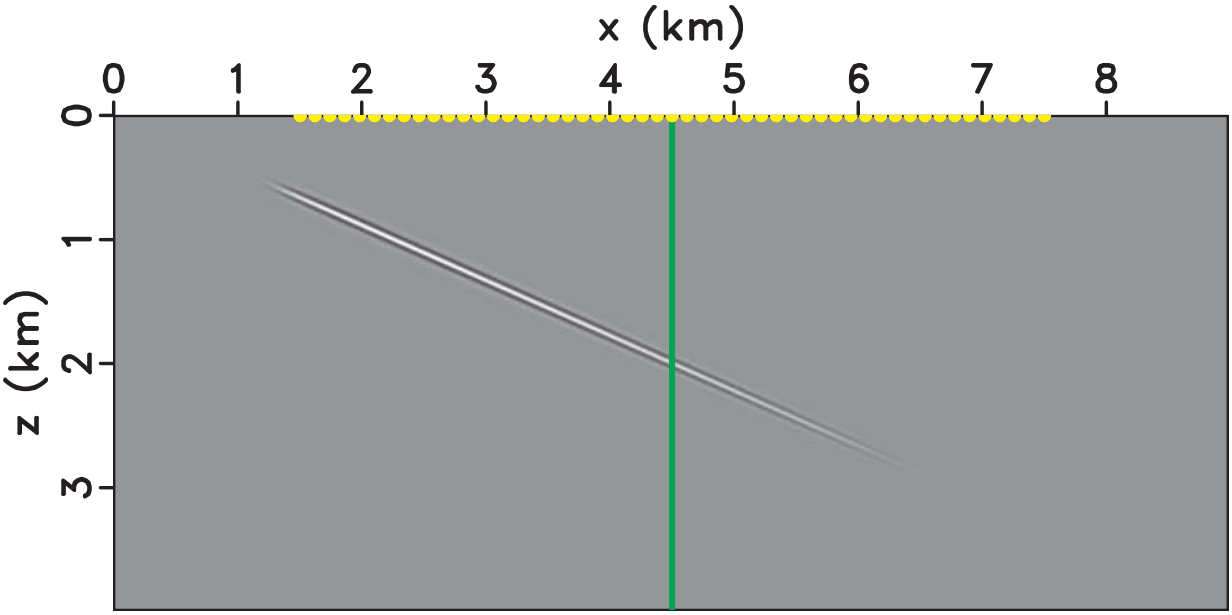
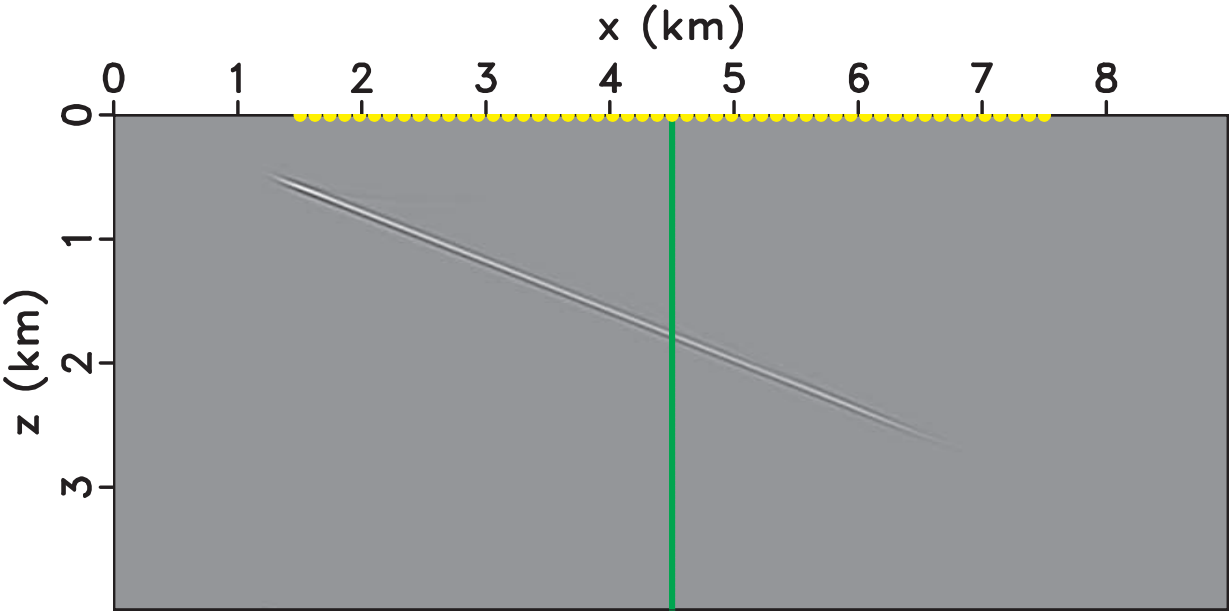


Figure 2.9: Time-lag CIG for $\lambda_x = \{-0.3, 0, +0.3\}$ km. Panels (a)-(c) correspond to correct velocity. Panels (d)-(f) correspond to incorrect velocity. The dash and solid line overlain corresponds to the derived analytic functions of point source and plane-wave source, respectively.



(a)



(b)

Figure 2.10: Migrated images corresponding to (a) correct velocity and (b) incorrect velocity.

right, the upper panels display the slices of t he cone at $\tau = \{-0.15, 0.0, +0.15\}$ s. The lower panels correspond to the same slices but overlain with the derived analytic envelope function $z(\lambda_x, \tau)$ given by 2.31 for various τ. In this case, because of the dipping reflector, the dip is changed when the image is obtained by migrating with an incorrect velocity. Since $\mathbf{n}_m$ is a normal vector to the reflection we obtain, it can be simply measured on the migrated image. Same logic applies to $\mathbf{q}_m$. slice at zero time-lag shows a curved event rather than a focused point, which demonstrates the shift of the apex of the cone. The slice at $\tau = 0.15$ s shows an event curved in the opposite direction, which means that the slice is passing to the apex of the cone. For both correct and incorrect velocities, the analytic functions match the experiments well, which demonstrates the accuracy of the envelope functions.

Finally, we use the Sigsbee model (Paffenholz et al., 2002) to illustrate the application of our analysis to inhomogeneous media. Figure 2.13 show the velocity profile of the model. The sources are distributed over the left area of the model, thus they mainly illuminate the left side of the image. Figure 2.14(a) and Figure 2.14(b) show the image migrated with correct and incorrect velocities respectively.

Figure 2.15(a) and Figure 2.15(b) depict the moveout surfaces at different time-lags for the case of imaging with correct velocity. The panels correspond to slices of the cone at different time-lags. Figure 2.15(a) shows the slice at $\tau = -0.15$ s. The events in the panel curve downward since the slice is cut at negative τ and corresponding to the upper half of the cone. Figure 2.15(b) shows the slice at $\tau = 0$ s, which is cut at the origin of the cone. The events in the panel appear focused at zero time-lag and space-lag, indicating correct velocity.

Figure 2.16(a) and Figure 2.16(b) depict moveout surfaces for different time-lags for the case of imaging with incorrect velocity. The panels correspond to slices of the cone at different time-lags. Because a higher migration velocity is used, the origin of the cone is expected to shift to negative τ. Figure 2.16(a) shows the slice at $\tau = -0.15$ s. The shallow events in the panel focus at zero space-lag, which means that the slice is cut at the origin

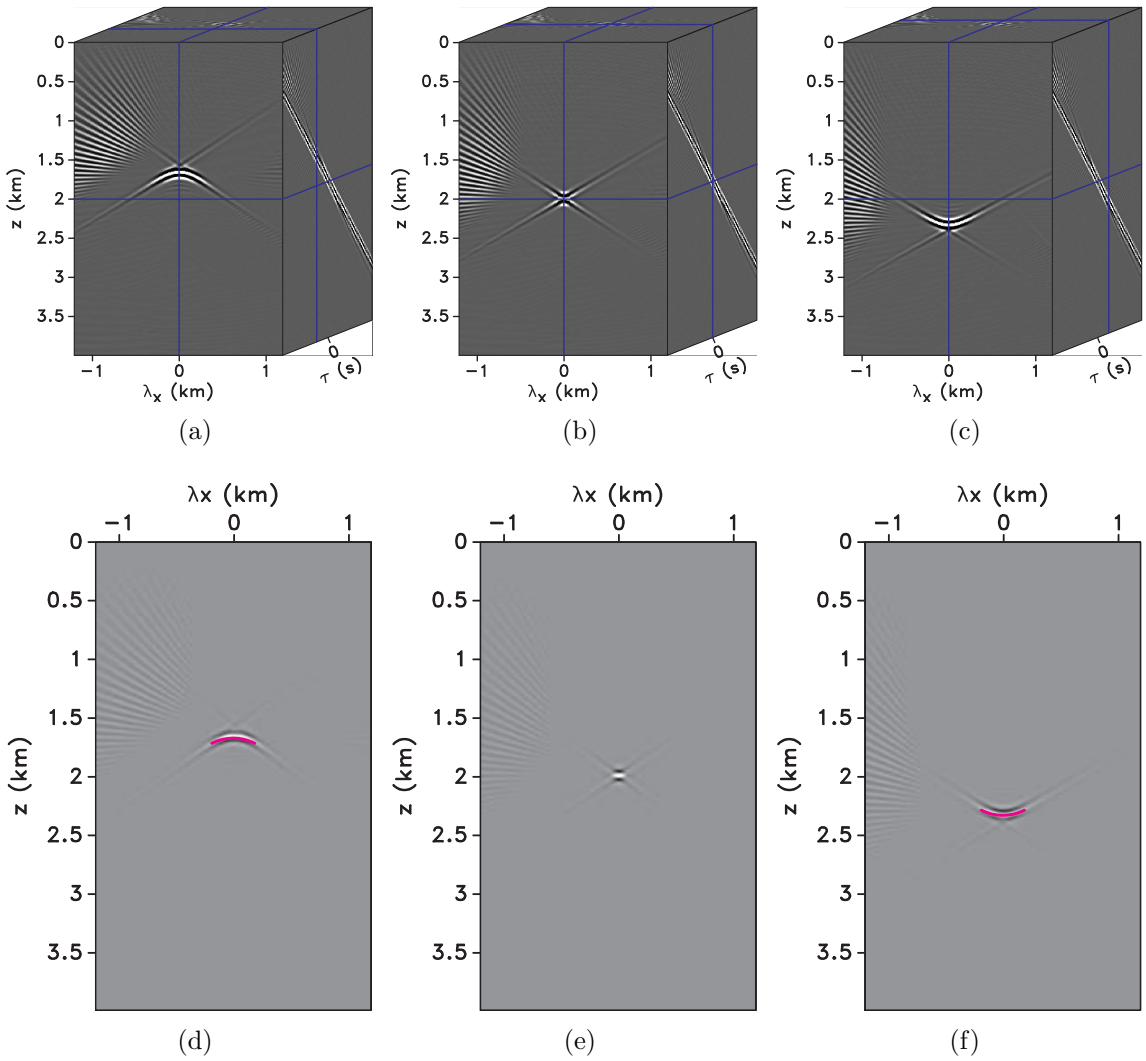


Figure 2.11: Envelope of the moveout surfaces at different time-lag for correct velocity. Panels (a)-(c) correspond to slices at $\tau = \{-0.15, 0, +0.15\}$ s, respectively. Panels (d)-(f) show the same slices overlain by the derived analytic envelope function.

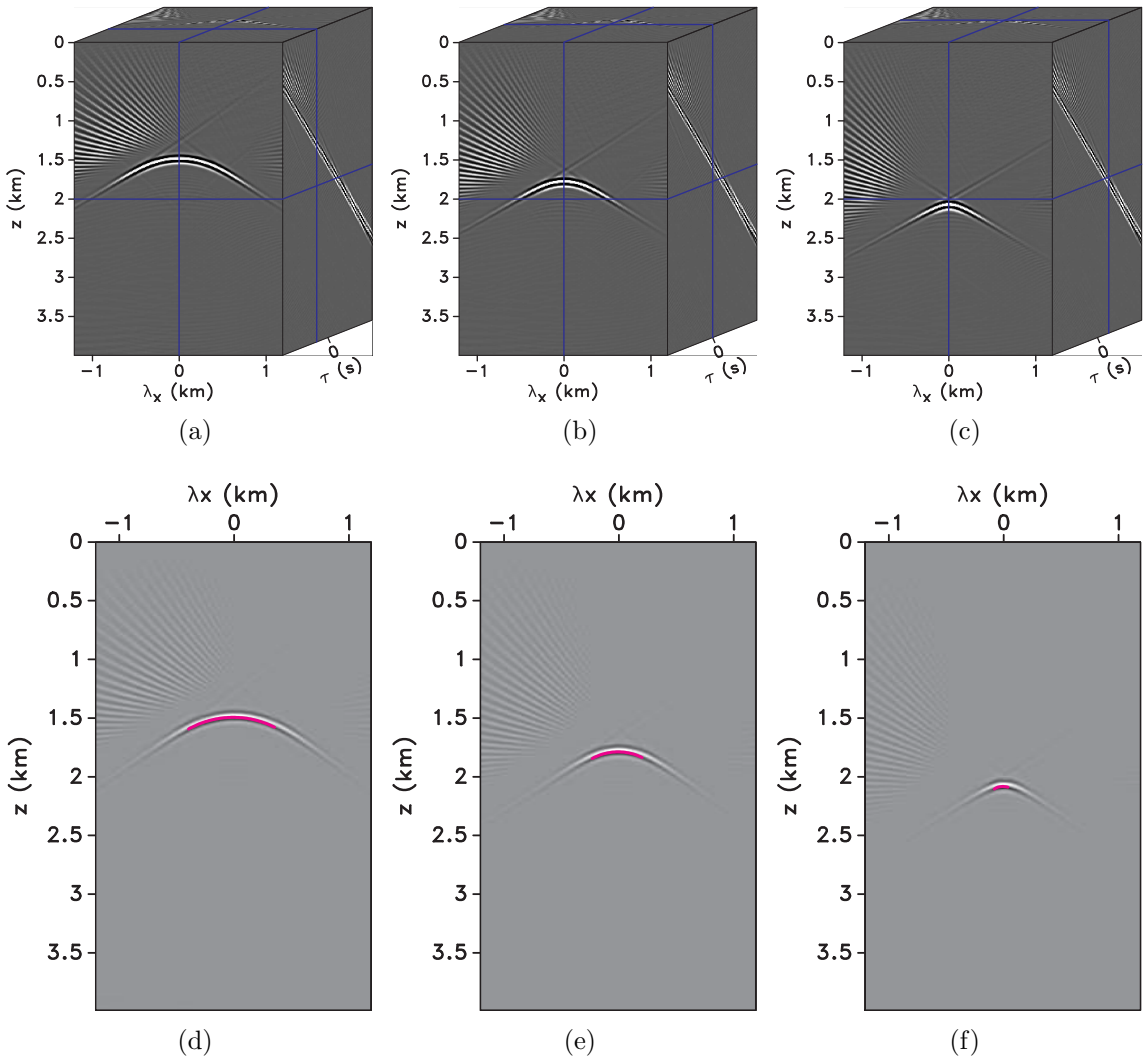


Figure 2.12: Envelope of the moveout surfaces at different time-lag for incorrect velocity. Panels (a)-(c) correspond slices to $\tau = \{-0.15, 0, +0.15\}$ s, respectively. Panels (d)-(f) show the same slices overlain by the derived analytic envelope function.

of the cone for those events. Deeper events have the focus of the cone at other values of τ. Figure 2.16(b) show the slices at $\tau = 0$ s. The events in the panels curve upward because the slice is cut away from the focus of the cone.

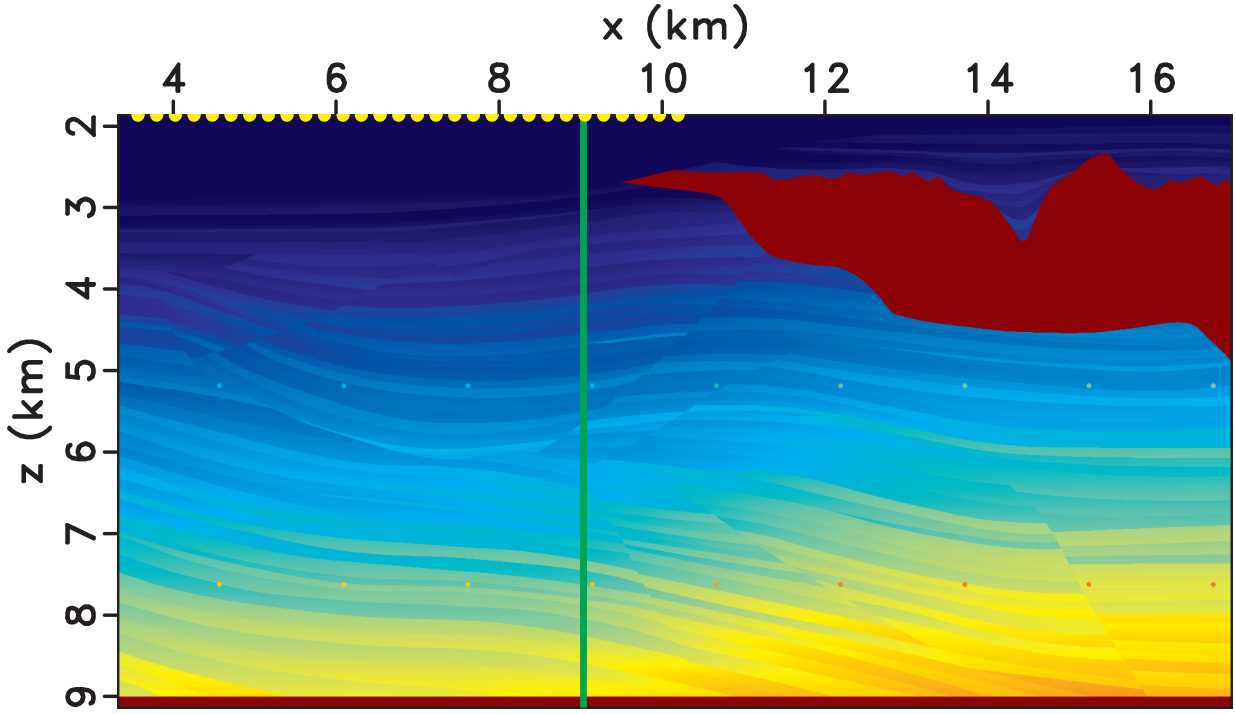
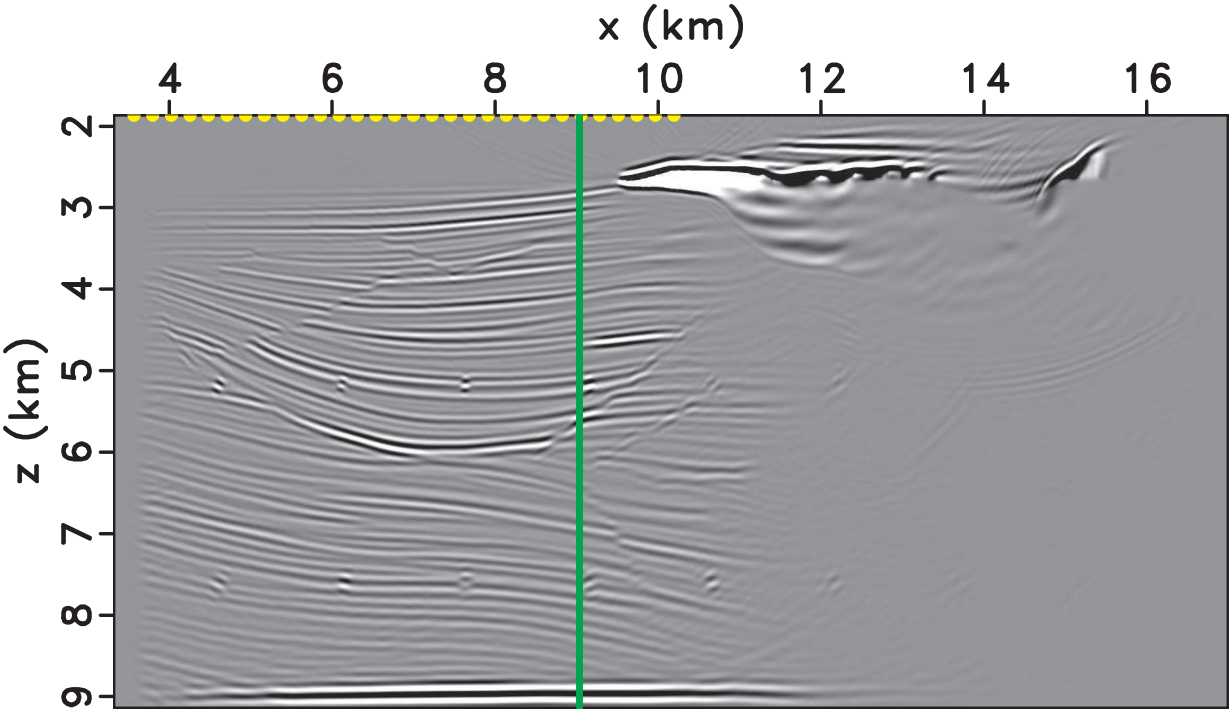


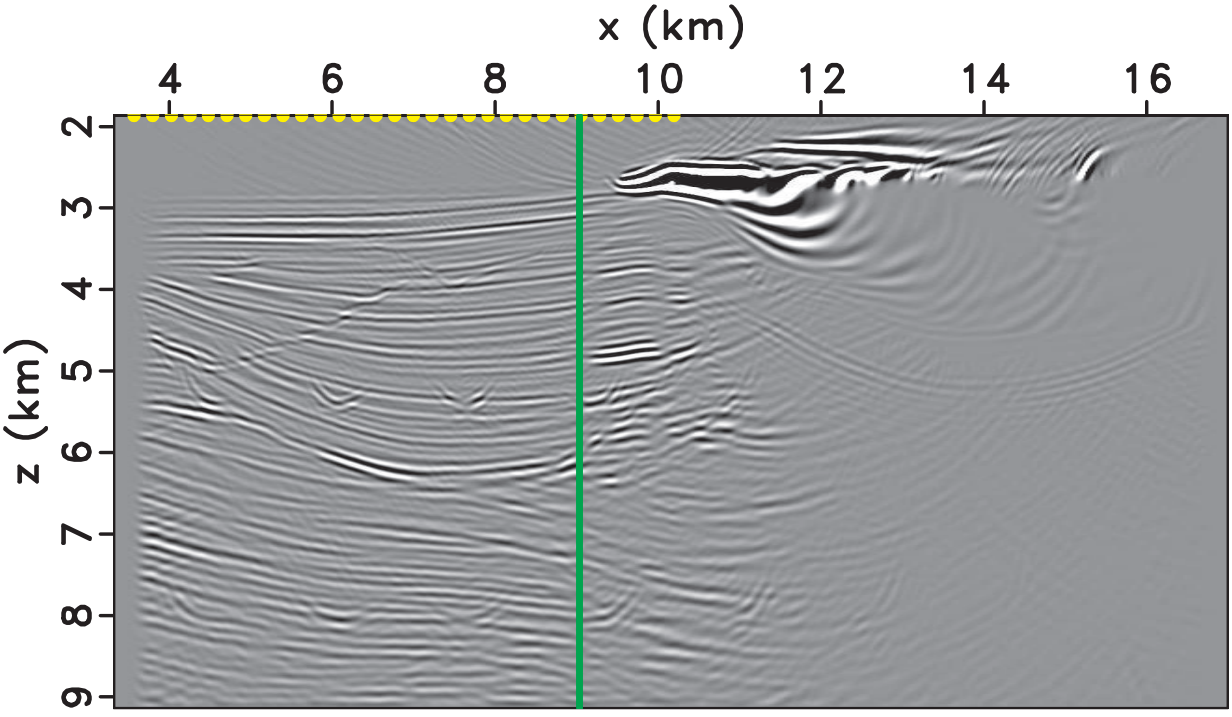
Figure 2.13: Velocity profile of the Sigsbee model.

2.5 Discussion

Extended imaging conditions have been used in the past as sources of information for migration velocity analysis. For example, Biondi and Sava (1999); Shen et al. (2003); Sava and Biondi (2004b); Shen and Calandra (2005); Shen and Symes (2008) use space-lags extensions for MVA, while Higginbotham and Brown (2008); Brown et al. (2008); Yang and Sava (2009) use time-lag extensions for MVA. Among the interesting questions one can ask based on the analysis presented in this paper are what is the connection between the two sets of extensions and is the information provided by space- and time-lags redundant or complementary? As indicated in the preceding sections, the space- and time-lag extensions are not

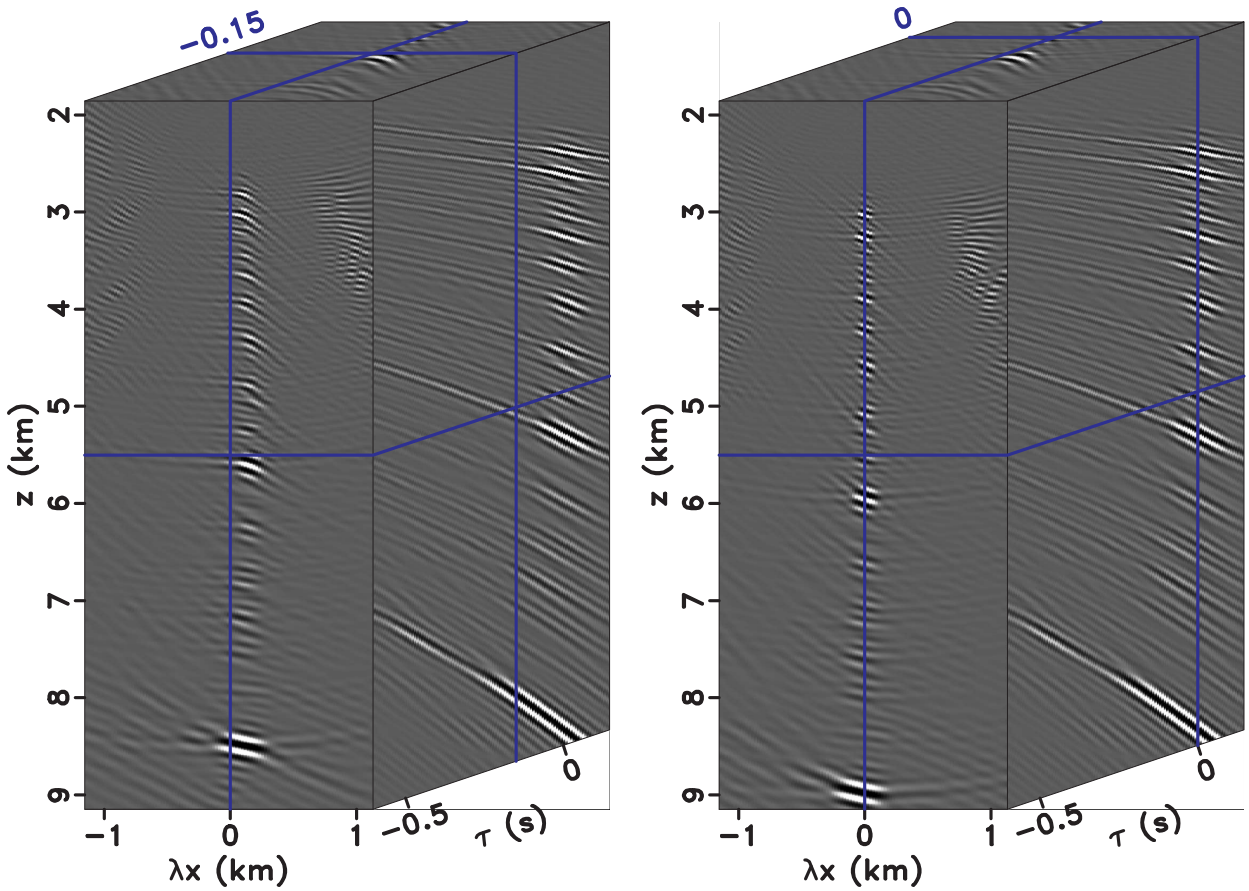


(a)



(b)

Figure 2.14: The migrated images corresponding to (a) correct velocity model and (b) incorrect velocity model.



(a) (b)

Figure 2.15: Moveout surfaces at different time-lags for correct velocity. Panels (a) and (b) correspond to slices of the cone at $\tau = \{-0.15, 0\}$ s, respectively.

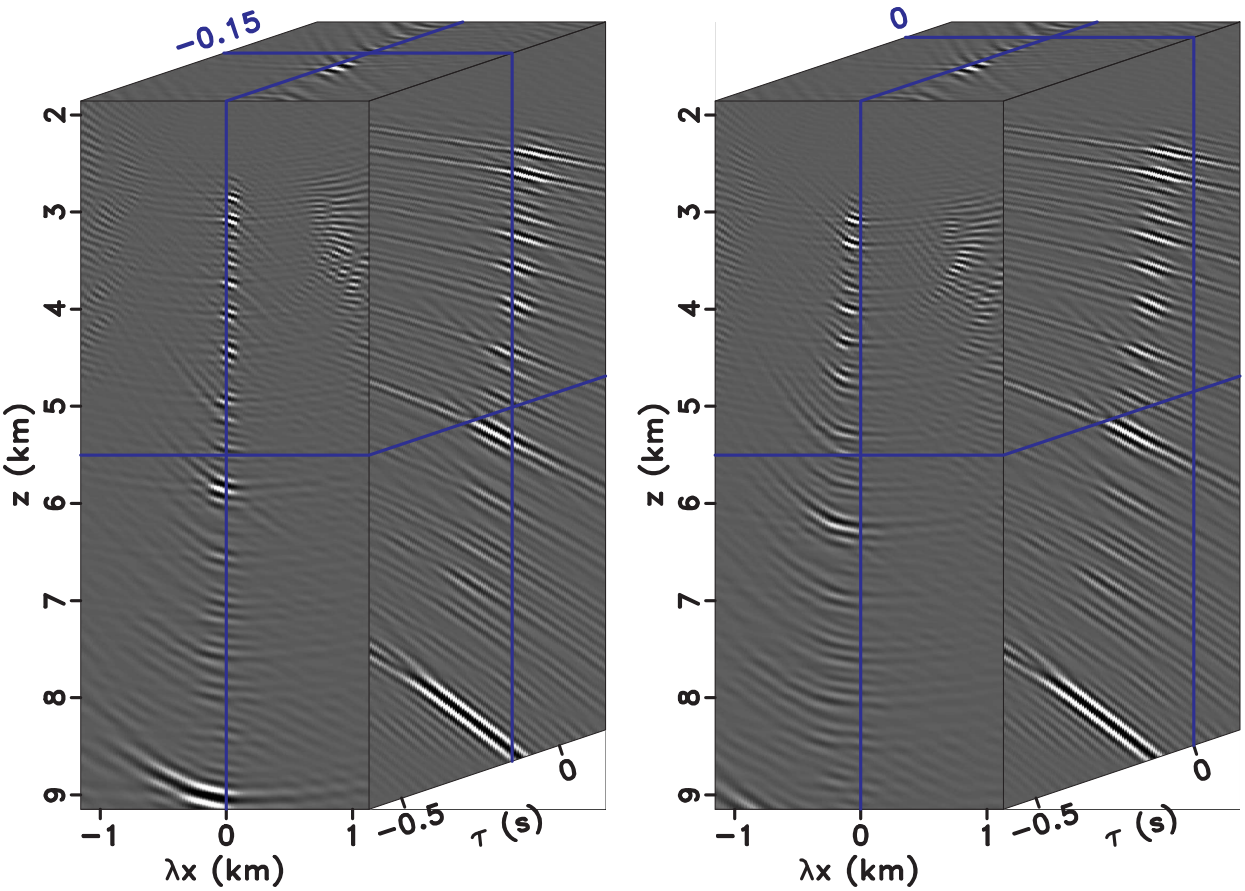


Figure 2.16: Moveout surfaces at different time-lags for incorrect velocity. Panels (a) and (b) correspond to slices of the cone at $\tau = \{-0.15, 0\}$ s, respectively.

independent on one-another. By simply observing reflectors in space-lag gathers (at $\tau = 0$) or in time-lag gathers (at $\boldsymbol{\lambda} = 0$), we are exploring subsets of the same object, as seen in Figure 2.6(a)- Figure 2.6(d). Therefore, the depth-$\boldsymbol{\lambda}$-τ gathers capture more completely the behavior of events in the extended space and provide access to more robust information to be used for velocity update. It is easier to evaluate the behavior of the "cones" characterizing a reflection event by observing them in their entirety, rather than by observing subsets.

On the other hand, using space-time extended gathers we can better formulate the optimization process that could be used for velocity model update. For example, conventional wavefield-based MVA based on differential semblance optimization (Shen and Calandra, 2005; Symes, 2009) indicates that velocity can be optimized by minimizing the objective function of space-lags at zero time-lag:

$$\min \frac{1}{2} \left|\left| r\left(z, \lambda_x, \lambda_y\right) \sqrt{\lambda_x^2 + \lambda_y^2} \right|\right|^2 , \tag{2.32}$$

where λ_x and λ_y are the horizontal components of the space-lag vector $\boldsymbol{\lambda}$ and $r\left(z, \lambda_x, \lambda_y\right)$ represents an extended image gather. This objective function corresponds to the case when we penalize reflector energy outside zero space-lag, but not the reflector energy at zero space-lag. From the analysis presented in this paper, it is apparent that this type of objective function is partial and that what we really need to do is to penalize the entire defocused events at all lags (including zero space-lag) by the same amount dependent on how far the apex of the respective event departs from zero time-lag. An objective function formulated this way includes both the information at zero time-lag (the semblance information), as well as the information at zero space-lag (the focusing information), thus being more robust and effective for mig ration velocity analysis. This topic is discussed in Yang and Sava (2009) and we do not elaborate further on it in this paper.

Finally, an important consideration for practical application of this methodology is that of computational cost. Computing extended images function of both space- and time-lags is costlier that computing extended images function of space-lag or time-lag separately. On the other hand, there is more information in extended images mixing space- and time-lags.

Therefore, what we need to do is balance the cost and benefits of the extended images. For example, we can reduce the cost by not evaluating the extended images at regions which are not appropriate for velocity update, such as salt body. Also, the extended images might be evaluated at relatively sparse locations in the image along the in-line and cross-line directions to further reduce the cost. However, this may decrease the spatial resolution of the velocity update so that a trade-off between the cost and resolution must be made. Furthermore, it is possible to restrict the range of space- and time-lags to the extent necessary to capture the character of the reflection events.

2.6 Conclusions

An extended imaging condition offers the possibility to design robust migration velocity analysis methods that simultaneously exploit conventional semblance analysis and depth focusing analysis. The analytic moveout functions provide quantitative descriptions of the shapes of events in extended images. The envelope of the moveout function characterizing extended images constructed from multiple experiments form cones in the lags-depth domain. The apex of the cone represents a well focused image of the reflector. If velocity is correct, the apex appears at zero time-lag and correct depth, otherwise the apex shifts to nonzero time-lags and to an incorrect depth. Such a characteristic can be used as an indicator of velocity error for tomographic techniques. Synthetic examples verify the validity of the analytic moveout functions and demonstrate that the analysis for properties of the extended images hold even for complex media.

CHAPTER 3

WAVE-EQUATION MIGRATION VELOCITY ANALYSIS WITH TIME-SHIFT IMAGING

A paper published in *Geophysical Prospecting*, 2011, 59, no. 4, 635-650

Tongning Yang [1,2] and Paul Sava [1]

3.1 Summary

Wave-equation migration velocity analysis is a technique designed to extract and update velocity information from migrated images. The velocity model is updated through the process of optimizing the coherence of images migrated with the known background velocity model. The capacity for handling multi-pathing of the technique makes it appropriate in complex subsurface regions characterized by strong velocity variation. Wave-equation migration velocity analysis operates by establishing a linear relation between a slowness perturbation and a corresponding image perturbation. The linear relationship and the corresponding operator are derived from conventional extrapolation operators and the operator inherits the main properties of frequency-domain wavefield extrapolation. A key step in the implementation is to design an appropriate procedure for constructing an image perturbation relative to a reference image that represents difference between current image and a true, or more correct image of the subsurface geology. The target of the inversion is to minimize such an image perturbation by optimizing the velocity model. Using time-shift common-image gathers, one can characterize the imperfections of migrated images by defining the focusing error as the shift of the focus of reflections along the time-shift axis. The focusing error is then transformed into an image perturbation by focusing analysis under the linear approximation.

[1]Center for Wave Phenomena, Colorado School of Mines
[2]Corresponding author

As the focusing error is caused by the incorrect velocity model, the resulting image perturbation can be considered as a mapping of the velocity model error in the image space. Such an approach for constructing the image perturbation is computationally efficient and simple to implement. Also, the technique provides a new alternative to use focusing information for wavefield-based velocity model building. Synthetic examples demonstrate the successful application of our method to a layered model and a subsalt velocity update problem.

3.2 Introduction

In regions characterized by complex subsurface structure, prestack wave-equation depth migration, i.e. one-way wave-equation migration or reverse-time migration, is a powerful tool for accurately imaging the earth's interior (Gray et al., 2001; Etgen et al., 2009). However, the quality of the final image greatly depends on the accuracy of the velocity model. Thus, a key challenge for seismic imaging in complex geology is an accurate determination of the velocity model in the area under investigation (Symes, 2008; Woodward et al., 2008; Virieux and Operto, 2009).

Migration velocity analysis (MVA) generally refers to tomographic methods implemented in the image domain. These velocity analysis techniques are based on the principle that the quality of the seismic image is optimized when the data are migrated with the correct velocity model. The techniques update the velocity model by optimizing the properties measuring the coherence of migrated images. As a result, the quality of both the image and velocity model is improved through the process of velocity analysis.

Typically, the input for MVA is represented by various types of common-image gathers (CIGs), e.g. shot-domain (Al-Yahya, 1989), surface-offset (Mulder and ten Kroode, 2002), subsurface-offset (Rickett and Sava, 2002), time-shift (Sava and Fomel, 2006), angle-domain (Sava and Fomel, 2003; Biondi and Symes, 2004), or space- and time-lag extended-image gathers (Yang and Sava, 2010; Sava and Vasconcelos, 2011). Different kinds of image gathers determine whether semblance or focusing analysis should be used to measure the coherence of the image.

In practice, there are many possible approaches for implementing velocity analysis with different image gathers. However, all such realizations share a common element that they need a carrier of information to connect the input image gathers to the output velocity model. Thus, one can categorize velocity analysis techniques into ray-based and wavefield-based methods in terms of the information carrier they use. Ray-based methods, which are often described as traveltime velocity analysis, refer to techniques using wide-band rays as the information carrier (Bishop et al., 1985; Al-Yahya, 1989; Stork and Clayton, 1991; Woodward, 1992; Stork, 1992; Liu and Bleistein, 1995; Jiao et al., 2002). Wavefield-based velocity analysis methods refer to techniques using band-limited wavefields as the information carrier (Biondi and Sava, 1999; Mulder and ten Kroode, 2002; Shen and Calandra, 2005; Soubaras and Gratacos, 2007; Xie and Yang, 2008). Generally speaking, ray-based methods have the advantage over wavefield-based methods in that they involve simple implementation and efficient computation. In contrast, wavefield-based methods are capable of handling complicated wave propagation phenomena which always occur in complex subsurface regions. Therefore, they are more robust and consistent with the wavefield-based migration techniques used in such regions. Furthermore, the resolution of wavefield-based methods is higher than that of ray-based methods because wavefield-based methods employ fewer approximations to wave propagation.

Different from traveltime velocity analysis methods, wavefield-based velocity analysis techniques require an image residual as the input, which is equivalent to the data misfit defined in the image domain. Wave-equation MVA (Sava and Biondi, 2004a,b) and differential semblance optimization (Shen et al., 2003; Shen and Symes, 2008) are two common wavefield-based velocity analysis approaches. The image residual for wave-equation MVA and differential semblance optimization are obtained either by constructing a linearized image perturbation (Sava et al., 2005) or by applying a penalty operator to offset- or angle-domain CIGs (Symes and Carazzone, 1991; Shen and Calandra, 2005), respectively.

Focusing analysis is a commonly used method for refining the velocity model (Faye and Jeannot, 1986b). It evaluates the coherence of migrated images by measuring the focusing of reflections in the image. The focusing information can be extracted from time-shift CIGs (Sava and Fomel, 2006), and it is quantified as the shift of the focus of reflections along the time-shift axis from the origin. Such a shift is often defined as focusing error and indicates the existence of the velocity model error (MacKay and Abma, 1992; Nemeth, 1995b). Therefore, the focusing error can be used for velocity model optimization. Wang et al. (2005) propose a tomographic approach using focusing analysis for re-datuming data sets. The approach is a ray-based method and thus may become unstable when the multi-pathing problem exists due to the complex geology. Higginbotham and Brown (2008) and Brown et al. (2008) also propose a method to convert this focusing error into velocity updates using an analytic formula. This approach is based on 1D assumptions and the measured focusing error is transformed into vertical updates only. Hence, the method become less accurate in models with complex subsurface environments. Nevertheless, Wang et al. (2008, 2009) illustrate that focusing analysis can effectively improve the image quality and be used for updating the velocity model in subsalt areas.

For the implementation of wave-equation MVA, one important component is the construction of an image perturbation which is linked directly to a velocity perturbation. To construct the image perturbation, one first needs to measure the coherence of the image. Sava and Biondi (2004b) discuss two types of measurement for the imperfections of migrated images, i.e. focusing analysis (MacKay and Abma, 1992; Lafond and Levander, 1993) and moveout analysis (Yilmaz and Chambers, 1984; Biondi and Sava, 1999). The most common approach for constructing the image perturbation is to compare a reference image with its improved version. However, such an image-comparison approach has at least two drawbacks. First, the improved version of the image is always obtained by re-migration with one or more models, which is often computationally expensive. Second, if the reference image is incorrectly constructed, the difference between two images might exceed the small perturba-

tion assumption. This can lead to cycle skipping which changes the convergence properties of the inversion. An alternative to this approach, discussed in Sava and Biondi (2004a), uses prestack Stolt residual migration (Stolt, 1996; Sava, 2003) to construct a linearized image perturbation. This alternative approach avoids the cycle skipping problem, but suffers from the approximation embedded in the underlying Stolt migration.

In this paper, we propose a new methodology for wavefield-based velocity analysis using focusing information of migrated images. The essential idea is to construct a linearized image perturbation from time-shift imaging condition through focusing analysis, and then use it for velocity updates. We demonstrate that such an image perturbation can be easily computed by a simple multiplication of the image derivative constructed from a background image and the measured focusing error. We also demonstrate that this type of image perturbation is fully consistent with the linearization embedded in wave-equation MVA. Finally, we illustrate the feasibility of our approach by testing the method on simple and complex synthetic data sets.

3.3 Theory

Under the single scattering approximation, seismic migration consists of two steps: wavefield reconstruction followed by the application of an imaging condition. We commonly consider a "source" wavefield, originating at the seismic source and propagating in the medium prior to any interaction with the reflectors, and a "receiver" wavefield, originating at discontinuities and propagating in the medium to the receivers (Berkhout, 1982b; Claerbout, 1985). The two wavefields are kinematically equivalent at discontinuities of material properties. Any mismatch between the wavefields indicates inaccurate wavefield reconstruction typically assumed to be due to inaccurate velocity models. The source and receiver wavefields u_s and u_r are four-dimensional objects as functions of position $\mathbf{x} = (x, y, z)$ and frequency ω,

$$u_s = u_s(\mathbf{x}, \omega) \ , \tag{3.1}$$
$$u_r = u_r(\mathbf{x}, \omega) \ . \tag{3.2}$$

An imaging condition is designed to extract from these extrapolated wavefields the locations where reflections occur in subsurface. A conventional imaging condition (Claerbout, 1985) forms an image as the zero cross-correlation lag between the source and receiver wavefields:

$$r(\mathbf{x}) = \sum_{\omega} \overline{u_s(\mathbf{x}, \omega)} u_r(\mathbf{x}, \omega) \ , \tag{3.3}$$

where r is the image of subsurface and overline represents complex conjugation. An extended imaging condition (Sava and Fomel, 2006) extracts the image by cross-correlation between the wavefields shifted by the time-lag τ:

$$r(\mathbf{x}, \tau) = \sum_{\omega} \overline{u_s(\mathbf{x}, \omega)} u_r(\mathbf{x}, \omega) \, e^{2i\omega\tau} \ . \tag{3.4}$$

Other possible extended imaging conditions include space-lag extension (Rickett and Sava, 2002) or space- and time-lag extensions (Sava and Vasconcelos, 2011), but we do not discuss these types of imaging conditions here.

In the process of seismic migration, if the source and receiver wavefields are extrapolated with the correct velocity model, the result of cross-correlation between reconstructed wavefields, i.e. the migrated image, is maximized at zero lags. In other words, if the velocity used for migration is correct, reflections in the image are focused at zero offset and zero time. If the source and receiver wavefields are extrapolated with an incorrect velocity model, the result of cross-correlation is not maximized at zero lags. As a consequence, reflections in the image are focused at nonzero time but zero offset. This indicates the existence of error for downward continuation of the reconstructed wavefields. In such a situation, we can apply focusing analysis and extract the information about the accuracy of the velocity model. A commonly used approach for focusing analysis is to measure the focusing error in either depth domain or time domain. The depth-domain focusing error is defined as the depth difference between focusing depth d_f and migration depth d_m (MacKay and Abma, 1992)

$$\Delta z = d_f - d_m \ , \tag{3.5}$$

where

$$d_f = \frac{d}{\rho} \ , \tag{3.6}$$

and

$$d_m = d\rho \ . \tag{3.7}$$

Here d is the true depth of the reflection point, $\rho = \frac{V_m}{V}$ is the ratio between migration and true velocities. The time-domain focusing error is defined as the time-shift being applied to the reconstructed wavefields to achieve focusing of reflections. Yang and Sava (2010) quantitatively analyze the influence of the velocity model error on focusing property of reflections, and derive the formula connecting depth-domain and time-domain focusing error:

$$\Delta\tau = \frac{d_f - d_m}{V_m} \ , \tag{3.8}$$

where V_m represents the migration velocity. Notice that the formulae for d_f and d_m are derived under the assumptions of constant velocity, small offset angle and horizontal reflector. As a consequence, the analytic formula in 3.8 is an approximation of the true focusing error, and has limited applicability in practice.

To use wave-equation MVA for model building, one needs to start from linearization of the problem since an image is usually a nonlinear function of the velocity model. Furthermore, a nonlinear optimization problem is more difficult to solve than a linear optimization problem. We represent the true slowness as the sum of a background slowness s_b and a slowness perturbation Δs:

$$s\left(\mathbf{x}\right) = s_b\left(\mathbf{x}\right) + \Delta s\left(\mathbf{x}\right) \ . \tag{3.9}$$

Likewise, the image can also be characterized as a sum of a background image r_b and an image perturbation Δr:

$$r\left(\mathbf{x}\right) = r_b\left(\mathbf{x}\right) + \Delta r\left(\mathbf{x}\right) \ . \tag{3.10}$$

The perturbation Δs and Δr are related by the wave-equation tomographic operator $\mathbf{L}$ derived from the linearization of one-way wave-equation migration operator, as demonstrated by Sava and Biondi (2004a). A brief summary of derivation and construction of $\mathbf{L}$ can be found in appendix A. Consequently, we can establish a linear relationship between the image perturbation and slowness perturbation:

$$\Delta r = \mathbf{L}\Delta s \ . \tag{3.11}$$

Sava and Vlad (2008) further illustrates the implementation of operator $\mathbf{L}$ for different imaging configurations, i.e. zero-offset, survey-sinking, and shot-record cases.

The information of focusing error $\Delta\tau$ is available on the extended images constructed with 3.4. In other words, the focus of reflections can be evaluated by locating the maximum energy of reflection events in time-shift CIGs. If the focus is located at zero time shift, the velocity model is correct. Otherwise, the distance of the focus from origin is measured along the time-shift axis and defined as the focusing error. Then, an improved image $\widetilde{r}$ can be obtained by choosing the image from the time-shift CIG at the τ value corresponding to the focusing error:

$$\widetilde{r}\,(\mathbf{x}) = r\,(\mathbf{x},\tau)|_{\tau=\Delta\tau} \ , \tag{3.12}$$

and an image perturbation can be constructed by a direct subtraction:

$$\Delta r\,(\mathbf{x}) = \widetilde{r}\,(\mathbf{x}) - r_b\,(\mathbf{x}) \ . \tag{3.13}$$

Although such an approach is straightforward, the constructed image perturbation might be phase-shifted too much with respect to the background image r_b and thus violates the Born approximation required by the tomographic operator $\mathbf{L}$. To overcome the challenge, Sava and Biondi (2004a) propose to construct a linearized image perturbation as

$$\Delta r\,(\mathbf{x}) \approx \mathbf{K}'|_{\rho=1}\,[r_b]\Delta\rho \ , \tag{3.14}$$

where $\mathbf{K}$ is the prestack Stolt residual migration operator (Stolt, 1996; Sava, 2003), the $'$ sign represents derivation relative to the velocity ratio ρ, and $\Delta\rho = \rho - 1$. Similarly, we can also

construct an image perturbation by the linearization of the image relative to the time-shift parameter τ:

$$\Delta r\left(\mathbf{x}\right) \approx \left.\frac{\partial r\left(\mathbf{x},\tau\right)}{\partial \tau}\right|_{\tau=0} \Delta\tau \ , \tag{3.15}$$

where the image derivative with respect to time-shift τ is

$$\frac{\partial r\left(\mathbf{x},\tau\right)}{\partial \tau} = \sum_{\omega} \left(2i\omega\right) \overline{u_s\left(\mathbf{x},\omega\right)} u_r\left(\mathbf{x},\omega\right) e^{2i\omega\tau} \ . \tag{3.16}$$

By constructing the image perturbation with 3.15, one can avoid the cycle-skipping problem because the linearized image perturbation is obtained from the background image, and thus has no phase shift with respect to the background image. Furthermore, 3.15 provides a straightforward way to convert the focusing error associated with the velocity model error into the image perturbation. In other words, 3.16 maps the velocity error into image domain, so that one can optimize the model by minimizing the image perturbation. The linearization of both the approaches in 3.14 and 3.15 is consistent with the characteristics of the tomographic operator $\mathbf{L}$.

One can follow the procedure outlined below to construct the image perturbations from time-shift imaging condition and use it for wavefield-based velocity optimization:

- Migrate the data and output time-shift CIGs according to 3.4;
- Measure $\Delta\tau$ on time-shift CIG panels by picking the focus, i.e. maximum energy, for all reflections;
- Construct the image derivative according to 3.16;
- Construct the linearized image perturbation according to 3.15.

After we construct the image perturbation Δr, we can solve for the slowness perturbation Δs by minimizing the objective function,

$$J\left(\Delta s\right) = \frac{1}{2}\|\Delta r - \mathbf{L}\Delta s\|^2 \ . \tag{3.17}$$

Such an optimization problem can be solved iteratively using conjugate-gradient-based methods. As most practical inverse problems are ill-posed, additional constraints must be imposed during the inversion to obtain a stable and convergent result. This can be done by adding a model regularization term in the objective function 3.17, leading to the modified objective function:

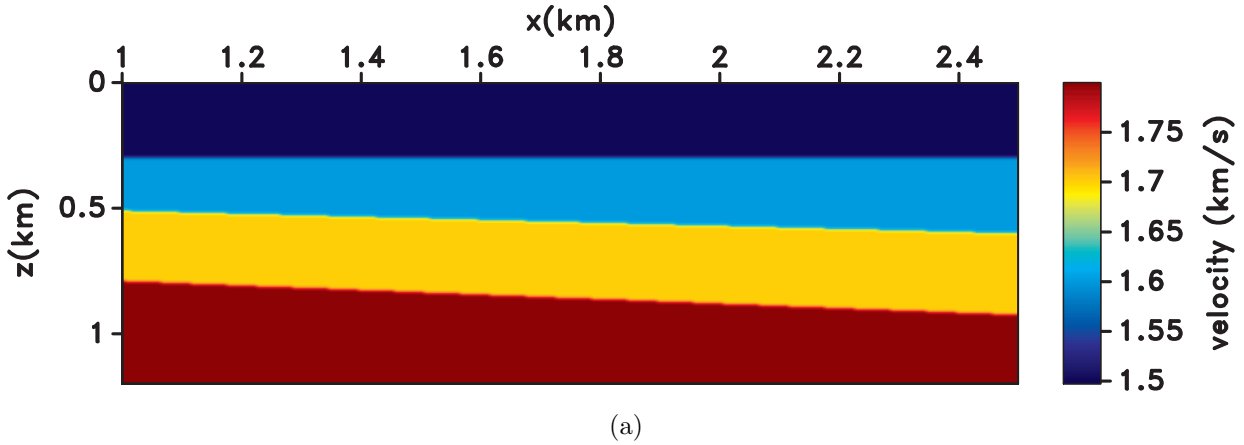
$$J(\Delta s) = \frac{1}{2}\|\Delta r - \mathbf{L}\Delta s\|^2 + \alpha^2\|\mathbf{A}\Delta s\|^2 \,, \tag{3.18}$$

where α is a scalar to control the relative weights between data residual and model norm, and $\mathbf{A}$ is a regularization operator (Fomel, 2007). How to chose $\mathbf{A}$ and α is outside the scope of discussion in this paper.

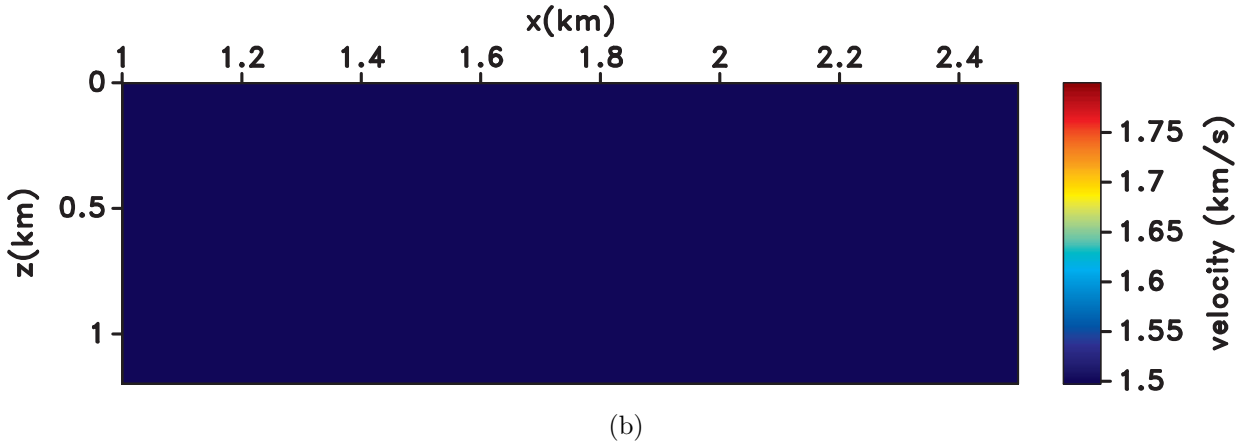
3.4 Example

We illustrate our methodology with two synthetic examples. The first example consists of four dipping layers with different thickness and dipping angle. The velocities of the four layers are 1.5, 1.6, 1.7, and 1.8 km/s, respectively. The background model is constant with velocity of 1.5 km/s. Figure 3.1(a) and Figure 3.1(b) show the true and background velocity models, respectively. Figure 3.2(a) and Figure 3.2(b) are the image migrated with the true and background velocity model, respectively. Comparing these two images, one can observe that the second and third reflectors in Figure 3.2(b) are positioned incorrectly due to the error of the velocity model.

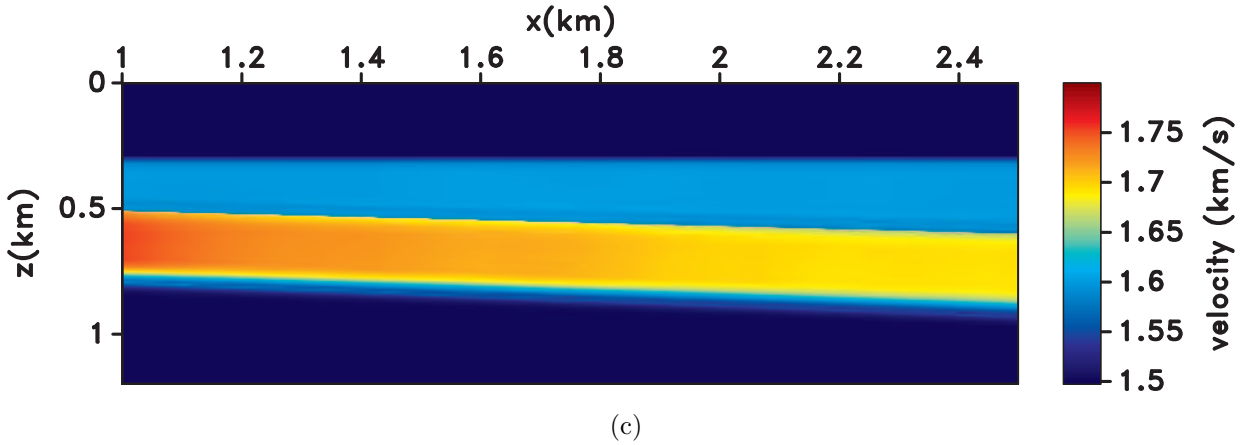
Figure 3.3(a)-Figure 3.3(c) shows three time-shift CIGs migrated with the background model. The image gathers are chosen at $x = 1.2$, $x = 1.8$, and $x = 2.3$ km, respectively. The focusing error picking is done by applying an automatic picker to the envelope of the original image gathers. The solid lines in the figure plot the picked focusing error, while the dashed lines represent zero time shift. In this case, as the velocity errors for the second and third layers increase with depth, the focusing error increases with depth accordingly. As a result, bigger time shifts can be observed for deeper events. Figure 3.4(a) shows the focusing error as a function of position and depth. This figure depicts the focusing error



(a)

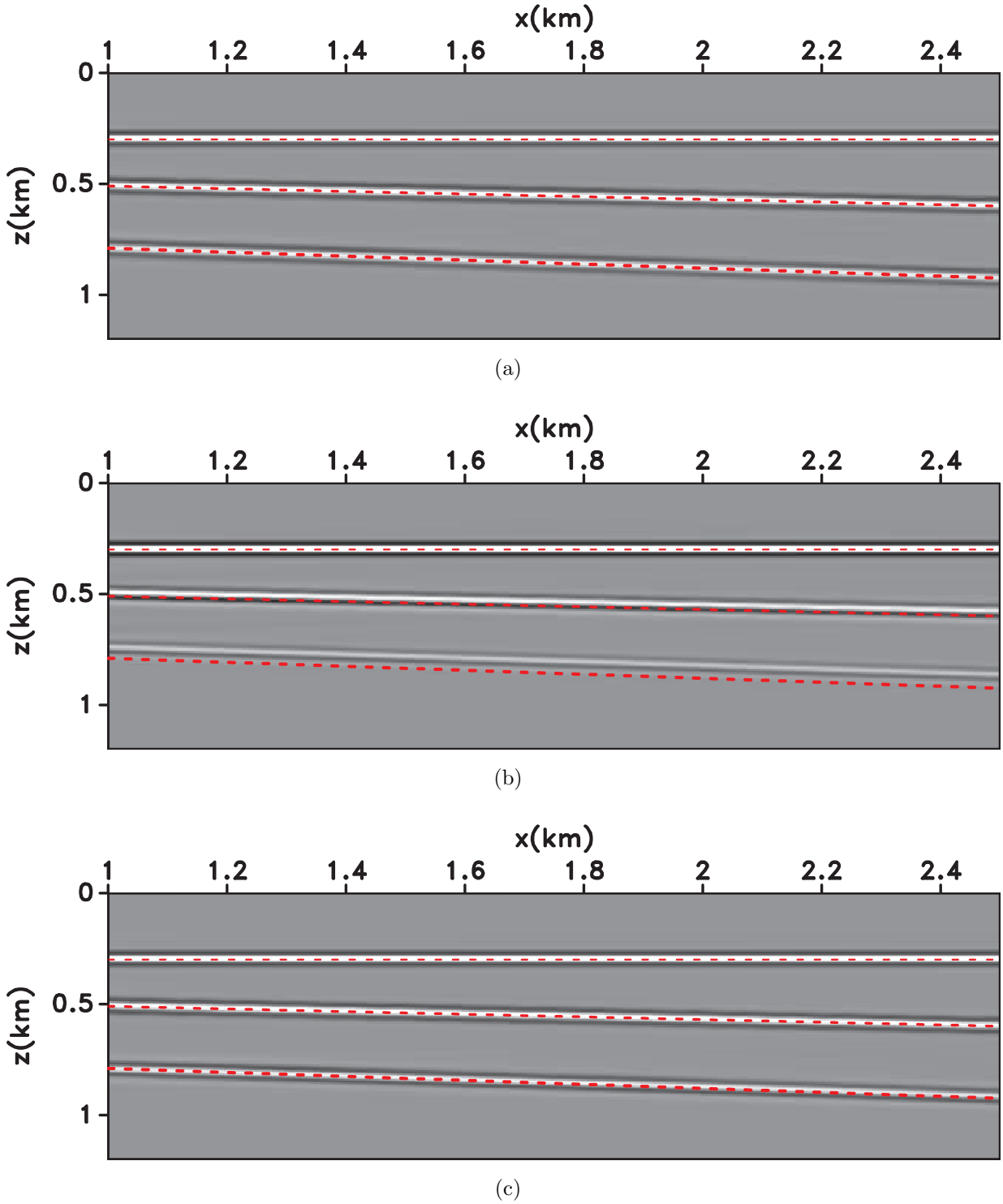


(b)



(c)

Figure 3.1: Velocity profiles of the layers model. (a) The true velocity model. (b) The background velocity model with a constant velocity of the first layer 1.5 km/s. (c) The updated velocity model.



(a)

(b)

(c)

Figure 3.2: Images migrated with (a) the true velocity model, (b) the background velocity model, and (c) the updated velocity model. The dash lines represent the true position of the reflections.

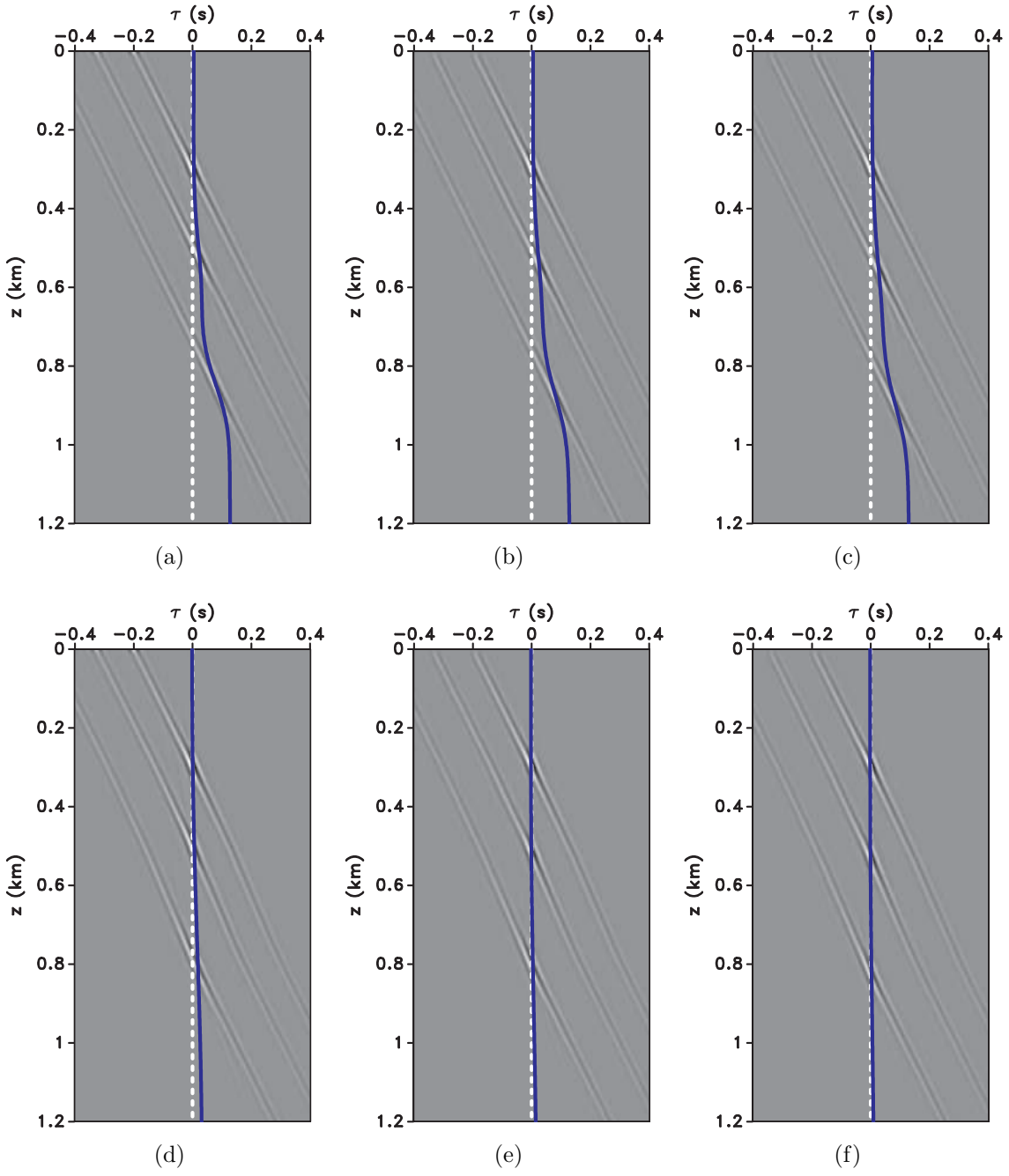
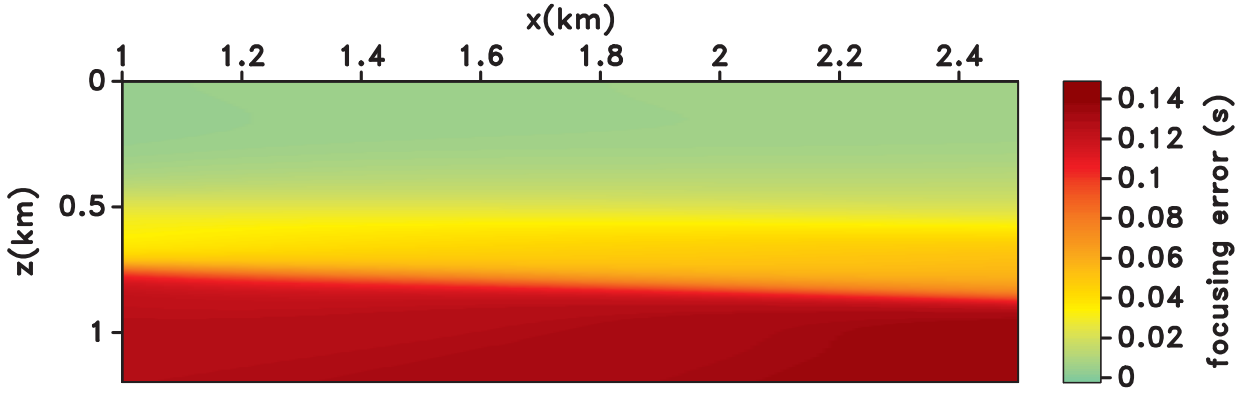
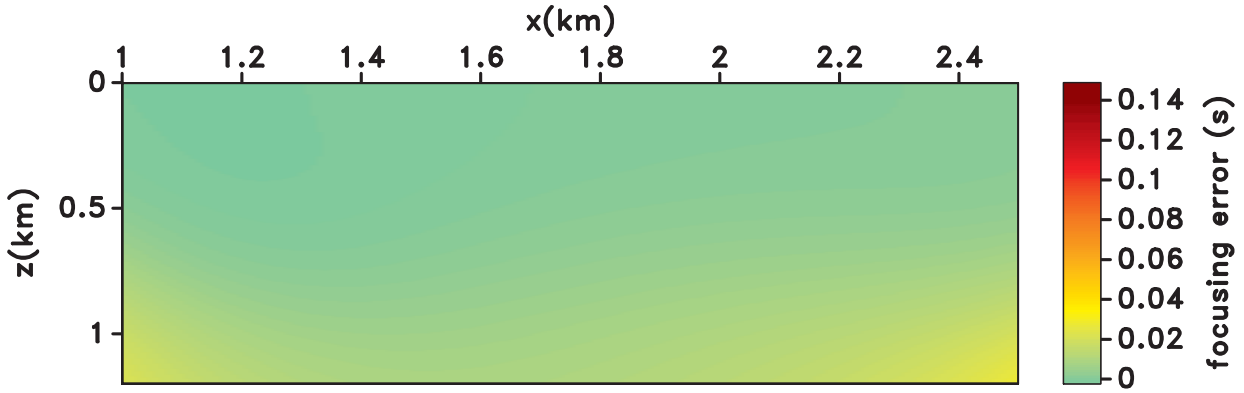


Figure 3.3: Time-shift CIGs migrated with the background model (a) at $x = 1.2$ km, (b) at $x = 1.8$ km, and (c) at $x = 2.3$ km. Time-shift CIGs migrated with the updated model at (d) $x = 1.2$ km, (e) at $x = 1.8$ km, and (f) at $x = 2.3$ km. The overlain solid lines represent picked focusing error. The dash lines represent zero time shift.



(a)



(b)

Figure 3.4: (a) Focusing error panel corresponding to the background model. (b) Focusing error panel corresponding to the updated model.

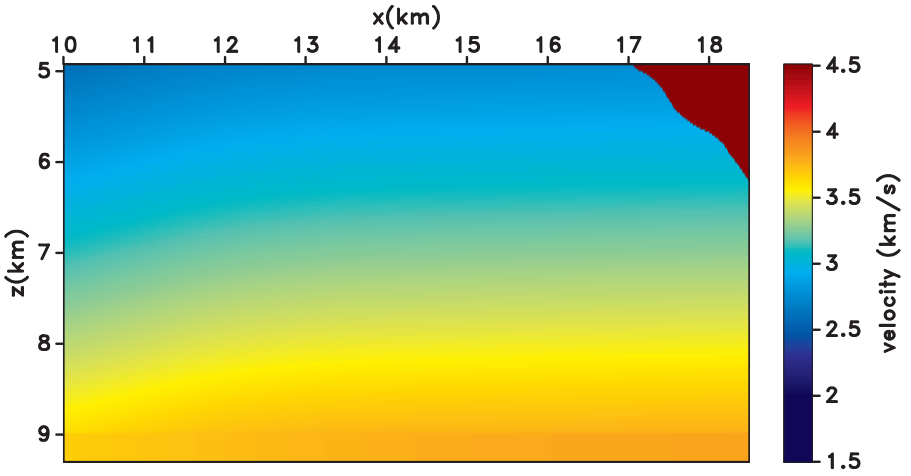
picked from the image gathers constructed at every horizontal location x. Since the layers have different thickness, the associated velocity errors change as a function of horizontal and vertical directions. Therefore, a spatially varying focusing error of the subsurface is observed.

We construct the image perturbation using the procedure discussed in the preceding sections. Next, we perform the inversion based on the objective function in 3.18. The inverse problem is solved using the conjugate-gradient method. For this simple model, two nonlinear iterations are enough to reconstruct the velocity model.

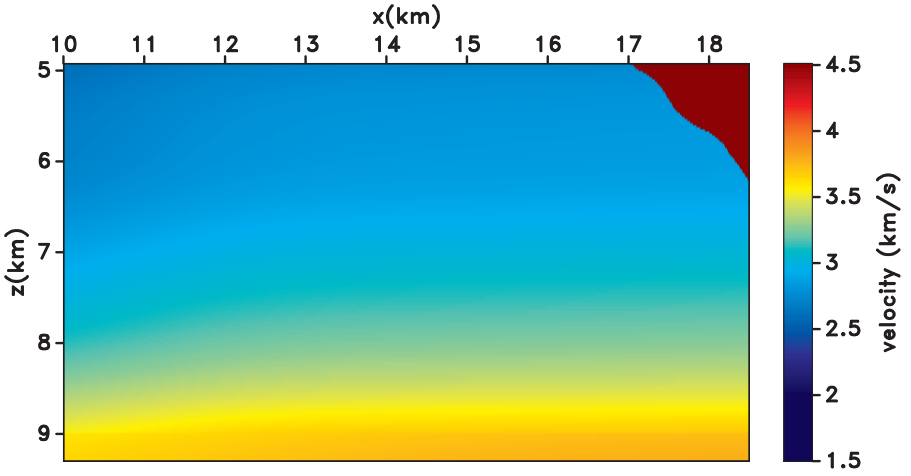
Figure 3.1(c) shows the updated model after the inversion. The velocity for the second and third layer are correctly inverted. Here, the velocity update occurs in the region above the fourth layer. This is due to the fact that no reflection exists in the bottom part of the model, and the input image perturbation carries no velocity information for the bottom layer. Thus, the inversion does not compute velocity updates in the area. Figure 3.2(c) shows the image migrated with the updated model. The reflections are positioned in the correct depth, as compared with Figure 3.2(a) and indicated by the dashed lines overlain on the figure.

Figure 3.3(d) - Figure 3.3(f) shows image gathers obtained by migration with the updated model. The gathers are chosen at the same positions as the gathers shown in Figure 3.3(a) - Figure 3.3(c), i.e. at $x = 1.2$, $x = 1.8$, and $x = 2.3$ km, respectively. The focus of all the reflections are located at zero time-shift, as demonstrated by the fact that the solid and dashed lines are overlapped with each other in the gathers. Figure 3.4(b) is the focusing error panel of the subsurface. The value of the focusing error is zero almost everywhere. This means that the inversion has achieved the target of minimizing the focusing error and confirms the successful reconstruction of the velocity model in this example.

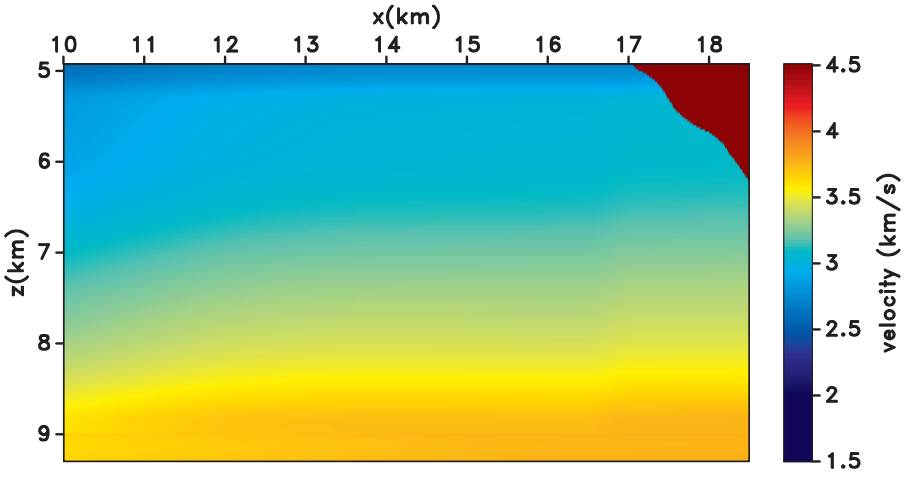
We also apply our methodology to a subsalt velocity update example. The target area is chosen from the subsalt portion of the Sigsbee 2A model (Paffenholz et al., 2002), ranging from $x = 9.5$ km, $z = 5.0$ km to $x = 18.5$ km, $z = 9.3$ km. For this example, the main goals are to image correctly the fault located between the point $x = 14.0$ km, $z = 6.0$ km



(a)

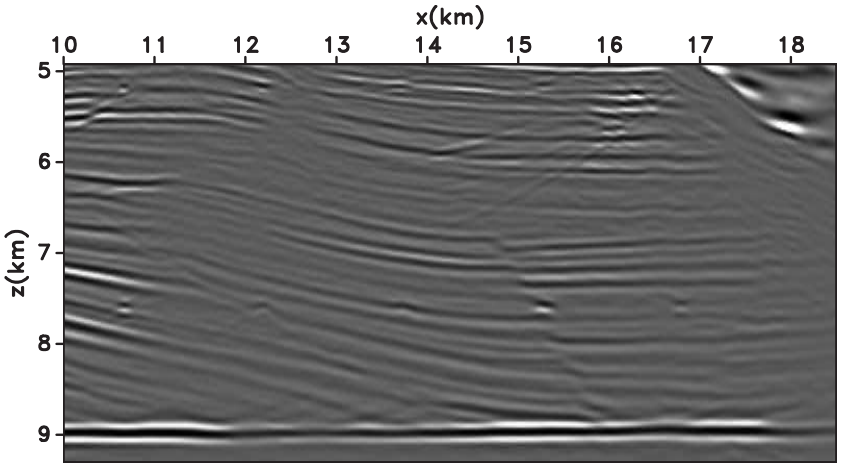


(b)

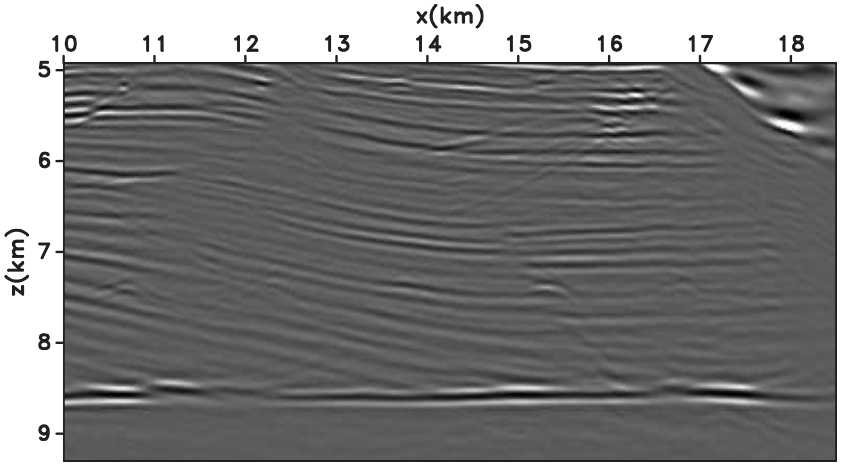


(c)

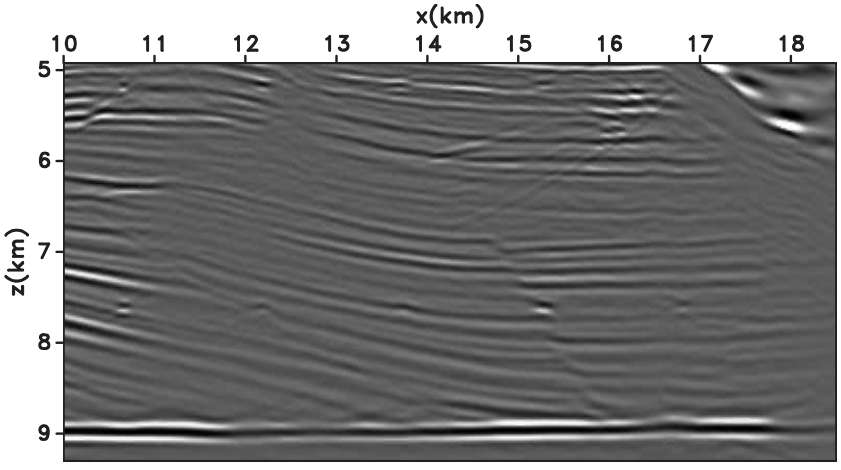
Figure 3.5: Velocity profiles of Sigsbee 2A model. (a) The true velocity model, (b) the background velocity model, and (c) the updated model.



(a)



(b)



(c)

Figure 3.6: Images migrated with (a) the true velocity model, (b) the background velocity model, and (c) the updated velocity model.

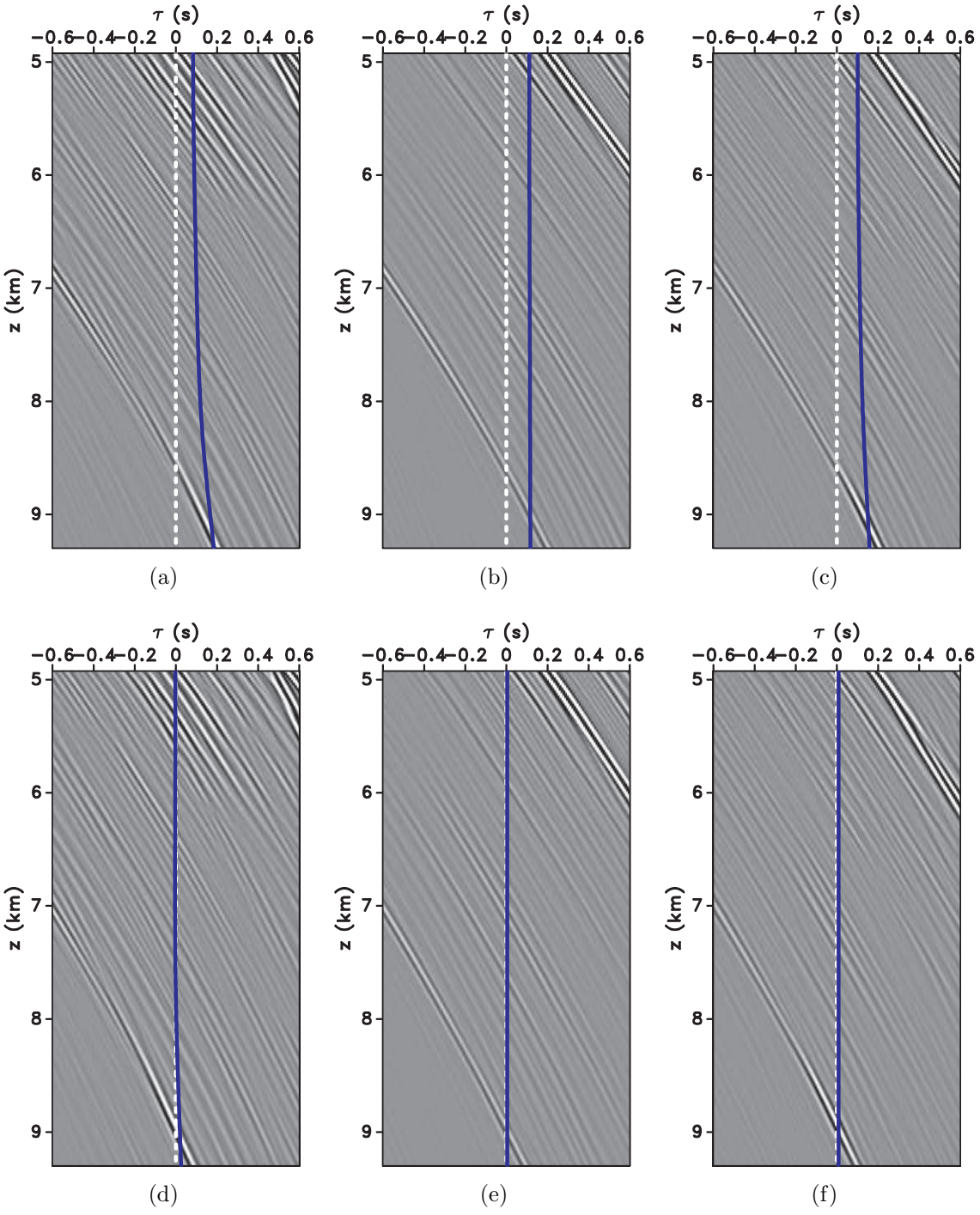
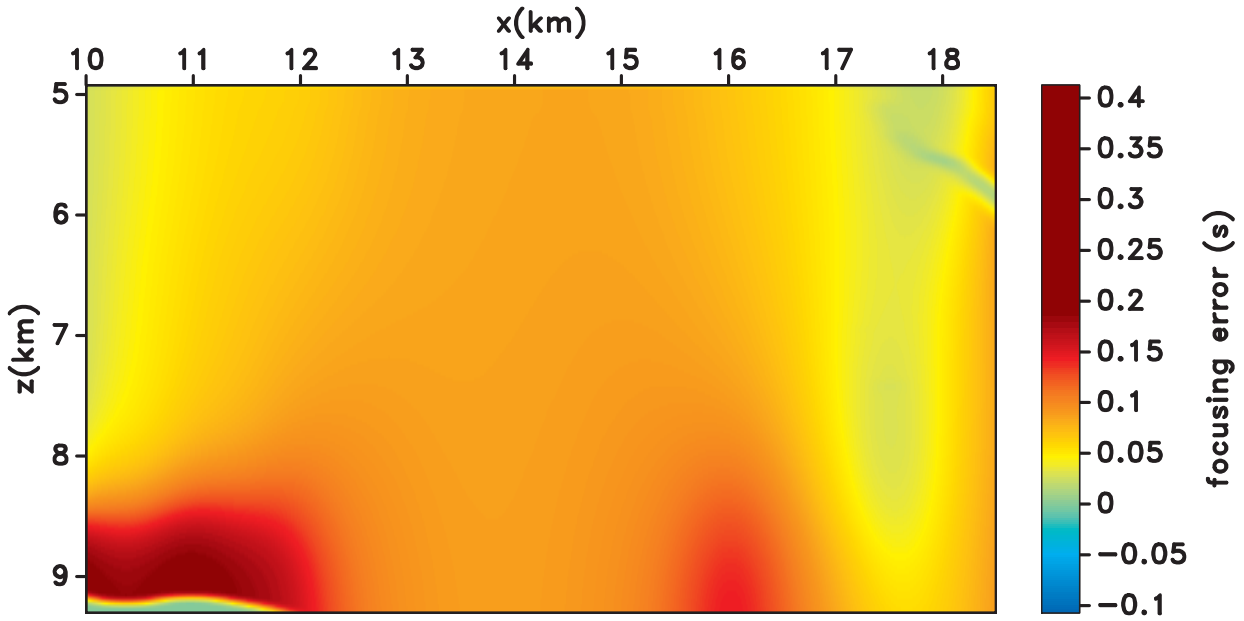
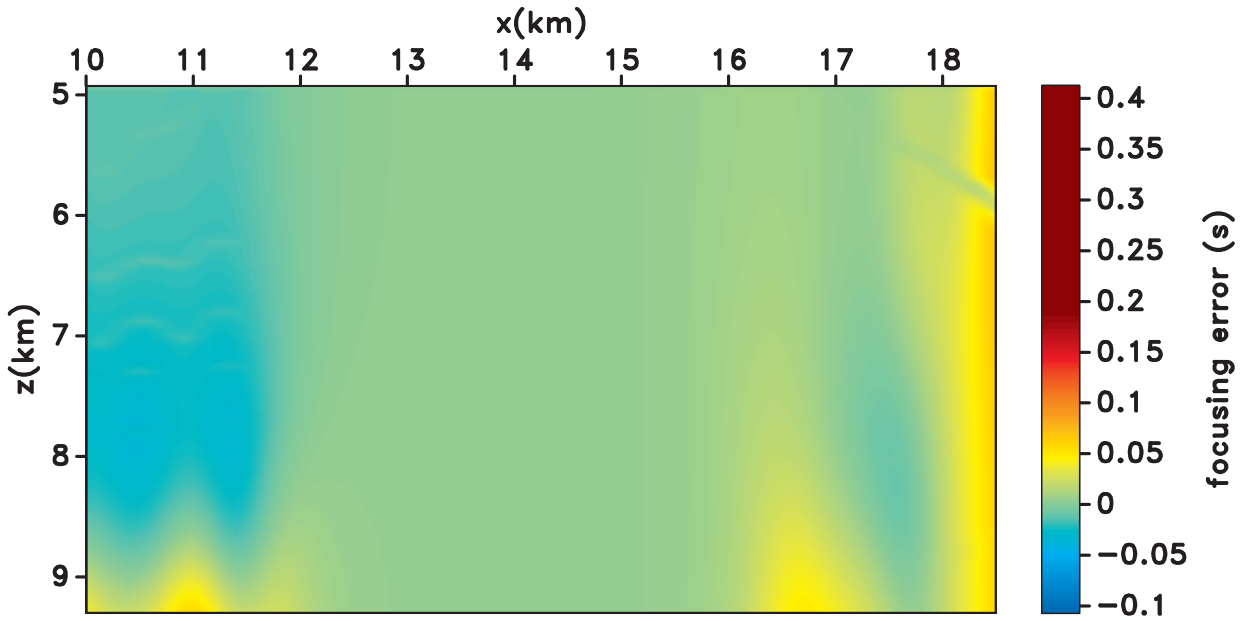


Figure 3.7: Time-shift CIGs migrated with the background model, (a) at $x = 13.0$ km, (b) at $x = 14.8$ km, and (c) at $x = 16.6$ km. Time-shift CIGs migrated with the updated model, (d) at $x = 13.0$ km, (e) at $x = 14.8$ km, and (f) at $x = 16.6$ km. The overlain solid lines represent picked focusing error. The dash lines represent zero time shift.



(a)



(b)

Figure 3.8: (a) Focusing error panel corresponding to the background model. (b) Focusing error panel corresponding to the updated model.

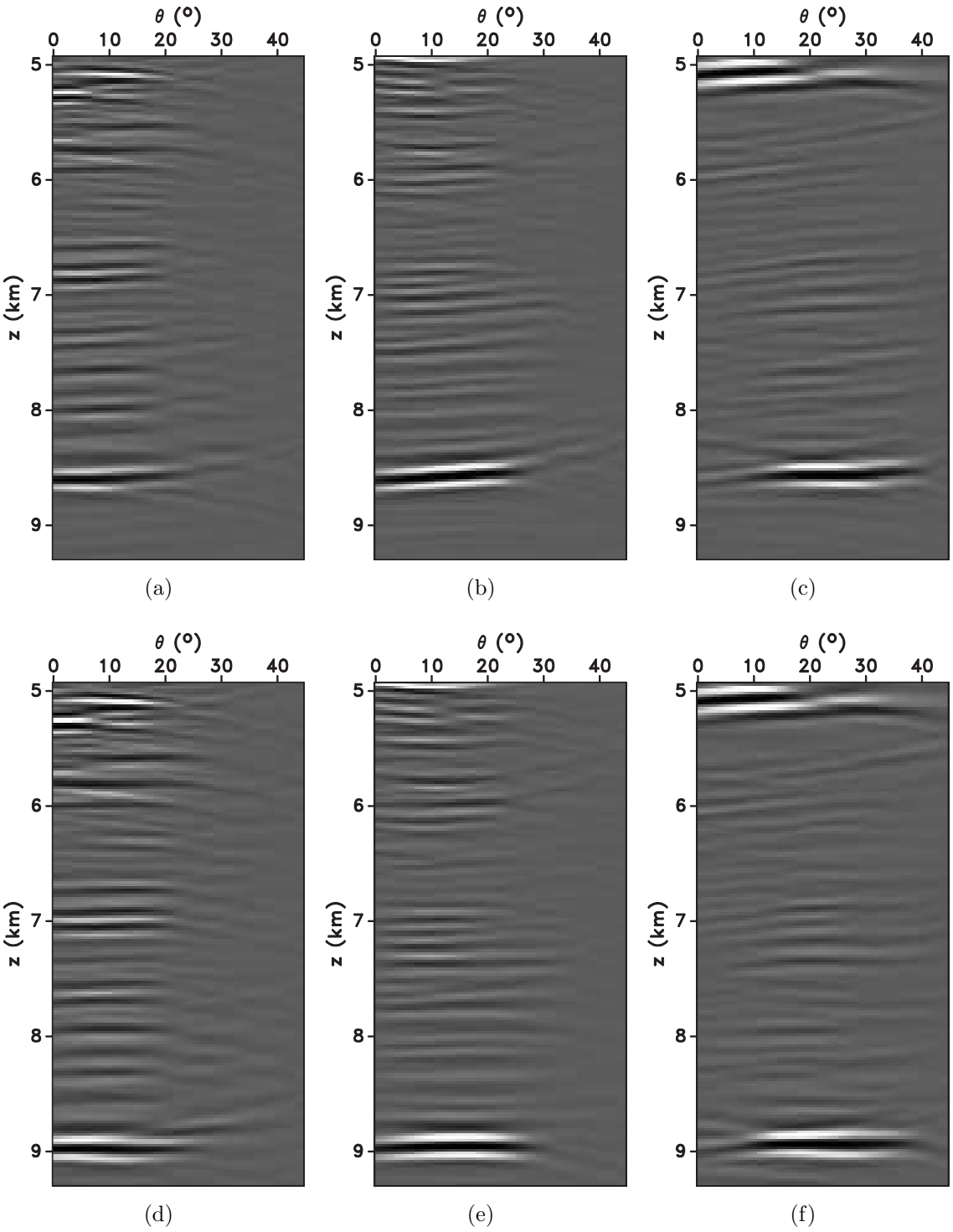


Figure 3.9: Angle-domain CIGs migrated with the background model, (a) at $x = 13.0$ km, (b) at $x = 14.8$ km, and (c) at $x = 16.6$ km. Angle-domain CIGs migrated with the updated model, (d) at $x = 13.0$ km, (e) at $x = 14.8$ km, and (f) at $x = 16.6$ km.

and the point $x = 16.0$ km, $z = 9.0$ km, to increase the focusing for the deeper diffractors, and to positioning correctly the bottom flat reflector. We assume correct knowledge of the velocity above the salt and known salt geometry. The background model for the target zone is obtained by scaling the true model with a constant factor 0.9. The true and background velocity models are depicted in Figure 3.5(a) and Figure 3.5(b), respectively. Figure 3.6(a) and Figure 3.6(b) show the images migrated with the true and background model, respectively. Due to the error of the background velocity model, the fault is obscured by nearby sediment reflections, the deeper diffractions are defocused, and the bottom flat reflector is positioned far away from its correct depth.

Figure 3.7(a) - Figure 3.7(c) show several time-shift CIGs migrated with the background model at $x = 13.0$, $x = 14.8$, and $x = 16.6$ km, respectively. The picked focusing error is directly overlain on the gathers, although the picking is done on the envelope of the original image gathers just as the previous example. Here, we notice that the picks do not start at zero on the top of the gathers, although the associated focusing error should be zero. Such an error is mainly caused by the truncation of reflections in the gathers. Figure 3.8(a) shows the focusing error in the target area. Notice that variation exists for the picked focusing error in lateral and vertical directions. Part of such a variation is caused by the uneven illumination of the subsalt area, which may lead to difficulties for the automatic picker.

Next, we use the same procedure to construct the image perturbation as introduced in the preceding section. Then we run the inversion to obtain the velocity update by minimizing the objective function in 3.18. Figure 3.5(c) shows the updated model after three nonlinear iterations. The inversion has correctly reconstructed the velocity model in the subsalt area. Figure 3.6(c) shows the image migrated with the updated model. The fault located between the point $x = 14.0$ km,$z = 6.0$ km and the point $x = 16.0$ km,$z = 9.0$ km is delineated and clearly visible in the image. The bottom reflector is positioned at the correct depth, and become more coherent. The deeper diffractions are also well focused. These improvements in the image imply a correct update of the velocity model.

Figure 3.7(d) - Figure 3.7(f) plot several image gathers migrated with the background model at $x = 13.0$, $x = 14.8$, and $x = 16.6$ km, respectively. The focusing error picks are overlain on the gathers. Most reflections are focused at zero time shift, which means the focusing error is reduced thanks to the more accurate velocity model after the inversion. Figure 3.8(b) plot the focusing error in the target area after velocity update and remigration. The focusing error is reduced after the inversion, which indicates the successful optimization of the velocity model.

To further confirm that the velocity model is correctly inverted, we also compute angle-domain CIGs with the background and updated models and use the flatness of reflection events in the gathers as the criterion to evaluate the result of inversion. The angle-domain gathers are chosen at the same locations at the time-shift gathers. Figure 3.9(a) - Figure 3.9(c) plot the gathers corresponding to the background velocity model, while Figure 3.9(d) - Figure 3.9(f) show the gathers for the updated velocity model. In comparison, the reflection events in the gathers obtained with the updated model are more flat than the events in the gathers obtained with the background model. This demonstrates the improvement of the quality of the velocity model after the optimization. However, we notice that the curvature of the residual moveout in the gathers obtained with the background model is not easily distinguishable. This can cause difficulties for curvature picking and thus degrades the velocity estimation methods relying on flattening the residual moveout. In such a situation, minimizing the focusing error, as in the case of our approach, may provide a reliable alternative for velocity optimization.

3.5 Discussion

Using focusing information extracted from time-shift imaging offers a good alternative to wavefield-based velocity model optimization. The key to the approach is to construct a linearized image perturbation associated with the focusing error. The computation of the linearized image perturbation is simple and straightforward. Also, the cost of the construction is trivial as no expensive re-migration scan and angle decomposition are required in this

procedure. Furthermore, such a velocity analysis method based on time-shift image gathers is computationally more attractive in 3D application as only one additional dimension is required for constructing image gathers, while two additional dimensions are needed for constructing lag-domain image gathers (Shen and Symes, 2008).

The inversion scheme described in the paper is a wave-equation-based tomographic approach. Although the information is extracted by applying focusing analysis to time-shift image gathers, the process of velocity updating does not rely on any analytic formulae as in the case for conventional depth-focusing analysis. Therefore, the technique discussed in this paper has applicability to models with arbitrary lateral velocity variations.

Finally, we emphasize that picking the focusing error is extremely important for our approach as the focusing error determines the direction and magnitude of the velocity update. Therefore, the process of the picking should be carefully implemented.

3.6 Conclusions

We develop a new method for implementing wave-equation migration velocity analysis based on time-shift imaging and focusing analysis. The objective of the velocity optimization is to minimize the focusing error measured from time-shift image gathers. The methodology relies on constructing linearized image perturbations by applying focusing analysis to the image gathers. The focusing error is defined as the shift of the focus for reflections along the time-shift axis and provides a measurement for the accuracy of the velocity model used in migration. We use this information in conjunction with image derivatives relative to the time-shift parameter to compute linearized image perturbations as the input for velocity model optimization. The image perturbation obtained by this approach is consistent with the Born approximation used for the wave-equation tomographic operators so that the cycle-skipping problem can be avoided. The construction of the image perturbation in our approach is efficient, since the main cost is just the construction of the time-shift image gathers and is much lower than the cost of re-migration scans and angle decomposition. In addition, our method is accurate, since it does not include strong assumptions about the smoothness

of the background model when constructing the linearized image perturbation. Thus, our approach is suitable for the areas with complex subsurface structure. The synthetic examples demonstrate the validity of the linearized image perturbation constructed using our new method. The inversion with such an image perturbation as the input can render satisfactory updates for the velocity model. The success of the velocity optimization is confirmed by the fact that the focusing error is reduced after the inversion.

CHAPTER 4

IMAGE-DOMAIN WAVEFIELD TOMOGRAPHY WITH EXTENDED COMMON-IMAGE-POINT GATHERS

A paper submitted to *Geophysical Prospecting*

Tongning Yang [1,2] and Paul Sava [1]

4.1 Summary

Waveform inversion is a velocity-model-building technique based on full waveforms as the input and seismic wavefields as the information carrier. Conventional waveform inversion is implemented in the data-domain. However, similar techniques referred to as image-domain wavefield tomography can be formulated in the image domain and use seismic image as the input and seismic wavefields as the information carrier. The objective function for the image-domain approach is designed to optimize the coherency of reflections in extended common-image gathers. The function applies a penalty operator to the gathers, thus highlighting image inaccuracies arising from the velocity model error. Minimizing the objective function optimizes the model and improves the image quality. The gradient of the objective function is computed using the adjoint-state method in a way similar to that in the analogous data-domain implementation. We propose an image-domain velocity-model building method using extended common-image-point gathers constructed at discrete locations in the image. Such gathers have the advantage over conventional common-image gathers that they are robust for imaging reflectors with a wide range of dips. The common-image-point gathers can extract the velocity information from steep reflectors imaged with a two-way wave propagator, this information improving accuracy of the gradient computation and vertical resolution of velocity estimates. The gathers moreover are effective in reconstructing the

[1]Center for Wave Phenomena, Colorado School of Mines
[2]Corresponding author

velocity model in complex geologic environments and can be used as an economical replacement for conventional common-image gathers in wave-equation tomography. A test on the Marmousi model illustrates successful updating of the velocity model using common-image point gathers and resulting improved image quality.

4.2 Introduction

Building an accurate and reliable velocity model remains one of the biggest challenges in current seismic imaging practice. In regions characterized by complex subsurface structure, prestack wave-equation depth migration (e.g., one-way wave-equation migration or reverse-time migration) is a powerful tool for accurately imaging the Earth's interior (Gray et al., 2001; Etgen et al., 2009). Because these migration methods are very sensitive to model errors, their widespread use significantly drives the need for high-quality velocity models because these migration methods are very sensitive to model errors (Symes, 2008; Woodward et al., 2008; Virieux and Operto, 2009).

Waveform inversion (WI) represents a family of techniques for velocity model building using seismic wavefields (Tarantola, 1984; Woodward, 1992; Pratt, 1999; Sirgue and Pratt, 2004; Plessix, 2006; Vigh and Starr, 2008a; Plessix, 2009; Symes, 2009). This type of methodology, although usually regarded as one of the costliest for velocity estimation, has been gaining momentum in recent years, mainly because of its accuracy as well as advances in computing technology. The core of WI is using a wave equation (typically constant-density acoustic) to simulate wavefields as the information carrier. Usually WI is implemented in the data domain by adjusting the velocity model such that simulated and recorded data match (Tarantola, 1984; Pratt, 1999). This match is based on the strong assumption that the wave equation used for simulation is consistent with the physics of the Earth. This, however, is unlikely to be the case when the Earth is characterized by strong (poro)elasticity. In data domain approaches, significant effort is often directed toward removing the components of the recorded data that are inconsistent with the assumptions used.

Velocity-model-building methods using seismic wavefields can be implemented in the image domain rather than in the data domain. Instead of minimizing the data misfit, the techniques in this category update the velocity model by optimizing the image quality, which is the cross-correlation of wavefields extrapolated from the data and from the source wavelet. The image quality is optimized when the data are migrated with the correct velocity model, as stated by the semblance principle (Al-Yahya, 1989; Yilmaz, 2001). The common idea is to optimize the coherency of reflection events in common-image gathers (CIGs) via velocity-model-updating. Since images are obtained using full waveforms, and velocity estimation also employs seismic wavefields as the information carrier, these techniques can be considered as a particular type of WI, and we refer to them as image-domain wavefield tomography (WT). Unlike traditional image-domain ray-based tomography methods, image-domain WT uses band-limited wavefields in the optimization procedure. Thus, this technique is capable of handling complicated wave propagation phenomena such as multi-pathing in the subsurface. In addition, the band-limited character of the wave-equation engine more accurately approximates wave propagation in the subsurface and produces more reliable velocity updates than do ray-based methods.

Sava and Biondi (2004a,b) describe the concept of wave-equation migration velocity analysis, which is one variation of image-domain WT. The method linearizes the downward continuation operator and establishes a linear relationship between the model perturbation and image perturbation. The model is inverted by exploiting this linear relationship and minimizing the image perturbation. Sava et al. (2005) demonstrate application of the technique to velocity model building in complex regions, and Sava and Vlad (2008) discuss its detailed numerical implementation. This methodology, however, is limited by its reliance on the one-way wave propagation operator, which constrains its ability to produce model updates in complicated geology with steep reflectors.

Differential semblance optimization (DSO) is another variation of image-domain WT. The essence of the method is to minimize the difference of any given reflection between

neighboring offsets or angles. Symes and Carazzone (1991) propose a criterion for measuring coherency within offset gathers and establish the theoretic foundation for DSO. The concept is then generalized to space-lag (subsurface-offset) and angle-domain gathers (Shen and Calandra, 2005; Shen and Symes, 2008). In practice, space-lag gathers (Rickett and Sava, 2002; Shen and Calandra, 2005) and angle-domain gathers (Sava and Fomel, 2003; Biondi and Symes, 2004) are two popular choices among various types of CIGs used for velocity analysis. These gathers are obtained by wave-equation migration and have fewer artifacts usually found in conventional offset gathers obtained by Kirchhoff migration, and thus they are suitable for applications in complex earth models (Stolk and Symes, 2004).

With recent developments in forward modeling and computing hardware, reverse-time migration (RTM) has become a common tool for imaging applications, especially in complex subsurface areas. One can characterize the wave propagation in the subsurface for the velocity estimation process more accurately using a two-way wave-equation propagator than using an one-way wave-equation propagator (Mulder, 2008). Furthermore, the capability of RTM for imaging steep reflections benefits velocity model building since more information can be extracted from the image to constrain the velocity updates (Gao and Symes, 2009). To effectively access the velocity information contained in steep reflections, Sava and Vasconcelos (2011) and Vasconcelos et al. (2010) propose common-image-point gathers (CIPs) as an alternative to space-lag or angle-domain gathers. CIPs are sparsely distributed in the subsurface on reflections and offer several advantages in the context of velocity inversion. First, the construction of a complete lag vector (space lags and time lag) avoids the bias toward nearly horizontal reflections. Thus, the gathers are sensitive to the velocity information in reflections with arbitrary dip and take advantage of the steep events imaged by RTM. Second, the discrete sampling of the gathers provides a flexible way to extract the velocity information from the image and facilitates target-oriented velocity updates. Furthermore, the sparse construction of the gathers reduces computational cost and storage requirements, both important in 3D applications.

In this paper, we propose an image-domain wavefield-based velocity-model-building approach using CIPs as the input. One key component of image-domain WT is wavefield simulation using a one-way or two-way wave-equation engine, similar to data-domain WI but with more flexibility. Another key component of the method is the objective function (OF), which is constructed by applying a penalty operator to CIPs whose minimization allows us to optimize image coherency and to update the velocity model simultaneously. The third component is an effective gradient calculation based on the adjoint state method (Plessix, 2006; Symes, 2009). In summary, gradient calculation with this method consists of the following steps: (1) compute the *state variables*, i.e., the seismic wavefields obtained from the source by forward modeling and from the data by backward modeling; (2) compute the *adjoint source*, i.e., a calculation based on the OF and on the state variables; (3) compute the *adjoint state variables*, i.e., the seismic wavefields obtained from the adjoint source by backward modeling; (4) compute the *gradient* using the state and adjoint state variables. We provide more details on this technique in the body of the paper.

This paper starts with a theoretical discussion of image-domain WT and its implementation with CIPs and CIGs. We show that CIPs overcome the bias toward nearly horizontal reflectors, which is important in the presence of steeply dipping structures because the information extracted from steep reflections provides additional constraints on the velocity model building. We use the Marmousi model to demonstrate that CIPs can be an economical and accurate replacement for CIGs used in the conventional wave-equation-based DSO approach to model building in complex subsurface areas. The results obtained from CIPs are comparable to those obtained from CIGs, but with smaller cost for computing and storing the image gathers.

4.3 Theory

In this section, we formulate image-domain wavefield tomography using both space- and time-lag extended images (extended CIPs) or space-lag extended images (also known as subsurface-offset CIGs). The gradient is computed by applying the adjoint-state method

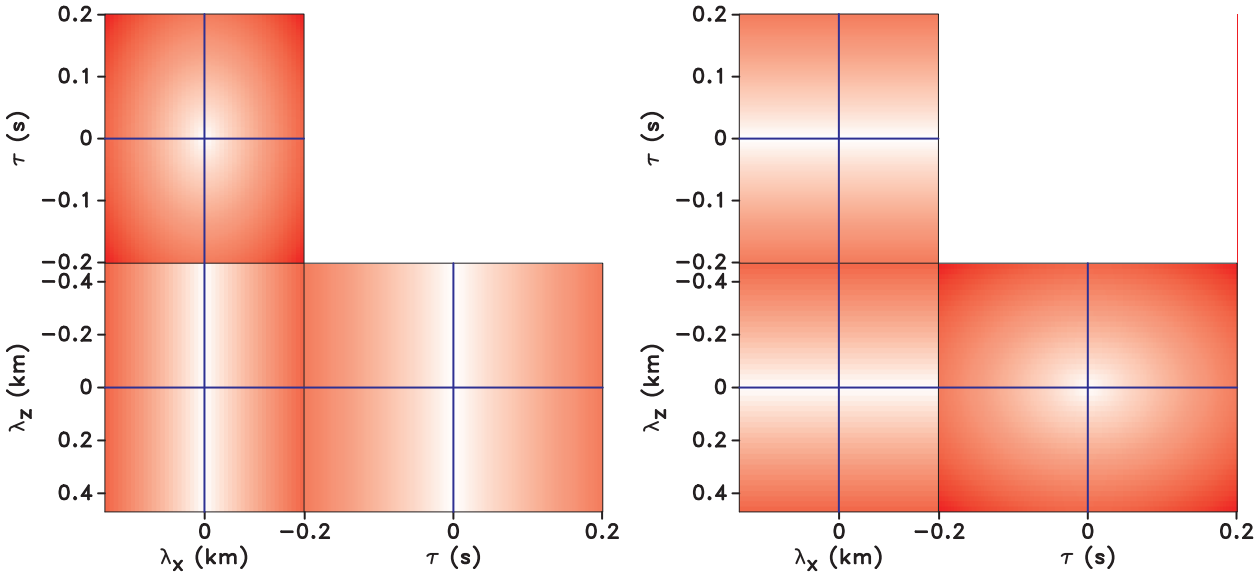


Figure 4.1: The penalty operators for CIPs on (a) horizontal reflector and (b) vertical reflector.

(Plessix, 2006; Symes, 2009), which is also a common practice for data-domain full-waveform inversion (Tarantola, 1984; Sirgue and Pratt, 2004; Virieux and Operto, 2009). This approach can easily be generalized to other image-domain wavefield tomography methods implemented with different input image gathers, e.g., time-lag CIGs (Yang and Sava, 2011b).

For simplicity, we discuss the methodology in the frequency-domain rather than in the time-domain although the latter is completely equivalent and analogous. We formulate the inverse problem by first defining the state variables, through which the OF is related to the model parameters. The state variables for our problem are the source and receiver wavefields u_s and u_r obtained by solving the following acoustic wave equation:

$$\begin{bmatrix} \mathcal{L}\left(\mathbf{x},\omega,m\right) & 0 \\ 0 & \mathcal{L}^{*}\left(\mathbf{x},\omega,m\right) \end{bmatrix} \begin{bmatrix} u_s\left(j,\mathbf{x},\omega\right) \\ u_r\left(j,\mathbf{x},\omega\right) \end{bmatrix} = \begin{bmatrix} f_s\left(j,\mathbf{x},\omega\right) \\ f_r\left(j,\mathbf{x},\omega\right) \end{bmatrix} , \tag{4.1}$$

where f_s is the source function, f_r are the recorded data, $j = 1,...N_s$, where N_s is the number of shots, ω is the angular frequency, and $\mathbf{x} = \{x, y, z\}$ are the space coordinates. The wave operator $\mathcal{L}$ and its adjoint $\mathcal{L}^{*}$ propagate the wavefields forward and backward in

time, respectively, using either a one-way or two-way wave equation. In this formulation, we designate the operator $\mathcal{L}$ to be

$$\mathcal{L} = -\omega^2 m - \Delta \ , \tag{4.2}$$

where Δ is the Laplace operator, and model parameter m represents slowness squared.

In the second step of the adjoint-state method, we first construct the OF and then the adjoint sources that are used to model the adjoint-state variables required by the gradient computation. The OF for image-domain wavefield tomography is defined using the semblance principle (Yilmaz, 2001) and measures the image incoherency caused by the model errors. Therefore, the inversion process of minimizing the OF simultaneously reconstructs the model and improves the image quality.

We consider the objective function in the $\boldsymbol{\lambda} - \tau$ domain ($\boldsymbol{\lambda}$ is a vector that pertains to space-lags in 2D or 3D space and τ pertains to time-lag) and use extended CIPs as the input to analyze and optimize the velocity model. Extended CIPs are obtained by applying the nonzero space- and time-lag cross-correlation imaging condition (Sava and Fomel, 2006) to the wavefields at selected points in the image. Sava and Vasconcelos (2011) analyze the kinematic characteristics of reflections in extended CIPs and point out that reflections focus at zero space- and time-lags when the migration velocity is correct. Therefore, the OF based on extended CIPs is defined as

$$\mathcal{H}_{\boldsymbol{\lambda},\tau} = \frac{1}{2} \| K_I \left(\mathbf{x} \right) P \left(\boldsymbol{\lambda}, \tau \right) r \left(\mathbf{x}, \boldsymbol{\lambda}, \tau \right) \|^2_{\mathbf{x},\boldsymbol{\lambda},\tau} \ , \tag{4.3}$$

where $P \left(\boldsymbol{\lambda}, \tau \right)$ is defined below, and $r \left(\mathbf{x}, \boldsymbol{\lambda}, \tau \right)$ are space- and time-lag extended images:

$$\begin{aligned} r \left(\mathbf{x}, \boldsymbol{\lambda}, \tau \right) &= \sum_j \sum_\omega \overline{u_s \left(j, \mathbf{x} - \boldsymbol{\lambda}, \omega \right)} u_r \left(j, \mathbf{x} + \boldsymbol{\lambda}, \omega \right) e^{2 i \omega \tau} \\ &= \sum_j \sum_\omega T \left(-\boldsymbol{\lambda} \right) \overline{u_s \left(j, \mathbf{x}, \omega \right)} T \left(\boldsymbol{\lambda} \right) u_r \left(j, \mathbf{x}, \omega \right) e^{2 i \omega \tau} \ , \end{aligned} \tag{4.4}$$

the overline represents complex conjugate. The operator T represents the space shift applied to the wavefields and is defined by

$$T(\boldsymbol{\lambda})\, u(j, \mathbf{x}, \omega) = u(j, \mathbf{x} + \boldsymbol{\lambda}, \omega) \ , \tag{4.5}$$

The mask operator $K_I(\mathbf{x})$ restricts the construction of extended images to chosen discrete locations only, such that the CIPs are constructed only on reflectors and are sampled sparsely in the subsurface. For two reasons, CIPs provide an effective and efficient way to extract velocity information from migrated images. First, no gathers are computed in areas without reflections so the computational cost can be reduced. Second, CIPs can be computed on steep reflectors where conventional CIGs fail to access the velocity information contained in these reflections. An example of a penalty operator $P(\boldsymbol{\lambda}, \tau)$ for vector lags is

$$P(\boldsymbol{\lambda}, \tau) = \sqrt{|\boldsymbol{\lambda} \cdot \mathbf{q}|^2 + (V\tau)^2} \ . \tag{4.6}$$

Here $\mathbf{q}$ is a unit vector in the reflection plane and $V(\mathbf{x})$ represents the local migration velocity. The operator $P(\boldsymbol{\lambda}, \tau)$ penalizes energy away from zero space- and time-lags, which indicates the existence of velocity errors. Hence, the defocused energy outside zero space-lag is enhanced by the operator $P(\boldsymbol{\lambda}, \tau)$ and forms a residual that is the basis for optimization. Figure 4.1(a) and Figure 4.1(b) show penalty operators for CIPs on horizontal and vertical reflectors, respectively. The penalty operator defined in 4.6 represents a cylinder oriented normal to the reflector in the $\boldsymbol{\lambda}-\tau$ space. If we consider only the case of horizontal space-lags, the penalty operator can be simplified as

$$P(\boldsymbol{\lambda}, \tau) = \sqrt{|\boldsymbol{\lambda}|^2 + (V\tau)^2} \ , \tag{4.7}$$

where the space-lag vector $\boldsymbol{\lambda} = \{\lambda_x, \lambda_y, 0\}$.

Given $\mathcal{H}_{\boldsymbol{\lambda},\tau}$ in 4.3, the adjoint sources are computed as OF's derivatives with respect to the state variables u_s and u_r (Shen and Symes, 2008). In this case, the adjoint sources g_s and g_r are complicated because the complete lags are involved in the computation.

$$
\begin{aligned}
g_s\left(j,\mathbf{x},\omega\right) = \sum_{\boldsymbol{\lambda},\tau} & T\left(\boldsymbol{\lambda}\right) P\left(\boldsymbol{\lambda},\tau\right) K_I\left(\mathbf{x}\right) \overline{K_I\left(\mathbf{x}\right) P\left(\boldsymbol{\lambda},\tau\right)} \\
& \overline{r\left(\mathbf{x},\boldsymbol{\lambda},\tau\right)} T\left(\boldsymbol{\lambda}\right) u_r\left(j,\mathbf{x},\omega\right) e^{-2i\omega\tau} \\
g_r\left(j,\mathbf{x},\omega\right) = \sum_{\boldsymbol{\lambda},\tau} & T\left(-\boldsymbol{\lambda}\right) P\left(\boldsymbol{\lambda},\tau\right) K_I\left(\mathbf{x}\right) \overline{K_I\left(\mathbf{x}\right) P\left(\boldsymbol{\lambda},\tau\right)} \\
& r\left(\mathbf{x},\boldsymbol{\lambda},\tau\right) T\left(-\boldsymbol{\lambda}\right) u_s\left(j,\mathbf{x},\omega\right) e^{-2i\omega\tau}
\end{aligned}
\tag{4.8}
$$

The adjoint state variables a_s and a_r are the wavefields obtained by backward and forward modeling respectively, using the corresponding adjoint sources defined in equation 4.8:

$$
\begin{bmatrix} \mathcal{L}^*\left(\mathbf{x},\omega,m\right) & 0 \\ 0 & \mathcal{L}\left(\mathbf{x},\omega,m\right) \end{bmatrix} \begin{bmatrix} a_s\left(j,\mathbf{x},\omega\right) \\ a_r\left(j,\mathbf{x},\omega\right) \end{bmatrix} = \begin{bmatrix} g_s\left(j,\mathbf{x},\omega\right) \\ g_r\left(j,\mathbf{x},\omega\right) \end{bmatrix} , \tag{4.9}
$$

and $\mathcal{L}$ and $\mathcal{L}^*$ are the same wave propagation operators used in equation 6.3.

The last step of the gradient computation is simply the correlation between state variables and adjoint state variables (Plessix, 2006):

$$
\begin{aligned}
& \frac{\partial \mathcal{H}_{\boldsymbol{\lambda},\tau}}{\partial m} = \\
& \sum_j \sum_\omega \frac{\partial \mathcal{L}}{\partial m} \left(u_s\left(j,\mathbf{x},\omega\right) \overline{a_s\left(j,\mathbf{x},\omega\right)} + u_r\left(j,\mathbf{x},\omega\right) \overline{a_r\left(j,\mathbf{x},\omega\right)} \right) ,
\end{aligned}
\tag{4.10}
$$

where $\frac{\partial \mathcal{L}}{\partial m}$ is the partial derivative of the wave propagation operator with respect to the model parameter. Using the definition of $\mathcal{L}$ in 5.2, we find that $\frac{\partial \mathcal{L}}{\partial m}$ is simply $-\omega^2$. In equation 4.10, we note that the gradient for image-domain wavefield tomography consists of two correlations because we define both the source and receiver wavefields as the state variables. In contrast, the gradient computed in the data-domain approach involves only one correlation on the source side because we use only the simulated wavefield as the state variable.

The derivation above shows the construction of OF and detailed gradient computation for image-domain wavefield tomography. Given these two components, the solution to the inverse problem is found by minimizing the OF using non-linear gradient-based iterative methods. In each iteration, the gradient is computed and the model update is calculated by

line search in the steepest descent or conjugate gradient directions. (Vigh and Starr, 2008b) This procedure is similar to that in data-domain waveform inversion.

4.4 Examples

In this section, we illustrate our method with two synthetic examples and emphasize the advantages of using CIPs for velocity model building. The first example highlights the robustness of CIPs in the presence of steeply dipping reflectors. The second example demonstrates the ability of CIPs to reconstruct velocity models in complex subsurface regions.

The first synthetic model is shown in Figure 4.2(a), and the initial model is just the vertical gradient extended to the entire model (Figure 4.2(b)). Figure 4.3(a)-Figure 4.3(b) show the images migrated using RTM with correct and initial velocities, respectively. The lack of 2D circular low-velocity anomaly in the initial model causes defocusing and image triplications.

To highlight the robustness of CIPs, we construct both the CIGs and CIPs in the subsurface at the positions indicated by the vertical lines and dots in Figure 4.3(b). Figure 4.4(a)-Figure 4.4(d) and Figure 4.5(a)-Figure 4.5(d) plot the CIGs and CIPs constructed on different reflectors for correct and initial velocities. Figure 4.4(c)-Figure 4.4(d) and Figure 4.5(c)-Figure 4.5(d) compare the CIGs and CIPs constructed on the horizontal reflector. Here, both CIGs and CIPs correctly characterize the reflection as the gathers show either focused reflections or residual moveout depending on the model used for imaging. Thus, one can assess the accuracy of the velocity models by analyzing the focusing information in the gathers. In contrast, Figure 4.4(a)-Figure 4.4(b) and Figure 4.5(a)-Figure 4.5(b) show that for the vertical reflector, only CIPs are able to correctly characterize the reflection and thus provide velocity information for the model building. The CIGs are contaminated by artifacts because we construct the gathers using horizontal lags for vertical reflections. The reflections are sampled at every depth level in the gathers, and thus their focusing cannot be correctly characterized. The difference between CIPs and CIGs is caused by the fact that both vertical and horizontal space-lags are used in CIPs while only the horizontal space-lag

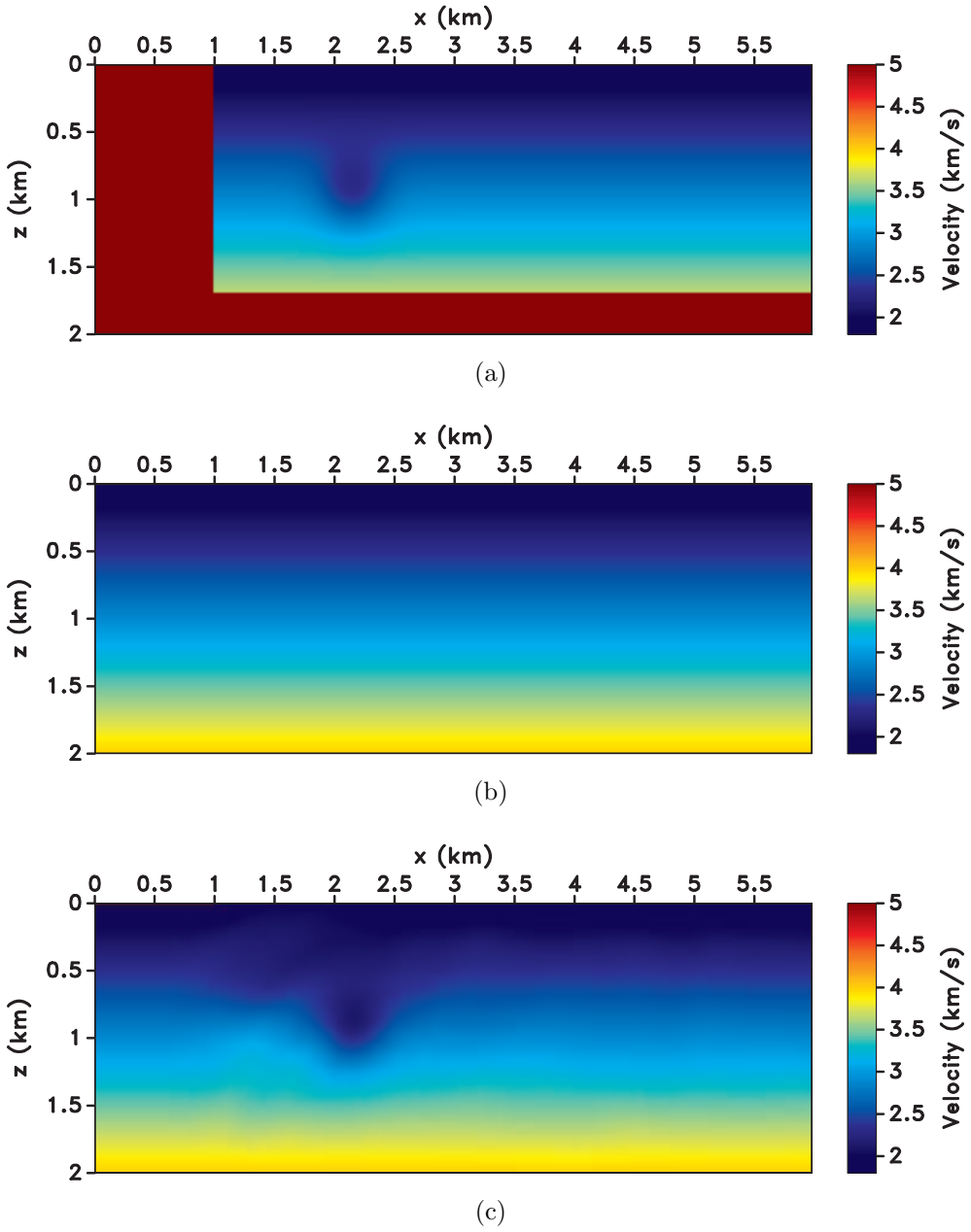
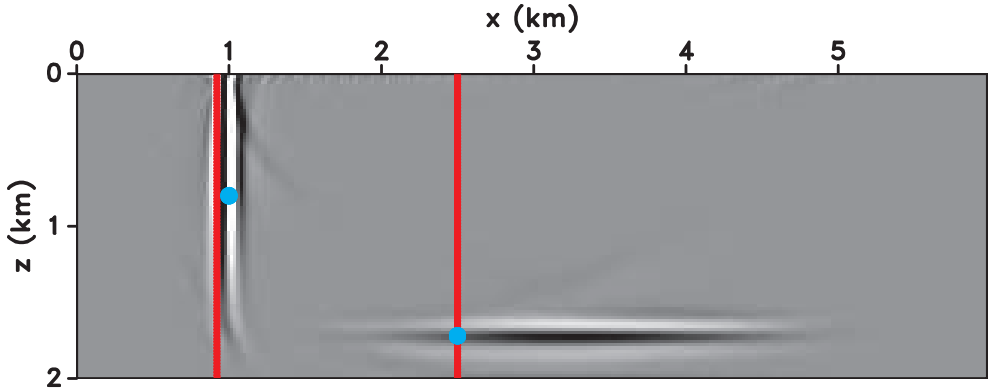
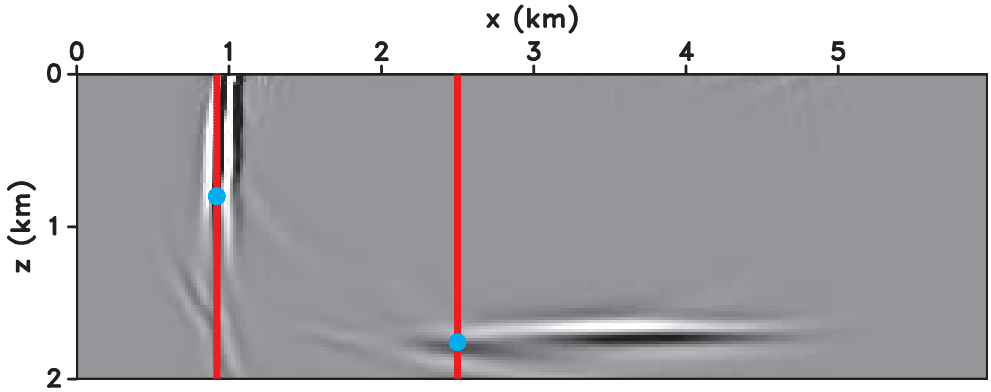


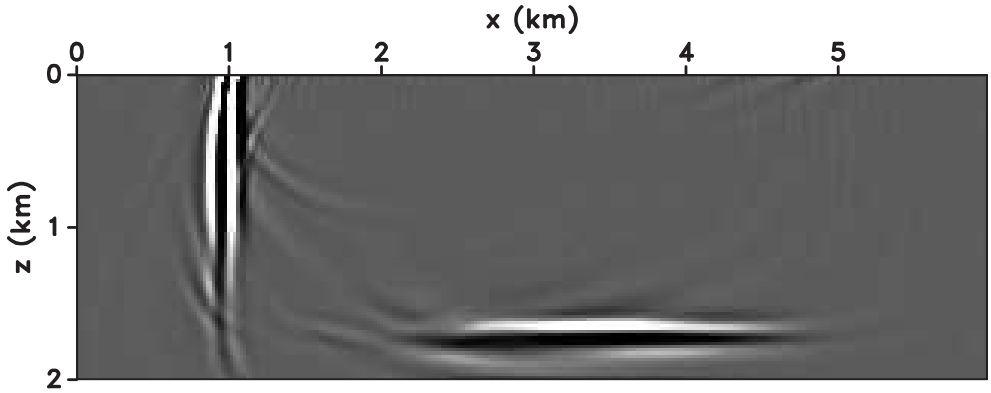
Figure 4.2: (a) The true velocity model, (b) the initial velocity model, and (c) the updated velocity model.



(a)



(b)



(c)

Figure 4.3: The images migrated with (a) the true velocity model, (b) the initial velocity model, and (c) the updated velocity model.

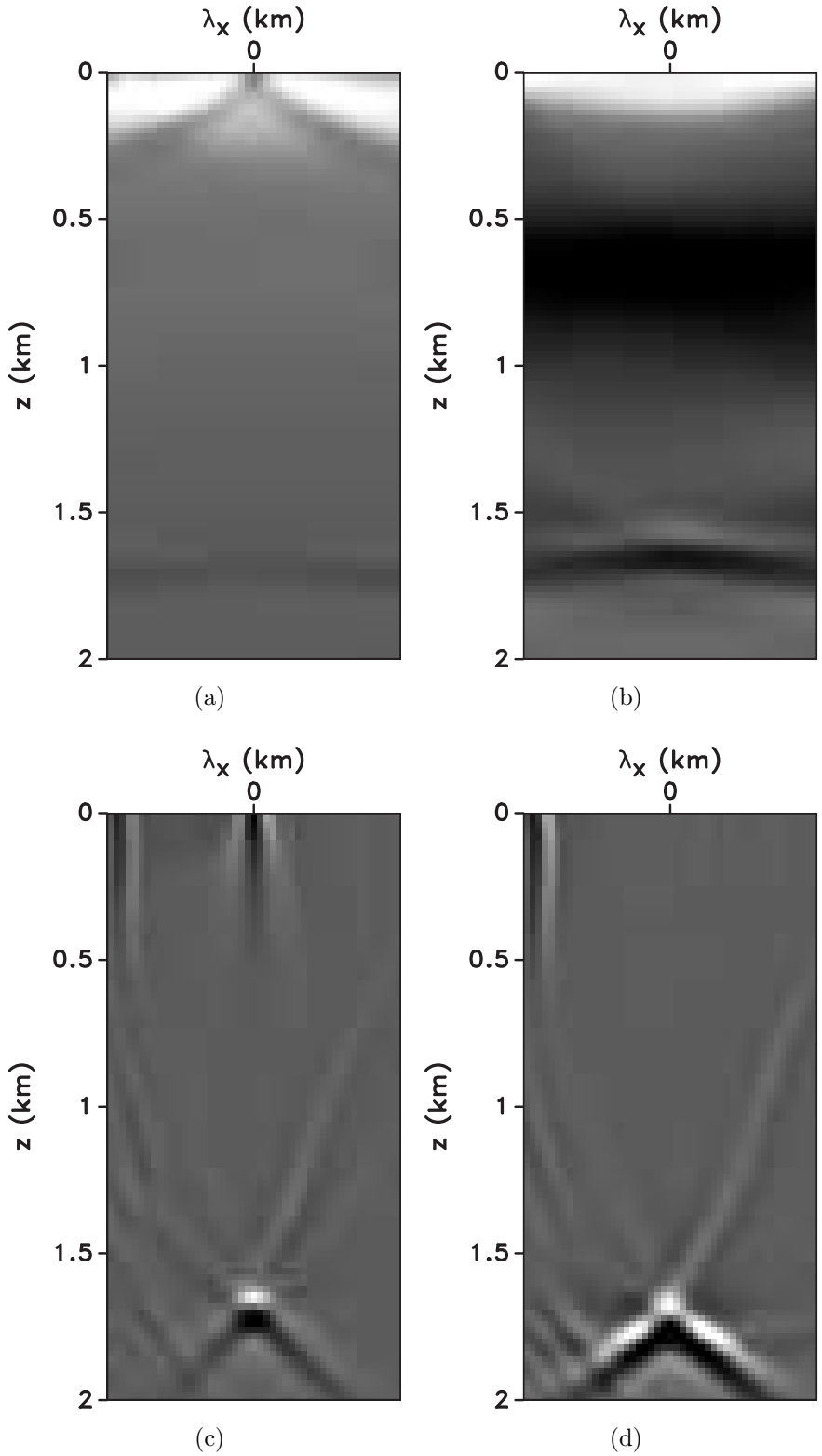


Figure 4.4: The space-lag CIGs constructed for the vertical reflector at x=1 km migrated with (a) the correct velocity, (b) the initial velocity, and CIGs at constructed for the horizontal reflector x=2.5 km migrated with (c) the correct velocity, (d) the initial velocity.

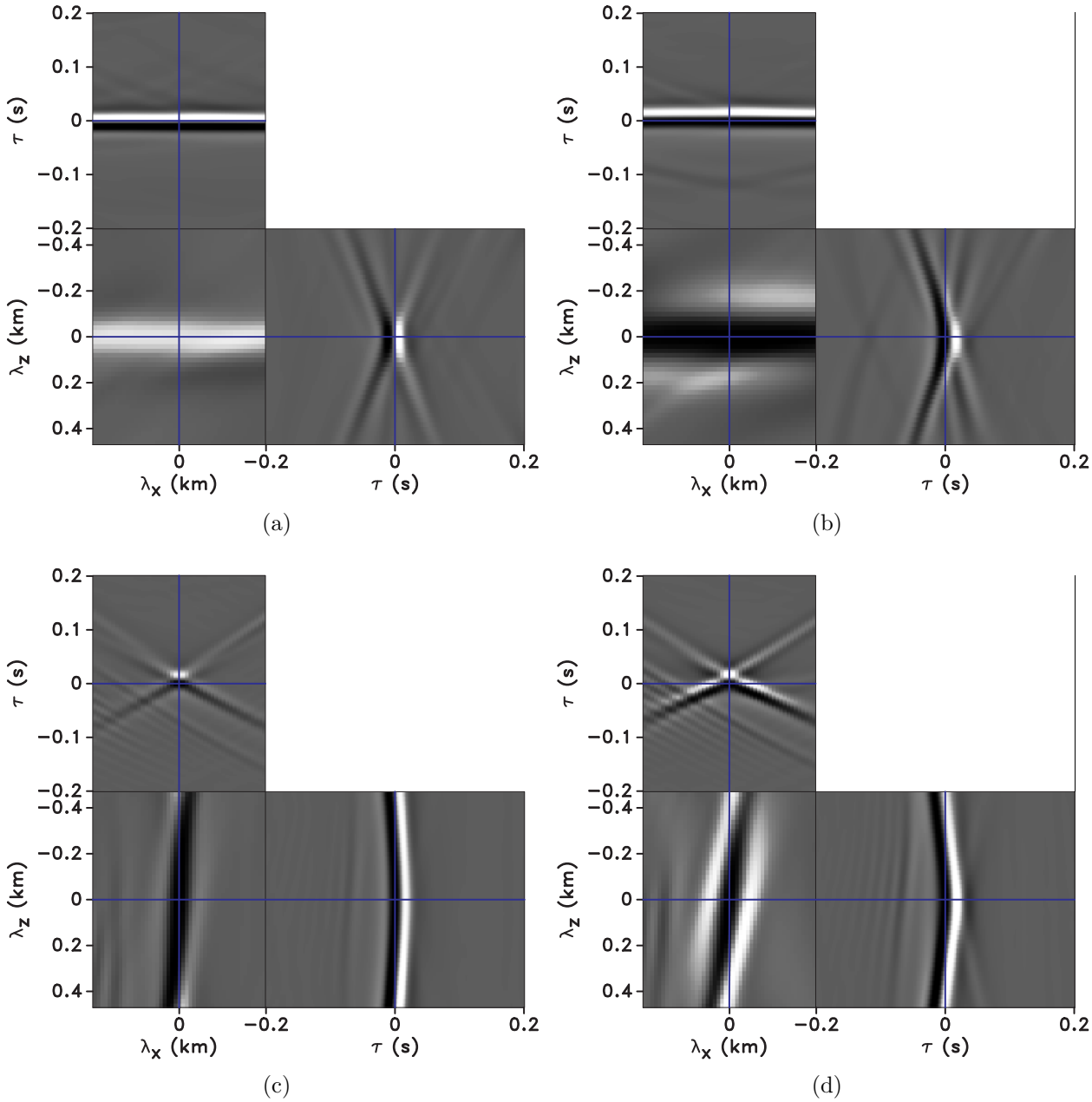


Figure 4.5: The CIPs at x=1 km, z=0.8 km migrated with (a) the correct velocity, (b) the initial velocity, compared with Figure 4.4(a) and Figure 4.4(b). CIPs at x=1.7 km, z=2.5 km migrated with (c) the correct velocity, (d) the initial velocity, compared with Figure 4.4(c) and Figure 4.4(d).

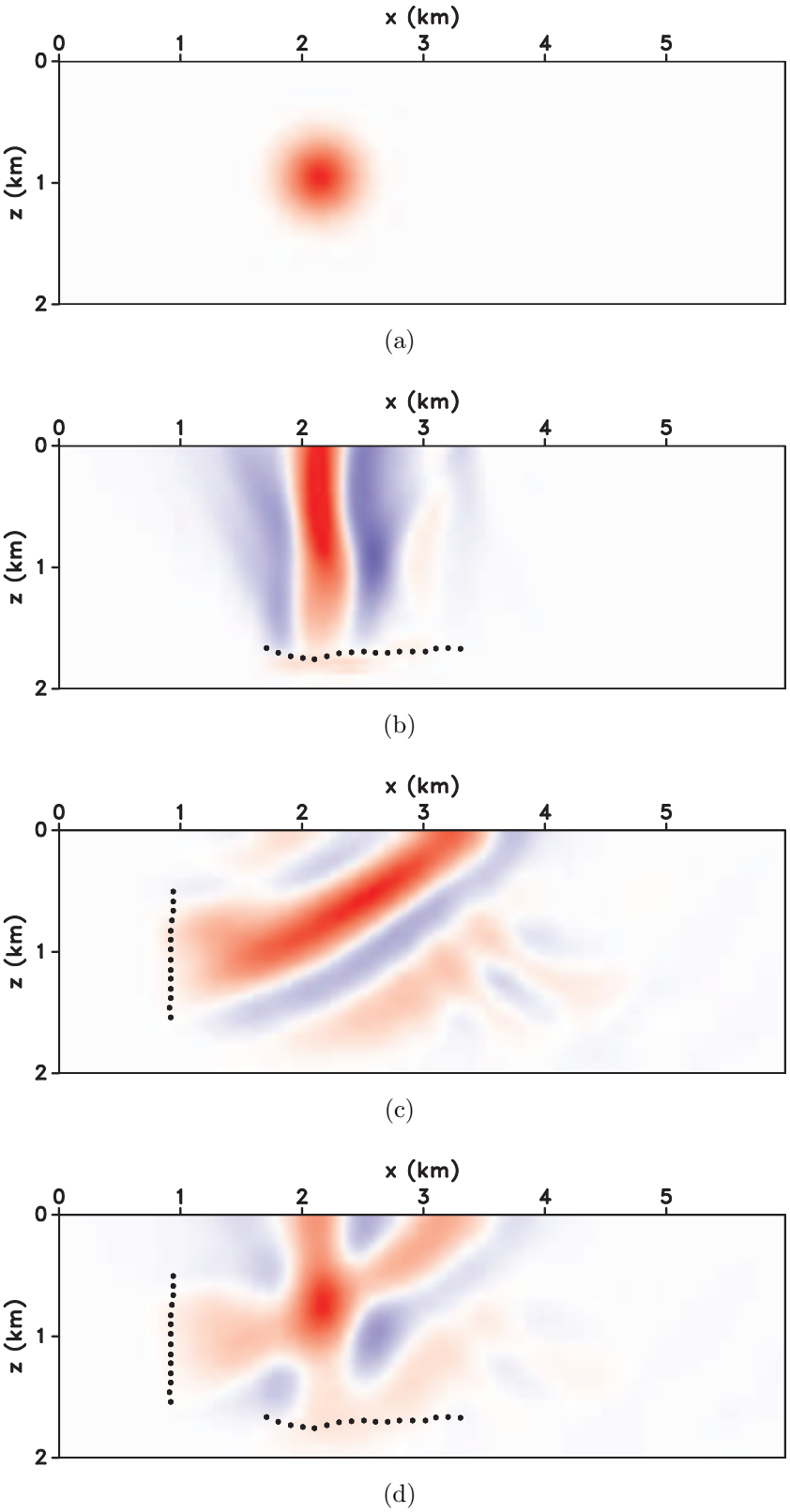


Figure 4.6: (a) The true velocity variation which is the target of inversion. The gradient constructed from (b) CIPs on the horizontal reflector only, (c) CIPs on the vertical reflector only, (d) CIPs on both the horizontal and vertical reflectors.

is used to construct CIGs. Therefore, CIGs are biased towards reflectors with small dips and fail to evaluate the velocity information available in steep reflectors. For CIPs, one can evaluate the model accuracy by analyzing focusing of vertical and horizontal reflectors in the $\lambda_z - \tau$ and $\lambda_x - \tau$ panels, respectively: the vector space-lags and time-lag of CIPs remove the directional bias toward horizontal reflectors, and CIPs are robust and able to analyze the velocity information from reflections regardless of the subsurface structure.

Next, we use the adjoint-state method as described in the previous section to calculate the gradient for three different scenarios: using CIPs on the horizontal reflector only, using CIPs on the vertical reflector only, and using CIPs on both reflectors. Figure 4.6(a) plots the difference between the correct and initial velocities. Figure 4.6(b)-Figure 4.6(d) show the gradient of the objective function computed using different groups of CIPs, indicated by the black dots. Observe that the gradients highlight the target in different ways. The gradient in Figure 4.6(b) constrains the model variation in the horizontal direction. In contrast, the gradient in Figure 4.6(c) constrains the model variation in the vertical direction. When the gradient is computed from CIPs picked on both vertical and horizontal reflectors, as shown in Figure 4.6(d), the variation is more effectively controlled in both the vertical and horizontal directions. Using the gradient computed from all CIPs, we reconstruct the velocity model shown in Figure 4.2(c). The image migrated with this updated model is shown in Figure 4.3(c). The coherency of both the vertical and horizontal reflectors is improved because of the more accurate gradient used in the inversion. This indicates that using CIPs, especially those sampled on the steeply dipping reflections, we can extract additional information from the migrated image and offer more constrains for the model building.

To show the performance of CIPs in wavefield tomography, we consider the synthetic Marmousi model. The correct model is shown in Figure 4.7(a). The source locations are evenly distributed on the surface from 1.0 km to 7.0 km at a spacing of 0.1 km. The receiver arrays are fixed for all the shots and span entirely the surface at a spacing of 0.01 km. The data are generated via finite-difference Born modeling, using a Ricker wavelet with peak

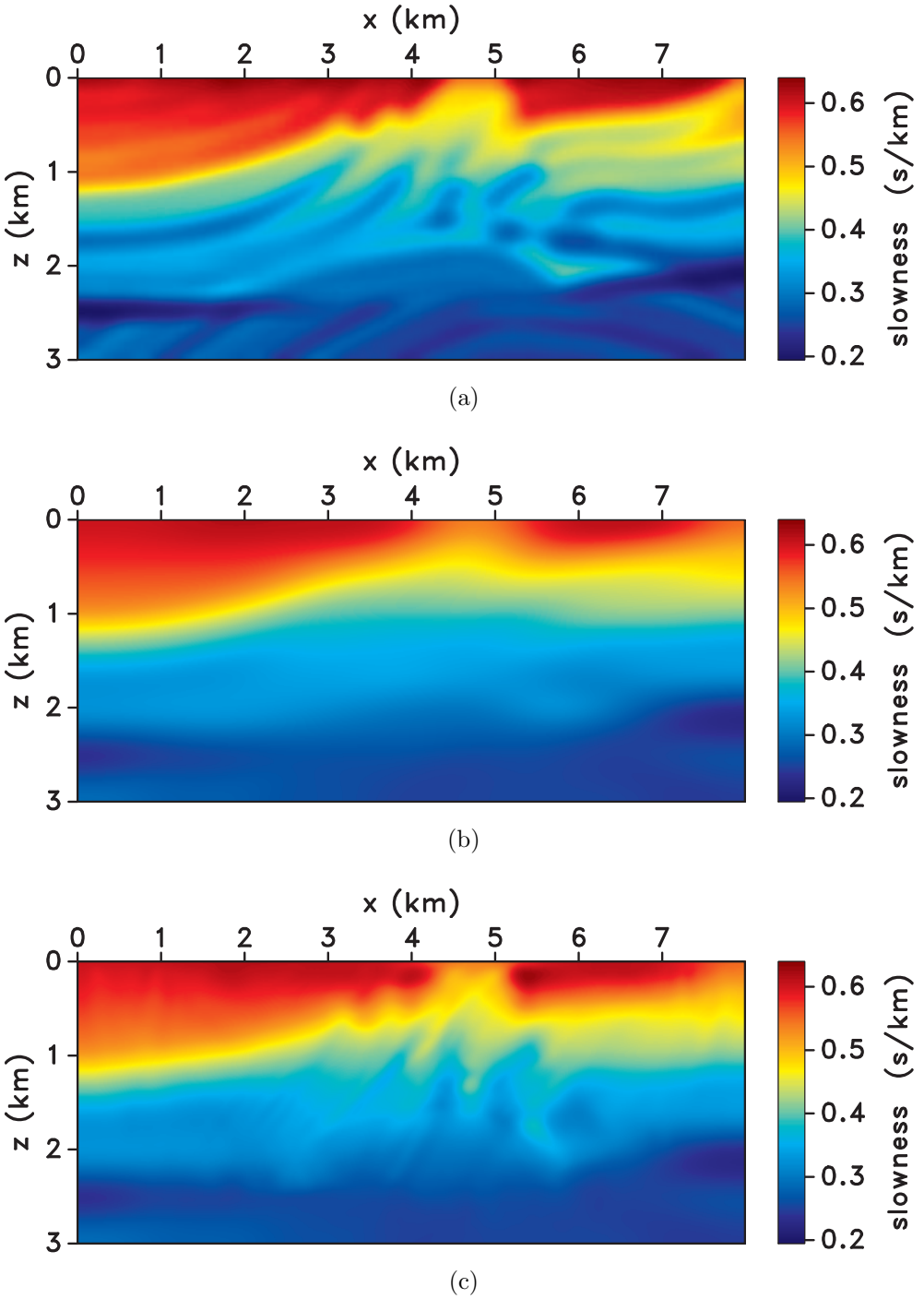
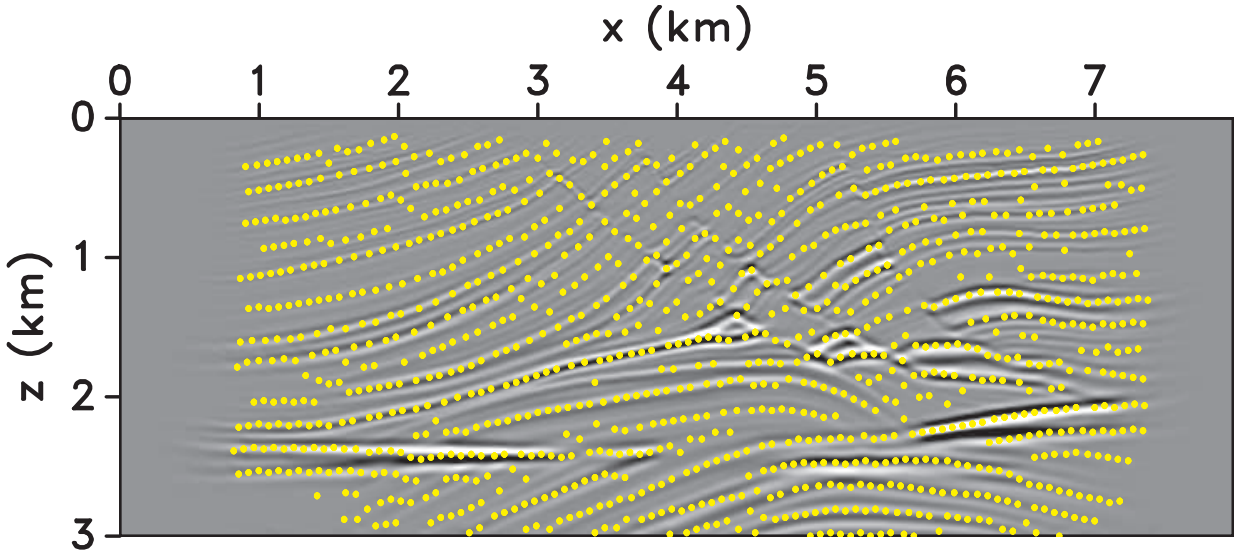
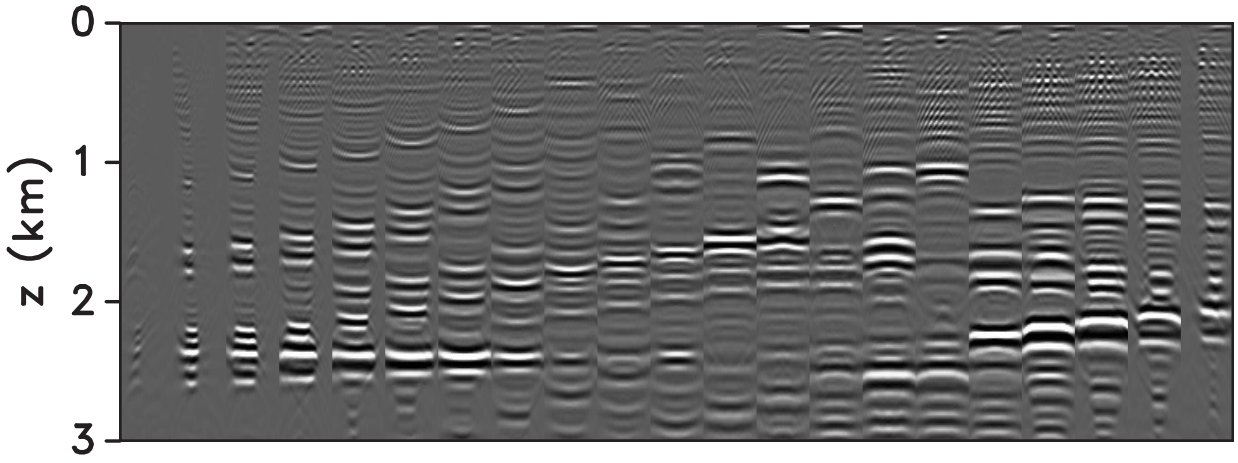


Figure 4.7: (a) The true model used to generate the data. (b) The initial model used in the velocity inversion. (c) The updated model after 20 iterations of inversion using CIPs.

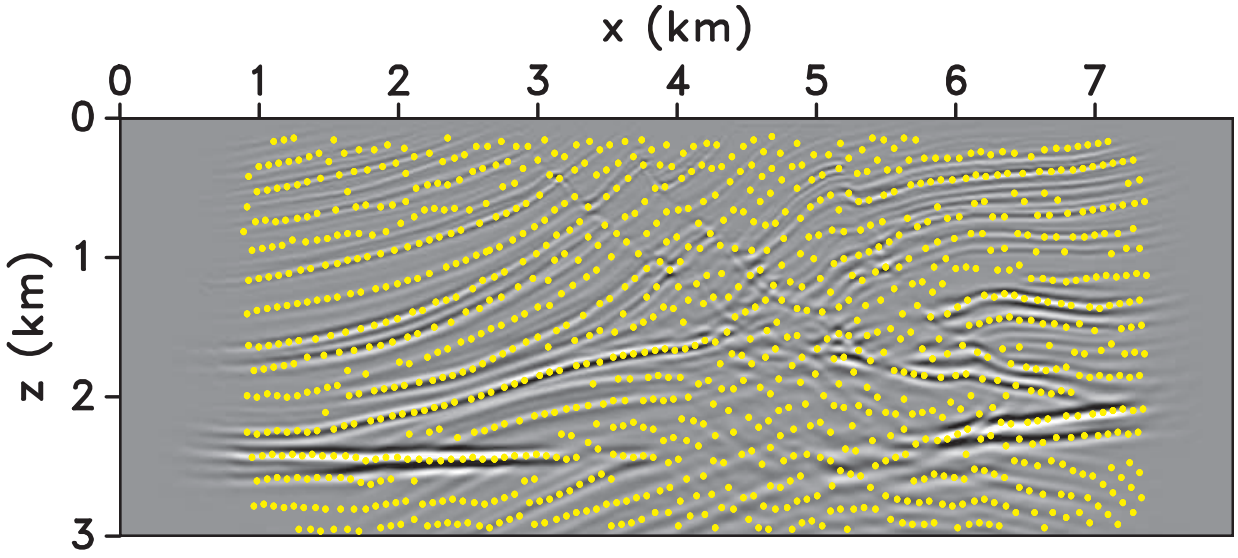


(a)

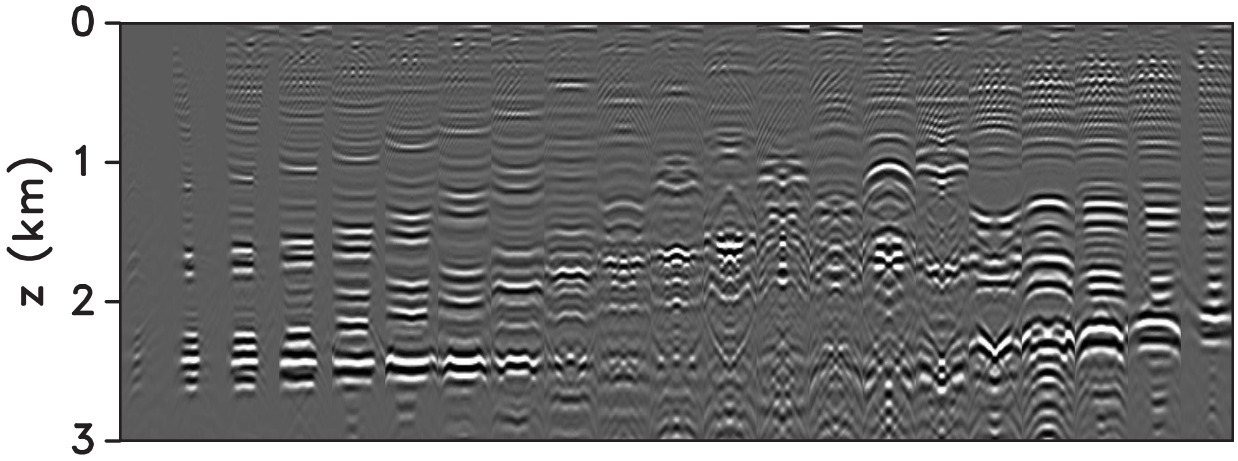


(b)

Figure 4.8: (a) The migrated image and (b) the angle-domain gathers obtained using the true model.



(a)



(b)

Figure 4.9: (a) The migrated image overlain with the CIPs location, and (b) the angle-domain gathers obtained using the initial model.

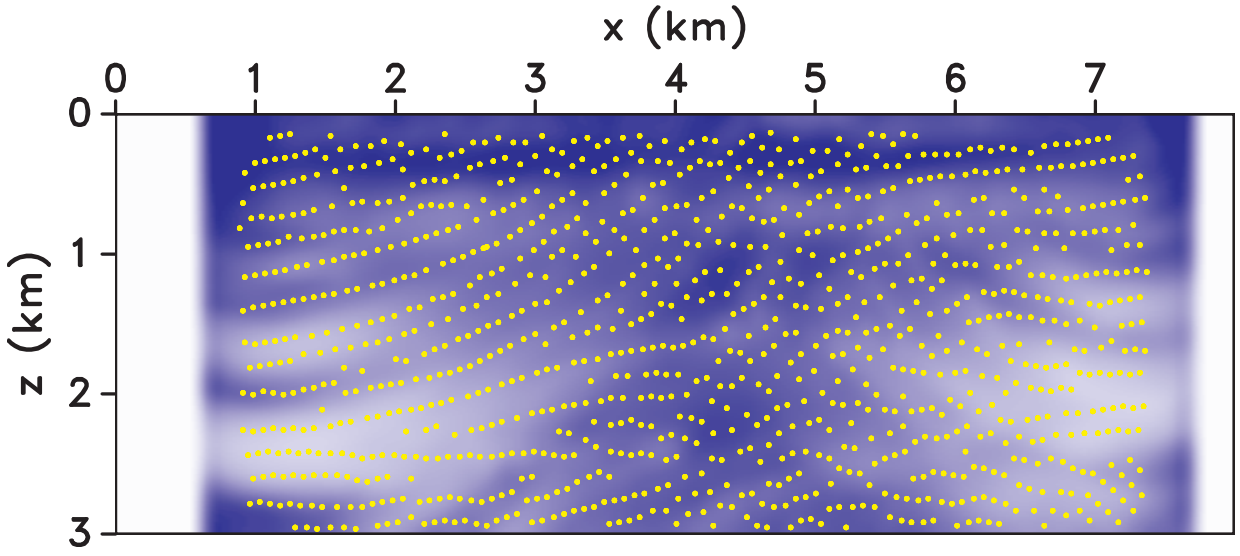
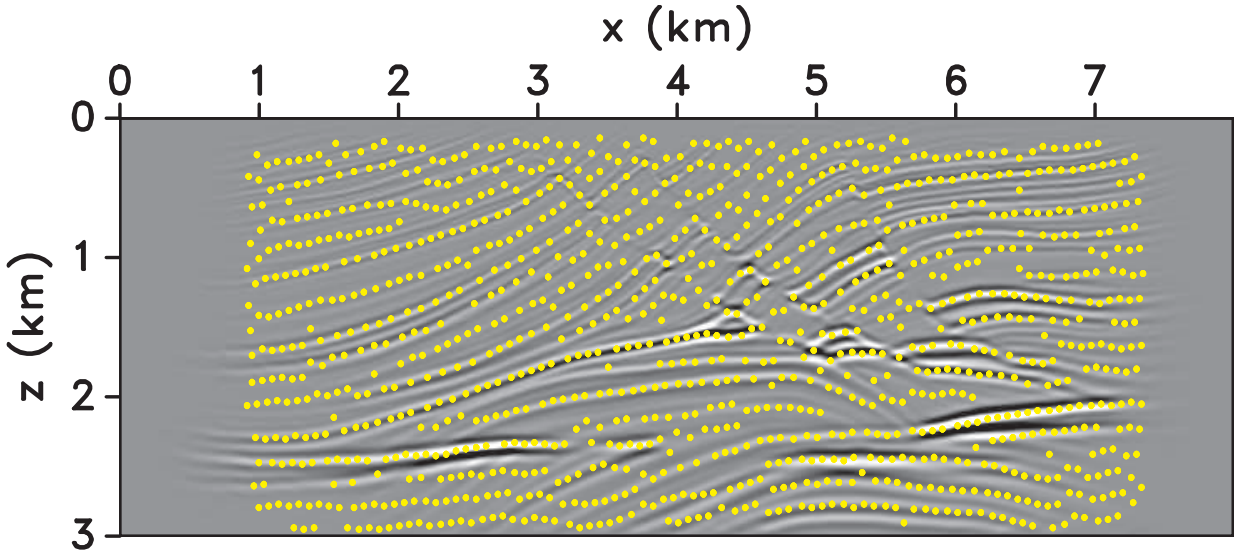
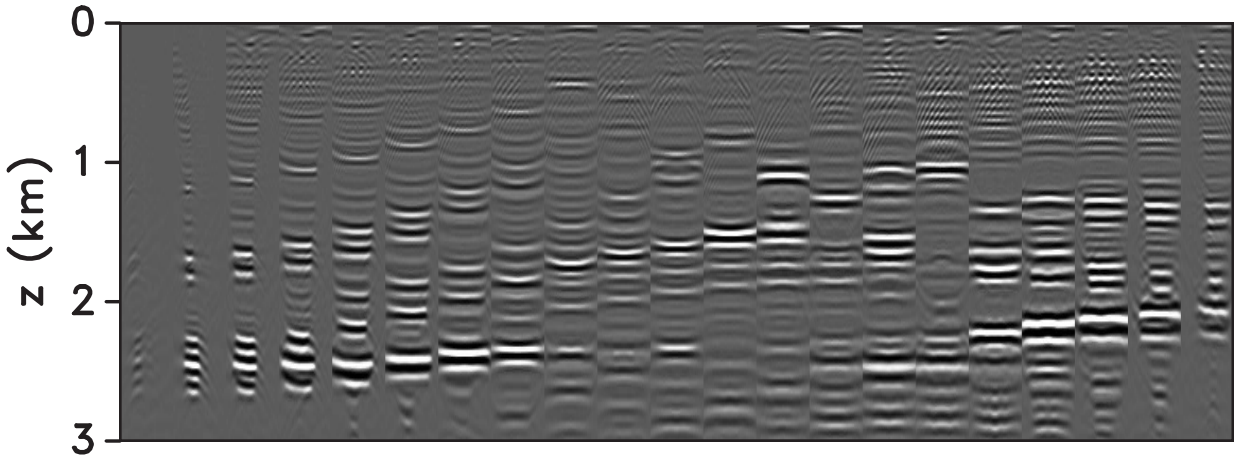


Figure 4.10: The weighting function based on the subsurface illumination.

frequency of 15 Hz. The data are then transformed into the frequency domain because both the migration an d wavefield tomography operators are based on the frequency-domain downward continuation method. In this way, we avoid using the same operator for both the modeling and inversion procedures. The image and angle gathers migrated with the true model are shown in Figure 4.8(a)-Figure 5.3(c). As one might expect, reflections events in the angle gathers are flat because the correct model is used for migration. The initial model used for the inversion, Figure 4.7(b), is a highly smoothed version of the true model . This model resembles the results one can obtain from conventional ray-based reflection tomography. Figure 4.9(a)-Figure 4.9(b) show the image and angle-domain CIGs migrated with the initial model. Since the initial model is highly smoothed, it lacks the necessary components required by the migration to produce an accurate result. Thus, the migrated im age exhibits severe distortions in the reservoir region around $x = 5$ km, $z = 2.5$ km. The reduced image quality can be further confirmed by the residual moveout in the angle gathers, as shown in Figure 4.9(b). In our example, the angle gathers are used only for quality control, rather than for model building.



(a)



(b)

Figure 4.11: (a) The migrated image overlain with the CIPs locations, and (b) the angle-domain gathers obtained using the updated model.

We initiate our velocity analysis process by selecting common-image-point gather locations at which we construct extended images necessary for velocity analysis. These locations are selected using the automatic picking algorithm developed by Cullison and Sava (2011). Figure 4.9(a) shows the picked locations overlain on the image. They follow the coherent structure of the image, and tend to be randomly positioned where the reflections are less coherent. Figure 4.10 shows the weighting function we apply to the input gathers in order to compensate for the uneven illumination in the subsurface. Light colors indicate low values of the weights applied in the poor illumination areas, and dark colors indicate high value of the weights applied in the good illumination areas. This weighting function is included in the objective function to speed up the convergence of the inversion. Figure 4.7(c) and Figure 4.11(a) show the inverted model after 20 nonlinear iterations and the corresponding migrated image. From the result, it is apparent that the updated model significantly improves the imaging quality as the reservoir area is better focused and more coherent in the migrated image. In addition, the reflections are flatter in angle gathers, as shown in Figure 4.11(b), as compared with those in Figure 4.9(b). These also indicate the improvement on the image due to the update.

4.5 Discussion

The synthetic examples demonstrate the successful velocity model updates produced by our approach using CIPs. In the first example, we show that CIPs do not bias their sensitivity toward any particular direction compared to the more conventional CIGs which sample image points more densely in the vertical direction than lateral direction. From the gradient computation, we notice that the CIPs located along nearly horizontal reflectors provide higher resolution laterally, whereas the CIPs located along nearly vertical reflectors provide higher resolution vertically.

In the second synthetic example, only the horizontal space lag and time lag are involved in CIPs computation. The vertical space lag is not required because there are no steeply dipping reflectors in the model. We thus significantly reduce the cost for computing and

storing the gathers for velocity analysis. After running the inversion, the main features of the model are resolved and they help improving the quality of the image. The improvements can be directly observed from the more coherent image, more focused reflections in space-lag gathers, and flatter events in angle gathers. The results demonstrate our image-domain wavefield tomography based on CIPs can achieve similar results to conventional methods but with reduced computational effort. This is especially crucial for velocity analysis in large-scale 3D applications.

4.6 Conclusions

We demonstrate a wavefield-based velocity model building method implemented in the image domain. The procedure optimizes the velocity model by minimizing the image incoherency caused by model errors. The objective function is particularly designed for common-image-point gathers constructed locally on the reflection event. The penalty operator used in the objective function is aimed at improving the focusing of the reflections in the gathers.

The two synthetic examples demonstrate the main advantages of using CIPs over conventional subsurface-offset common-image gathers in the wave-equation tomographic approach. First, the CIPs avoid the bias toward horizontal reflection events and thus are more robust in analyzing velocity information for steeply dipping structure in the complex geologic regions. Second, CIPs significantly reduce the cost for computing and storing the extended images compared with more conventional common-image gathers while producing reliable model updates. This is mainly attributed to the optimized sampling of CIPs in the subsurface as only the significant reflections are analyzed to provide information for velocity update.

CHAPTER 5

ILLUMINATION COMPENSATION FOR IMAGE-DOMAIN WAVEFIELD TOMOGRAPHY

A paper submitted to *Geophysics*

Tongning Yang [1,2], Paul Sava [1], and Jeffrey Shragge [3]

5.1 Summary

Image-domain wavefield tomography is a velocity model building technique using seismic images as the input and seismic wavefields as the information carrier. However, the method suffers from the uneven illumination problem when it applies a penalty operator to highlighting image inaccuracies due to the velocity model error. The uneven illumination caused by complex geology such as salt or by incomplete data creates defocusing in common-image gathers even when the migration velocity model is correct. This additional defocusing violates the wavefield tomography assumption stating that the migrated images are perfectly focused in the case of the correct model. Therefore, defocusing rising from illumination mixes with defocusing rising from the model errors and degrades the model reconstruction. We address this problem by incorporating the illumination effects into the penalty operator such that only the defocusing by model errors is used for model construction. This is done by first characterizing the illumination defocusing in gathers by illumination analysis. Then an illumination-based penalty is constructed which does not penalize the illumination defocusing. This method improves the robustness and effectiveness of image-domain wavefield tomography applied in areas characterized by poor illumination. Our synthetic examples demonstrate that velocity models are more accurately reconstructed by our method using

[1]Center for Wave Phenomena, Colorado School of Mines
[2]Corresponding author
[3]School of Earth and Environment, University of Western Australia

the illumination compensation, leading to more accurate model and better subsurface images than those in the conventional approach without illumination compensation.

5.2 Introduction

Building an accurate and reliable velocity model remains one of the biggest challenges in current seismic imaging practice. In regions characterized by complex subsurface structure, prestack wave-equation depth migration, (e.g., one-way wave-equation migration or reverse-time migration), is a powerful tool for accurately imaging the earth's interior (Gray et al., 2001; Etgen et al., 2009). The widespread use of these advanced imaging techniques drives the need for high-quality velocity models because these migration methods are very sensitive to model errors (Symes, 2008; Woodward et al., 2008; Virieux and Operto, 2009).

Wavefield tomography represents a family of techniques for velocity model building using seismic wavefields (Tarantola, 1984; Woodward, 1992; Pratt, 1999; Sirgue and Pratt, 2004; Plessix, 2006; Vigh and Starr, 2008a; Plessix, 2009; Symes, 2009). The core of wavefield tomography is using a wave equation (typically constant density acoustic) to simulate wavefields as the information carrier. Wavefield tomography is usually implemented in the data domain by adjusting the velocity model such that simulated and recorded data match (Tarantola, 1984; Pratt, 1999). This match is based on the strong assumption that the wave equation used for simulation is consistent with the physics of the earth. However, this is unlikely to be the case when the earth is characterized by strong (poro)elasticity. Significant effort is often directed toward removing the components of the recorded data that are inconsistent with the assumptions used.

Wavefield tomography can also be implemented in the image domain rather than in the data domain. Instead of minimizing the data misfit, the techniques in this category update the velocity model by optimizing the image quality, which is the cross-correlation of wavefields extrapolated from the source and receiver. Such techniques are also known as Wave-equation migration velocity analysis (Sava and Biondi, 2004a,b). For such methods, the image quality is optimized when the data are migrated with the correct velocity model,

as stated by the semblance principle (Al-Yahya, 1989). The common idea is to optimize the coherency of reflection events in common-image gathers (CIGs) via velocity model updating. Since images are obtained using full seismograms, and velocity estimation also employs seismic wavefields as the information carrier, these techniques can be regarded as a particular type of wavefield tomography, and we refer to them as image-domain wavefield tomography. The terminology simply to highlight the fact that the methods belong to the wavefield tomography family. Unlike traditional ray-based reflection tomography methods, image-domain wavefield tomography uses band-limited wavefields in the optimization procedure. Thus, this technique is capable of handling complicated wave propagation phenomena such as multi-pathing in the subsurface. In addition, the band-limited character of the wave-equation engine more accurately approximates wave propagation in the subsurface and produces more reliable velocity updates.

Differential semblance optimization (DSO) is one implementation of image-domain wavefield tomography. The essence of the method is to minimize the difference of the same reflection between neighboring offsets or angles. Symes and Carazzone (1991) propose a criterion for measuring coherency from offset gathers and establish the theoretic foundation for DSO. The concept is then generalized to space-lag (subsurface-offset) and angle-domain gathers (Shen and Calandra, 2005; Shen and Symes, 2008). Space-lag gathers (Rickett and Sava, 2002; Shen and Calandra, 2005) and angle-domain gathers (Sava and Fomel, 2003; Biondi and Symes, 2004) are two popular choices among various types of gathers used for velocity analysis. These gathers are obtained by wave-equation migration and are free of artifacts usually found in conventional offset gathers obtained by Kirchhoff migration, and thus they are suitable for applications in complex earth models (Stolk and Symes, 2004).

DSO implemented using horizontal space-lag gathers constructs a penalty operator which annihilates the energy at zero lag and enhances the energy at nonzero lags (Shen et al., 2003). This construction assumes that migrated images are perfectly focused at zero lag when the model is correct. If the model is incorrect, reflections in the gathers are defocused and the

reflection energy spreads to nonzero lags. As a result, any energy left after applying the penalty is attributed to the result of model errors. However, this assumption is violated in practice when the subsurface illumination is uneven. Uneven illumination introduces additional defocusing such that images are not perfectly focused even if the velocity is correct, and it usually results from incomplete surface recorded data or from complex subsurface structure. Incomplete data cause loss of signal at some reflection angles and thus degrade the image. Nemeth et al. (1999) show that least-squares migration method can compensate the poor image quality due to the data deficiency. This method, however, is costly because of it requires many iterations to converge (Shen et al., 2011). In complex subsurface regions, such as sub-salt, uneven illumination is a general problem and it deteriorates the quality of imaging and velocity model building (Leveille et al., 2011). Gherasim et al. (2010) and Shen et al. (2011) show that the quality of migrated images can be optimized by illumination-based weighting generated from a demigration/remigration procedure. Tang and Biondi (2011) compute the diagonal of the Hessian matrix for the migration operator and use it for illumination compensation of the image before velocity analysis. These approaches effectively improve the quality of subsurface images, especially the balance of the amplitude. Nonetheless, they do not investigate the negative impact of illumination on the velocity model building. Furthermore, the misleading velocity updates due to uneven illumination remain an unsolved problem.

In this article we address the problem of uneven illumination associated with image-domain wavefield tomography. We analyze the illumination problem using the analytical formula of extended images, and find that uneven illumination causes imperfect interference in image stacking and result in defocusing in the gathers. We solve the problem by excluding such defocusing from tomography using an illumination-based penalty operator obtained from illumination analysis. In the following sections, we first review the theory for wavefield tomography in the image-domain including the formulation of the objective function and the gradient calculation. Next we explain how the uneven illumination affects the focusing

of space-lag gathers and breaks down the assumption for DSO. We then propose a solution to this problem by using the illumination information in the construction of the penalty operator which is an integral part of the objective function. The construction of the penalty operator is also explained in details. We illustrate our method with two synthetic examples representing two different types of illumination problems. The success of the approach is confirmed by the improvements of the results obtained with our method compared to that obtained with the conventional method.

5.3 Theory

For clarity, we organize the theory section into three subsections. In the first part, we explain how to compute the gradient for conventional DSO using the adjoint-state method. Readers who are familiar with the computation can safely skip it. In the second part, we analyze how the illumination affects gathers focusing by examining the formula for stacking the gathers. We then derive our formulation for the new penalty operator which compensates the illumination effects. In the last part, we illustrate the gradient computation given the new penalty operator.

5.3.1 Gradient computation for DSO

In image-domain wavefield tomography using horizontal space-lag extended images (subsurface-offset CIGs), the objective function is formulated by applying the idea of DSO and the gradient is computed using the adjoint-state method (Plessix, 2006). More details and advantages of using adjoint-state method for gradient computation can be also found in the paper by Plessix (2006). For simplicity, we show the computation in the frequency domain rather than in the time domain. The first step of the adjoint-state method is defining the state variables, through which the objective function is related to the model parameter. The state variables for our problem are the source and receiver wavefields u_s and u_r obtained by solving the following acoustic wave equation:

$$\begin{bmatrix} \mathcal{L}(\mathbf{x},\omega,m) & 0 \\ 0 & \mathcal{L}^*(\mathbf{x},\omega,m) \end{bmatrix} \begin{bmatrix} u_s(j,\mathbf{x},\omega) \\ u_r(j,\mathbf{x},\omega) \end{bmatrix} = \begin{bmatrix} f_s(j,\mathbf{x},\omega) \\ f_r(j,\mathbf{x},\omega) \end{bmatrix} , \tag{5.1}$$

where f_s is a point or plane source, f_r are the record data, $j = 1, 2, ..., N_s$ where N_s is the number of shots, ω is the angular frequency, and $\mathbf{x}$ are the space coordinates $\{x, y, z\}$. The wave operator $\mathcal{L}$ and its adjoint $\mathcal{L}^*$ propagate the wavefields forward and backward in time respectively using a two-way wave equation. Thus, $\mathcal{L}$ is formulated as

$$\mathcal{L} = -\omega^2 m - \Delta , \tag{5.2}$$

where Δ is the Laplace operator, and m represents the model (slowness squared). Such a formulation treats the wavefields as unknown vectors in the linear system of 6.3 and we can obtain the solution by solving the system of linear equations. Similar representation can also be found in Pratt (1999).

In the second step of the adjoint-state method, the objective function is first formulated. Then, the adjoint sources are derived from the objective function. The adjoint sources are used to compute the adjoint-state variables required by the gradient computation. The objective function for image-domain wavefield tomography measures the image incoherency caused by the model errors. Therefore, the inversion simultaneously reconstructs the model and improves the image quality by minimizing the objective function.

The DSO objective function based on space-lag CIGs (Symes, 2009) is

$$\mathcal{H}_{\boldsymbol{\lambda}} = \frac{1}{2} \| P(\boldsymbol{\lambda})\, r(\mathbf{x},\boldsymbol{\lambda}) \|^2_{\mathbf{x},\boldsymbol{\lambda}} , \tag{5.3}$$

where r is the extended images defined as

$$\begin{aligned} r(\mathbf{x},\boldsymbol{\lambda}) &= \sum_j \sum_\omega \overline{u_s(j,\mathbf{x}-\boldsymbol{\lambda},\omega)} u_r(j,\mathbf{x}+\boldsymbol{\lambda},\omega) \\ &= \sum_j \sum_\omega T(-\boldsymbol{\lambda})\, \overline{u_s(j,\mathbf{x},\omega)} T(\boldsymbol{\lambda})\, u_r(j,\mathbf{x},\omega) \ . \end{aligned} \tag{5.4}$$

The overline represents complex conjugate. In this article, we consider the space lags in the horizontal directions only, i.e. $\boldsymbol{\lambda} = \{\lambda_x, \lambda_y, 0\}$.

The operator T represents the space shift applied to the wavefields and is defined by

$$T(\boldsymbol{\lambda})\, u(j, \mathbf{x}, \omega) = u(j, \mathbf{x} + \boldsymbol{\lambda}, \omega) \ , \tag{5.5}$$

The penalty operator $P(\boldsymbol{\lambda})$ annihilates the focused energy at zero lag and highlights the energy of residual moveout at nonzero lag (Shen and Symes, 2008):

$$P(\boldsymbol{\lambda}) = |\boldsymbol{\lambda}| \ . \tag{5.6}$$

Our contribution consists of replacing this operator with a new illumination-based penalty operator, as it will be explained in the following subsection. The objective function $\mathcal{H}_{\boldsymbol{\lambda}}$ is minimized when the reflections focus at zero lag, which is an indication of the correct velocity model.

The adjoint sources g_s and g_r are computed as the derivatives of the objective function $\mathcal{H}_{\boldsymbol{\lambda}}$ shown in 5.3 with respect to the state variables u_s and u_r:

$$\begin{bmatrix} g_s(j, \mathbf{x}, \omega) \\ g_r(j, \mathbf{x}, \omega) \end{bmatrix} = \begin{bmatrix} \frac{\partial \mathcal{H}_{\boldsymbol{\lambda}}}{\partial u_s} \\ \frac{\partial \mathcal{H}_{\boldsymbol{\lambda}}}{\partial u_r} \end{bmatrix} \\ \begin{bmatrix} \sum\limits_{\boldsymbol{\lambda}} T(\boldsymbol{\lambda})\, P(\boldsymbol{\lambda}) & \overline{P(\boldsymbol{\lambda}) r(\mathbf{x}, \boldsymbol{\lambda})} T(\boldsymbol{\lambda})\, u_r(j, \mathbf{x}, \omega) \\ \sum\limits_{\boldsymbol{\lambda}} T(-\boldsymbol{\lambda})\, P(\boldsymbol{\lambda}) & \overline{P(\boldsymbol{\lambda})} r(\mathbf{x}, \boldsymbol{\lambda})\, T(-\boldsymbol{\lambda})\, u_s(j, \mathbf{x}, \omega) \end{bmatrix} \ . \tag{5.7}$$

The adjoint state variables a_s and a_r are the wavefields obtained by backward and forward modeling, respectively, using the corresponding adjoint sources defined in equation 5.7:

$$\begin{bmatrix} \mathcal{L}^*(\mathbf{x}, \omega, m) & 0 \\ 0 & \mathcal{L}(\mathbf{x}, \omega, m) \end{bmatrix} \begin{bmatrix} a_s(j, \mathbf{x}, \omega) \\ a_r(j, \mathbf{x}, \omega) \end{bmatrix} = \begin{bmatrix} g_s(j, \mathbf{x}, \omega) \\ g_r(j, \mathbf{x}, \omega) \end{bmatrix} \ , \tag{5.8}$$

where $\mathcal{L}$ and $\mathcal{L}^*$ are the same wave propagation operators used in equation 6.3.

The last step of the gradient computation is simply the correlation between state variables and adjoint state variables:

$$\frac{\partial \mathcal{H}_{\boldsymbol{\lambda}}}{\partial m} = \sum_j \sum_{\omega} \frac{\partial \mathcal{L}}{\partial m} \left(u_s(j, \mathbf{x}, \omega)\, \overline{a_s(j, \mathbf{x}, \omega)} + u_r(j, \mathbf{x}, \omega)\, \overline{a_r(j, \mathbf{x}, \omega)} \right) \ , \tag{5.9}$$

where $\frac{\partial \mathcal{L}}{\partial m}$ is the partial derivative of the wave propagation operator with respect to the model parameter. Using the definition of $\mathcal{L}$ in 5.2, it is apparent that $\frac{\partial \mathcal{L}}{\partial m} = -\omega^2$. From equation

5.9 one may notice that the gradient for image-domain wavefield tomography consists of two correlations because both the source and receiver wavefields are defined as the state variables.

The derivation above shows the construction of the image-domain wavefield tomography objective function and its gradient. Given these two components, the solution to the inverse problem is found by minimizing the objective function using non-linear gradient-based iterative methods (Knyazev and Lashuk, 2007). In each iteration, the gradient is computed and the model update is calculated by a line search in the steepest descent or conjugate gradient directions.

5.3.2 Construction of illumination-based penalty

To analyze the illumination effects on focusing and construct the illumination-based penalty, we first illustrate the focusing mechanism for reflections in space-lag gathers. Yang and Sava (2010) derive the analytic formula for the reflection moveout in the extended images. Assuming constant local velocity, a reflection in space-lag gathers obtained by migrating one shot experiment is a straight line in 2D and a plane in 3D:

$$z\left(\boldsymbol{\lambda}\right) = d_0 - \frac{\tan\theta\left(\mathbf{q}\cdot\boldsymbol{\lambda}\right)}{n_z}\ . \tag{5.10}$$

Here d_0 represents the depth of the reflection corresponding to the chosen CIGs location, $\boldsymbol{\lambda}$ represents the horizontal space lag $\boldsymbol{\lambda} = \{\lambda_x, \lambda_y, 0\}$, n_z is the vertical component of the unit vector normal to the reflection plane, $\mathbf{q}$ is the unit vector parallel to the reflection plane, and θ is the reflection angle. When we stack the gathers obtained with a correct model from all available shots, the straight lines or planes corresponding to reflections from different shots are superimposed and interfere to form a focused point at zero lag (Yang and Sava, 2010). Good interference of such events, however, occurs only if the reflector point is well illuminated by the experiments. In other words, the surface shot coverage must be large enough and regularly distributed. Also, the subsurface illumination must be even so that the reflector is illuminated on a sufficient range of reflection angles from the surface. If either

of these conditions is not satisfied, the reflection energy does not interfere perfectly and the gathers defocus, even if the correct model is used for the imaging.

We conclude that the defocusing of reflections in the space-lag gathers may result from velocity errors, as well as from the imperfect stacking due to uneven illumination. In general, these two different kinds of defocusing are indistinguishable to the velocity analysis procedure. The penalty operator in 5.6 emphasizes all energy away from zero lag and includes both the defocusing caused by the velocity error and by the uneven illumination. Thus, the penalty operator leads to a residual that is much larger than what would be expected for a given error in the model. Penalizing the defocusing due to the illumination misleads the inversion and results in overcorrection and artificial updates.

To alleviate the negative influence of uneven illumination, we need to include the illumination information in the tomographic procedure. One approach uses the illumination information as a weighting function to preconditioning the gathers. The gathers in poor illumination areas are down-weighted as the defocusing information is less reliable than the gathers in good illumination areas. This approach stabilizes the inversion but decreases the accuracy of the results as the useful velocity information in poor illumination areas is ignored. The poor illumination area, however, is exactly the place where we want to make use of all available information for the model building. To overcome the illumination problem and preserve the useful information in the tomography, we introduce a new illumination-based penalty operator to replace the conventional DSO penalty operator. The new operator is constructed such that it only emphasizes the defocusing caused by the velocity error and ignores the defocusing caused by uneven illumination. To achieve this goal, we analyze the image defocusing due to uneven illumination by applying illumination analysis.

Illumination analysis in the framework of wave-equation migration is formulated using the solution to migration deconvolution problems (Berkhout, 1982a; Yu and Schuster, 2003). Migration deconvolution first establishes a linear relationship between a reflectivity distribution $\tilde{r}$ and seismic data d:

$$\mathcal{M}\tilde{r}\left(\mathbf{x}\right) = d \ , \tag{5.11}$$

where $\mathcal{M}$ represents a forward Born modeling operator which is linear with respect to the reflectivity. A migrated image is obtained by applying the adjoint of the modeling operator $\mathcal{M}^*$ to the data,

$$\mathcal{M}^* d = \mathcal{M}^*\mathcal{M}\tilde{r}\left(\mathbf{x}\right) = r\left(\mathbf{x}\right) \ , \tag{5.12}$$

where r is a migrated image. Here, no extended images are involved yet. Note that the migrated image is the result of blurring the reflectivity $\tilde{r}$ by $(\mathcal{M}^*\mathcal{M})$, which is the Hessian (second-order derivative of the operator with respect to the model) for the operator $\mathcal{M}$. Thus, the reflectivity can be computed from the migrated image by

$$\tilde{r}\left(\mathbf{x}\right) = \left(\mathcal{M}^*\mathcal{M}\right)^{-1} r\left(\mathbf{x}\right) \ , \tag{5.13}$$

where $\left(\mathcal{M}^*\mathcal{M}\right)^{-1}$ includes the subsurface illumination information associated with the velocity structure and acquisition geometry. In practice, the full $\left(\mathcal{M}^*\mathcal{M}\right)^{-1}$ matrix is too costly to construct, but we can evaluate its impact by applying a cascade of demigration and migration $(\mathcal{M}^*\mathcal{M})$ to an image:

$$r_e\left(\mathbf{x}\right) = \mathcal{M}^*\mathcal{M}r\left(\mathbf{x}\right) \ . \tag{5.14}$$

The resulting image r_e approximates the diagonal elements of the Hessian and characterizes the illumination effects. One application of such analysis is to construct weights for illumination compensation of migrated image (Guitton, 2004; Gherasim et al., 2010; Tang and Biondi, 2011). 5.14 only computes the illumination effects distributed at image points. In our problem, we are concerned with the defocusing caused by the illumination in the space-lag gathers, and need to evaluate the illumination effects at image points and along their space-lag extension. To achieve this, we can generalize equation 12 to the extended image space $\mathbf{x} - \boldsymbol{\lambda}$:

$$r_e\left(\mathbf{x}, \boldsymbol{\lambda}\right) = \mathcal{M}^*\mathcal{M}r'\left(\mathbf{x}\right) \ , \tag{5.15}$$

where $r'(\mathbf{x})$ is the reference image, and $r_e(\mathbf{x}, \boldsymbol{\lambda})$ are the output illumination gathers containing defocusing associated with illumination effects. Such defocusing is the consequence of uneven illumination and should not be penalized by the penalty operator in the velocity updating process. However, the implementation of the equation consists of several steps. First, we need to construct an image using the current velocity model. Although the image is not perfect because the model is not the true model, we only extract the information about the reflection locations. Second, we put point scatters on all reflections in the image and construct the reference image $r'(\mathbf{x})$. Note that $r'(\mathbf{x})$ is not the same image $r(\mathbf{x})$ as constructed before using the current model. $r'(\mathbf{x})$ contains point scatters on every image point of the reflections in the original image. We take this reference image as the reflectivity, and use the current velocity model to run Born modeling operator $\mathcal{M}$. After we generate the data, we migrate the data using the adjoint of the modeling operator $\mathcal{M}^*$ and apply the extended imaging condition to obtain illumination gathers $r_e(\mathbf{x}, \boldsymbol{\lambda})$. During the process, we use the same velocity model for both the modeling and migration. This is equivalent to migrating the data using the true model. The resulting gathers should be perfectly focused. If not, the defocusing can only be attributed to acquisition or illumination. Therefore, Applying 5.15 characterizes the defocusing due to illumination effects in space-lag gathers given the current acquisition and estimated model. In other words, reference image $r'(\mathbf{x})$ acts like an impulse, and illumination gathers $r_e(\mathbf{x}, \boldsymbol{\lambda})$ contain the impulse response for the acquisition system and subsurface structure. Given the illumination gathers, we are able to isolate the defocusing due to illumination using a new penalty in the inversion. Thus, we can construct the illumination-based penalty operator as

$$P_e(\mathbf{x}, \boldsymbol{\lambda}) = \frac{1}{r_e(\mathbf{x}, \boldsymbol{\lambda}) + \epsilon}\ , \tag{5.16}$$

where ϵ is a damping factor used to stabilize the division. By definition, this penalty operator has low values in the area of defocusing due to uneven illumination and high values in the rest. Thus, this operator is consistent with our idea of avoiding penalty to reflection energy irrelevant to velocity errors, e.g., the artifacts caused by illumination. Replacing the

conventional penalty in 5.6 with the one in 5.16 is the basis for our illumination compensated image-domain wavefield tomography. Note that the DSO penalty operator is a special case of our new penalty operator and corresponds to the case of perfect subsurface illumination and wide-band data.

5.3.3 Gradient computation with illumination-based penalty

Using the new penalty operator $P_e(\mathbf{x},\boldsymbol{\lambda})$ defined in 5.16, we can formulate the objective function for illumination-compensated wavefield tomography as

$$\mathcal{H}'_{\boldsymbol{\lambda}} = \frac{1}{2}\| P_e(\mathbf{x},\boldsymbol{\lambda})\, r(\mathbf{x},\boldsymbol{\lambda}) \|^2_{\mathbf{x},\boldsymbol{\lambda}} . \tag{5.17}$$

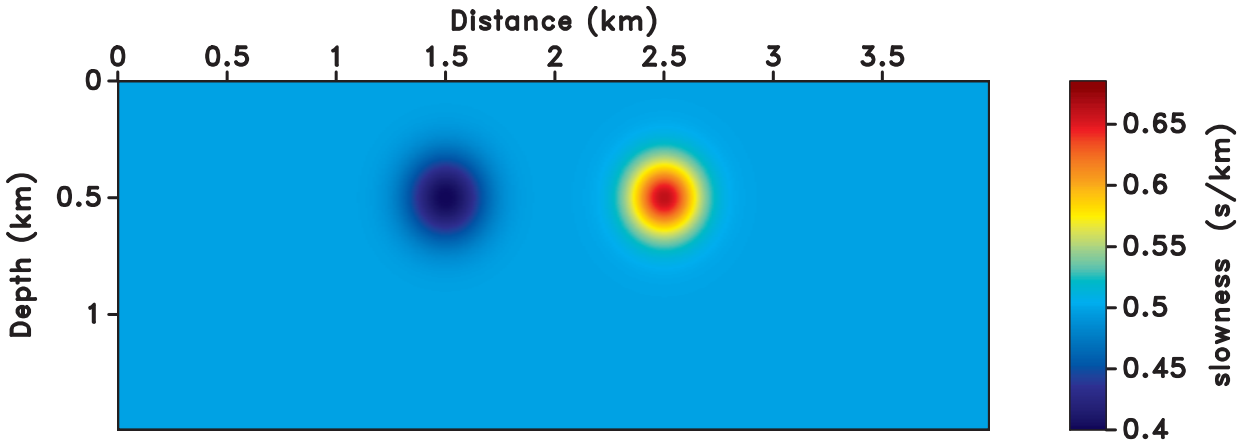
The gradient computation for the new objective function can also be done using the adjoint-state method. One difference, however, is that the penalty operator P_e is model-dependent in the new formulation. Thus, we need to take this into account when we compute the adjoint sources, which can be computed as

$$\begin{aligned}
&\begin{bmatrix} g_s(j,\mathbf{x},\omega) \\ g_r(j,\mathbf{x},\omega) \end{bmatrix} = \begin{bmatrix} \frac{\partial \mathcal{H}'_{hh}}{\partial u_s} \\ \frac{\partial \mathcal{H}'_{\boldsymbol{\lambda}'}}{\partial u_r} \end{bmatrix} = \\
&\begin{bmatrix} P_e(\mathbf{x},\boldsymbol{\lambda})\, r(\mathbf{x},\boldsymbol{\lambda})\, \frac{\partial (P_e(\mathbf{x},\boldsymbol{\lambda}) r(\mathbf{x},\boldsymbol{\lambda}))}{\partial u_s} \\ P_e(\mathbf{x},\boldsymbol{\lambda})\, r(\mathbf{x},\boldsymbol{\lambda})\, \frac{\partial (P_e(\mathbf{x},\boldsymbol{\lambda}) r(\mathbf{x},\boldsymbol{\lambda}))}{\partial u_r} \end{bmatrix} = \\
&\begin{bmatrix} P_e(\mathbf{x},\boldsymbol{\lambda})\, r(\mathbf{x},\boldsymbol{\lambda}) \left(P_e(\mathbf{x},\boldsymbol{\lambda})\, \frac{\partial r(\mathbf{x},\boldsymbol{\lambda})}{\partial u_s} + r(\mathbf{x},\boldsymbol{\lambda})\, \frac{\partial P_e(\mathbf{x},\boldsymbol{\lambda})}{\partial u_s} \right) \\ P_e(\mathbf{x},\boldsymbol{\lambda})\, r(\mathbf{x},\boldsymbol{\lambda}) \left(P_e(\mathbf{x},\boldsymbol{\lambda})\, \frac{\partial r(\mathbf{x},\boldsymbol{\lambda})}{\partial u_r} + r(\mathbf{x},\boldsymbol{\lambda})\, \frac{\partial P_e(\mathbf{x},\boldsymbol{\lambda})}{\partial u_r} \right) \end{bmatrix} = \\
&\begin{bmatrix} \sum\limits_{\boldsymbol{\lambda}} T(\boldsymbol{\lambda}) \left(P_e \overline{r} T(\boldsymbol{\lambda})\, u_r(j,\mathbf{x},\omega) - \overline{P_e}\overline{r} \mathcal{M}^* \mathcal{M} T(\boldsymbol{\lambda})\, u_r(j,\mathbf{x},\omega)\, r(\mathbf{x},\boldsymbol{\lambda}) \right) \\ \sum\limits_{\boldsymbol{\lambda}} T(-\boldsymbol{\lambda}) \left(P_e r T(-\boldsymbol{\lambda})\, u_s(j,\mathbf{x},\omega) - \overline{P_e} r \mathcal{M}^* \mathcal{M} T(-\boldsymbol{\lambda})\, u_s(j,\mathbf{x},\omega)\, r(\mathbf{x},\boldsymbol{\lambda}) \right) \end{bmatrix} .
\end{aligned} \tag{5.18}$$

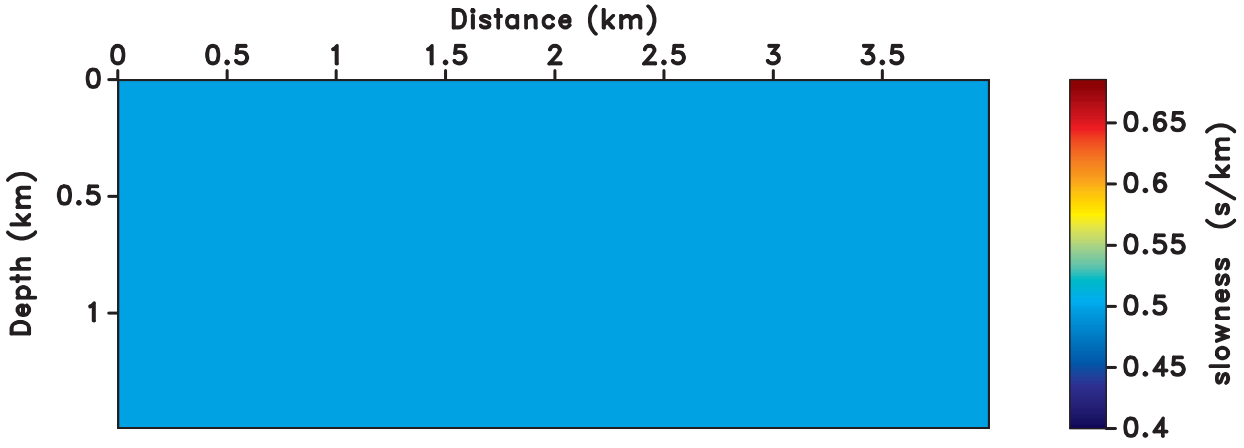
Since the adjoint sources computation is the only step associated with the objective function, the rest of the computation are the same as the gradient computation for conventional DSO.

5.4 Examples

In this section, we use two synthetic examples to illustrate our illumination compensated image-domain wavefield tomography. In the first example, we use incomplete data to simulate



(a)



(b)

Figure 5.1: (a) The true model used to generate the data, and (b) the initial constant model for inversion.

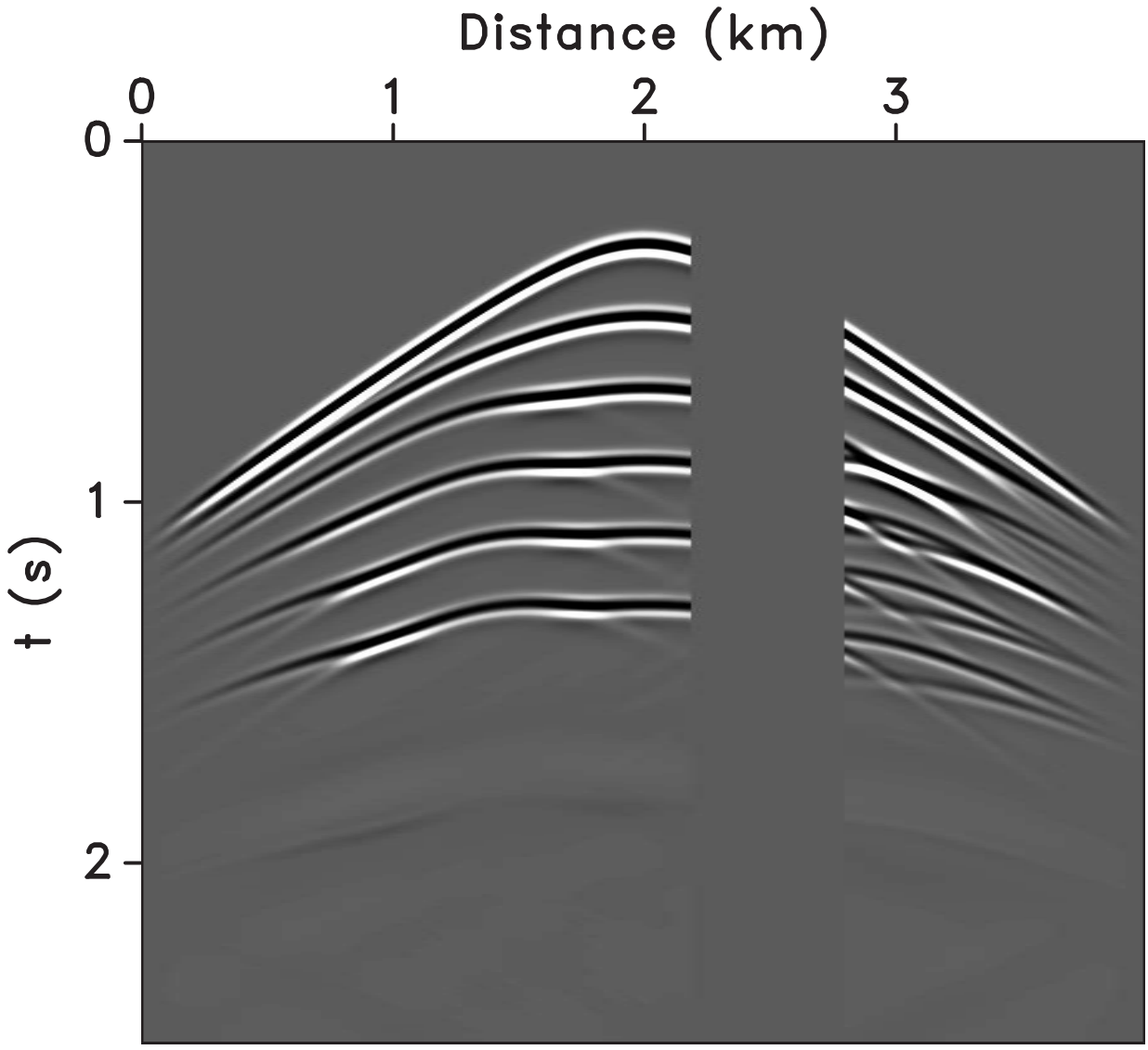
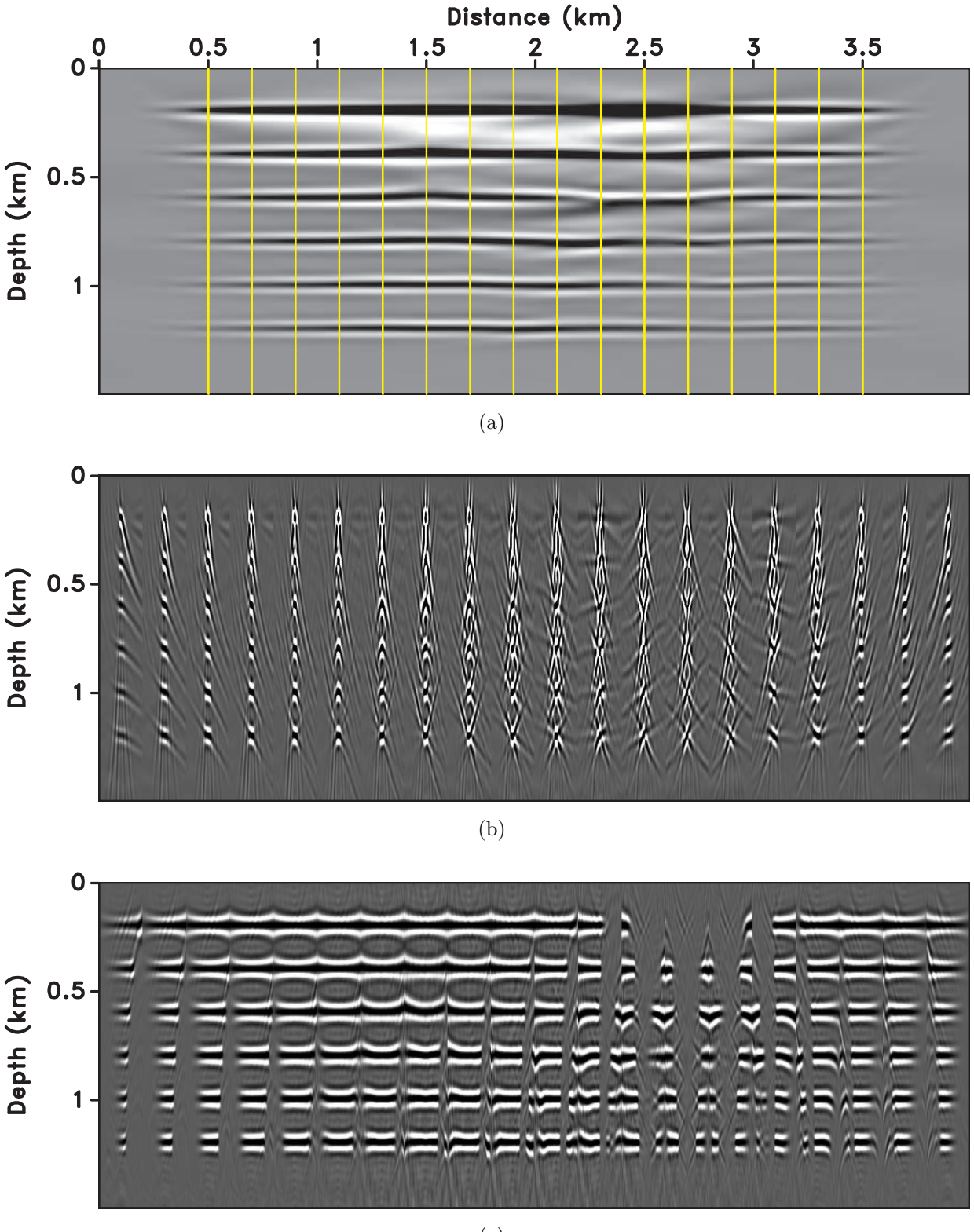


Figure 5.2: The shot gathers at 2.0 km showing a gap of 0.6 km in the acquisition surface. The gap simulate an obstacle which prevents data acquisition, e.g., a drilling platform.

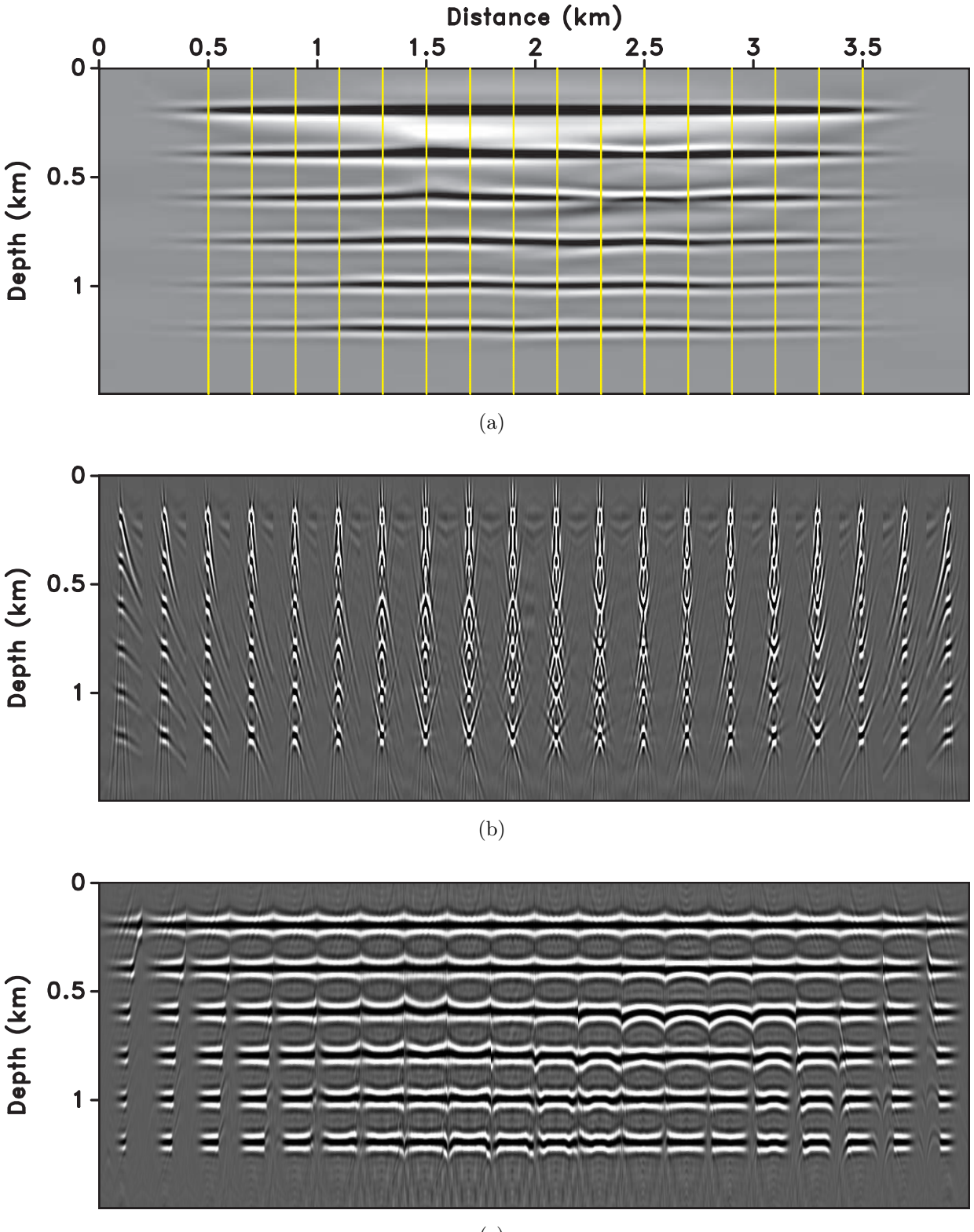


(a)

(b)

(c)

Figure 5.3: (a) The migrated image, (b) space-lag gathers, and (c) angle-domain gathers obtained using the true model and gap data.



(a)

(b)

(c)

Figure 5.4: (a) The migrated image, (b) space-lag gathers, and (c) angle-domain gathers obtained using the true model and full data.

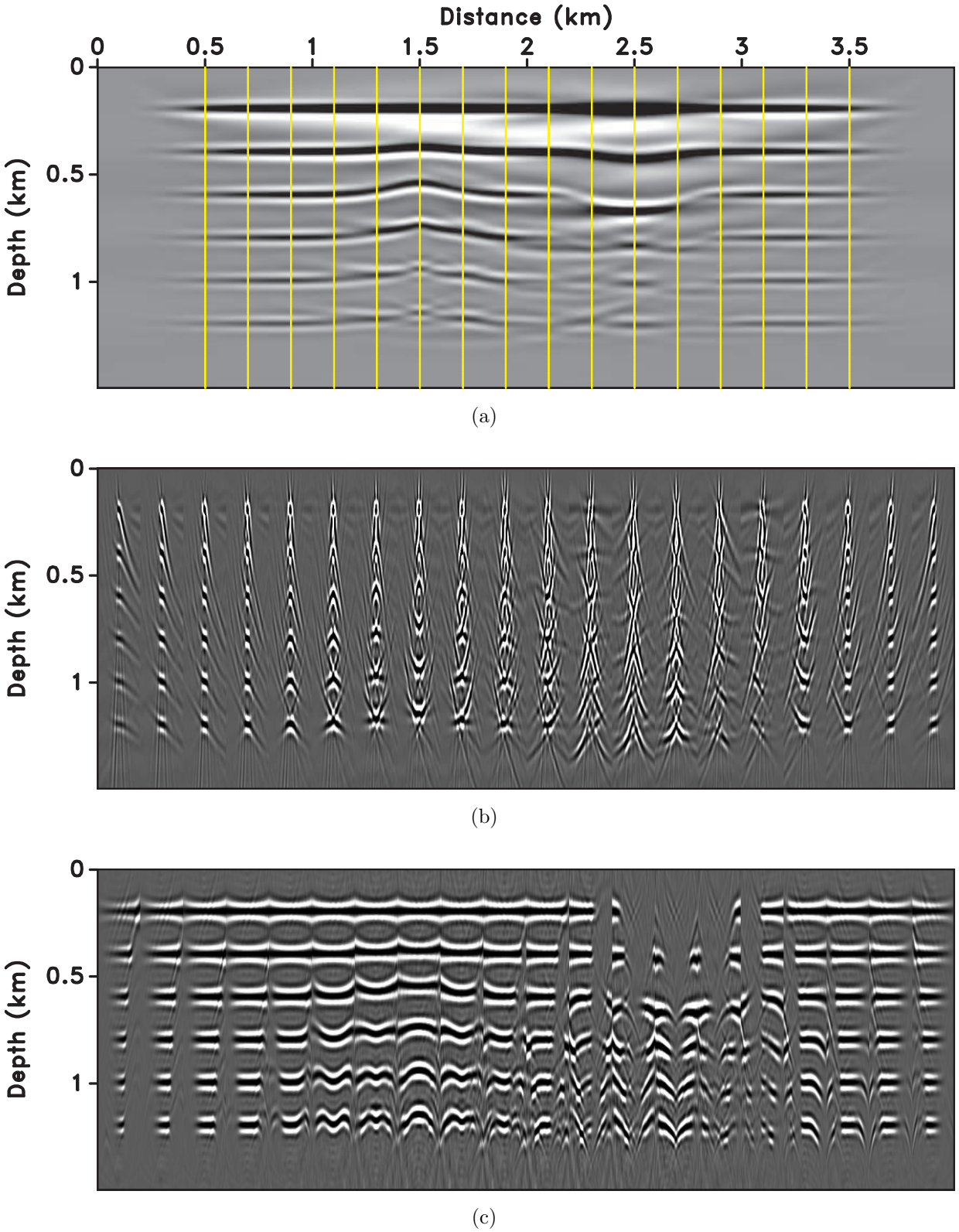


Figure 5.5: (a) The migrated image, (b) space-lag gathers, and (c) angle-domain gathers obtained using the initial model and gap data.

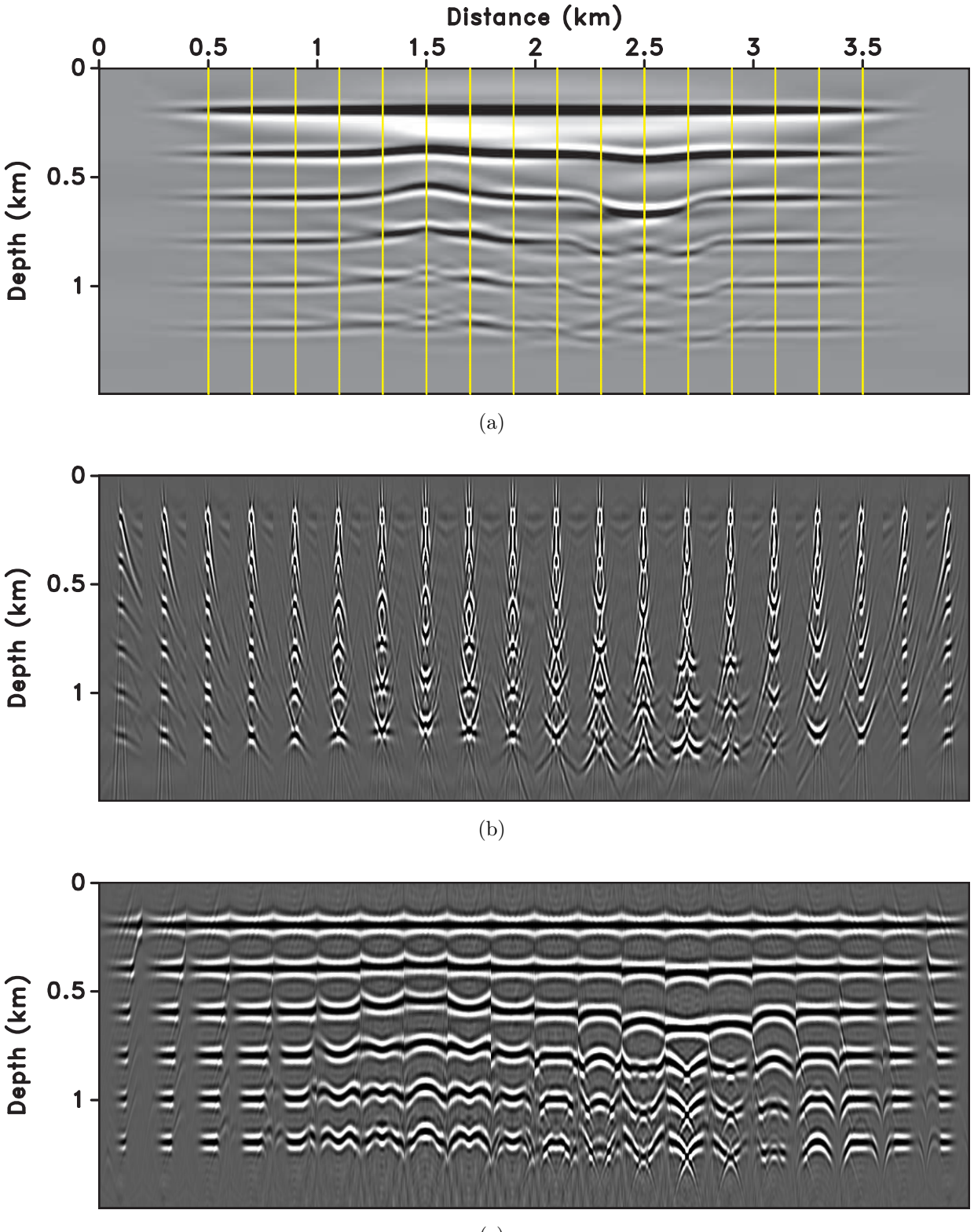


Figure 5.6: (a) The migrated image, (b) space-lag gathers, and (c) angle-domain gathers obtained using the initial model and gap data.

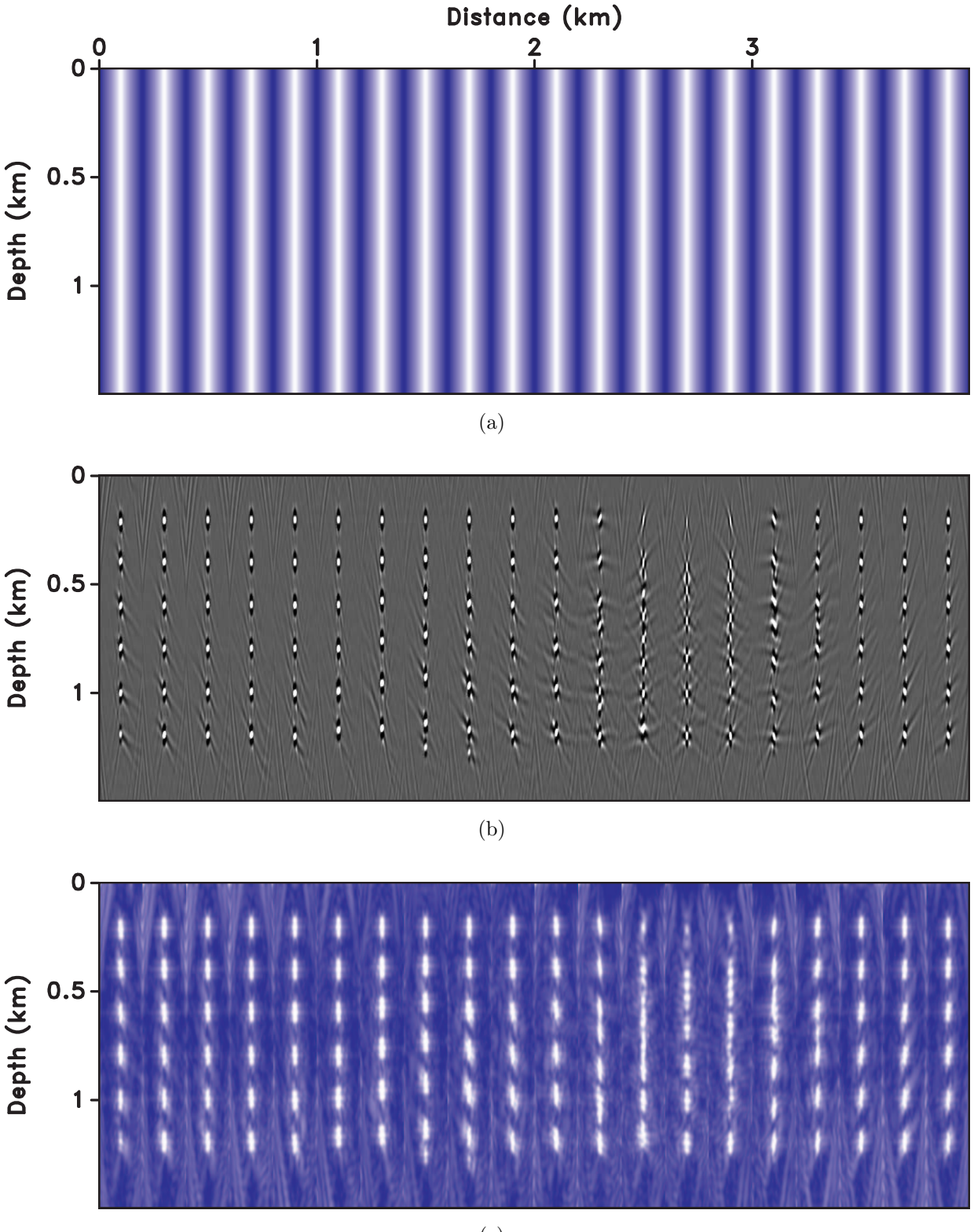
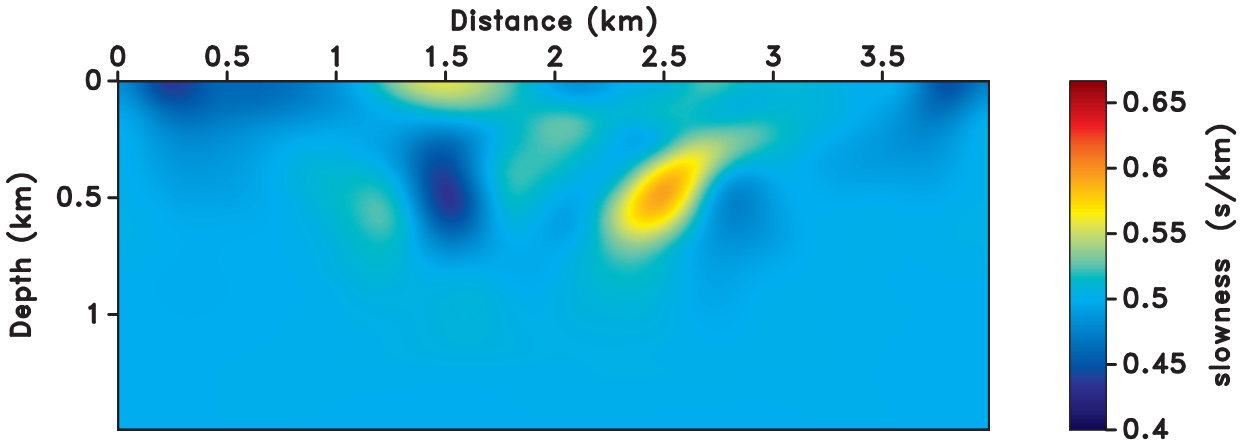
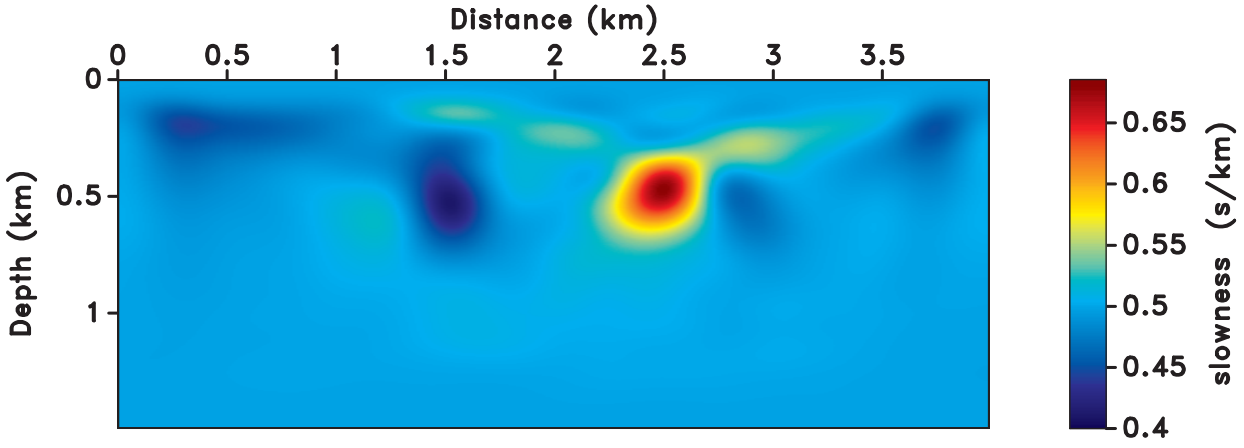


Figure 5.7: (a) The conventional DSO penalty operator. (b) The gathers obtained with demigration/migration showing the illumination effects. (c) The illumination-based penalty operator constructed from the gathers in Figure 5.7(b).

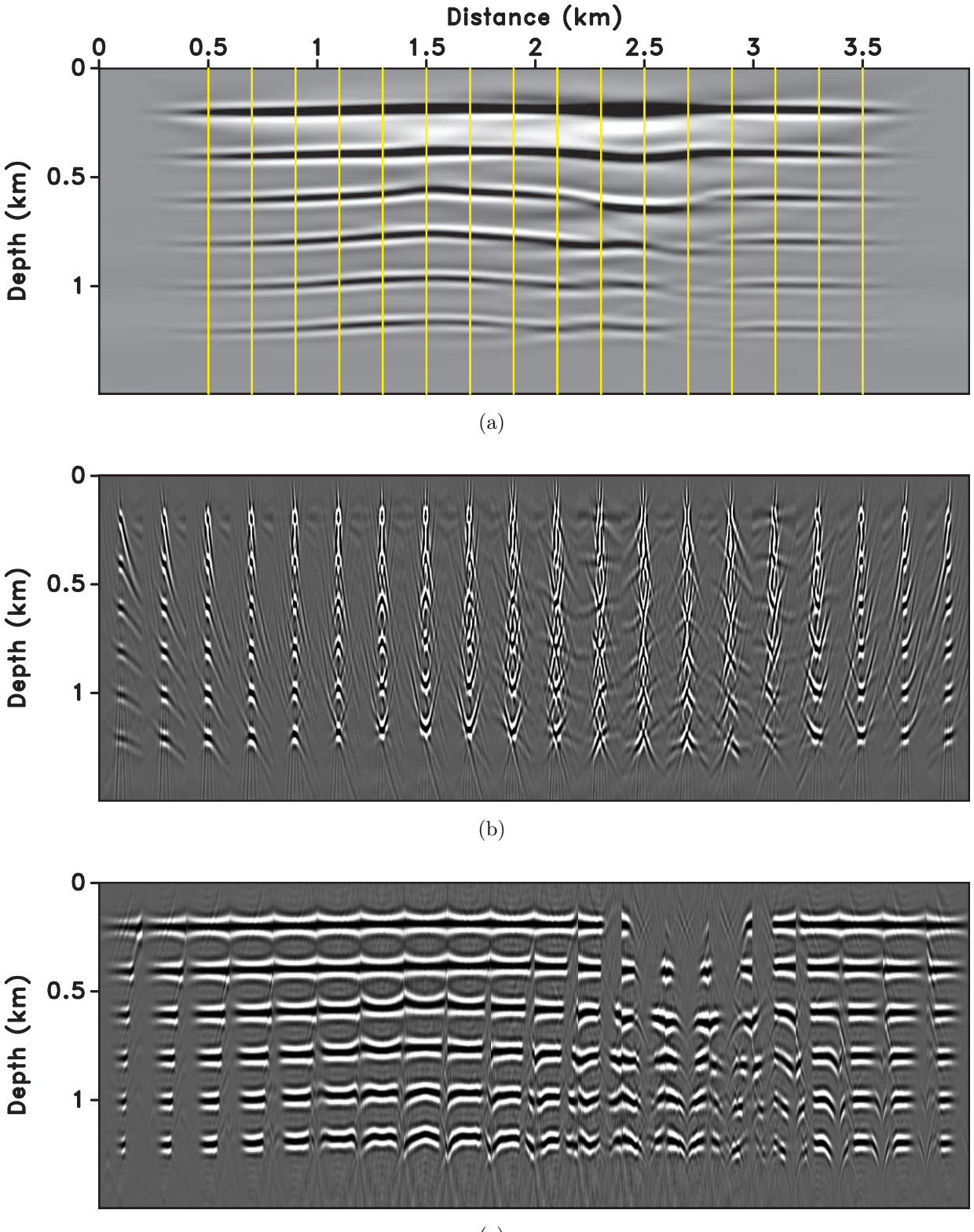


(a)



(b)

Figure 5.8: The reconstructed models using (a) the conventional DSO penalty, and (b) the illumination-based penalty.

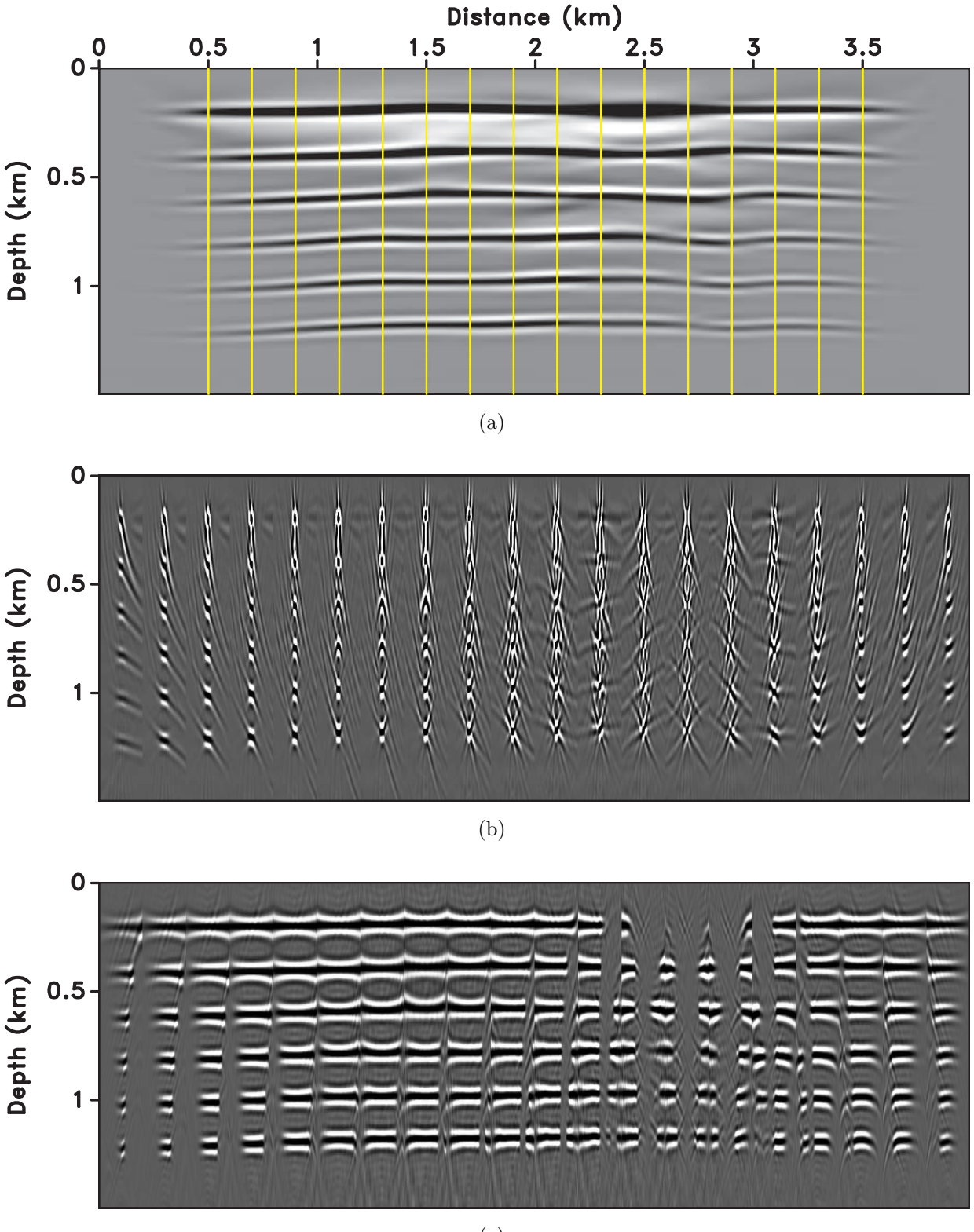


(a)

(b)

(c)

Figure 5.9: (a) The migrated image, (b) space-lag gathers, and (c) angle-domain gathers obtained using the reconstructed model with the DSO penalty.



(a)

(b)

(c)

Figure 5.10: (a) The migrated image, (b) space-lag gathers, and (c) angle-domain gathers obtained using the reconstructed model with the illumination-based penalty.

illumination problems due to the acquisition. In the second example, we use the Sigsbee model to test our method in regions of complex geology with poor subsurface illumination caused by irregular salt.

The velocity model for the first example is shown in Figure 5.1(a), and the initial model is the constant background of the true model (Figure 5.1(b)). Using six horizontal interfaces as density contrasts, we generate the data at receivers distributed along the surface using a two-way wave-equation finite-difference modeling code. A shot gather is shown in Figure 5.2. The data are truncated from $2.2 - 2.8$ km to simulate an acquisition gap.

To highlight the influence of illumination, we first plot the migrated image and gathers obtained using both the gap and full data in the case of the true model. The image and gathers obtained using the gap data and true model are shown in Figure 5.3(a)-Figure 5.3(c), while the image and gathers obtained using the full data and true model are shown in Figure 5.4(a) -Figure 5.4(c). Note that the angle gathers are displayed at selected locations corresponding to the vertical bars overlain in Figure 5.3(a) and Figure 5.4(a). It is obvious that illumination due to missing data generates defocusing in space-lag gathers and gaps in angle-domain gathers. Such defocusing is irrelevant to the velocity model error. Next, we plot the migrated image and gathers obtained using both the gap and full data in the case of the initial model. The image and gathers obtained using the gap data and initial model are shown in Figure 5.5(a)-Figure 5.5(c), while the image and gathers obtained using the full data and true model are shown in Figure 5.6(a) -Figure 5.6(c). The migrated image for the initial model shows defocusing and crossing events caused by the incorrect model. The space-lag gathers obtained with gap data contain the defocusing due to both the illumination and velocity error. More importantly, we cannot distinguish between these two different types of defocusing. The illumination gap due to the missing data and the residual moveout caused by the wrong velocity can also be observed in the angle gathers obtained using the gap data.

For comparison with our method, we run the inversion using conventional DSO penalty operator. Figure 5.7(a) plots the penalty operators at the same selected locations shown in

Figure 5.3(a). The actual spacing of the gathers and penalty operators are 0.2 km. Since the conventional penalty is laterally invariant, the figure consists of the same operators duplicated at different lateral position. The inverted model after 30 nonlinear iterations is plotted in Figure 5.8(a), and the corresponding migrated image, space-lag gathers, and angle gathers are shown in Figure 5.9(a)- Figure 5.9(c). The reconstruction of the model is not satisfactory, especially for the anomaly under the acquisition gap. As a result, the reduced quality of the image obtained with the inverted model is not surprising. Although the reflections on the left of the image are quite continuous and flat, those on the right, especially under the acquisition gap, are not flat and are even discontinuous. This result clearly shows the negative impact of the poor illumination on image-domain wavefield tomography.

To show the defocusing due to illumination effects in the gathers, we construct the illumination gathers from the current image. We first pick all the horizons from the image in Figure 5.5(a) and replace all the image points on the horizons by point scatters. The result is the reference image used to generate illumination gathers. We then apply the demigration/migration workflow from 5.15 to the reference image. The result, as shown in Figure 5.7(b), characterizes the illumination effects given the velocity model and acquisition setup. Most reflection energy is focused indicating good illumination, but we can still observe defocusing as the consequence of incomplete data in the area under the acquisition gap. The illumination-based penalty operator is constructed from the gathers in Figure 5.7(b) using 5.16, as plotted in Figure 5.7(c). We can observe that the areas in light color coincide with the focused energy at zero lag and defocusing energy away from zero lag in Figure 5.7(b). Thus, the new operator does not penalize the defocusing due to the uneven illumination and highlights only the defocusing due to velocity errors.

sing the new penalty operator, we update the model under the same conditions as in the example using DSO, Figure 5.8(b). Compared with the result in Figure 5.8(a), the result obtained with the new penalty is cleaner. Also, the anomaly under the acquisition gap is more accurately reconstructed and closer to the true model. The migrated image, space-lag

gathers, and angle-domain gathers are shown in Figure 5.10(a)-Figure 5.10(c). Because of the improved model, the images are also improved, as seen in Figure 5.10(a). The reflections under the acquisition gap are more continuous and flat than the image in Figure 5.9(a). In addition, one can observe from the angle gathers in Figure 5.9(c) that more events appear in the area under the acquisition gap and overall reflections are flatter, which indicates an improved signal-to-noise ratio rising from the more accurate reconstructed model.

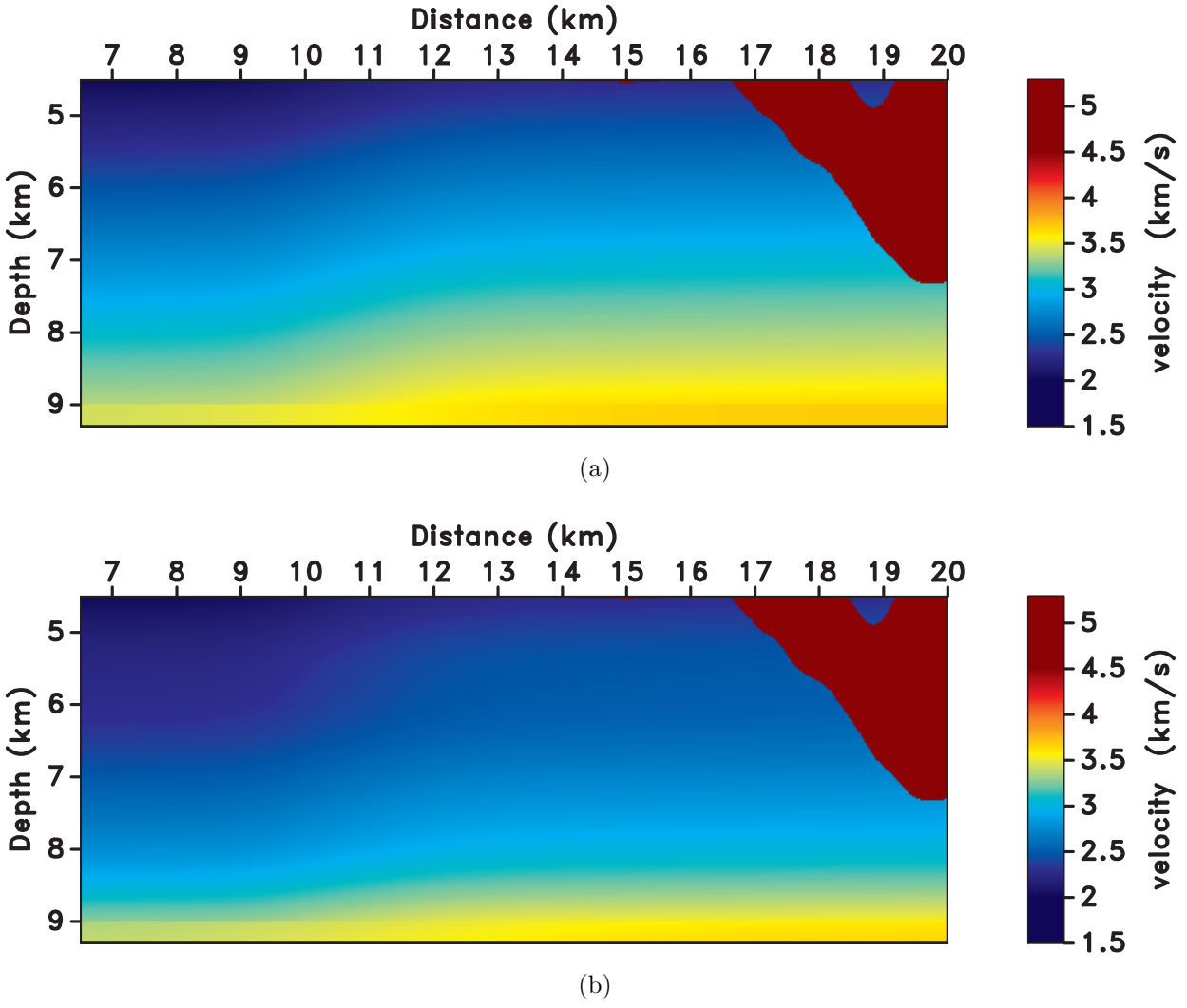


Figure 5.11: (a) The true model and (b) the initial model in the target area of the Sigsbee model.

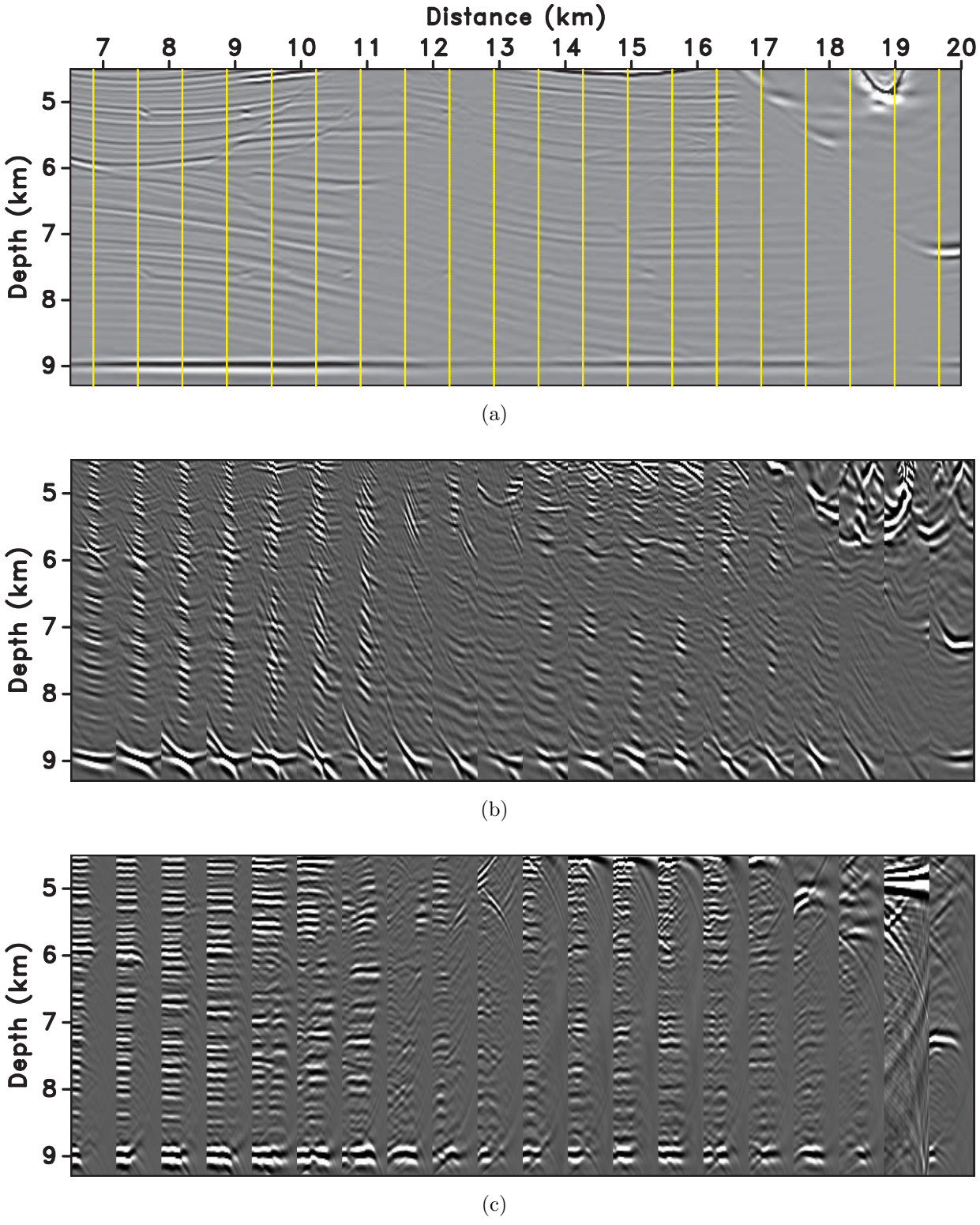
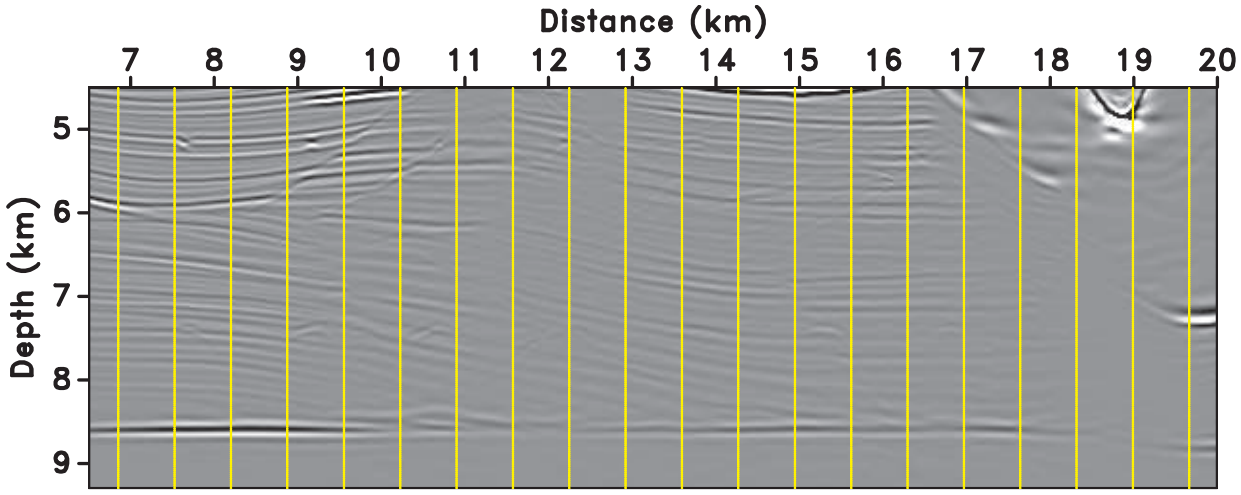
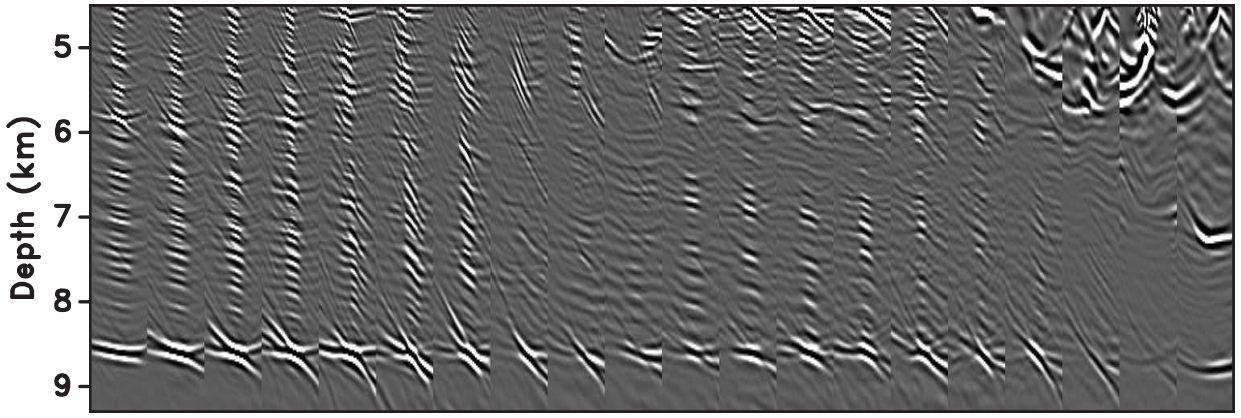


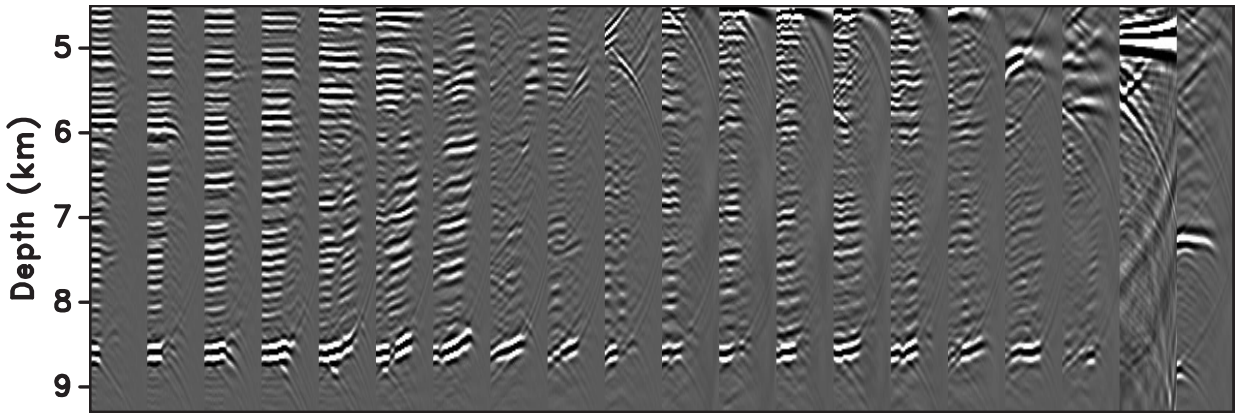
Figure 5.12: (a) The migrated image, (b) space-lag gathers, and (c) angle-domain gathers obtained using the reconstructed model with the true model.



(a)

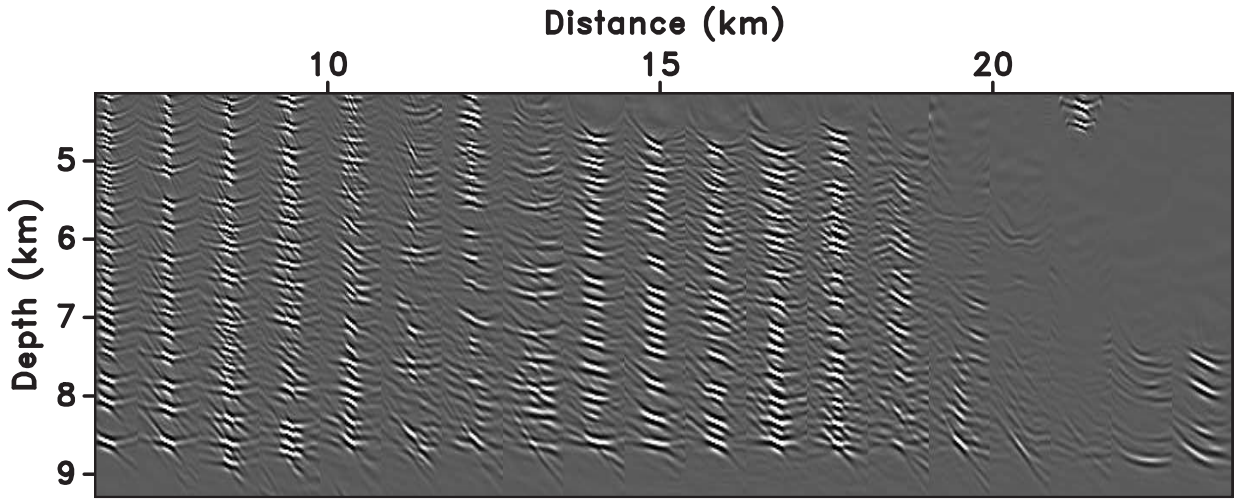


(b)

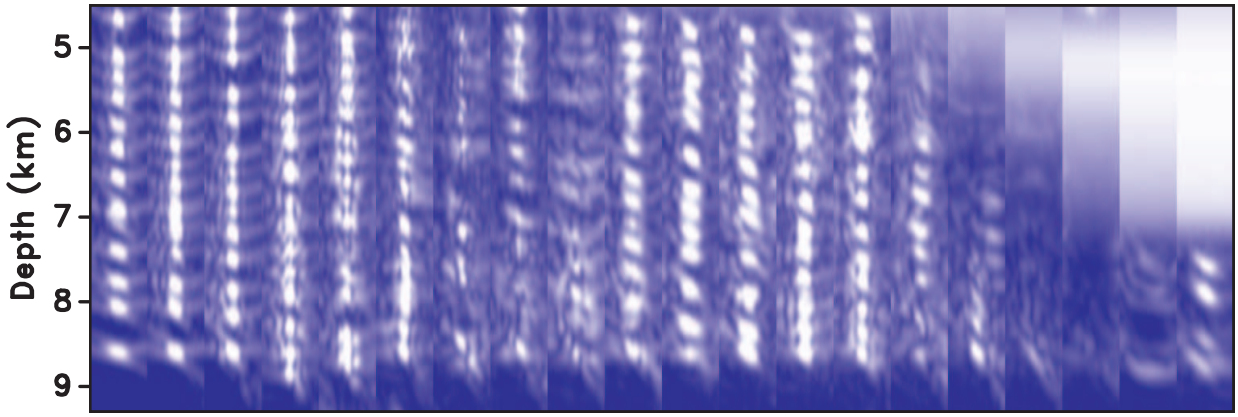


(c)

Figure 5.13: (a) The migrated image, (b) space-lag gathers, and (c) angle-domain gathers obtained using the reconstructed model with the initial model.

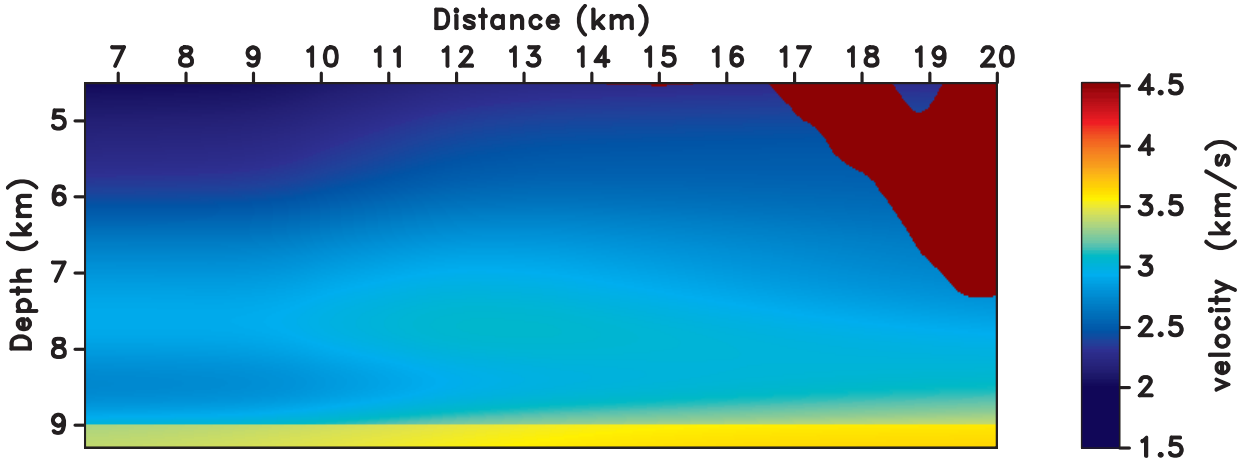


(a)

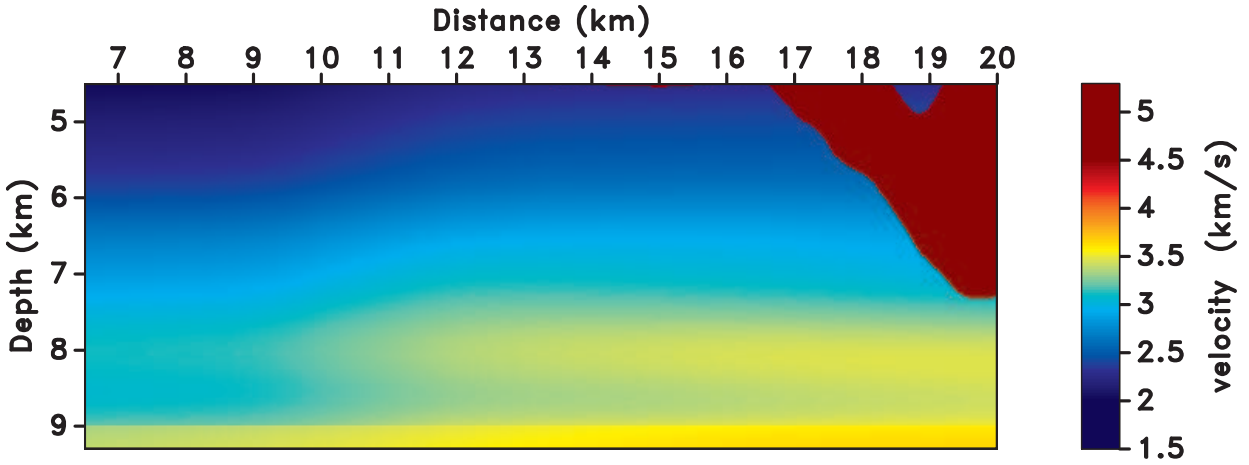


(b)

Figure 5.14: (a) The gathers obtained with demigration/migration showing the illumination effects. (b) The illumination-based penalty operator constructed from the gathers in Figure 5.14(a). The light areas cover the defocusing due to the illumination.



(a)



(b)

Figure 5.15: The reconstructed models using (a) the DSO penalty and (b) the illumination-based penalty.

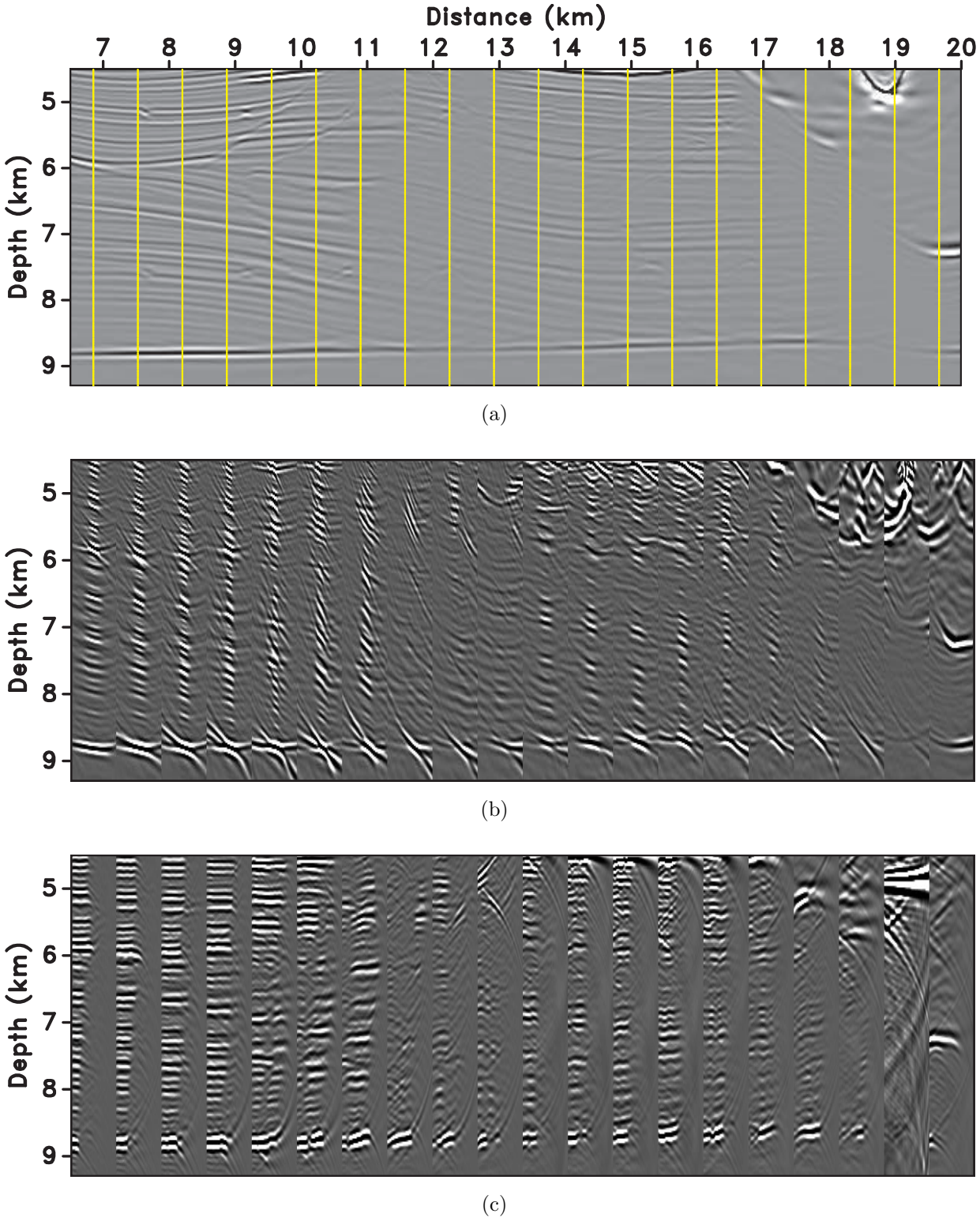
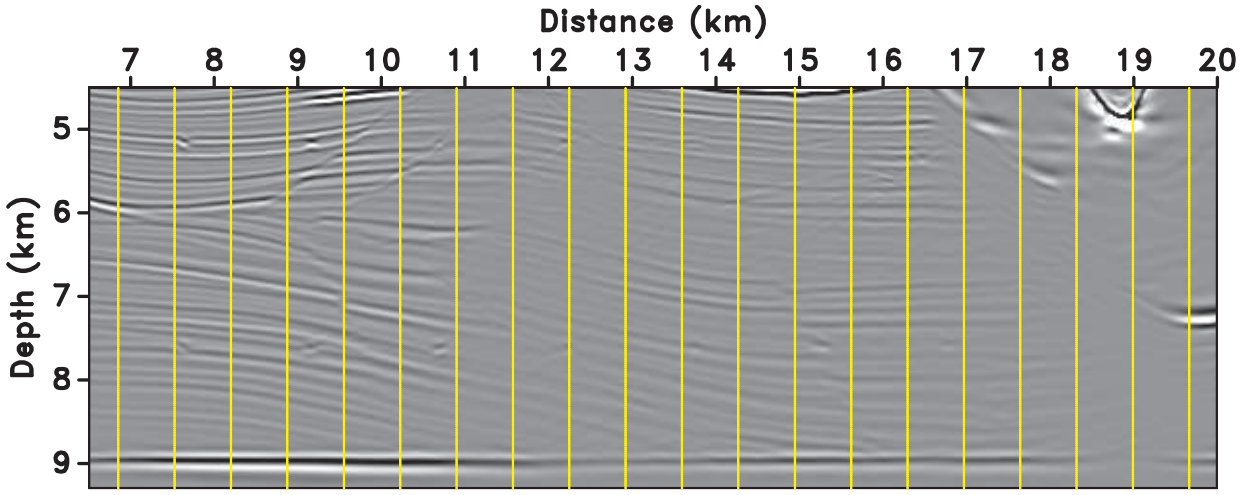
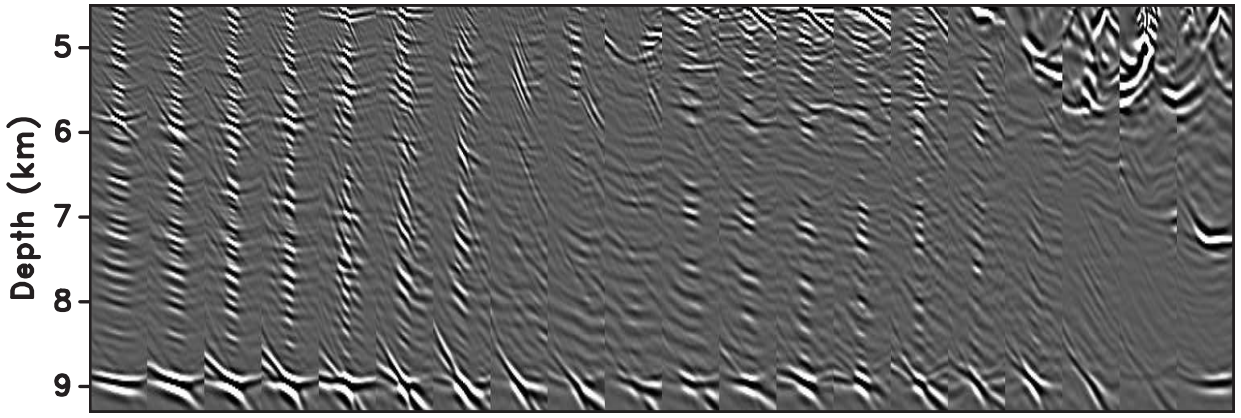


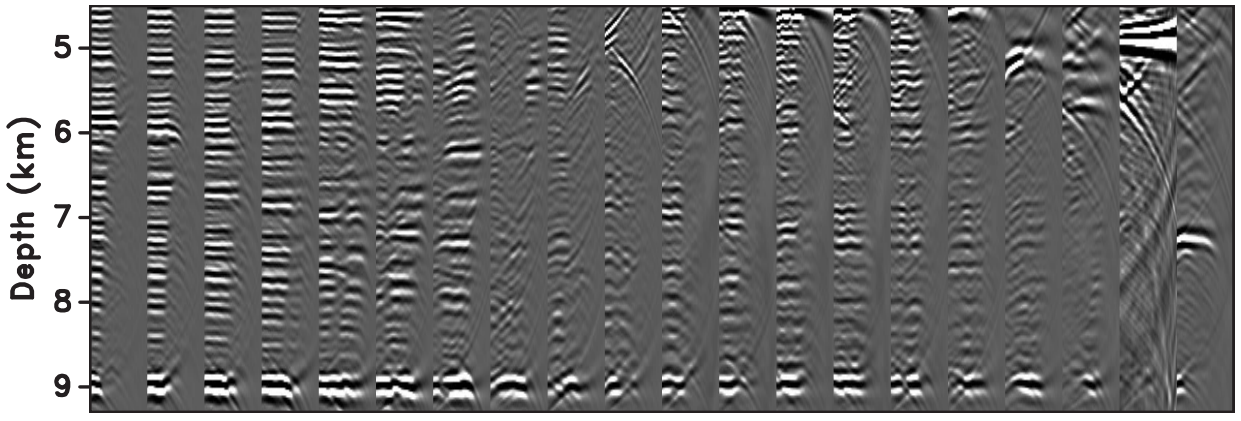
Figure 5.16: (a) The migrated image, (b) space-lag gathers, and (c) angle-domain gathers obtained using the reconstructed model with the DSO penalty.



(a)



(b)



(c)

Figure 5.17: (a) The migrated image, (b) space-lag gathers, and (c) angle-domain gathers obtained using the reconstructed model with the illumination-based penalty.

We also apply our method to the Sigsbee 2A model (Paffenholz et al., 2002), and concentrate on the subsalt region. The target area ranges from $x = 6.5 - 20$ km, and from $z = 4.5 - 9$ km. The true and initial models are shown in Figure 5.11(a) and Figure 5.11(b). Here, we switch to show velocity instead of slowness to better visualize the model. The migrated image, space-lag gathers and angle-domain gathers for correct and initial models are shown in Figure 5.12(a)-Figure 5.12(c) and Figure 5.13(a)-Figure 5.13(c), respectively. The angle gathers are displayed at selected locations corresponding to the vertical bars overlain in Figure 5.12(a) and Figure 5.13(a). The actual spacing of the gathers and penalty operators are 0.45 km. Note that the reflections in the angle gathers appear only at positive angles, as the data are simulated for towed streamers and the subsurface is illuminated from one side only. Just as for the previous example, we run the inversion using both the conventional DSO penalty and the illumination-based penalty operators. For the illumination-based operator, we first generate gathers containing defocusing due to illumination (Figure 5.14(a)), and then we construct the penalty operator as shown in Figure 5.14(b) using 5.16. From the gathers characterizing the illumination effects, we can observe the significant defocusing in the subsalt area as the salt distorts the wavefields used for imaging and causes the poor illumination in this area.

We run both inversions for 20 iterations, and obtain the reconstructed models shown in Figure 5.15(a)-Figure 5.15(b). The corresponding migrated image, space-lag gathers, and angle-domain gathers shown in Figure 5.16(a)-Figure 5.16(c), and Figure 5.17(a)-Figure 5.17(c), respectively. The model obtained using the illumination-based penalty is much closer to the true model than the model obtained using DSO penalty. The DSO model is not sufficiently updated and is too slow. This is because the severe defocusing due to the salt biases the inversion when we do not take into accounts the uneven illumination for tomography. The comparison of the images also suggests that the inversion using the illumination-based penalty is superior to the inversion using DSO penalty. The image obtained with the new penalty is significantly improved, as illustrated, for example, by that the diffractors dis-

tributed at $z = 7.6$ km focus, and the faults located between $x = 14.0$ km, $z = 6.0$ km and $x = 16.0$ km, $z = 9.0$ km are more visible in the images. If we concentrate on the bottom reflector (around 9 km), we can see that the bottom reflector is corrected to the right depth for inversion using the illumination-based penalty, while the bottom reflector for inversion using DSO penalty is still away from the right depth and not as flat as the reflector in Figure 5.17(a). From the angle gathers obtained using different models, we can see that the gathers for both reconstructed models show flatter reflections, indicates that reconstructed models are more accurate than the initial model. We can, nonetheless, observe that the reflections in Figure 5.17(c) are flatter than those in Figure 5.16(c), and conclude that the reconstructed model using the illumination-based penalty is more accurate.

5.5 Discussion

Uneven illumination is often a challenge faced by the exploration activities in complex subsurface environments, particularly in subsalt areas. Furthermore, imperfect acquisition can also cause illumination problems. In either case, the reflections from various angles cannot be observed on the surface, either because of the complexity of the subsurface or because of limited/partial acquisition on the surface. The more essential reason of the illumination problem, however, is due to the non-unitary nature of the migration operator. One can also use an improved migration operator to compensate the illumination problem, as suggested by Tang and Biondi (2009). In any of these situations, the effectiveness of image-domain wavefield tomography deteriorates. In comparison, data-domain wavefield tomography methods suffer less from the illumination. However, image-domain approach is more effective to extract velocity model information from reflections than data-domain approach in deeper target such as subsalt. To make the image-domain method more applicable in practice, we must compensate the illumination effects to improve its accuray. From the synthetic example, we see that the imbalanced illumination creates defocusing in space-lag gathers regardless of the accuracy of the velocity model. Minimizing such defocusing through wavefield tomography generates incorrect updates and artifacts in the result. Therefore, the

defocusing caused by the uneven illumination must be excluded from the model building process. This is done by replacing the DSO penalty operator with a modified penalty operator, which is constructed based on the illumination information. One might also implement similar idea for DSO formulated in the angle domain as uneven illumination appears a hole and velocity error generates residual moveout. However, the transformation to angle domain brings additional computational cost. Shen and Symes (2008) also observe that the results obtained in angle domain is worse than the results obtained in lags domain because of the larger condition number of the system. Thus, we only present the approach implemented based on the space-lag gathers. During our iterative inversion, we update penalty operator at each iteration, as the velocity model is changing during the iterations and the subsurface illumination information needs to be re-evaluated. In the theory section, we discuss the formulation of image-domain wavefield tomography and our solution to illumination problems based on a two-way wave equation. The formulation, however, applies well when a one-way wave equation is used. The construction of the illumination-based penalty operator is similar, except for the wave equation used in all modeling and migrations.

5.6 Conclusions

We demonstrate an illumination compensation strategy for wavefield tomography in the image domain. The idea is to measure the illumination effects on space-lag extended images, and replace the conventional DSO penalty operator with new one that compensates for illumination. This approach isolates the defocusing caused by the illumination such that the inversion minimizes only the defocusing relevant to the velocity error. Synthetic examples demonstrate the negative effects of uneven illumination on the reconstructed model and show the improvements on both the inversion results and migrated images after the illumination information is included in the penalty operator. Our approach enhances the robustness and effectiveness of image-domain wavefield tomography when the surface data are incomplete or when the subsurface illumination is uneven due to complex geologic structures such as salt.

CHAPTER 6

3D IMAGE-DOMAIN WAVEFIELD TOMOGRAPHY USING TIME-LAG EXTENDED IMAGES

A paper to be submitted to *Geophysics*

Tongning Yang [1,2] and Paul Sava [1]

6.1 Summary

We present a 3D image-domain wavefield tomography method that reconstructs the velocity model by minimizing the focusing error extracted from time-lag extended images. The focusing error, which evaluates the velocity model accuracy, represents the traveltime residual in the image domain. The objective function is similar to that used by wave-equation traveltime inversion, but, unlike wave-equation traveltime inversion wherein traveltime residual is obtained from crosscorrelation of a single-shot experiment, the focusing error is extracted from time-lag gathers, which are the crosscorrelation of multi-shot experiments. Because of the higher signal-to-noise ratio in the common-image gathers than that in shot gathers, the technique is able to measure focusing error more accurately in presence of noisy data and complex structure. In addition, the image-domain approach is robust as it does not suffer from cycle-skipping, which is common in conventional data-domain waveform inversion. The focusing error is also used to precondition the gradient of the objective function in order to improve the convergence of the inversion. This is done by constructing a gradient mask which restricts the model updates in areas where the focusing error exceeds a certain threshold. This preconditioning of the gradient limits the model update only in areas containing velocity model errors. We illustrate the method using both synthetic and field data. The North Sea 3D field data example demonstrates that the technique is effective in optimizing

[1]Center for Wave Phenomena, Colorado School of Mines
[2]Corresponding author

the velocity model and improving image quality. In addition, the method is efficient in 3D because only the time-lag extension of the gathers is computed and stored, compared to differential semblance optimization wherein the in-line and cross-line space-lag extensions must be computed.

6.2 Introduction

In seismic imaging, building an accurate and reliable velocity model remains one of the biggest challenges. The need for high-quality velocity models is driven by the wide-spread use of advanced imaging techniques such as one-way wave-equation migration (WEM) and reverse-time migration (RTM) (Etgen et al., 2009).

In the past decade, velocity model-building methods using full seismic wavefields (Vigh and Starr, 2008a; Symes, 2009) have become popular mainly because of their accuracy and increased computational power. One can divide the family of such velocity-estimation techniques into data-domain methods (Sirgue and Pratt, 2004; Plessix, 2009) and image-domain methods (Sava and Biondi, 2004a; Shen and Symes, 2008). Data-domain methods adjust the velocity model by minimizing the difference between simulated and recorded data (Tarantola, 1984; Pratt, 1999). This formulation is based on the strong assumption that the wave equation used for data simulation is consistent with the physics of the earth, which is often violated in practice. In addition, the methods also require low-frequency data and sufficiently accurate initial model to avoid the cycle-skipping problem.

Unlike the data-domain approaches, image-domain methods update the velocity model by optimizing the image quality. As stated by the semblance principle (**?**Yilmaz, 2001), the image coherence is optimized when the correct velocity model is used to migrate the data. The common practice is to optimize the coherency of reflection events in common-image gathers by updating the velocity model. In complex geology, image-domain wavefield tomography is capable of handling complicated wave propagation because it uses wave-equation engine to simulate the wavefields. Furthermore, the band-limited wavefields used in the velocity model building procedure are consistent with the wave-equation migration

algorithms used in imaging.

The cycle-skipping problem in conventional data-domain full-waveform inversion is mainly caused by its objective function, which is the L-2 norm of the difference between the observed and simulated data. When the initial model is not accurate enough or the data do not have sufficiently low frequency components, cycle-skipping occurs. To overcome this problem, wave-equation traveltime inversion was proposed to reconstruct the velocity model in complex geologic environments (Luo and Schuster, 1991; van Leeuwen and Mulder, 2010; Zhang and Wang, 2009). The essential idea behind this method is to invert the velocity model using only the traveltime information rather than full waveforms. In this way, the nonlinearity of the objective function with respect to the model is significantly reduced, and the objective function is less sensitive to data noise and the accuracy of the initial model. For wave-equation traveltime inversion, the traveltime residual is obtained from the cross-correlation between the recorded and simulated data, and then spread along the wavepath computed from the wave equation to update the model. Nonetheless, this kind of techniques is aimed at inverting velocity model using transmission waves but not reflected waves. As a result, they are limited to cross-well experiments or surface experiments with diving waves only.

Using traveltime residual to update the velocity model is also commonly done in the image domain, where it is known as *focusing analysis*. In fact, focusing analysis has been a commonly used method for refining the velocity model for several decades (Faye and Jeannot, 1986b). The traveltime residual is defined as *focusing error*, since it uses the focusing of reflections as a measure for the coherence of migrated images. Such information indicates the accuracy of the velocity model and thus can be used for model building. For wave-equation migration, one can extract focusing information from time-lag extended images (Sava and Fomel, 2006); it is quantified as the lag of the reflection focus shifted along the time-lag axis. Wang et al. (2005) propose a velocity analysis method using focusing analysis applied to re-datumed data sets. The approach is ray-based and thus may become unstable when the

complex geology results in multi-pathing. Higginbotham and Brown (2008) and Brown et al. (2008) also propose a model-building method that converts the focusing error into velocity updates using an analytic formula. However, the formula is derived under the 1D assumption, and the focusing error is transformed into vertical updates only. Hence, the accuracy of the method is degraded in areas with strong lateral velocity variations. Wang et al. (2008, 2009) illustrate that focusing analysis can be used as an image-enhancement tool to improve the image quality and to update subsalt velocity models. To gain a quantitative understanding of the focusing analysis, Yang and Sava (2010) analyze the relationship between the focusing error and velocity model accuracy. They also develop a wave-equation migration velocity analysis in 2D (Yang and Sava, 2011a).

Here, we propose a methodology for 3D image-domain tomography using the focusing information of migrated images. The essential idea is to extract focusing error from time-lag extended images and then convert it into velocity updates in a way similar to wave-equation traveltime inversion. In addition, the focusing error is used as a priori information to constrain the updates in target areas only and to speed up the convergence of the inversion. In the theory section, we first define the objective function and gradient computation. We also illustrate how we use the focusing error to construct a gradient mask. Then we use a simple synthetic model to illustrate the workflow of the method and present an application of the method to a North Sea 3D OBC field dataset. The improved image quality and flattened events in common-image gathers in the field data example illustrate that the method is a robust and effective 3D velocity model-building tool. The strength of our approach compared to wave-equation traveltime inversion is also analyzed in discussion section.

6.3 Theory

The objective function for our wavefield tomography approach is

$$J = \frac{1}{2}\|\Delta\tau\|^2 \ . \tag{6.1}$$

Here $\Delta\tau$ stands for the focusing error, which is the lag of a reflection focus away from zero in time-lag extended images. Time-lag extended images are the crosscorrelation between extrapolated wavefields (u_s and u_r)

$$R(\mathbf{x},\tau) = \sum_j \sum_\omega \overline{u_s(j,\mathbf{x},\omega)} u_r(j,\mathbf{x},\omega)\, e^{-2i\omega\tau} \;, \tag{6.2}$$

where j is the shot index, ω is the angular frequency, and $\mathbf{x}$ are the space coordinates $\{x, y, z\}$. The source and receiver wavefields u_s and u_r satisfy

$$\begin{bmatrix} \mathcal{L}(\mathbf{x},\omega,m) & 0 \\ 0 & \mathcal{L}^*(\mathbf{x},\omega,m) \end{bmatrix} \begin{bmatrix} u_s(j,\mathbf{x},\omega) \\ u_r(j,\mathbf{x},\omega) \end{bmatrix} = \begin{bmatrix} f_s(j,\mathbf{x},\omega) \\ f_r(j,\mathbf{x},\omega) \end{bmatrix} \;, \tag{6.3}$$

where $\mathcal{L}$ and $\mathcal{L}^*$ are forward and adjoint frequency-domain wave operators, and f_s and f_r are the source and receiver data. The wave operator $\mathcal{L}$ and its adjoint $\mathcal{L}^*$ propagate the wavefields forward and backward in time, respectively, using a two-way wave equation, i.e., $\mathcal{L} = -\omega^2 m - \Delta$, where m represent slowness squared and Δ is the Laplacian operator.

The objective function in 6.1 is the same as that defined in wave-equation traveltime inversion (Luo and Schuster, 1991; Zhang and Wang, 2009). However, the physical meanings of $\Delta\tau$ in the objective functions differ. In our approach, $\Delta\tau$ is the focusing error measured from the stack of multiple-shots crosscorrelation. In contrast, $\Delta\tau$ in wave-equation traveltime inversion is the traveltime misfit measured from a single-shot crosscorrelation.

After defining the objective function, we compute its gradient using the adjoint-state method (Plessix, 2006). The first step is to construct state variables u_s and u_r, which relate the objective function to the model parameters (6.3). The next step is to construct the adjoint sources, which are used to obtain adjoint-state variables. The adjoint sources are the derivative of the objective function with respect to the state variables. In our case, as $\Delta\tau$ is not directly dependent on the wavefields, we use the *connective function* developed by Luo and Schuster (1991). Since the focusing error represents the time lag when the reflection events focus, we have

$$R(\mathbf{x},\Delta\tau) = max\{R(\mathbf{x},\tau)\,|\tau \in [-T,T]\} \;. \tag{6.4}$$

As a result, the connective function can be written as

$$\begin{aligned}\dot{R}_{\Delta\tau} &= \left.\frac{\partial R}{\partial \tau}\right|_{\Delta\tau} \\ &= \sum_j \sum_\omega \left(-2i\omega\right) \overline{u_s\left(j,\mathbf{x},\omega\right)} u_r\left(j,\mathbf{x},\omega\right) e^{-2i\omega\Delta\tau} \ .\end{aligned} \tag{6.5}$$

The adjoint sources are then obtained as

$$\begin{aligned}g_s\left(j,\mathbf{x},\omega\right) &= \frac{\partial J}{\partial\left(u_s\right)} = \Delta\tau \frac{\partial\left(\Delta\tau\right)}{\partial\left(u_s\right)} \\ &= \Delta\tau \frac{\frac{\partial\left(\dot{R}_{\Delta\tau}\right)}{\partial(u_s)}}{\frac{\partial\left(\dot{R}_{\Delta\tau}\right)}{\partial(\Delta\tau)}} = \frac{\Delta\tau}{E}\left(2i\omega\right) \overline{u_r\left(j,\mathbf{x},\omega\right)} e^{2i\omega\Delta\tau}\end{aligned} \tag{6.6}$$

and

$$\begin{aligned}g_r\left(j,\mathbf{x},\omega\right) &= \frac{\partial J}{\partial\left(u_r\right)} = \Delta\tau \frac{\partial\left(\Delta\tau\right)}{\partial\left(u_r\right)} \\ &= \Delta\tau \frac{\frac{\partial\left(\dot{R}_{\Delta\tau}\right)}{\partial(u_r)}}{\frac{\partial\left(\dot{R}_{\Delta\tau}\right)}{\partial(\Delta\tau)}} = \frac{\Delta\tau}{E}\left(-2i\omega\right) u_s\left(j,\mathbf{x},\omega\right) e^{-2i\omega\Delta\tau} \ ,\end{aligned} \tag{6.7}$$

where

$$E = \sum_j \sum_\omega 4\omega^2 \overline{u_s\left(j,\mathbf{x},\omega\right)} u_r\left(j,\mathbf{x},\omega\right) e^{-2i\omega\Delta\tau} \ . \tag{6.8}$$

The adjoint-state variables are constructed similarly to state variables as follows:

$$\begin{bmatrix} \mathcal{L}^*\left(\mathbf{x},\omega,m\right) & 0 \\ 0 & \mathcal{L}\left(\mathbf{x},\omega,m\right) \end{bmatrix} \begin{bmatrix} a_s\left(j,\mathbf{x},\omega\right) \\ a_r\left(j,\mathbf{x},\omega\right) \end{bmatrix} = \begin{bmatrix} g_s\left(j,\mathbf{x},\omega\right) \\ g_r\left(j,\mathbf{x},\omega\right) \end{bmatrix} \ . \tag{6.9}$$

The gradient of the objective function is simply the crosscorrelation between state and adjoint-state variables:

$$\frac{\partial J}{\partial m} = \sum_j \sum_\omega \frac{\partial \mathcal{L}}{\partial m} \left(u_s\left(j,\mathbf{x},\omega\right) \overline{a_s\left(j,\mathbf{x},\omega\right)} + u_r\left(j,\mathbf{x},\omega\right) \overline{a_r\left(j,\mathbf{x},\omega\right)} \right) \ , \tag{6.10}$$

where $\frac{\partial \mathcal{L}}{\partial m}$ is just $-\omega^2$.

One general problem for image-domain wavefield tomography is that the computed gradient always distributes along the wavepaths from image points to the surface. This is because

the focusing error actually measures velocity model error accumulated from top to bottom, and the gradient spreads the updates all the way up to the surface. If certain areas above the image point do not contain error in the velocity model, the inversion needs additional iterations to eliminate the update in this region, which consequently slows the convergence of the inversion. To ameliorate this weakness of the method, we use the focusing error as a constraint in the inversion. Because the focusing error is associated with the accuracy of the velocity model, it indicates the distribution of the velocity model error as well. If the focusing error for a certain area is close to zero, then the velocity model for this area and above is accurate and needs no updates. Therefore, we can construct a gradient mask to mute areas where the focusing error is sufficiently small and no model update is required. The mask W is constructed as follows:

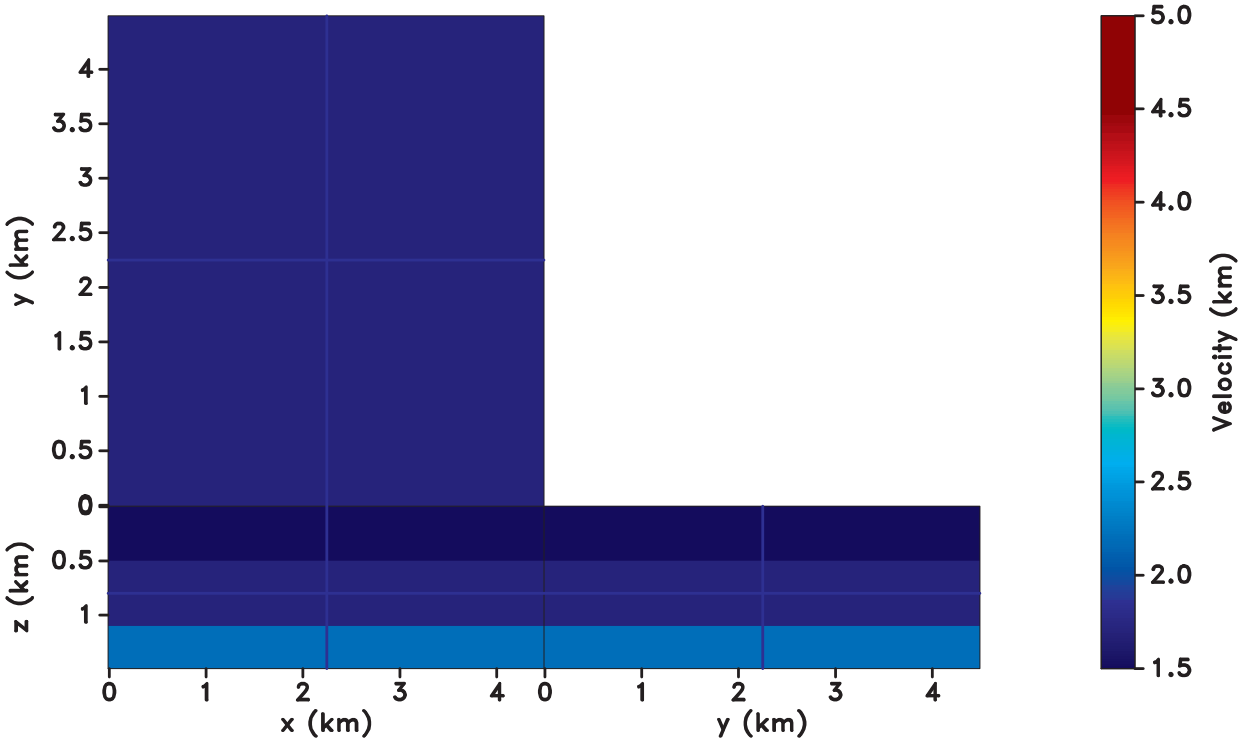
$$W = \begin{cases} 0 & \text{if } |\Delta\tau| < \tau_0 \\ 1 & \text{elsewhere} \end{cases}, \tag{6.11}$$

where τ_0 is the threshold. By applying the gradient mask and limiting the model updates in the target regions, we can reduce the number of iterations in the inversion and improve the convergence of the method.

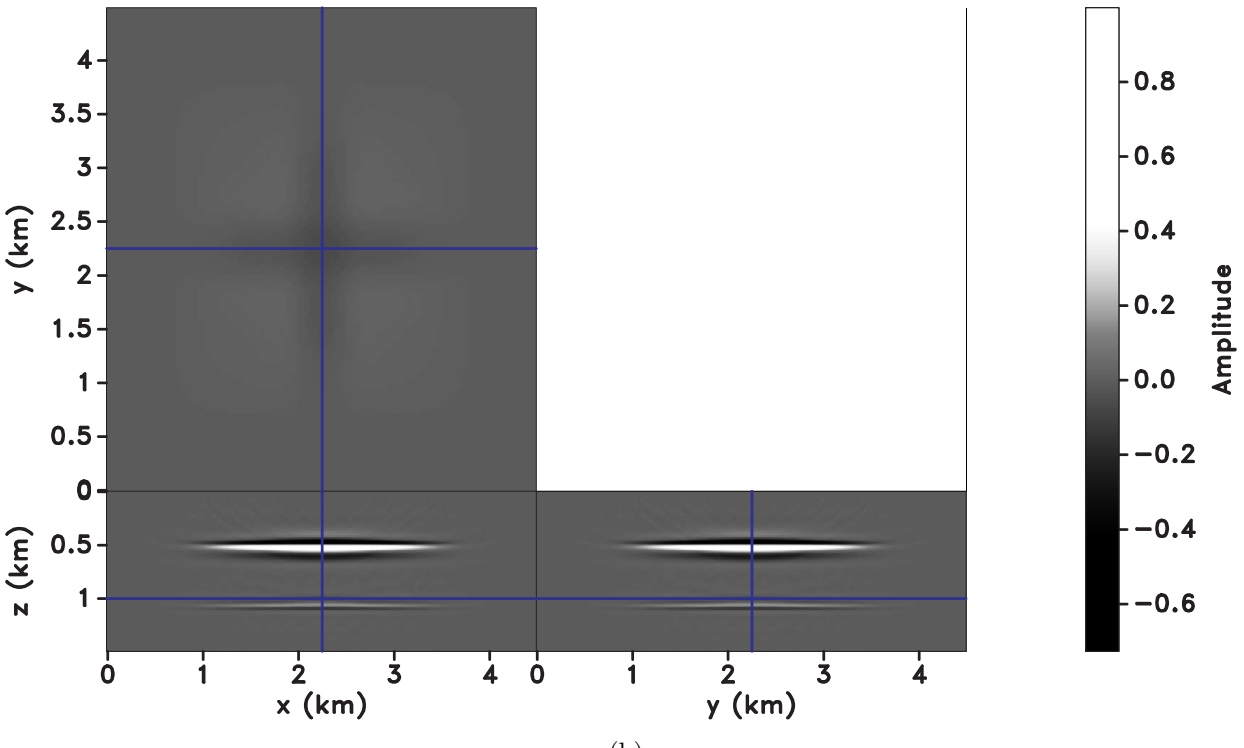
6.4 Examples

We first demonstrate the sensitivity kernel and gradient computation of our method using a simple synthetic horizontally layered model. Then, we apply the method to a North Sea 3D OBC field dataset.

Figure 6.1(a) shows the velocity profile of the synthetic model. The model has two interfaces located at $z = 0.5$ km and $z = 1.1$ km, and the velocities for the three layers from top to bottom are 2.0, 2.2, and 2.4 km/s. We simulate the data using acoustic two-way wave-equation finite-difference modeling. The initial model is a constant with the velocity value in the first layer of the true model, which is 2.0 km/s. We use this model to migrate the data and to obtain the image and time-lag gathers. As the initial model is correct in the first layer, we expect that the first interface to be correctly imaged, and the second interface shifted.



(a)



(b)

Figure 6.1: (a) The layered velocity model, and (b) migrated image obtained with the initial model, the constant velocity of the first layer of the true model.

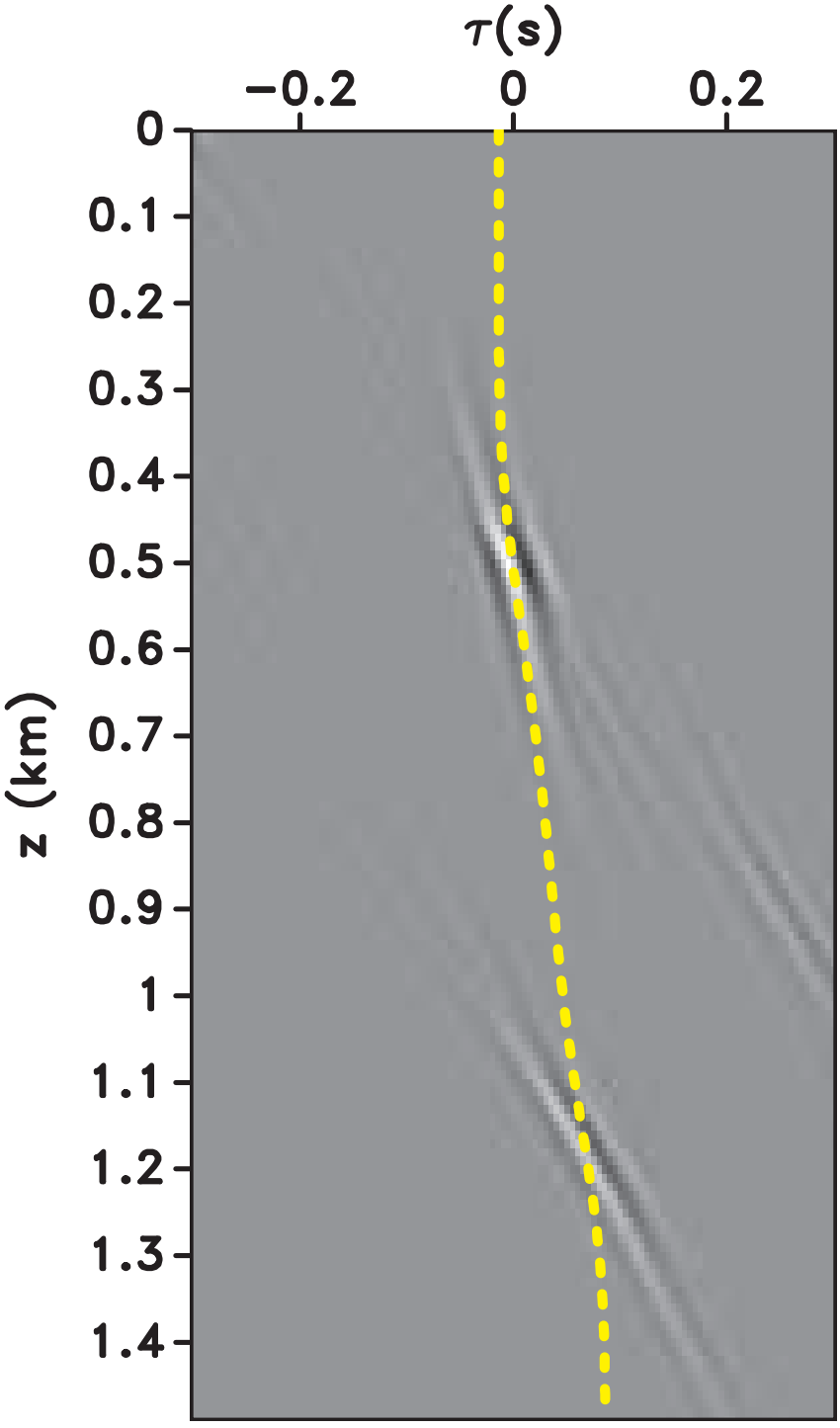
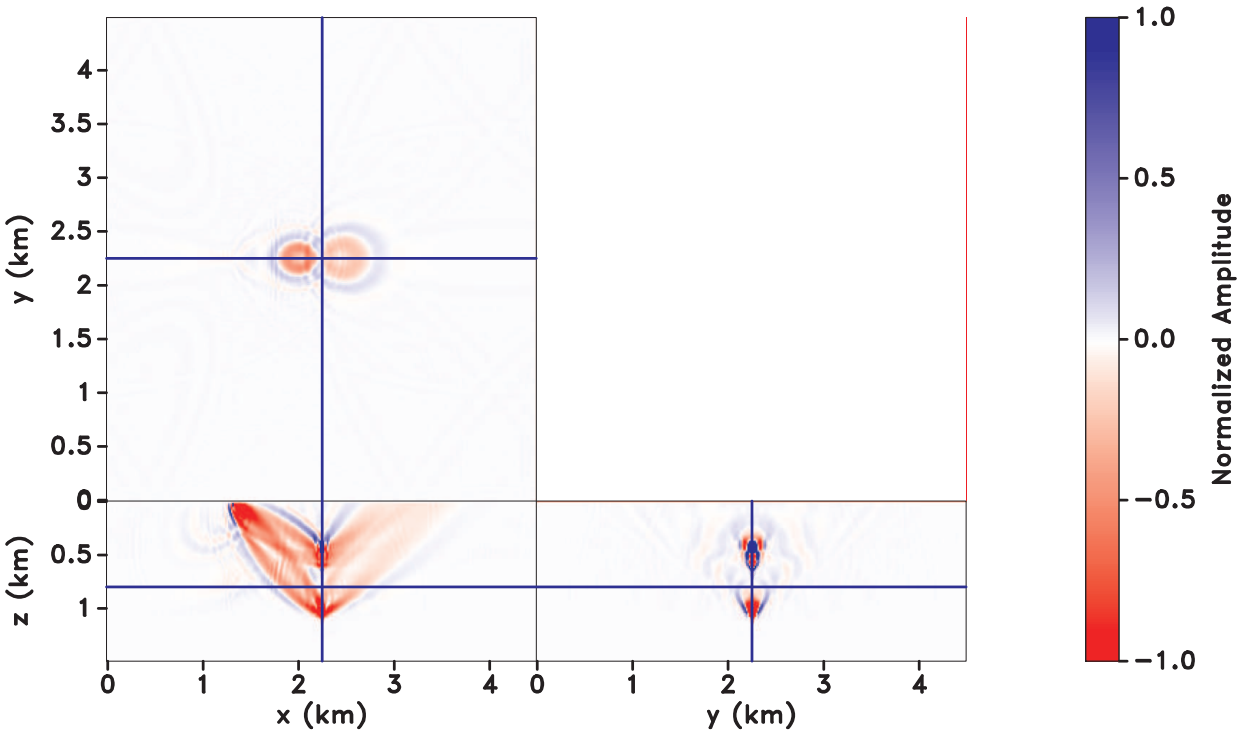
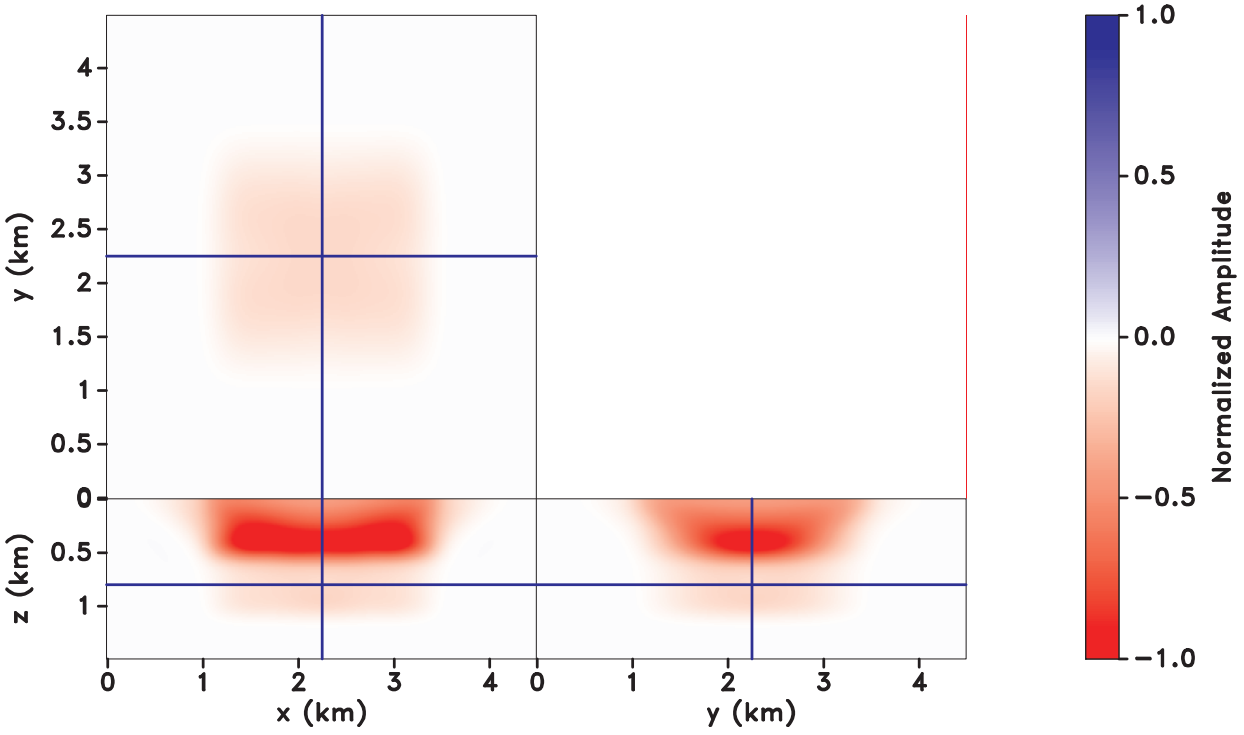


Figure 6.2: Time-lag gathers obtained with the initial model. The gather is located at at $x = 2.25$ km, $y = 2.25$ km. The yellow dash line corresponds to the picked focusing error $\Delta\tau$.

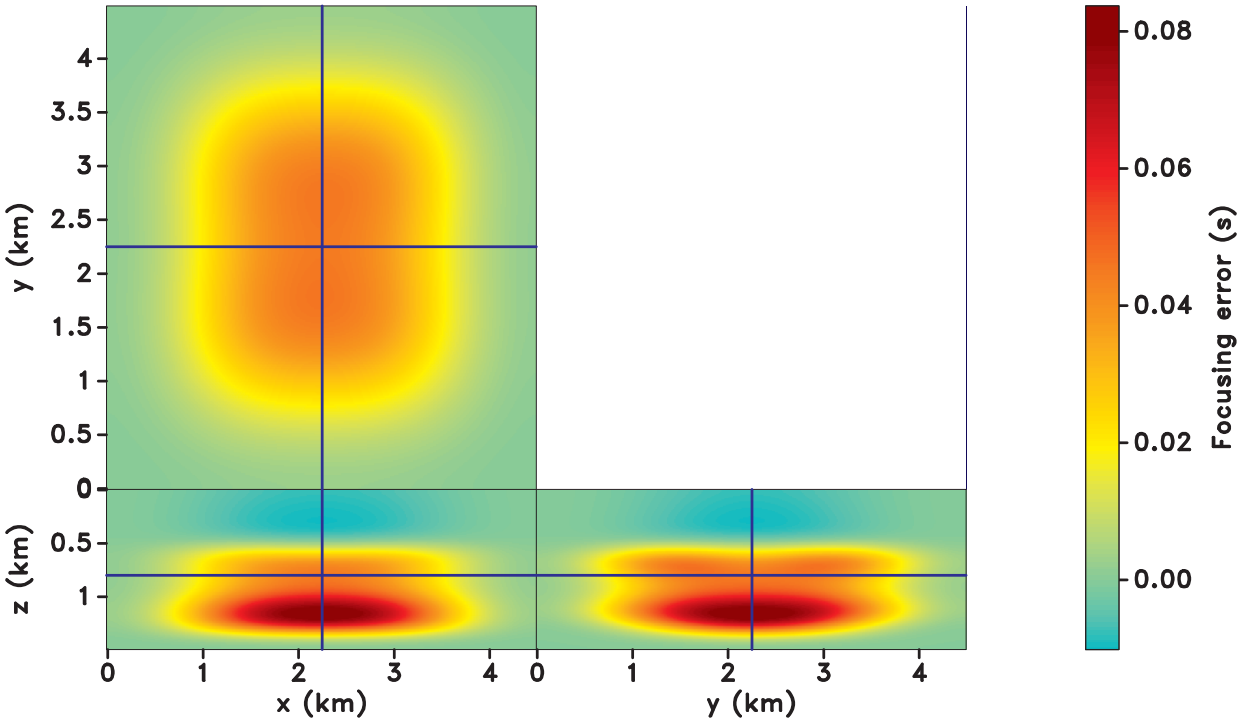


(a)

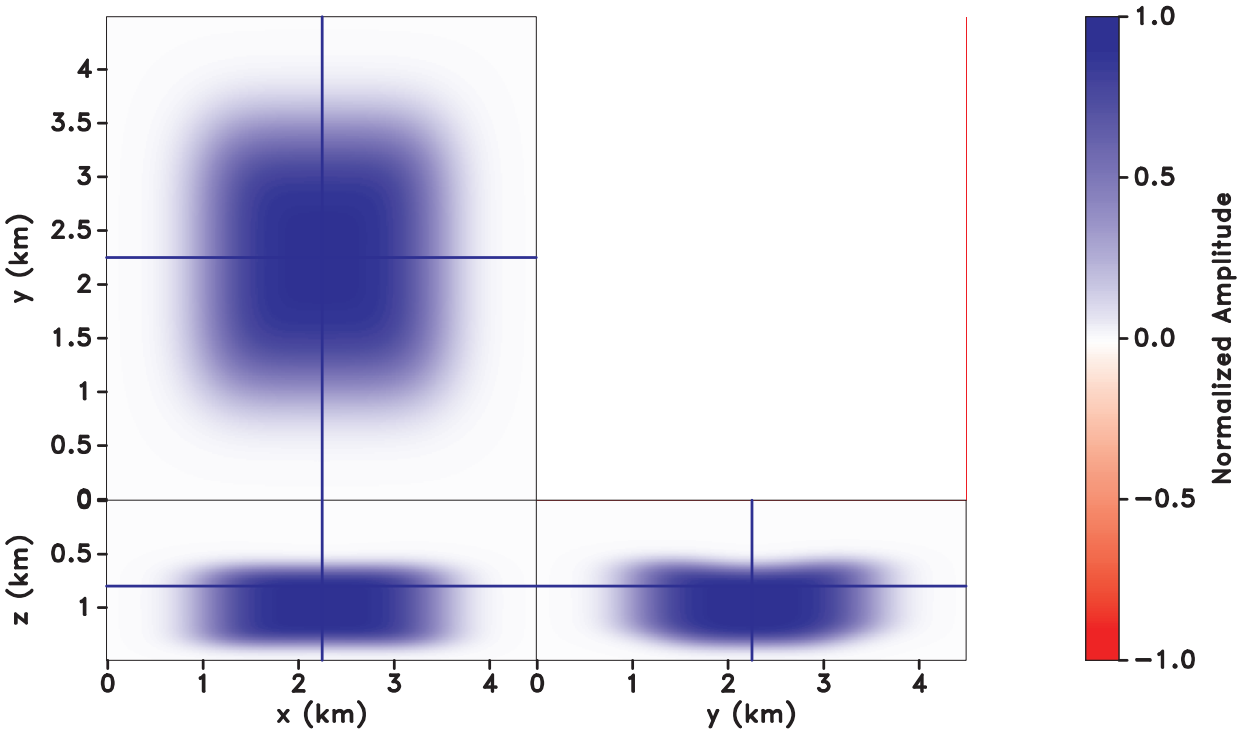


(b)

Figure 6.3: (a) The sensitivity kernel obtained with a single shot, and (b) the gradient obtained with all shots.



(a)



(b)

Figure 6.4: (a) The focusing error extracted from the time-lag gathers. (b) The gradient mask obtained using 6.11.

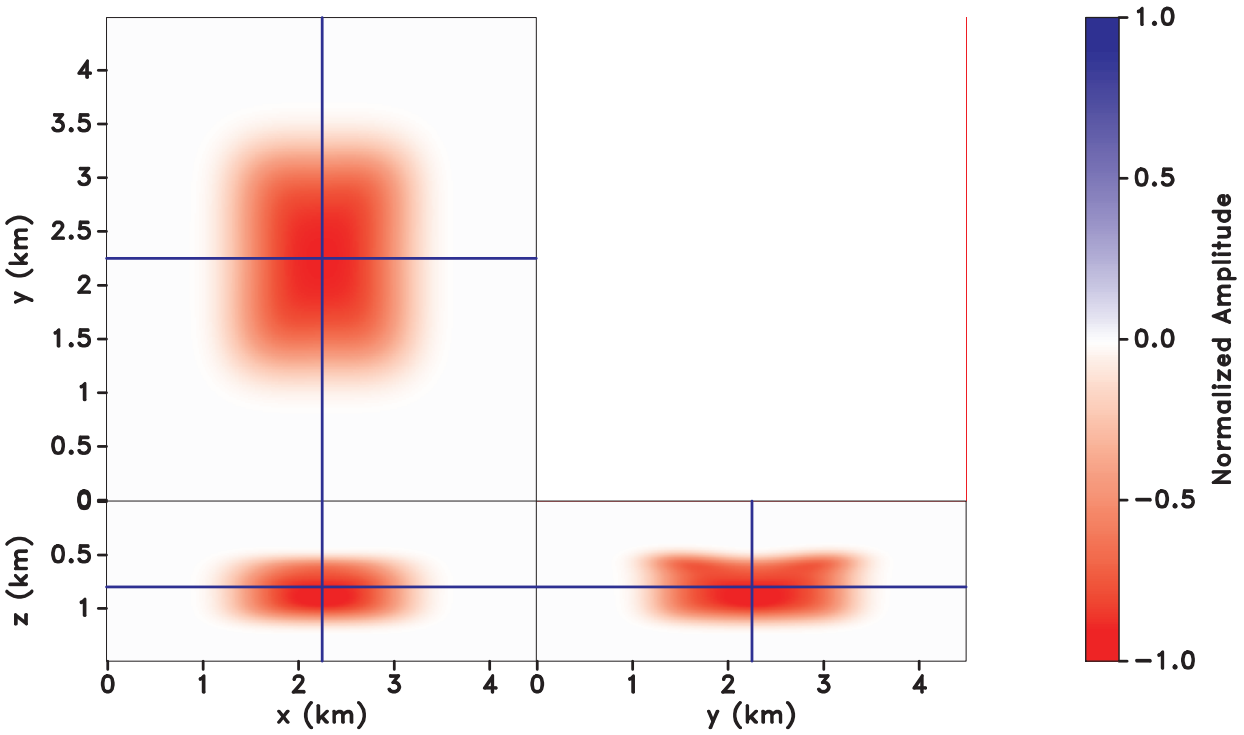
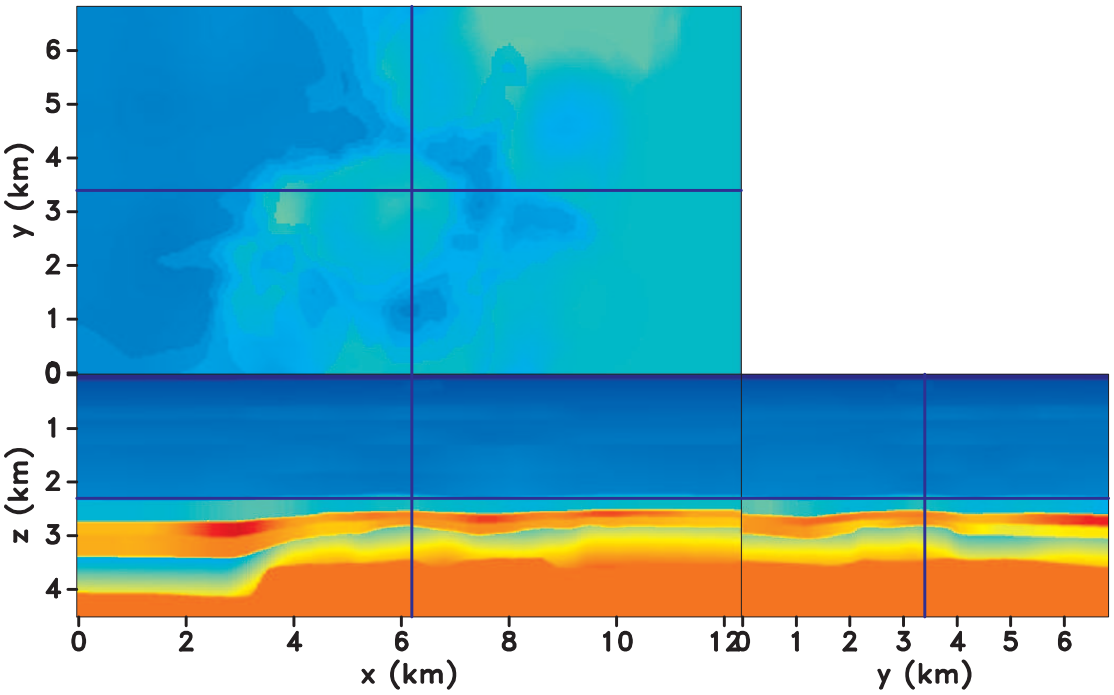


Figure 6.5: The gradient obtained after applying the mask.

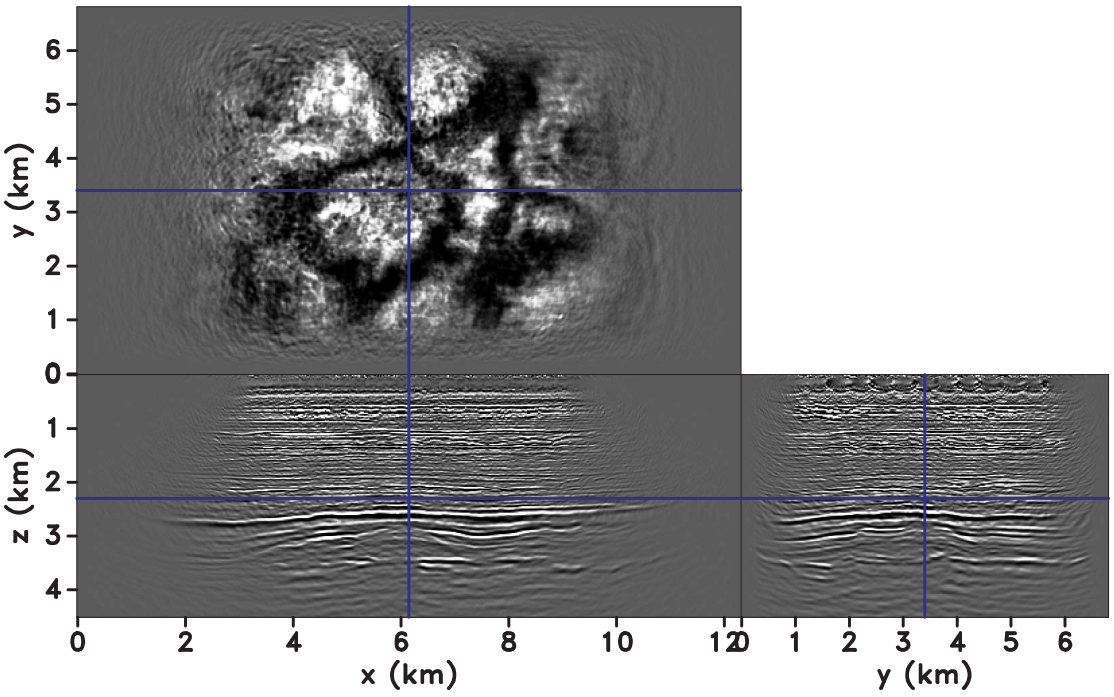
The migrated image in Figure 6.1(b) indeed shows that the second reflector is too shallow, at $z = 1.0$ km. Figure 6.2 shows a gather located at the center of the model. Given the gathers, we can extract the focusing error $\Delta\tau$ by measuring the lag of the focus from zero τ. The Yellow dash line overlain on the gathers is the focusing error extracted by an automatic picker. In this case, the focusing error accurately captures the velocity information: as there is no velocity model error associated with the first layer, the corresponding reflection focus is located at zero time lag. In contrast, the reflection focus of second layer is shifted along the positive τ direction indicating that the migration velocity is lower than that of the true model. After the focusing error is obtained, we construct the objective function and compute the gradient following the workflow discussed in the previous section. Figure 6.3(a) plots the gradient obtained for one gather at the center and one shot located at $x = 1.1$ km, $y = 2.25$ km which corresponds to the sensitivity kernel of the method. One may notice, however, that there is also kernels connecting the source and receivers to the image point of

the first layer. This is because the focusing error picked at that point although small is not perfectly zero. Such a small error is still taken into account by the gradient computation and converted into model updates as well. Figure 6.3(b) plots the gradient obtained for all gathers and all shots. Here, the gradient is negative, which indicates that the velocity of the initial model should be increased. This result is consistent with the error in the initial model which is lower than the true model. Nonetheless, the gradient in Figure 6.3(b) shows a strong update in the area between $z = 0$ km and $z = 0.5$ km. This phenomena is attributed to two reasons. The first reason is that the focusing error picked for the first layer is not zero, just as the case of the sensitivity kernel. Second, the sensitivity kernels for the second layer are distributed along the path from the source to image points to receivers. The kernels for the first and second layers stack in the area of the first layer and leads to a much stronger update than that in the area of the second layer. Such a update is not consistent with the velocity error distribution. The focusing error for the whole model, which also characterizes the velocity model error distribution, is plotted in Figure 6.4(a). The focusing error in the first layer is close to zero because there is no velocity error in this area. This demonstrates that the computed gradient is not consistent with the velocity error distribution. As a result, we need to restrict the updates in the second layer only. Using the focusing error as a priori information, we construct the gradient mask using 6.11, as shown in Figure 6.4(b). Because the mask is zero in the first layer, this effectively removes the updates there. The final preconditioned gradient, after applying the mask, is plotted in Figure 6.5. The update is now limited to the second layer only, has resulted in a faster convergence for the inversion.

The North Sea 3D OBC field dataset was acquired in the Volve field, and the construction of the initial model is described in Szydlik et al. (2007). The original models are anisotropic and include V_p, ϵ, and δ models. Here we assume that the medium is isotropic and use the V_p model only as the initial model to test our algorithm. The size of the model is 12.3 km in in-line, 6.8 km in cross-line, and 4.5 km in depth. The original dataset consists of 2880 common-receiver gathers, here we only use 240 gathers. Figure 6.6(a) and Figure 6.6(b) show the

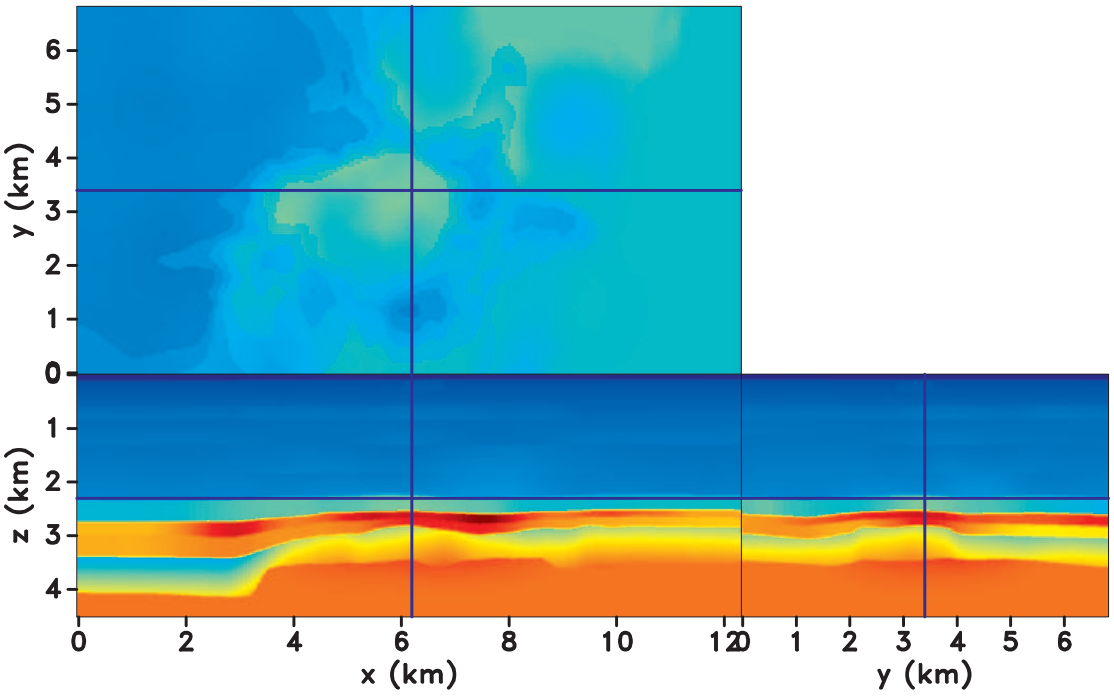


(a)

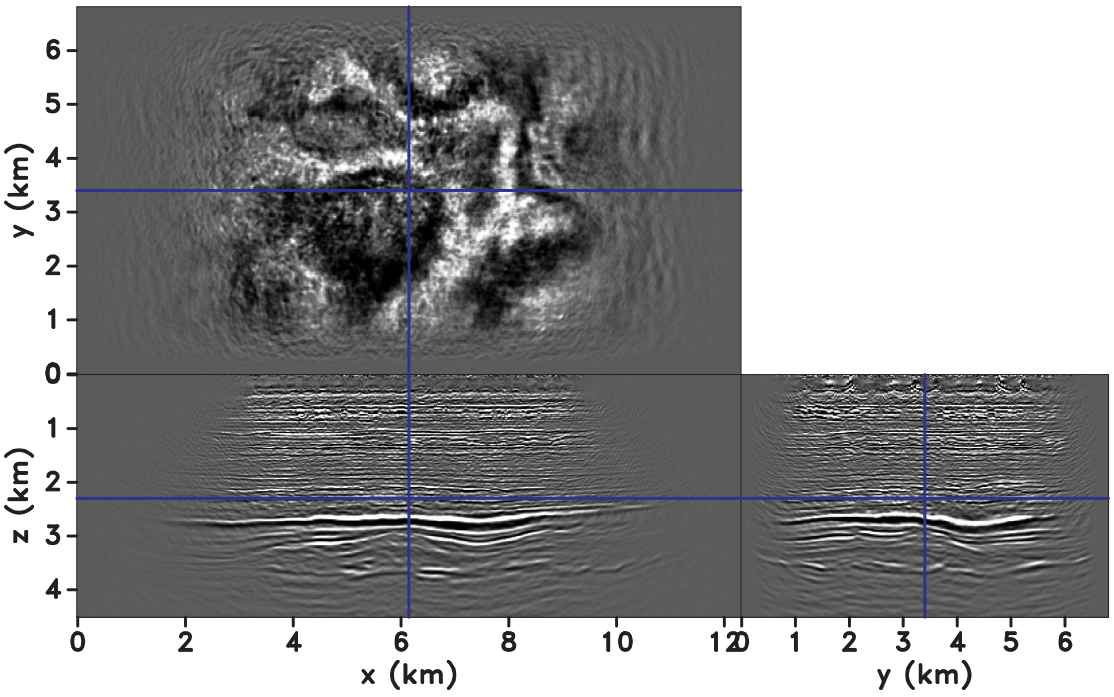


(b)

Figure 6.6: North Sea field data example. (a) The inital model used for the inversion, and (b) the migrated image obtained with the initial model.

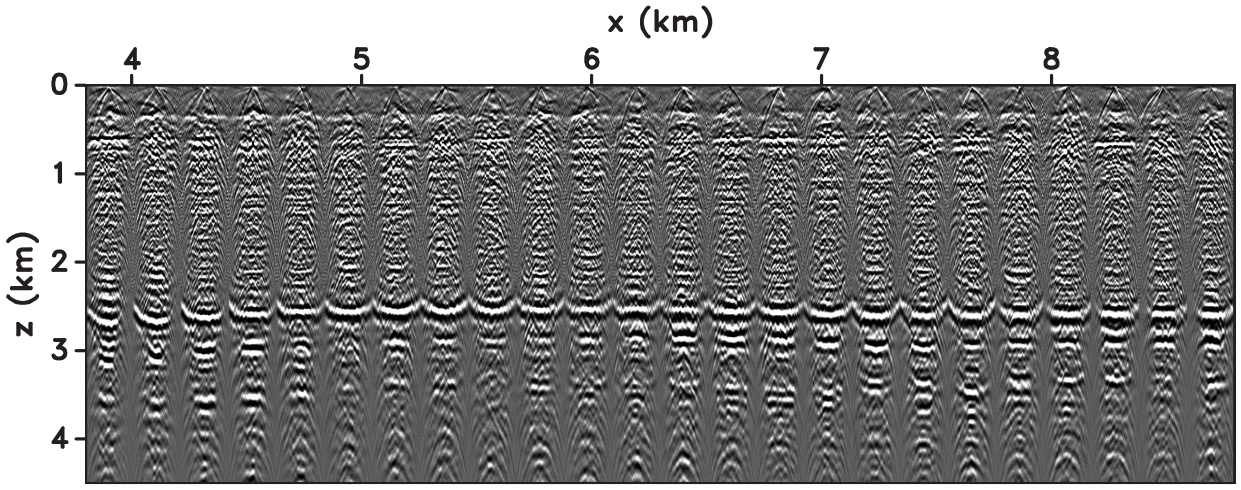


(a)

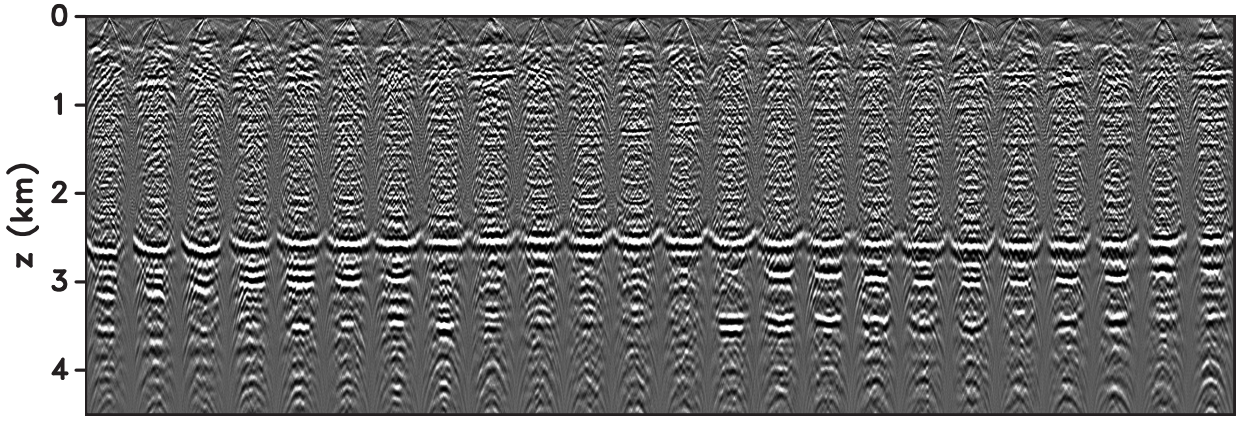


(b)

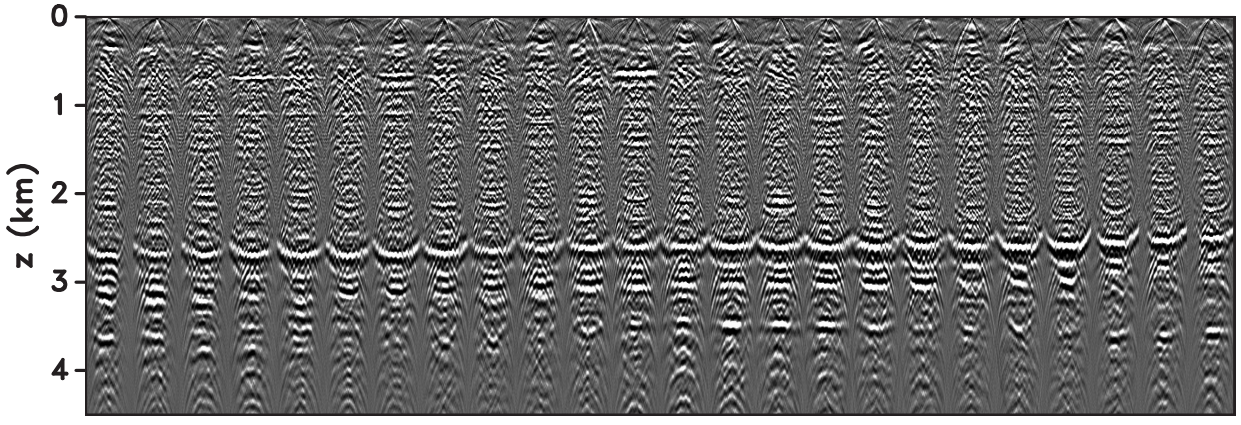
Figure 6.7: North Sea field data example. (a) The updated model obtained after the inversion, and (b) the migrated image obtained with the updated model.



(a)

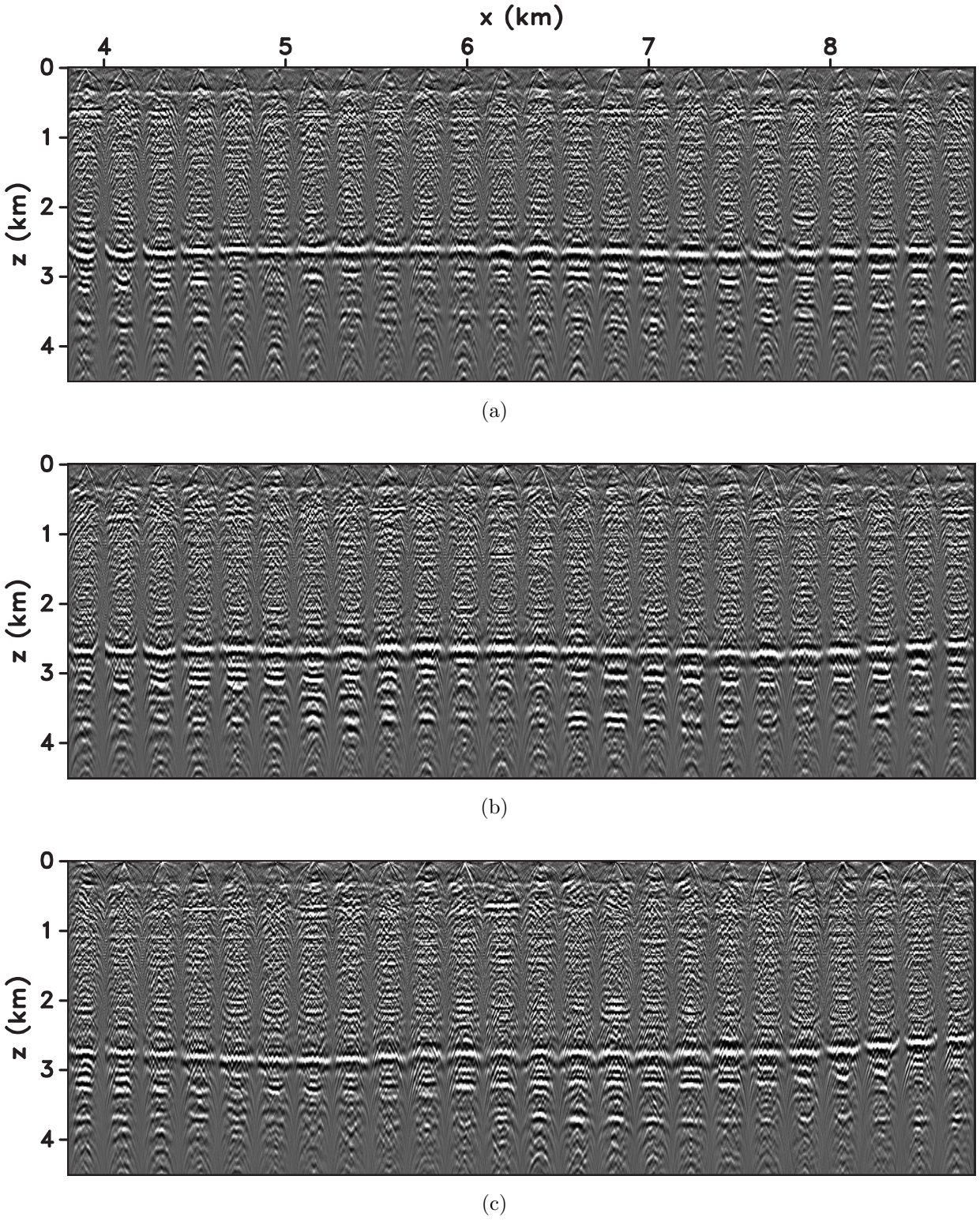


(b)



(c)

Figure 6.8: Angle-domain gathers obtained with the initial model at (a) $y = 3$ km, (b) $y = 6$ km, and (c) $y = 9$ km.



(a)

(b)

(c)

Figure 6.9: Angle-domain gathers obtained with the updated model at (a) $y = 3$ km, (b) $y = 6$ km, and (c) $y = 9$ km.

initial model obtained by a layer-stripping method and the corresponding migrated image. The color scale of Figure 6.6(a) is the same as that used in Figure 6.1(a). Using the objective function and gradient computation discussed in the previous section, we run the inversion for five iterations. The updated velocity model and its corresponding migrated image are plotted in Figure 6.7(a) and Figure 6.7(b). Observe that the velocity is increased around the center part of the model after the inversion. This significantly improves the image quality, as the main reflections around $z = 2.8$ km are more focused and coherent. The continuity of the deeper reflections is improved as well. To further assess the improvement resulting from the inversion, we also construct angle-domain common-image gathers before and after the inversion to evaluate the model accuracy. Figure 6.8(a)-Figure 6.8(c) and Figure 6.9(a)-Figure 6.9(c) plot the gathers sampled along in-line direction at three different cross-line locations using the initial and updated models, respectively. Notice that the main reflection around $z = 2.8$ km is characterized by flatter gathers after the inversion, indicative of the success of the method in improving model accuracy.

6.5 Discussion

We have demonstrated an image-domain wavefield tomography approach that can be considered as an alternative to wave-equation traveltime inversion implemented in the image domain. We used the focusing error to measure the traveltime error, which also evaluates the velocity model error. That is, we have formulated the objective function by minimizing the focusing error.

Our method shares many similarities with wave-equation traveltime inversion, e.g., the objective function construction and gradient computation. The main difference between these two techniques, however, lies in how the focusing information is extracted. In wave-equation traveltime inversion, the traveltime residual $\Delta\tau$ is obtained from the cross-correlation between individual recorded and simulated shot gathers. In comparison, our method estimates the focusing error $\Delta\tau$ from the time-lag gathers, which are the cross-correlation of extrapolated source and receiver wavefields stacked over all experiments. In general, the

signal-to-noise ratio in common-image gathers are higher than that in shot gathers. Thus, the approach proposed here is expected to render more accurate estimation of focusing information in presence of the noise and complex geology. Besides, wave-equation traveltime inversion is designed to extract the traveltime information from transmission waves, which can be used only in cross-well geometry or for first arrivals in surface acquisition. Our approach, in contrast, extracts the traveltime information from reflected waves, and thus is capable of inverting the velocity model in deeper target regions.

Furthermore, our method requires less computational efforts than that of differential semblance optimization (DSO). DSO uses space-lag gathers and needs to compute the lags in both the inline and crossline directions in 3D. This leads to an 5D hypercube which is too expensive to compute and store. In comparison, our method uses time-lag gathers and requires only the time lag to evaluate velocity information even in 3D. As a result, the computational and storage cost is at least one order of magnitude lower than the case of space-lag gathers.

6.6 Conclusions

We develop a 3D image-domain velocity model building technique based on time-lag extended images and test it on a North Sea field dataset. The method extracts focusing information from time-lag extended images, which characterize the traveltime residual due to the velocity model error. The velocity is optimized when the focusing error is minimal. We formulate the optimization problem by minimizing the focusing error and compute the gradient using the adjoint-state method, which puts our technique in the larger wavefield tomography family of techniques. The focusing information is also used as a priori information to precondition the gradient such that the model update is target-oriented. The field data example illustrate that the method is effective to improve the model accuracy and image quality. In addition, the method is computationally efficient in 3D velocity model building applications.

6.7 Acknowledgments

The authors would also like to thank Statoil ASA and the Volve license partners ExxonMobil E&P Norway and Bayerngas Norge, for the release of the Volve data.

6.8 Disclaimer

The views expressed in this paper belong to the authors and do not necessarily reflect the views of Statoil ASA and the Volve field license partners.

CHAPTER 7
GENERAL CONCLUSIONS

In this thesis, I design different wavefield-based velocity model building methods using various subsets of extended images.

7.1 Main Results

The main contributions of this thesis are summarized as follows.

7.1.1 Moveout characterization of extended images

In Chapter 2, I analyze the kinematics of reflections in extended images and derive the analytic formula characterizing the moveout. I show that the reflection form a cone in the extended image space, and the velocity model error shifts the cone along time-lag axis. The analysis build a connection between two common image features due to velocity error: the residual moveout in space-lag subset and defocusing in time-lag subset of extended images. The investigation also establishes the theoretical foundation for the velocity model updating schemes developed in the following chapters of the thesis.

7.1.2 Velocity analysis using time-lag gathers

In Chapter 3, I design a velocity analysis method based on minimizing the focusing error in time-lag extended images. The approach first extracts the focusing information from the gathers, then uses this information to construct an image perturbation which is a representation of velocity model error in the image domain. The inverse problem is formulated as a linearized problem using the Born approximation. The slowness perturbation is solved by conjugate- gradient method and used to update the model. I test the method using the synthetic Sigsbee model and show that it can be an effective velocity model building tool for complex geology. In Chapter 6, I develop a 3D image-domain wavefield-based velocity

analysis approach using a similar idea. To avoid the linearization used for the method in Chapter 3 and to improve the accuracy, I reformulate the problem using an objective function which directly minimized the focusing error in the gathers. The more sophisticated gradient computation is done by the application of the adjoint-state method. I test the method with a 3D OBC field dataset and demonstrate that the method is effective to improve the velocity model and optimize the coherence of the image. In addition, the technique is affordable and more efficient than differential semblance optimization in 3D velocity model building.

7.1.3 Velocity analysis using space- and time-lag extended images

In Chapter 4, I design a velocity analysis method using common-image-point gathers constructed with both the space and time lags. Because of the similarity between point gathers and space-lag gathers in characterizing the velocity information, I formulate the optimization problem using the differential semblance optimization scheme which originally applies to space-lag gathers. Since the point gathers are constructed using only the space and time lags, they overcome the dip limitation in space-lag gathers and contain fewer artifacts for steeply dipping reflections. In addition, the point gathers are computationally cheap attributed to their sparse sampling in the subsurface. The synthetic Marmousi example demonstrate that point gathers in velocity analysis can produce results comparable to space-lag gathers, while achieving lower computational cost. Thus, the method using point gathers can be an efficient alternative to conventional differential semblance optimization using space-lag gathers in velocity model building.

7.1.4 Illumination compensated wavefield tomography

In Chapter 5, I develop an illumination compensation method to improve the robustness of conventional differential semblance optimization using space-lag gathers in presence of uneven illumination. I analyze the mechanism of defocusing due to uneven illumination which is generally caused by missing data or by complex subsurface structure. I include illumination analysis in the inversion by replacing the conventional differential semblance penalty with

an illumination-based penalty. The defocusing due to illumination is isolated by the new penalty operator and therefore does not bias the inversion. In this way, only the defocusing from velocity error are penalized and contribute to the model updates. I test the method on the synthetic Sigsbee model, and the results demonstrate that the approach effectively mitigates the negative illumination effects in the inversion and improve the accuracy of the updated velocity model.

7.2 Future Work

For this thesis, I mainly focus on acoustic isotropic wavefield-based velocity analysis using extended images. I realize some problems potentially for future research work.

7.2.1 More waves: from reflection to full wavefields

In this thesis, I only use the reflection events in the extended images to extract velocity model information. Given a two-way wave-equation imaging algorithm, diving waves, turning waves, multiples, etc. can be generated in the wavefields used for imaging and thus appear in the extended images. These waves also carry information about the accuracy of the velocity model. As a result, they provide more constraints on inversion and should improve the accuracy and resolution of the model building. Since these waves have different kinematics from reflections, one has to understand their characteristics in the gathers first. More importantly, the connections between the velocity model error and corresponding image features must be investigated as well. Once the relationship is established, the principle of velocity analysis methods introduced here should be valid and can be used to design new velocity model building methods.

7.2.2 More parameters: from isotropy to anisotropy

In this thesis, all the methods are designed based on the isotropic assumption, and thus they only reconstruct the P-wave velocity model. Among other parameters such as S-wave velocity, anisotropy, attenuation, density, which more accurately represent the subsurface

structure, anisotropy has a great impact on the image quality. Ignoring anisotropy degrades the focusing of the image and mispositions the reflection. As the image quality is sensitive to the accuracy of the anisotropic model, the velocity model building techniques developed here can be potentially extended to anisotropic medium. To achieve this goal, however, one needs to study how different model errors affect the gathers in order to design effective model building methods using the information from the gathers. In addition, increasing the number of model parameters results in a larger null space in the inversion, which requires preconditioning and regularization to help convergence of the inversion.

7.2.3 More domains: from image domain to image and data domains

Full waveform inversion is a powerful data-domain velocity model building tool which can construct high resolution model in complex geology. To avoid the cycle-skipping problem, however, successful full waveform inversion requires a very accurate initial model and very low frequency components in the data. In contrast, image-domain approaches as introduced in this thesis, are very robust with respect to the initial model and do not require low-frequency data. As a result, a combination of these two techniques should result in velocity analysis methods which leverage the advantages and avoid the deficiencies of these techniques. The key issues are to explore how the different methods can be combined or cascaded, and to design automatic workflow without human interference.

REFERENCES CITED

Al-Yahya, K. M., 1989, Velocity analysis by iterative profile migration: Geophysics, **54**, 718–729.

Berkhout, A., 1982a, Seismic migration: Imaging of acoustic energy by wavefield extrpolation a: Theoretical aspects, 2nd edition: Elsevier Science Publ. CO., Inc.

Berkhout, A. J., 1982b, Imaging of acoustic energy by wave field extrapolation: Elsevier.

Biondi, B., and P. Sava, 1999, Wave-equation migration velocity analysis: 69th Annual International Meeting, SEG, Expanded Abstracts, 1723–1726.

Biondi, B., and G. Shan, 2002, Prestack imaging of overturned reflections by reverse time migration: 72th Annual International Meeting, SEG, Expanded Abstracts, 1284–1287.

Biondi, B., and W. Symes, 2004, Angle-domain common-image gathers for migration velocity analysis by wavefield-continuation imaging: Geophysics, **69**, 1283–1298.

Bishop, T. N., K. P. Bube, R. T. Cutler, R. T. Langan, P. L. Love, J. R. Resnick, R. T. Shuey, D. A. Spindler, and H. W. Wyld, 1985, Tomographic determination of velocity and depth in laterally varying media: Geophysics, **50**, 903–923. (Slide set available from SEG Publications Department).

Brown, M. P., J. H. Higginbotham, and R. G. Clapp, 2008, Velocity model building with wave equation migration velocity focusing analysis: 78th Annual International Meeting, SEG, Expanded Abstracts, 3078–3082.

Chauris, H., M. S. Noble, G. Lambare, and P. Podvin, 2002, Migration velocity analysis from locally coherent events in 2-D laterally heterogeneous media, Part I: Theoretical aspects: Geophysics, **67**, 1202–1212.

Claerbout, J. F., 1985, Imaging the Earth's interior: Blackwell Scientific Publications.

Cullison, T., and P. Sava, 2011, An image-guided method for automatically picking common-image-point gathers: Presented at the 81th Annual International Meeting, SEG, Expanded Abstracts.

Etgen, J., S. H. Gray, and Y. Zhang, 2009, An overview of depth imaging in exploration geophysics: Geophysics, **74**, WCA5–WCA17.

Faye, J. P., and J. P. Jeannot, 1986a, Prestack migration velocities from focusing depth analysis: 56th Ann. Internat. Mtg., Soc. of Expl. Geophys., Session:S7.6.

———, 1986b, Prestack migration velocities from focusing depth analysis: 56th Annual International Meeting, SEG, Expanded Abstracts, 438–440.

Fomel, S., 2004, Theory of 3-D angle gathers in wave-equation imaging: 74th Annual International Meeting, SEG, Expanded Abstracts, Soc. of Expl. Geophys., 1053–1056.

———, 2007, Shaping regularization in geophysical-estimation problems: Geophysics, **72**, R29–R36.

Gao, F., and W. Symes, 2009, Differential semblance velocity analysis by reverse time migration: Image gathers and theory: 77th Annual International Meeting, SEG, Expanded Abstracts, 2317–2320.

Gherasim, M., U. Albertin, B. Nolte, and O. Askim, 2010, Wave-equation angle-based illumination weighting for optimized subsalt imaging: Presented at the 80th Annual International Meeting, SEG, Expanded Abstracts.

Gray, S. H., J. Etgen, J. Dellinger, and D. Whitmore, 2001, Seismic migration problems and solutions: Geophysics, **66**, 1622–1640.

Guitton, A., 2004, Amplitude and kinematic corrections of migrated images for nonunitary imaging operators: Geophysics, **69**, 1017–1024.

Higginbotham, J. H., and M. P. Brown, 2008, Wave equation migration velocity focusing analysis: 78th Annual International Meeting, SEG, Expanded Abstracts, 3083–3086.

———, 2009, Wave-equation simulation and angle-domain imaging for acquisition testing, velocity analysis, and more: 71th EAGE Conference and Exhibition, Extended Abstracts, U040–U043.

Jiao, J., P. L. Stoffa, M. K. Sen, and R. K. Seifoullaev, 2002, Residual migration-velocity analysis in the plane-wave domain: Geophysics, **67**, 1252–1269.

Knyazev, A. V., and I. Lashuk, 2007, Steepest descent and conjugate gradient methods with variable preconditioning: Matrix Analysis and Applications, **29**, 1267–1280.

Lafond, C. F., and A. R. Levander, 1993, Migration moveout analysis and depth focusing: Geophysics, **58**, 91–100.

Leveille, J. P., I. F. Jones, Z. Z. Zhou, B. Wang, and F. Liu, 2011, Subsalt imaging for exploration, production, and development: A review: Geophysics, **76**, WB3–WB20.

Liu, Z., 1997, An analytical approach to migration velocity analysis: Geophysics, **62**, 1238–1249.

Liu, Z., and N. Bleistein, 1995, Migration velocity analysis: Theory and an iterative algorithm: Geophysics, **60**, 142–153.

Luo, Y., and G. Schuster, 1991, Wave equation traveltime inversion: Geophysics, **56**, 645–653.

MacKay, S., and R. Abma, 1992, Imaging and velocity estimation with depth-focusing analysis: Geophysics, **57**, 1608–1622.

———, 1993, Depth-focusing analysis using a wavefront-curvature criterion: Geophysics, **58**, 1148–1156.

Mora, P. R., 1987, Nonlinear two-dimensional elastic inversion of multioffset seismic data: Geophysics, **52**, 1211–1228.

Mulder, W. A., 2008, Automatic velocity analysis with the two-way wave equation: Presented at the 70th EAGE Conference and Exhibition, Extended Abstracts.

Mulder, W. A., and A. P. E. ten Kroode, 2002, Automatic velocity analysis by differential semblance optimization: Geophysics, **67**, 1184–1191.

Nemeth, T., 1995a, Velocity estimation using tomographic depth-focusing analysis: 65th Ann. Internat. Mtg, Soc. of Expl. Geophys., 465–468.

———, 1995b, Velocity estimation using tomographic depth-focusing analysis: 65th Annual International Meeting, SEG, Expanded Abstracts, 465–468.

———, 1996, Relating depth-focusing analysis to migration velocity analysis: 66th Ann. Internat. Mtg, Soc. of Expl. Geophys., 463–466.

Nemeth, T., C. Wu, and G. T. Schuster, 1999, Least-square migration of incomplete reflection data: Geophysics, **64**, 208–221.

Paffenholz, J., B. McLain, J. Zaske, and P. Keliher, 2002, Subsalt multiple attenuation and imaging: Observations from the sigsbee 2b synthetic dataset: 72nd Annual International Meeting, SEG, Expanded Abstracts, 2122–2125.

Plessix, R.-E., 2006, A review of the adjoint state method for computing the gradient of a functional with geophysical applications: Geophysical Journal International, **167**, 495–503.

———, 2009, Three-dimensional frequency-domain full-waveform inversion with an iterative solver: Geophysics, **74**, WCC53–WCC61.

Pratt, R. G., 1999, Seismic waveform inversion in the frequency domain, Part 1: Theory and verification in a physical scale model: Geophysics, **64**, 888–901.

Rickett, J., and P. Sava, 2002, Offset and angle-domain common image-point gathers for shot-profile migration: Geophysics, **67**, 883–889.

Sava, P., 2003, Prestack residual migration in the frequency domain: Geophysics, **67**, 634–640.

Sava, P., and B. Biondi, 2004a, Wave-equation migration velocity analysis - I: Theory: Geophysical Prospecting, **52**, 593–606.

———, 2004b, Wave-equation migration velocity analysis - II: Subsalt imaging examples: Geophysical Prospecting, **52**, 607–623.

Sava, P., B. Biondi, and J. Etgen, 2005, Wave-equation migration velocity analysis by focusing diffractions and reflections: Geophysics, **70**, U19–U27.

Sava, P., and S. Fomel, 2003, Angle-domain common image gathers by wavefield continuation methods: Geophysics, **68**, 1065–1074.

———, 2006, Time-shift imaging condition in seismic migration: Geophysics, **71**, S209–S217.

Sava, P., and I. Vasconcelos, 2011, Extended imaging condition for wave-equation migration: Geophysical Prospecting, **59**, 35–55.

Sava, P., and I. Vlad, 2008, Numeric implementation of wave-equation migration velocity analysis operators: Geophysics, **73**, VE145–VE159.

Schleicher, J., 2008, Residual depth moveout and velocity determination for parametric media: Geophysics, **73**, VE361–VE367.

Shen, H., S. Mothi, and U. Albertin, 2011, Improving subsalt imaging with illumination-based weighting of rtm 3d angle gathers: Presented at the 81th Annual International Meeting, SEG, Expanded Abstracts.

Shen, P., and H. Calandra, 2005, One-way waveform inversion within the framework of adjoint state differential migration: 75th Annual International Meeting, SEG, Expanded Abstracts, 1709–1712.

Shen, P., C. Stolk, and W. Symes, 2003, Automatic velocity analysis by differential semblance optimization: 73th Annual International Meeting, SEG, Expanded Abstracts, 2132–2135.

Shen, P., and W. Symes, 2008, Automatic velocity analysis via shot profile migration: Geophysics, **73**, VE49–VE59.

Sirgue, L., and R. Pratt, 2004, Efficient waveform inversion and imaging: A strategy for selecting temporal frequencies: Geophysics, **69**, 231–248.

Song, Z. M., P. R. Williamson, and R. G. Pratt, 1995, Frequency-domain acoustic-wave modeling and inversion of crosshole data: Part Ii: Inversion method, synthetic experiments and real-data results: Geophysics, **60**, 796–809.

Soubaras, R., and B. Gratacos, 2007, Velocity model building by semblance maximization of modulated-shot gathers: Geophysics, **72**, U67–U73.

Stolk, C. C., and W. W. Symes, 2004, Kinematic artifacts in prestack depth migration: Geophysics, **69**, 562–575.

Stolt, R. H., 1996, Short note - A prestack residual time migration operator: Geophysics, **61**, 605–607.

Stork, C., 1992, Reflection tomography in the postmigrated domain: Geophysics, **57**, 680–692.

Stork, C., and R. W. Clayton, 1991, An implementation of tomographic velocity analysis: Geophysics, **56**, 483–495.

Symes, W., 2009, Migration velocity analysis and waveform inversion: Geophysical Prospecting, **56**, 765–790.

Symes, W. W., 2008, Migration velocity analysis and waveform inversion: Geophysical Prospecting, **56**, 765–790.

Symes, W. W., and J. J. Carazzone, 1991, Velocity inversion by differential semblance optimization: Geophysics, **56**, 654–663.

Szydlik, T., P. Smith, S. Way, L. Aamodt, and C. Friedrich, 2007, 3d pp/ps prestack depth migration on the volve field: First break, **25**, 43–47.

Tang, Y., and B. Biondi, 2009, Least-squares migration/inversion of blended data: 80th Annual International Meeting, SEG, Expanded Abstracts, 2859–2863.

———, 2011, Target-oriented wavefield tomography using synthesized born data: Geophysics, **76**, WB191–WB207.

Tarantola, A., 1984, Inversion of seismic reflection data in the acoustic approximation: Geophysics, **49**, 1259–1266.

Toldi, J. L., 1989, Velocity analysis without picking: Geophysics, **54**, 191–199.

van Leeuwen, T., and W. A. Mulder, 2010, A correlation-based misfit criterion for wave-equation traveltime tomography: Geophysical Journal International, **182**, 1383–1394.

Vasconcelos, I., P. Sava, and H. Douma, 2010, Nonlinear extended images via image-domain interferometry: Geophysics, **75**, SA105–SA115.

Vigh, D., and E. W. Starr, 2008a, 3D prestack plane-wave, full-waveform inversion: Geophysics, **73**, VE135–VE144.

———, 2008b, Comparisons for waveform inversion, time domain or frequency domain?: 78th Annual International Meeting, SEG, Expanded Abstracts, 1890–1894.

Virieux, J., and S. Operto, 2009, An overview of full-waveform inversion in exploration geophysics: Geophysics, **74**, WCC1–WCC26.

Wang, B., Y. Kim, C. Mason, and X. Zeng, 2008, Advances in velocity model-building technology for subsalt imaging: Geophysics, **73**, VE173–VE181.

Wang, B., C. Mason, M. Guo, K. Yoon, J. Cai, J. Ji, and Z. Li, 2009, Subsalt velocity update and composite imaging using reverse-time-migration based delayed-imaging-time scan: Geophysics, **74**, WCA159–WCA166.

Wang, B., F. Qin, V. Dirks, P. Guilaume, F. Audebert, and D. Epili, 2005, 3d finite angle tomography based on focusing analysis: 78th Annual International Meeting, SEG, Expanded Abstracts, 2546–2549.

Woodward, M., D. Nichols, O. Zdraveva, P. Whitfield, and T. Johns, 2008, A decade of tomography: Geophysics, **73**, VE5–VE11.

Woodward, M. J., 1992, Wave-equation tomography: Geophysics, **57**, 15–26.

Xia, X., Y. Ren, and S. Jin, 2008, Tomographic migration-velocity analysis using comman angle image gathers: 78th Annual International Meeting, SEG, Expanded Abstracts, 3103–3106.

Xie, X. B., and H. Yang, 2008, The finite-frequency sensitivity kernel for migration residual moveout and its applications in migration velocity analysis: Geophysics, **73**, S241–S249.

Yang, T., and P. Sava, 2009, Wave-equation migration velocity analysis using extended images: 79th Annual International Meeting, SEG, Expanded abstracts, 3715–3719.

———, 2010, Moveout analysis of wave-equation extended images: Geophysics, **75**, S151–S161.

———, 2011a, Wave-equation migration velocity analysis with time-shift imaging: Geophysical Prospecting, **59**, 635–650.

———, 2011b, Waveform inversion in the image domain: Presented at the 73th EAGE Conference and Exhibition, Extended Abstracts.

Yang, T., J. Shragge, and P. Sava, 2012, Illumination compensation for image-domain wavefield tomography: Presented at the 74th Mtg., Abstracts, Eur. Assoc. Expl. Geophys.

Yilmaz, O., 2001, Seismic Data Analysis (2nd edition): Society of Exploration Geophysicists.

Yilmaz, O., and R. E. Chambers, 1984, Migration velocity analysis by wave-field extrapolation: Geophysics, **49**, 1664–1674.

Yoon, K., and K. J. Marfurt, 2006, Reverse-time migration using the poynting vector: Exploration Geophysics, **37**, 102–107.

Yu, J., and T. Schuster, 2003, Migration deconvolution vs. least squares migration: Presented at the 74th Annual International Meeting, SEG, Expanded Abstracts.

Zhang, Y., and D. Wang, 2009, Traveltime information-based wave-equation inversion: Geophysics, **74**, WCC27–WCC36.

APPENDIX - PERMISSION OF PAPERS

Below are the permissions for the papers in this thesis.

A.1 Permission From Publishers

The screen snapshots below show the permission grant to authors of the papers in the thesis from the publishers. Figure A.1 is the permission for Chapter 2 and Chapter 5. Figure A.2 is the permission for Chapter 3 and Chapter 4.

Authors' right to redistribute
Authors of articles in GEOPHYSICS, THE LEADING EDGE, and the Technical Program *Expanded Abstracts* may post their own articles on their personal Web sites or the Web sites of their institutions without obtaining further permission from SEG. Authors of journal articles and *Expanded Abstracts* retain similar rights for print redistribution. If an author or an author's institution redistributes an author's article online or in print, the original publication venue encompassed in a complete citation and including SEG's status as publisher must be identified. Authors of SEG books, or portions of SEG books, must seek permission from the SEG publications director to redistribute these works in any form. Such permission will not be withheld if SEG's investment in the original publication of the works is not threatened. Questions should be directed to the publications director.

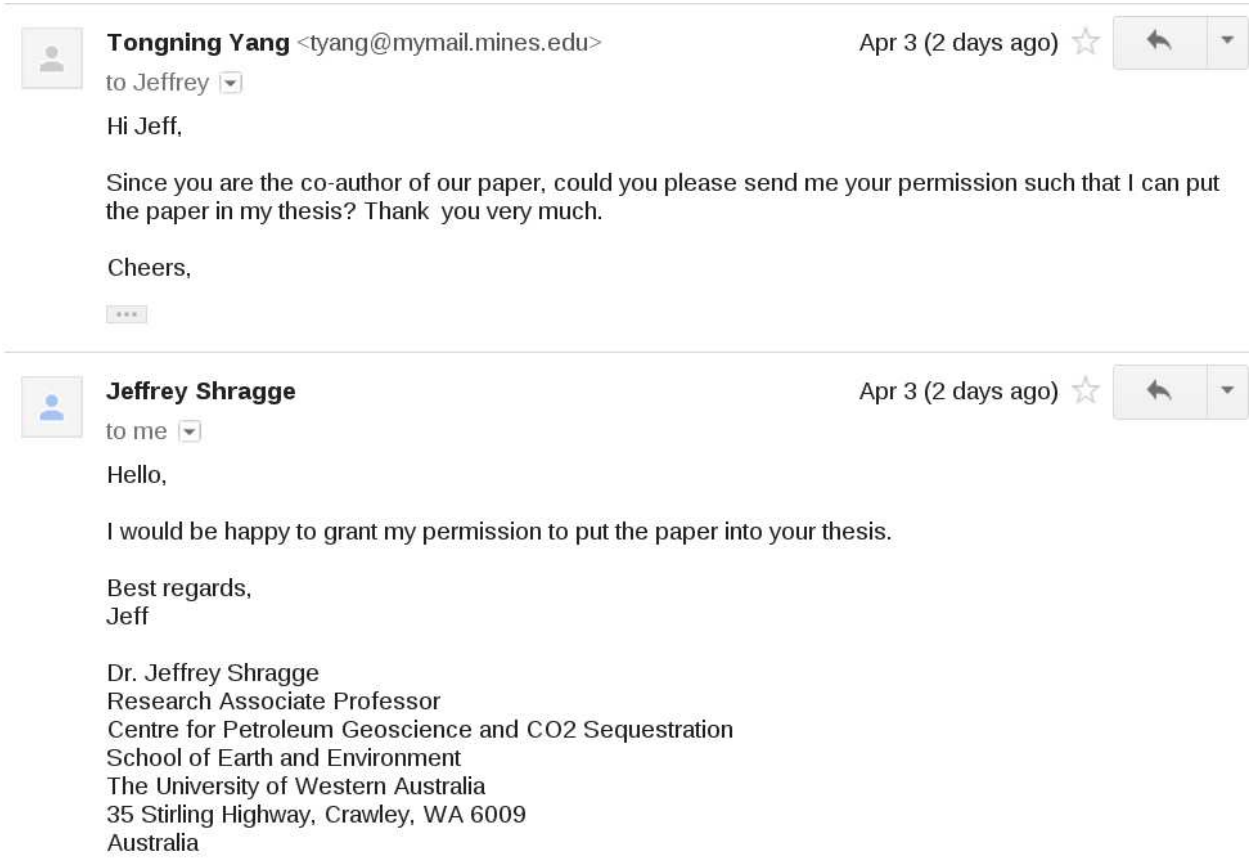
Figure A.1: Permission from journal *Geophysics*.

AUTHORS - If you wish to reuse your own article (or an amended version of it) in a new publication of which you are the author, editor or co-editor, prior permission is not required (with the usual acknowledgements). However, a formal grant of license can be downloaded free of charge from RightsLink if required.

Figure A.2: Permission from journal *Geophysical Prospecting*.

A.2 Permission From Co-authors

The screen snapshots below show the permission grant to the papers in the thesis from the co-authors. Figure A.3 is the permission for Chapter 5. Figure A.4 is the permission for Chapter 2, Chapter 3, Chapter 4, Chapter 5, and Chapter 6.



Tongning Yang <tyang@mymail.mines.edu> Apr 3 (2 days ago)

to Jeffrey

Hi Jeff,

Since you are the co-author of our paper, could you please send me your permission such that I can put the paper in my thesis? Thank you very much.

Cheers,

Jeffrey Shragge Apr 3 (2 days ago)

to me

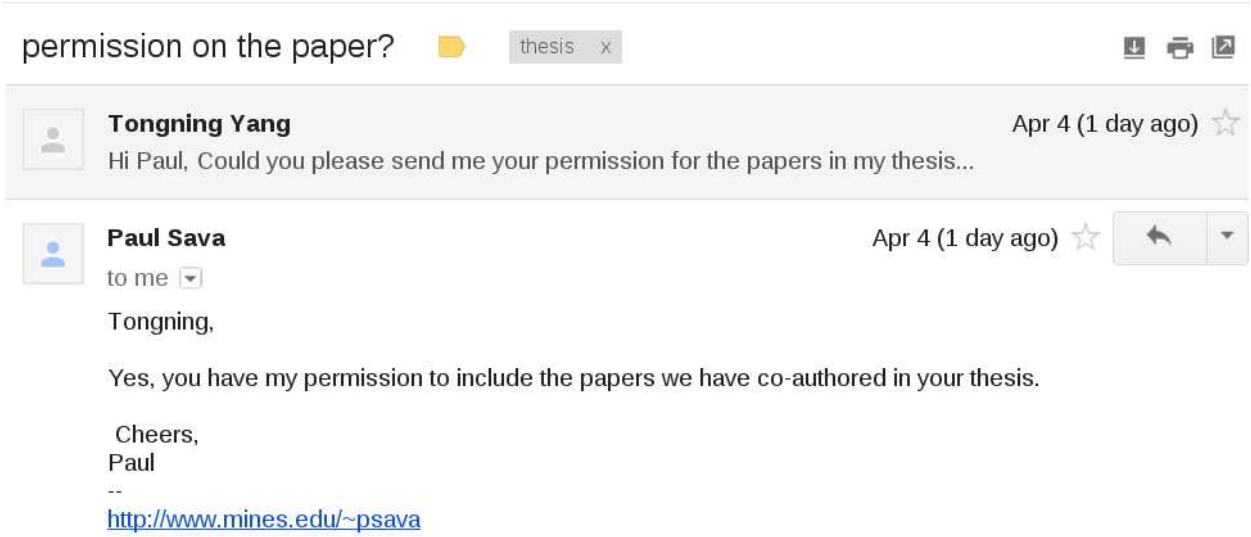
Hello,

I would be happy to grant my permission to put the paper into your thesis.

Best regards,
Jeff

Dr. Jeffrey Shragge
Research Associate Professor
Centre for Petroleum Geoscience and CO2 Sequestration
School of Earth and Environment
The University of Western Australia
35 Stirling Highway, Crawley, WA 6009
Australia

Figure A.3: Permission from co-author Jeffrey Shragge.



permission on the paper? thesis x

Tongning Yang Apr 4 (1 day ago)

Hi Paul, Could you please send me your permission for the papers in my thesis...

Paul Sava Apr 4 (1 day ago)

to me

Tongning,

Yes, you have my permission to include the papers we have co-authored in your thesis.

Cheers,
Paul
--
http://www.mines.edu/~psava

Figure A.4: Permission from co-author Paul Sava.